NEW METHODS FOR TRACKING GALAXY AND BLACK HOLE EVOLUTION USING POST-STARBURST GALAXIES

by

Katheryn Decker French

A Dissertation Submitted to the Faculty of the

DEPARTMENT OF ASTRONOMY

In Partial Fulfillment of the Requirements
For the Degree of

DOCTOR OF PHILOSOPHY
WITH A MAJOR IN ASTRONOMY AND ASTROPHYSICS

In the Graduate College

THE UNIVERSITY OF ARIZONA

2017

THE UNIVERSITY OF ARIZONA
GRADUATE COLLEGE

As members of the Dissertation Committee, we certify that we have read the dissertation prepared by Katheryn Decker French, titled New Methods for Tracking Galaxy and Black Hole Evolution using Post-Starburst Galaxies and recommend that it be accepted as fulfilling the dissertation requirement for the Degree of Doctor of Philosophy.

_____   Date: 9 May 2017
   Ann Zabludoff

_____   Date: 9 May 2017
   Yancy Shirley

_____   Date: 9 May 2017
   Daniel Marrone

_____   Date: 9 May 2017
   Daniel Stark

_____   Date: 9 May 2017
   Stephanie Juneau

Final approval and acceptance of this dissertation is contingent upon the candidate's submission of the final copies of the dissertation to the Graduate College.

I hereby certify that I have read this dissertation prepared under my direction and recommend that it be accepted as fulfilling the dissertation requirement.

_____   Date: 9 May 2017
   Dissertation Director: Ann Zabludoff

STATEMENT BY AUTHOR

This dissertation has been submitted in partial fulfillment of requirements for an advanced degree at the University of Arizona and is deposited in the University Library to be made available to borrowers under rules of the Library.

Brief quotations from this dissertation are allowable without special permission, provided that accurate acknowledgment of source is made. Requests for permission for extended quotation from or reproduction of this manuscript in whole or in part may be granted by the head of the major department or the Dean of the Graduate College when in his or her judgment the proposed use of the material is in the interests of scholarship. In all other instances, however, permission must be obtained from the author.

SIGNED: Katheryn Decker French

ACKNOWLEDGEMENTS

TABLE OF CONTENTS

TABLE OF CONTENTS – *Continued*

TABLE OF CONTENTS – *Continued*

LIST OF FIGURES

3.1 Hδ absorption vs. Hα emission equivalent width for our parent sample of 595,268 galaxies in the SDSS DR10. The region outlined in black shows our post-starburst selection criteria. To select galaxies with little-to-no current star formation, we require Hα EW < 3 Å. To select galaxies with a recent ($\lesssim$ Gyr) starburst population indicated by strong Balmer absorption lines, we require Hδ_A $-$ σ(Hδ_A) > 4 Å, where σ(Hδ_A) is the measurement error of the Hδ_A index. Post-starburst galaxies are located on this spur of the distribution of blue cloud and red sequence galaxies. We show two example tracks of a 100 Myr burst added to an old stellar population, with a mass fraction of 5 or 10%. A starburst must form a substantial fraction of the galaxy's stars, and be over a short duration, in order to go through the post-starburst spur. Star-forming galaxies in the parent sample are at higher Hα absorption, and moderate Hδ_A (the turnover in Hδ_A at high Hα is due to absorption line filling). Quiescent galaxies have little Hα emission and little Hδ absorption. Due to our use of the A-star optimized Hδ_A index, these galaxies extend to negative values. 96

3.18 (Previous page.) Post-burst ages vs. molecular gas fractions and WISE colors for three samples of starburst/post-starburst galaxies. The left panels show the full set of galaxies, broken down into those with burst mass fractions $\leq 20\%$ (middle panel) and $> 20\%$ (right panel). The top panels show molecular gas mass fractions vs. post-burst age for three samples: post-starburst galaxies (blue squares) from French et al. (2015), shocked post-starbursts (teal stars) from Alatalo et al. (2016b), and starburst/post-starbursts (pink diamonds) from Rowlands et al. (2015). We observe a significant trend in the molecular gas fraction with the post-burst age, at 4σ significance. Split up into the two burst fraction bins, the significance drops to 2.7σ in each bin. Early type galaxies are typically gas-poor, with molecular gas fractions of $\lesssim 10^{-3}$ (Young et al., 2011). With the observed molecular gas depletion rate, the post-starburst galaxies should reach early-type levels of molecular gas in $600-800$ Myr. The middle panels show the WISE [4.6]-[12] μm colors vs. post-burst age for the post-starburst galaxies studied in this work, shocked post-starbursts from Alatalo et al. (2016c), and starburst/post-starbursts from Rowlands et al. (2015). The bottom panels show the WISE [3.4]-[4.6] μm colors vs. post-burst age for the same samples. We see significant ($> 3\sigma$) anti-correlations for each of the WISE colors with post-burst age, and for all of the burst mass fraction bins. These WISE colors represent a combination of the dust mass and dust heating. Various heating sources can act to change the WISE colors: star-formation, young (A) stars, evolved stars (post-AGB or TP-AGB), or AGN. Given the anti-correlations of bluer WISE colors with post-burst age, either the dust mass could be declining with the gas mass, and/or the sources of dust heating could be declining. Early type galaxies have WISE [3.4]-[4.6] colors of $-0.1-0$, and [4.6]-[12] colors of $0-1$. If the WISE [4.6]-[12] colors decline linearly with post-burst age, they should reach colors typical of early types at ~ 1 Gyr post-burst. The WISE [3.4]-[4.6] colors have significantly more scatter, and it is not clear when

LIST OF TABLES

ABSTRACT

Galaxies in transition from star-forming to quiescence are a natural laboratory for exploring the processes responsible for this evolution. Using a sample of post-starburst galaxies identified to have recently experienced a recent burst of star formation that has now ended, I explore both the fate of the molecular gas that drives star formation and the increased rate of stars disrupted by the central super-massive black hole. Chapter 1 provides an introduction to galaxy evolution through the post-starburst phase and to tidal disruption events, which surprisingly favor post-starburst galaxy hosts.

In Chapter 2, I present a survey of the molecular gas properties of 32 post-starburst galaxies traced by CO (1–0) and CO (2–1). In order to accurately put galaxies on an evolutionary sequence, we must select likely progenitors and descendants. We do this by identifying galaxies with similar starburst properties, such as the amount of mass produced in the burst and the burst duration. In Chapter 3, I describe a method to determine the starburst properties and the time elapsed since the starburst ended, and discuss trends in the molecular gas properties of these galaxies with time. In Chapter 4, I present the results of followup observations with ALMA of HCN (1–0) and HCO+ (1–0) in two post-starburst galaxies. CO (1–0) is detected in over half (17/32) the post-starburst sample and the molecular gas mass traced by CO declines on $\sim$100 Myr timescales after the starburst has ended. HCN (1–0) is not detected in either galaxy targeted, indicating the post-starbursts are now quiescent because of a lack of the denser molecular gas traced by HCN.

In Chapter 5 I quantify the increase in TDE rate in quiescent galaxies with strong Balmer absorption to be $30 - 200\times$ higher than in normal galaxies. Using the stellar population fitting method from Chapter 3, I examine possible reasons for the increased TDE rate in post-starburst galaxies in Chapter 6. The TDE rate could

be boosted due to a binary supermassive black hole coalescing after a major merger or an increased density of stars or gas remaining near the nucleus after the starburst has ended. In Chapter 7, I present a summary of the findings of this dissertation and an outlook for future work.

CHAPTER 1

Introduction

1.1   Post-Starburst Galaxies

Observational surveys of galaxies reveal two broad classes: star-forming and quiescent. This bimodality in color extends to star-formation properties, gas properties, kinematics, morphologies, and connects to mean shifts in stellar mass and absolute magnitude. Post-starburst (or "E+A") galaxies have been caught in the midst of a rapid transition between these classes of star-forming and quiescent. They are not currently forming stars at a significant rate, as indicated by their lack of nebular emission lines. Yet, their strong Balmer absorption lines reveal a substantial population of A stars, indicating these galaxies have experienced a burst of star formation sometime in the past billion years (Dressler & Gunn, 1983; Couch & Sharples, 1987). Post-starburst galaxies show disturbed morphologies and tidal features in at least half of the studied cases, providing evidence that mergers and interactions can drive this transition (Zabludoff et al., 1996; Yang et al., 2004, 2008). Their range of angular momentum properties is likewise consistent with a variety of possible merger histories (Pracy et al., 2009; Swinbank et al., 2012; Pracy et al., 2013).

Post-starburst galaxies represent our best candidates for the rapid, non-secular, mode of galaxy evolution (Schawinski et al., 2014; Smethurst et al., 2015) that half to all red sequence galaxies are expected to experience (Martin et al., 2007; Snyder et al., 2011; Wild et al., 2016). Post-starburst galaxies are generally found in the "green valley" (Wong et al., 2012) of the optical color-magnitude diagram, indicating stellar populations that could redden and evolve passively onto the red sequence. Post-starburst galaxy morphologies (Yang et al., 2004, 2008) and spatially resolved

kinematics (Norton et al., 2001; Swinbank et al., 2012) are also consistent with evolution into early-type galaxies.

A critical part of galaxy evolution is the end, or possible "quenching," of star formation. As transitional objects, post-starburst galaxies serve as a unique laboratory for understanding the processes that drive this cessation. Explanations for the end of the starburst fall into two general categories: elimination of the molecular gas or suppression of star formation.

One possibility is that the starburst uses up the dense molecular clouds in forming stars (Kennicutt, 1998; Gao & Solomon, 2004). Another possibility is that the molecular gas is removed from the galaxy in outflows (Narayanan et al., 2008) driven by AGN or star formation activity (a.k.a. "feedback"). Evidence of LINER activity and large outflows are seen in post-starbursts (Yan et al., 2006; Yang et al., 2006; Tremonti et al., 2007), and AGN are observed to eject molecular gas in outflows (Feruglio et al., 2010), although the driver of the outflows in post-starbursts may be due to star formation, not AGN activity (Sell et al., 2014). Some environmental effects, such as starvation (e.g., Larson et al., 1980; Boselli & Gavazzi, 2006), are thought to eliminate molecular gas reservoirs in galaxies. The molecular gas mass is several orders of magnitude lower in early types than in late types (e.g., Young et al., 2011; Crocker et al., 2011). If post-starbursts are becoming early types, they must lose or consume most of their gas.

Feedback mechanisms could be responsible for suppressing star formation in addition to perhaps removing the gas supply, ending the starburst. Molecular gas heating and suppressed star formation efficiency have been claimed in galaxies with AGN (Nesvadba et al., 2010), resulting in higher observed molecular gas surface densities than the Kennicutt-Schmidt relation (Kennicutt, 1998) would predict for their star formation rate (SFR) densities. In post-starburst galaxies, 0.3-1 Gyr has passed since the starburst ended, so if AGN feedback has significantly reduced the molecular gas reservoirs, we should observe the galaxies in their depleted state.

A lower star formation efficiency is suggested in gas-rich, fast-rotating early type galaxies by Davis et al. (2014), who observe lower SFR surface densities than the molecular gas surface densities would predict by a factor of ~ 2.5. These authors favor dynamical methods of lowering star formation efficiency in this sample of galaxies, such as morphological quenching (Martig et al., 2009), where the gravitational stability of the gas prevents it from collapsing and forming stars. In early type galaxies with AGN and recent small bursts of star formation, the molecular gas supply declines steeply with the age since the last period of star formation (Schawinski et al., 2009). Although post-starburst galaxies are likely to evolve into early types, it is not clear that the samples studied by Davis et al. (2014) or Schawinski et al. (2009) are on the same evolutionary sequence as post-starbursts.

Post-starburst galaxies are also useful laboratories for studying how galaxies evolve to quiescence, after star formation has been shut down, especially when we can connect galaxies in a time sequence from the starburst phase to quiescence. The ability to connect time sequences of starbursting and post-starburst galaxies is important to understand the physics of how star formation shuts down, by identifying the likely timescales for various physical mechanisms. While simulations often assume the molecular gas reservoirs are depleted via star formation, stellar feedback, and AGN feedback, ending the starburst (e.g., Hopkins et al., 2006), recent evidence has emerged that AGN activity may be delayed after the end of the starburst. QSOs with post-starburst signatures have older stellar populations than some samples of post-starburst galaxies (Cales & Brotherton, 2015), which similarly indicates a delay between the end of the starburst and the period of QSO activity. Studies of AGN activity in galaxies with ongoing and recent starbursts (Davies et al., 2007; Wild et al., 2010) indicate a delay of 50-300 Myr between the onset of star-formation and the onset of AGN activity. The intermediate stellar ages of Seyfert and LINER galaxies (Schawinski et al., 2009) also suggest such a delay. In simulations, the delay between the starburst or merger, and the peak of AGN activity or feedback,

depends on the details of how AGN feedback is implemented (see e.g., Pontzen et al., 2016; Sparre & Springel, 2016). To make progress, we need to compare the gas reservoirs of post-starbursts in an evolutionary sequence. Identifying the period over which they lose their gas, and determining whether the loss can be explained by consumption by residual star formation, is critical.

In Chapter 2, I present a survey of the molecular gas properties of 32 post-starburst galaxies using IRAM 30m and SMT observations of CO (1–0) and CO (2–1). In order to accurately put galaxies on an evolutionary sequence, we must select likely progenitors and descendants. In Chapter 3, we do this by identifying galaxies with similar starburst properties, such as the amount of mass produced in the burst, and the burst duration. I create a method to determine the starburst properties and the time elapsed since the starburst ended, and discuss trends in the molecular gas properties of these galaxies with time. In Chapter 4, I present the results of followup observations with ALMA of HCN (1–0) and HCO+ (1–0) in two post-starburst galaxies. These chapters shed new light on what processes could have ended star formation in these galaxies.

1.2 Tidal Disruption Events

In addition to being useful laboratories for studying galaxy evolution, recent studies have found a large number of tidal disruption events in galaxies with post-starburst signatures (Arcavi et al., 2014). If a star passes close enough to a supermassive black hole that the tidal forces overcome the self-gravity of the star, the star will be destroyed in a tidal disruption event (TDE; Hills, 1975). Such events are expected to generate an observable flare (Rees, 1988; Evans & Kochanek, 1989; Phinney, 1989) if the tidal radius is greater than the Schwarzschild radius.

Real-time discoveries of TDE candidates have enabled extensive followup observations and classification. The first was *Swift* J1644 (Bloom et al., 2011; Burrows et al., 2011; Levan et al., 2011; Zauderer et al., 2011), displaying non-thermal emis-

sion in γ-rays, X-rays, and the radio. Two additional events had similar properties: *Swift* J2058 (Cenko et al., 2012b) and *Swift* J1112 (Brown et al., 2015). Hereafter we refer to these events as "high energy TDEs".

In parallel, a different class of transients were also identified as likely TDEs. The first was PS1-10jh (Gezari et al., 2012), which had thermal optical and UV emission, but no observed X-rays. Since the discovery of PS1-10jh, many more objects with similar TDE spectral features have been found. Arcavi et al. (2014) discovered three in Palomar Transient Factory (PTF) data, PTF09axc, PTF09djl, and PTF09ge, grouping them together as a class with PS1-10jh, SDSS J0748 (identified in the Sloan Digital Sky Survey (SDSS); Wang et al., 2011), and ASASSN-14ae (Holoien et al., 2014). Recently, additional members of this class have been discovered: ASASSN-14li (Holoien et al., 2016), and PTF15af (in the galaxy SDSS J084828.13+220333.4; Blagorodnova et al., in prep). This optical/UV-selected class of transients all display hot blackbody ($\sim$ few $\cdot$ 10^4K) emission and several-month-long smooth light curves peaking at an absolute optical magnitude of ~ -20. They are all located in the centers of their host galaxies. Their clear broad H and/or He emission lines (Arcavi et al., 2014) cleanly distinguish them from other transient events. Hereafter we refer to these events as "optical/UV TDEs".

Curiously, the host galaxy spectra of these optical/UV-bright events show Balmer line absorption, and all but SDSS J0748 have weak or no emission lines. Similarly, the host galaxy of the high energy TDE candidate *Swift* J1644 was reported to have significant Balmer absorption with a low current star formation rate (SFR) predicted from its Hα flux (Levan et al., 2011). Yoon et al. (2015) find a young < 1 Gyr stellar population, suggesting a recent starburst. The two other known high energy TDE candidates do not yet have host galaxy spectra covering the full Balmer series.

The clear preference of optical/UV TDE candidates and at least one high energy TDE candidate for rare Balmer-strong galaxies like post-starbursts has important

implications for the mechanisms driving TDE rates. In Chapter 5, I quantify the increase in TDE rate in quiescent Balmer-strong galaxies. Using the stellar population fitting method from Chapter 3, I examine possible reasons for the increased TDE rate in post-starburst galaxies in Chapter 6.

CHAPTER 2

Discovery of Large Molecular Gas Reservoirs in Post-Starburst Galaxies

Post-starburst (or "E+A") galaxies are characterized by low Hα emission and strong Balmer absorption, suggesting a recent starburst, but little current star formation. Although many of these galaxies show evidence of recent mergers, the mechanism for ending the starburst is not yet understood. To study the fate of the molecular gas, we search for CO (1–0) and (2–1) emission with the IRAM 30m and SMT 10m telescopes in 32 nearby ($0.01 < z < 0.12$) post-starburst galaxies drawn from the Sloan Digital Sky Survey. We detect CO in 17 (53%). Using CO as a tracer for molecular hydrogen, and a Galactic conversion factor, we obtain molecular gas masses of $M(H_2) = 10^{8.6}$–$10^{9.8} M_\odot$ and molecular gas mass to stellar mass fractions of $\sim 10^{-2}$–$10^{-0.5}$, comparable to those of star-forming galaxies. The large amounts of molecular gas rule out complete gas consumption, expulsion, or starvation as the primary mechanism that ends the starburst in these galaxies. The upper limits on $M(H_2)$ for the 15 undetected galaxies range from $10^{7.7} M_\odot$ to $10^{9.7} M_\odot$, with the median more consistent with early-type galaxies than with star-forming galaxies. Upper limits on the post-starburst star formation rates (SFRs) are lower by $\sim 10\times$ than for star-forming galaxies with the same $M(H_2)$. We also compare the molecular gas surface densities (Σ_{H_2}) to upper limits on the SFR surface densities (Σ_{SFR}), finding a significant offset, with lower Σ_{SFR} for a given Σ_{H_2} than is typical for star-forming galaxies. This offset from the Kennicutt-Schmidt relation suggests that post-starbursts have lower star formation efficiency, a low CO-to-H$_2$ conversion factor characteristic of ULIRGs, and/or a bottom-heavy initial mass function, although uncertainties in the rate and distribution of current star formation remain.

2.1   Introduction

Post-starburst (or "E+A") galaxies show signs of being caught in the middle of a dramatic, but brief, stage in their evolution. Emission line indicators suggest little-to-no current star formation, but strong Balmer absorption lines indicate a population of A stars that formed in a substantial burst of star formation before a sudden stop $\sim$ 1 Gyr ago (Dressler & Gunn, 1983; Couch & Sharples, 1987).

Post-starburst galaxies are likely in transition between star-forming gas-rich disk galaxies and passively evolving gas-poor early types. Their disturbed morphologies indicate that many are post-merger, and most have spheroid-dominated kinematics (Zabludoff et al., 1996; Norton et al., 2001; Yang et al., 2004, 2008). Many have blue cores, which can fade into the color gradients observed in early type galaxies (Yamauchi & Goto, 2005; Yang et al., 2006, 2008), and many lie in the "green valley" of the color magnitude diagram (Wong et al., 2012). Although only $\sim$ 0.2% of local galaxies are post-starbursts, the short duration of this phase suggests that $\sim$ 40% of galaxies could have passed through it (Zabludoff et al., 1996; Snyder et al., 2011).

A critical part of galaxy evolution is the end, or possible "quenching," of star formation. As transitional objects, post-starburst galaxies serve as a unique laboratory for understanding the processes that drive this cessation. Explanations for the end of the starburst fall into two general categories: elimination of the molecular gas or suppression of star formation.

One possibility is that the starburst uses up the dense molecular clouds in forming stars (Kennicutt, 1998; Gao & Solomon, 2004). Molecular gas could also be removed

---

[1]A version of this chapter originally appeared as a published paper in the Astrophysical Journal (French et al., 2015). All of the work described below was carried out by me, with help from co-authors Yujin Yang, Ann Zabludoff, Desika Narayanan, Yancy Shirley, Fabian Walter, John-David Smith, and Christy Tremonti.

from the galaxy in outflows (Narayanan et al., 2008). Evidence of LINER activity and large outflows are seen in post-starbursts (Yan et al., 2006; Yang et al., 2006; Tremonti et al., 2007), and AGN are observed to eject molecular gas in outflows (Feruglio et al., 2010), although the driver of the outflows in post-starbursts may be due to star formation, not AGN activity (Sell et al., 2014). Some environmental effects, such as starvation (e.g., Larson et al., 1980; Boselli & Gavazzi, 2006), are thought to eliminate molecular gas reservoirs in galaxies. The molecular gas mass is several orders of magnitude lower in early types than in late types (e.g., Young et al., 2011; Crocker et al., 2011). If post-starbursts are becoming early types, they must lose or repurpose most of their gas.

Feedback mechanisms could be responsible for suppressing star formation, resulting in the end of the starburst. Molecular gas heating and suppressed star formation efficiency have been claimed in galaxies with AGN (Nesvadba et al., 2010), resulting in higher observed molecular gas surface densities than the Kennicutt-Schmidt relation (Kennicutt, 1998) would predict for their star formation rate (SFR) densities. Observations of cold gas in early type galaxies with AGN and recent bursts of star formation reveal little molecular gas ($< 10^9 M_\odot$), which declines steeply with the age since the last period of star formation (Schawinski et al., 2009). In our sample, the timescales necessary for outflows to expel the molecular gas from the galaxy are less than the time elapsed since the starburst ended (about 0.3-1 Gyr), so if AGN feedback has significantly reduced the molecular gas reservoirs, we should observe the galaxies in their depleted state.

A lower star formation efficiency is suggested in gas-rich, fast-rotating early type galaxies by Davis et al. (2014), who observe lower SFR surface densities than the molecular gas surface densities would predict by a factor of ~ 2.5. These authors favor dynamical methods of lowering star formation efficiency in this sample of galaxies, such as morphological quenching (Martig et al., 2009), where the gravitational stability of the gas prevents it from collapsing and forming stars. Although

post-starburst galaxies are likely to evolve into early types, it is not clear that the gas-rich sample studied by Davis et al. (2014) are on the same evolutionary sequence as post-starbursts.

We aim to test these explanations for the starbursts' end by constraining the properties of molecular gas within post-starbursts. Reservoirs of HI have been observed in post-starburst galaxies (Chang et al., 2001; Buyle et al., 2006; Zwaan et al., 2013). In six of the eleven post-starbursts targeted in these samples, HI 21 cm emission is detected, with atomic gas to stellar mass fractions typically between those of early and late type galaxies. However, HI is not a good tracer of star formation fuel (Kennicutt, Jr. et al., 2007), and we must look at molecular gas signatures to understand the starbursts' end.

Detailed CO maps have been measured for only a handful of local post-starburst galaxies (Kohno et al., 2002; Alatalo et al., 2013). Even then, the two galaxies studied, NGC5195 and NGC1266, are not universally agreed-upon as post-starbursts due to their Hα emission. The molecular gas in these galaxies is centrally concentrated, reaching starburst-like gas surface densities. Their kinematics led these authors to suggest morphological quenching (Martig et al., 2009), where the gravitational stability of the gas prevents it from collapsing and forming stars. There is a need for a survey of the molecular gas content in a representative sample of post-starburst galaxies.

We set out here to determine how much molecular gas remains in a sample of 32 post-starburst galaxies drawn from the Sloan Digital Sky Survey (SDSS, York et al., 2000), and to determine whether the molecular gas densities are consistent with the small or negligible levels of current star formation. We observe the CO (1–0) and CO (2–1) lines with the IRAM 30m telescope, and observe a subset of 13 galaxies in CO (2–1) with the SMT 10m telescope. By assuming that the CO traces H$_2$, we test whether the cessation of star formation was due to a lack of molecular gas, or to the gas being consumed by the burst, expelled in outflows, or prevented

from entering the galaxy (starvation of HI (Larson et al., 1980)). By comparing to the molecular gas vs SFR surface density relation for other galaxies, we will be able to determine if the star formation efficiency in post-starbursts is reduced by either gas heating, morphological quenching, or some other mechanism.

We discuss our sample and observations in §2.2. Measurements of molecular gas masses and comparisons to the SFRs are presented in §2.3. We test these results and consider their implications for galaxy evolution in §2.4, presenting our conclusions in §2.5. When needed, we assume a cosmology of $\Omega_m = 0.3$, $\Omega_\Lambda = 0.7$, and $h = 0.7$.

2.2 Observations and Data Analysis

2.2.1 Sample Selection

Our parent sample is drawn from the SDSS main galaxy spectroscopic sample (Strauss et al., 2002), which is selected to have a limiting magnitude of $r < 17.77$ mag. The initial sample was selected from the SDSS DR7 (Abazajian et al., 2009), using the line fluxes and indices from the MPA-JHU catalogs (Aihara et al., 2011). We exclude galaxies with $z < 0.01$ to eliminate those that are very large on the sky relative to the $3''$ diameter of the SDSS fibers. We also exclude galaxies with unreliable [2] Hα equivalent widths (EW), or median signal-to-noise (S/N) values of less than 10 per pixel. These cuts ensure that the line index measurements are reliable. Our final parent sample from DR10 is composed of 595,268 galaxies.

We select post-starburst galaxies from our parent sample by identifying galaxies with strong stellar Balmer absorption lines signifying a recent ($\lesssim$ Gyr) starburst but little nebular emission indicative of on-going star formation. We use the Lick Hδ index to characterize the stellar Balmer absorption. We require H$\delta_A - \sigma(H\delta_A) > 4\,\text{Å}$, where $\sigma(H\delta_A)$ is the measurement error of the Hδ_A index. We ensure that the galaxies have little on-going star formation by requiring Hα EW $< 3\,\text{Å}$ in the

---

[2]We require `h_alpha_eqw_err > -1`

rest frame. These selection criteria result in a sub-sample of 1207 galaxies from the parent sample (0.20%).

We have chosen two sub-samples for *HST*, *Spitzer*, and *Herschel* imaging, which we follow-up here. 15 galaxies designated "S" throughout were selected to represent a variety of ages since the end of the burst and based on their projected 8μm flux from SDSS spectra and serendipitous *Spitzer* observations. Galaxies with nearby companions and large [OIII] equivalent widths indicative of AGN activity were excluded. The post-burst ages are determined by fitting stellar population synthesis (SPS) models to the galaxy spectrum, assuming a combination of a young and old single burst stellar populations (French et al. in prep). 17 galaxies designated "H" throughout were selected from their bright WISE $12\mu m$ fluxes and again for a range of post-burst ages (although without the [OIII] equivalent width cut). More details on the "H" and "S" selection processes are available in Smercina et al. (in prep). The effect of these selection criteria on properties of the resultant sample is studied in §2.4.1. Basic parameters of this sample are listed in Table 1.

2.2.2   IRAM 30m CO Observations

Observations were carried out with the IRAM 30m telescope over two observing campaigns in January 2012 (project ID: 218-11) and in August – September 2012 (ID: 074-12). We use the Eight Mixer Receiver (EMIR) to observe both CO(1–0) and CO(2–1) lines (rest frequency: 115.271 and 230.538 GHz). For each target, we tuned the 3mm band (E090) and 1.3mm band (E230) receivers to the redshifted CO(1–0) and CO(2–1) frequencies, $\nu_{\rm obs} = 103.5 - 113.5\,{\rm GHz}$ and $207.1 - 227.1\,{\rm GHz}$, respectively. EMIR provides a bandwidth of $4\,$GHz in dual polarization corresponding to $\sim$11000 and 5500 $\rm km\,s^{-1}$ for CO(1–0) and CO(2–1) lines, respectively. The Wideband Line Multiple Autocorrelator (WILMA) was used as the backend, with a resolution of $2\,$MHz corresponding to $\sim$5 $\rm km\,s^{-1}$ in the 3mm band. Data were taken with a wobbler-switching mode with a frequency of $0.5\,$Hz or $1\,$Hz with a throw

distance of $120''$ in azimuth. The weather varied significantly: the precipitable water vapor (PWV) ranged from 1mm to 10mm with medians of 3mm (winter) and 6.8mm (summer). Calibration was performed every 15 min with standard hot/cold load absorbers. The pointing was checked every 2 hours and was found to be stable within $3''$. The FWHMs of beam are $\approx 22''$ and $11''$ for CO(1–0) and CO(2–1) lines, respectively.

We reduced the data with `CLASS` within the `GILDAS` software package[3] and IDL routines. We use the velocity intervals [-1200, -400] and [400, 1200] $\mathrm{km\,s^{-1}}$ to fit first order polynomials for baseline subtraction. The spectra are coadded weighted by the rms noise of each scan. The on-source time (T_{ON}) ranges from 12 to 100 min depending on the strength of the line toward the targets. If the source was not detected within 3 hours at the telescope ($T_{\mathrm{ON}} \approx 1\mathrm{hr}$), we moved on to the next target. The resulting rms noise per $5\,\mathrm{km\,s^{-1}}$ bin are $1.1 - 4.4\,\mathrm{mK}$ and $1.9 - 9.7\,\mathrm{mK}$ for the CO(1–0) and CO(2–1) observations, respectively (T_{A}^* scale). The conversion factors from K (T_{A}^* scale) to Jy at our observed frequencies are $\sim 7.7\,\mathrm{Jy\,K^{-1}}$ and $\sim 6.0\,\mathrm{Jy\,K^{-1}}$ for the 1.3 mm and 3 mm bands, respectively. We summarize the IRAM 30m CO observations in the Tables 2.5 and 2.3.

2.2.3 SMT CO Observations

Observations at the SMT 10-m telescope were performed over four runs in May 2011, February 2012, December 2012, and February 2013. We used the 1mm ALMA Band 6 dual polarization sideband separating SIS receiver and 1MHz filterbank to measure the CO(2–1) 230.5 GHz (redshifted to 207.1 – 227.1 GHz for our sample) line for 13 post-starburst galaxies. The beam size of the SMT for this line is $\approx 33''$. Beam switching was done with the secondary at 2.5 Hz and a throw of $120\ ''$. Calibration using a hot load and the standard chopper wheel method was performed every 6 minutes. Calibration using a cold load was performed at every tuning.

---

[3] `http://www.iram.fr/IRAMFR/GILDAS`

To reduce the data, we again use `CLASS`. The main beam efficiency η_{mb} is calculated using Jupiter in each polarization. We subtract a first-order polynomial baseline from the spectrum using data between $[-500, 500]\,\mathrm{km\,s^{-1}}$, excluding the central region of $[-300, 300]\,\mathrm{km\,s^{-1}}$. The spectra are scaled using η_{mb}, and coadded, weighting each spectra by the rms noise. We rebin the spectra by a factor of 10, to achieve $\approx 14\,\mathrm{km\,s^{-1}}$ velocity bins. Typical rms per 14 $\mathrm{km\,s^{-1}}$ channel is 1 mK. These observations are summarized in Table 2.3.

2.2.4 Galaxy Properties from the SDSS

We use a variety of data products from the SDSS to study properties of the post-starburst sample, including emission line fluxes, stellar masses, SFRs, and BPT classifications from the MPA-JHU group catalogs (described in Aihara et al., 2011). We use Petrosian (Petrosian, 1976) optical sizes measured in the r band from the SDSS photometric catalogs, and redshifts from DR7.

We use the stellar masses calculated from the SDSS spectra (method described in Kauffmann et al., 2003a; Salim et al., 2007) and included in the MPA-JHU data products. Because the star formation histories of post-starbursts may not be well represented by the templates assumed in the spectral fitting, we estimate the systematic error by comparing stellar masses from several different algorithms run on SDSS data. We compare the stellar masses from the MPA-JHU data products to those calculated by Chen et al. (2012), who use both the Bruzual & Charlot (2003) and Maraston & Strömbäck (2011) SPS models. All three stellar mass calculations use a Kroupa initial mass function (IMF). The systematic error from this method slightly exceeds the formal errors on the MPA-JHU measurements and is typically $\sim 30\%$.

2.2.5   Star Formation Rate Upper Limits

We use two different methods to calculate SFRs for the post-starburst sample, one employing the Hα luminosity and the other the $D_n(4000)$ break. Both are contaminated by other effects (principally LINER and A-stellar emission, see below), and serve as upper limits on the actual current SFR.

Using the emission line fluxes from the MPA-JHU dataset (Aihara et al., 2011), we calculate SFR limits from Hα luminosities using the relation from Kennicutt et al. (1994). We use the Balmer decrement of Hα/Hβ to calculate dust extinction, assuming the standard case B recombination at T$= 10^4$ K and an intrinsic value of 2.86. We use the reddening curve of O'Donnell (1994). For the cases where the Hβ line flux is uncertain, we use the mean value of $E(B-V)$ of the other post-starburst galaxies. The mean attenuation is then $A_V = 0.92$ mag, or $A_{H\alpha} = 0.77$ mag.

A complicating factor in determining the SFRs from Hα for the post-starburst sample is the high incidence of LINER spectra. A BPT diagram for the post-starburst sample is shown in Figure 2.1. Two galaxies lie in the transition region, and the rest are categorized as LINERs. Although the source of the LINER may not be an AGN (LINER emission is commonly seen in late stage mergers; Rich et al. 2011 and from post-AGB stars; Singh et al. 2013), processes in addition to star formation will contribute to nebular line fluxes here, making the derived SFRs upper limits.

The MPA-JHU group use the $D_n(4000)$ break as a less precise, but less contaminated way to estimate SFRs when galaxies do not lie in the star-forming sequence on the BPT diagram (Brinchmann et al., 2004). The $D_n(4000)$ break is a measure of the specific SFR (sSFR), and is calculated from regions of the rest-frame spectra bracketing the strong "break" observed near 4000Å. $D_n(4000)$ is not expected to be influenced by the presence of a Type II AGN (Kauffmann et al., 2003b). The conversion between $D_n(4000)$ and sSFR is calibrated from those galaxies in the SDSS categorized as star-forming. The scatter in this relation is large, and the error bars

we show on the $D_n(4000)$ SFRs (derived using the MPA-JHU stellar masses) reflect the low precision of this calibration.

The problem with using the $D_n(4000)$-based SFRs in post-starburst galaxies is its sensitivity to the bright A-stellar populations produced in the recent burst. During ongoing star formation, the 4000Å break is minimal, so $D_n(4000)$ is low. In passive galaxies, $D_n(4000)$ is large. However, the timescale over which $D_n(4000)$ is affected by a strong burst ($\sim$1 Gyr, see e.g., Kauffmann et al., 2003a) is larger than the post-burst ages of our sample, so $D_n(4000)$ here will reflect both previous and current rates of star formation. $D_n(4000)$ will be lower (more like star-forming galaxies) in post-starbursts than expected given their instantaneous SFRs. Lower values of $D_n(4000)$ correspond to higher SFRs, so $D_n(4000)$ will overestimate the current SFR due to the recent burst. We use $D_n(4000)$-based SFRs as upper limits on the current SFR.

To use the SDSS fiber spectra to calculate global SFRs, we must account for any star formation outside the $3''$ fiber aperture. Like Brinchmann et al. (2004), we see a trend of increasing fiber-based SFR per total stellar mass with redshift, after breaking up our complete SDSS post-starburst sample (1207 galaxies) into stellar mass bins. Thus, we expect some contribution to the SFR from outside of the fiber, so we require an aperture correction [4]. We apply the aperture correction used in the MPA-JHU SFRs (Brinchmann et al., 2004; Salim et al., 2007; Aihara et al., 2011), which is based on galaxy photometry outside the fiber. Although this aperture correction is calibrated on star-forming galaxies, it successfully removes the trend of sSFR with redshift for our complete post-starburst sample. While our use of this correction assumes that it also applies to our post-starbursts, the corrected SFRs remain likely upper limits as post-starbursts tend to have more positive color gradients (relatively bluer cores) than star-forming galaxies (Yang et al., 2006, 2008).

---

[4]We consider the case where star formation is limited to the fiber aperture in §2.4.2, see Figure 2.9b.

One case where Hα and $D_n(4000)$ would not provide upper limits on the SFRs is if we have significantly underestimated the dust extinction in post-starbursts. Radio continuum emission at 1.4 GHz is often used as an "extinction-free" SFR indicator (Condon, 1992). We search the FIRST (Faint Images of the Radio Sky at Twenty centimeters, Becker et al., 1995) and NVSS (NRAO VLA Sky Survey, Condon et al., 1998) 1.4GHz surveys for matches within $10''$ of each galaxy in our sample. We find 6 detections in the FIRST survey (S06, H01, H03, H07, H08, and H09). The galaxies H07, H08, and H09 are also detected in the NVSS. Using the conversion found in Condon (1992), the SFRs suggested by these detections are higher than the Hα SFRs. If we were to accept that the standard 1.4GHz - SFR relation is valid for the post-starburst sample, it would require these galaxies to have up to 4.7 magnitudes of additional extinction on top of the ~ 1 magnitude already accounted for using the Balmer decrement. While dust extinctions of 5-6 magnitudes are not unheard of, especially for starbursts, the dust extinction is consistent with that implied by Balmer decrement in those cases (Choi et al., 2006; Kennicutt et al., 2009). The huge difference between the extinction derived from the Balmer decrement and implied by the 1.4Ghz-SFR relation is unprecedented and suggests a problem with the SFRs derived from the 1.4GHz data for our post-starbursts.

The LINER and recent starburst in these galaxies complicates the standard 1.4GHz SFR conversion. Galaxies with LINER spectra have enhanced 1.4GHz fluxes when compared to other measures of their SFRs (de Vries et al., 2007; Morić et al., 2010). Morić et al. (2010) find that 90% of the 1.4GHz flux can come from the LINER, not from star formation, and that the scatter in the 1.4GHz-SFR relation for LINERs is large, of order 2 dex. For our sample, the 1.4GHz-based SFRs and limits scatter evenly about the Hα-based SFRs after the radio SFRs are reduced by the expected factor of 10. While the LINER will also contribute to the Hα flux, its contribution is typically $\lesssim 40\%$, with less scatter (Brinchmann et al., 2004), implying that Hα is more reliable than 1.4GHz as a SFR upper limit. Additionally, the recent

large starburst may boost the amount of 1.4GHz flux on timescales overlapping with the post-burst ages of our sample (Bressan et al., 2002). As discussed above in §2.2.1, the galaxies marked "S" were selected with a cut on the [OIII] equivalent widths, intended to exclude galaxies with strong AGN activity from the sample. This cut was not applied to the selection of galaxies marked "H," and the higher incidence of 1.4GHz detections in the "H" sample may be tied to a higher incidence of AGN.

Both the TIR luminosity (total IR, from 8-1000 μm; Hayward et al., 2014) and 24 μm flux (Utomo et al., 2014) are strongly affected by dust heating by the substantial A stellar population in post-starbursts, so we do not consider these SFR indicators here. Ongoing analysis of our sample observed in PAH emission and high ionization species (Smercina et al., in prep) will provide further constraints on any current SFR.

In the following analysis, we use the Hα-derived SFR as an upper limit, as well as showing the effect of assuming the $D_n(4000)$-based SFRs.

2.3 Results

2.3.1 Detection of Molecular Gas

We detect molecular gas at $> 3\sigma$ in 17 of the 32 galaxies observed, using IRAM 30m measurements of the CO (1–0) line. If we increase our detection threshold to 4σ, we detect 14 galaxies, and at $> 5\sigma$, we detect 11 galaxies. To calculate the integrated CO line intensity I_{CO}, we fit a Gaussian profile to each line, allowing the center velocity to differ from the optical velocity up to 200 $\mathrm{km\,s^{-1}}$. We use the Gaussian width σ_{gauss} to choose integration limits of $\pm 3\sigma_{\mathrm{gauss}}$. Although many of the line shapes are not exactly Gaussian, this method allows us to estimate appropriate velocity intervals for integration in a systematic way. FWHMs given by these fits are listed in Tables 2.5 and 2.3. If the signal to noise ratio for σ_{gauss} is < 3, we use the interval [-260, 260] $\mathrm{km\,s^{-1}}$ These velocity limits were chosen to be the median
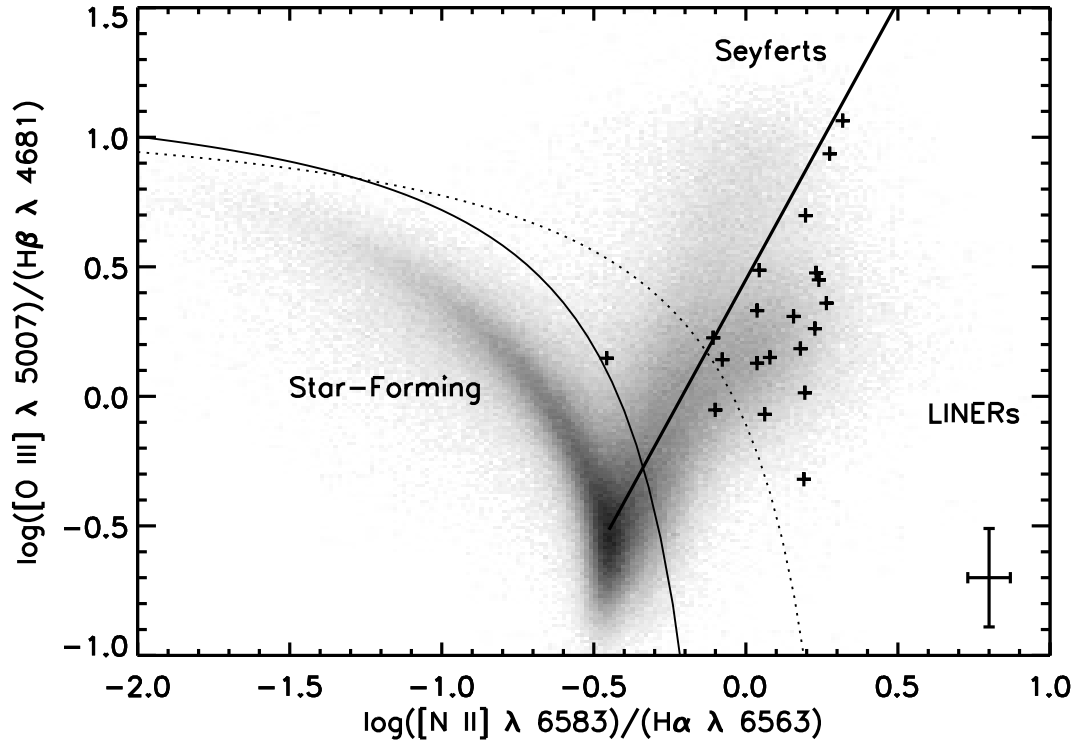
Figure 2.1: BPT (Baldwin et al., 1981) diagram for post-starburst sample, measured from SDSS spectra. Galaxies from the SDSS DR7 (Abazajian et al., 2009) with well-measured lines are shown as a shaded background. The lines separating star-forming and AGN-like activity from Kewley et al. (2001) and Kauffmann et al. (2003b) are shown as dotted and solid lines, respectively. The line at $\Phi = 25$ degrees separates Seyferts from LINERs. The post-starburst sample is plotted as individual points, for galaxies with all lines detected at $> 3\sigma$, with a characteristic errorbar shown in the bottom right. Most of the post-starburst sample, except S12, is solidly in the LINER category. The presence of LINERs complicates our calculation of the current SFR, as the nebular emission lines will be contaminated.

Figure 2.2: 60″ by 60″ SDSS postage stamps of the 17 post-starburst galaxies with CO (1–0) detected at $> 3\sigma$ with the IRAM 30m. The size of the 3″ SDSS fiber is overplotted in blue, and the size of the IRAM 30m CO (1–0) 22″ beam is overplotted in orange. Galaxies are ordered by decreasing $M(\mathrm{H_2})$. Given the size estimates in §2.4.2, we could be underestimating L'_{CO} by factors of $\sim 1.1 - 2.2\times$, with a median of 1.4, due to aperture effects.
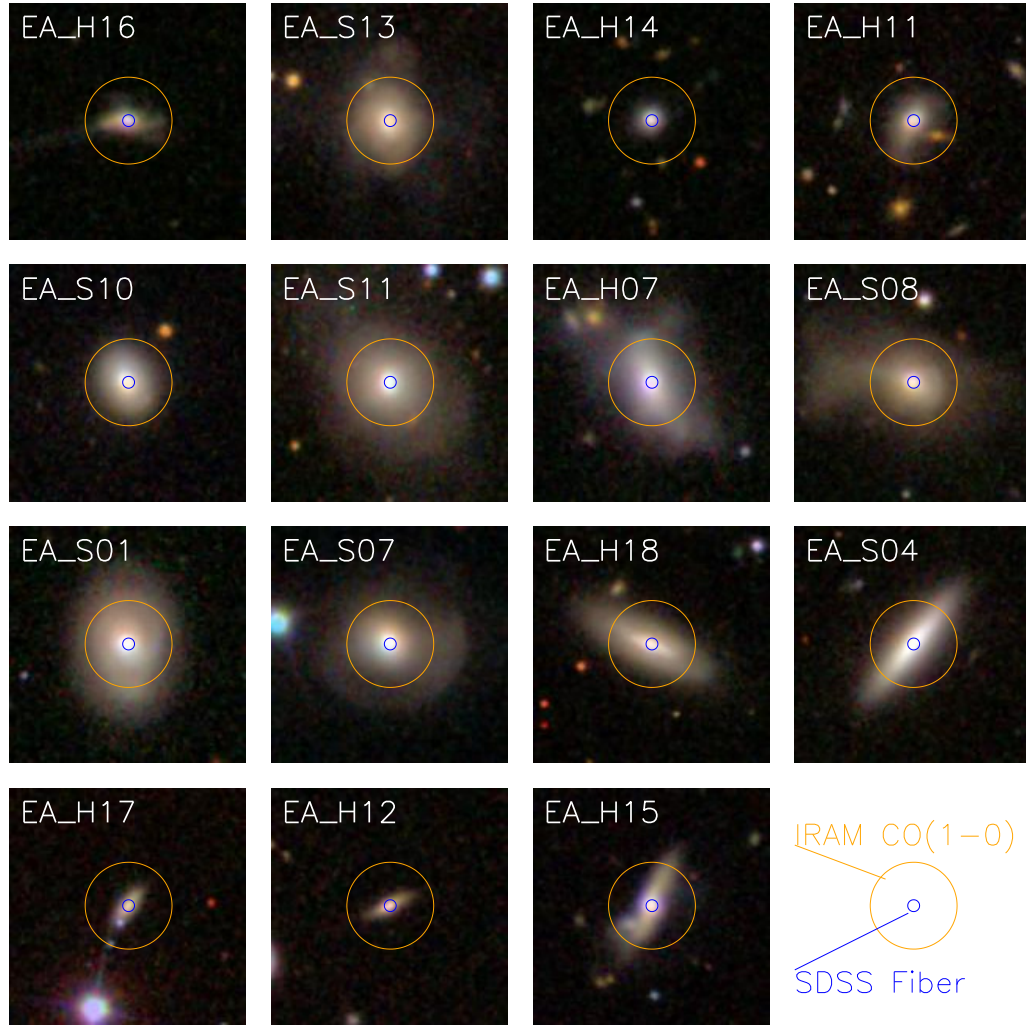
Figure 2.3: Same as Figure 2.2, but for the galaxies not detected in CO (1–0).
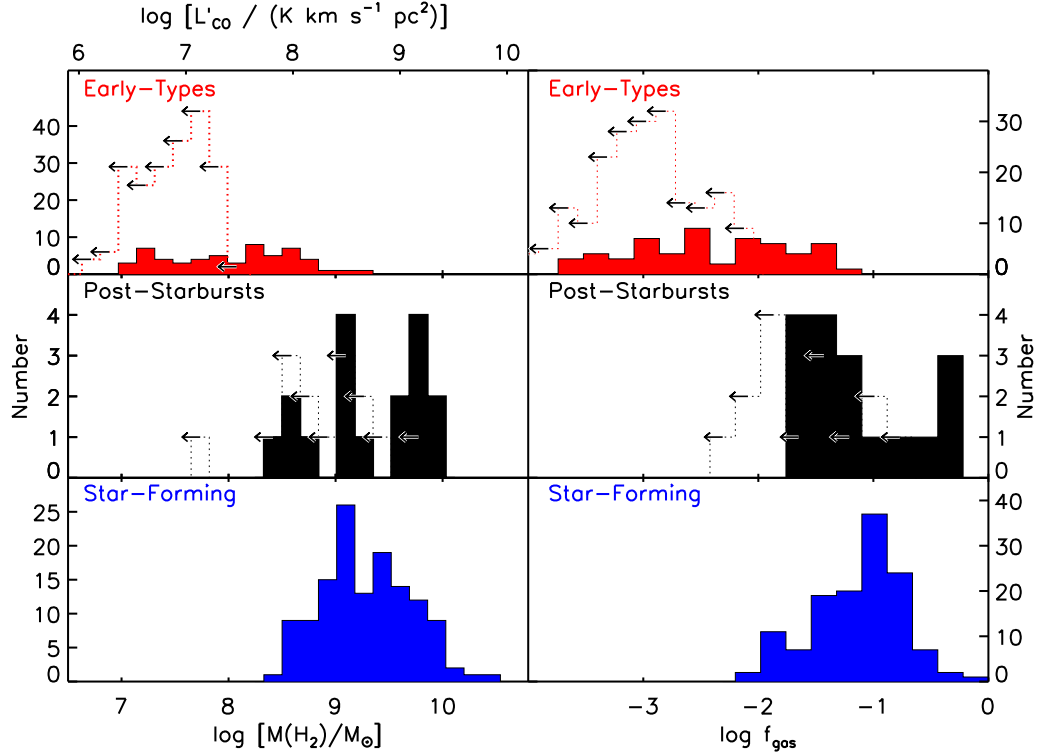
Figure 2.4: Left: Histograms of derived molecular gas masses $M(\mathrm{H}_2)$ for a variety of galaxy types: early types (top, from Atlas-3D Young et al., 2011), star-forming (bottom, from COLD GASS; Saintonge et al., 2011), and our post-starburst sample (middle). $\alpha_{\mathrm{CO}} = 4 M_\odot \ (\mathrm{K\,km\,s^{-1}\,pc^2})^{-1}$ is assumed for all samples. Bin size represents the mean error in the post-starburst sample, excluding systematic error from uncertainties in α_{CO}. A histogram of 3σ upper limits is overplotted for non-detections. Right: Histograms of molecular gas normalized to stellar mass (f_{gas}) for the same samples. For both $M(\mathrm{H}_2)$ and f_{gas}, we see considerable overlap between the post-starburst sample and star-forming samples, which is surprising given the difference in SFRs. The lower end and upper limits of the post-starburst sample are consistent with $M(\mathrm{H}_2)$ and f_{gas} measured for the early type sample. As seen in Figure 2.5, overlap persists even if a ULIRG-type value of α_{CO} is assumed for the post-starburst sample.

of those of the well-fit sample, and are centered around the optical velocity. The velocity intervals fit from the CO (1–0) data are used for the CO (2–1) data, though we note that fitting the CO (2–1) data separately does not change our results by $> 1\sigma$. We calculate the error in the integrated CO line intensity as

$$\sigma_I^2 = (\Delta v)^2 \, \sigma^2 \, N_l \, (1 + \frac{N_l}{N_b}), \tag{2.1}$$

where Δv is the channel velocity width, σ is the channel rms noise, N_l is the number of channels used to integrate over the line, and N_b is the number of channels used to fit the baseline. We also take into account an estimated flux calibration error of 10%. We calculate upper limits on I_{CO} as $< 3\sigma_I$. Following Solomon et al. (1997), the CO line luminosity $L'_{\rm CO}$ (in $\rm K\,km\,s^{-1}\,pc^2$) is

$$L'_{\rm CO} = 23.5 \, \Omega_{s*b} \, D_L^2 \, I_{CO} \, (1+z)^{-3} \ , \tag{2.2}$$

where $I_{CO} = \int T_{mb} \, dV$ is the integrated line intensity (in $\rm K\,km\,s^{-1}$) as described above, z is the SDSS redshift, and D_L is the luminosity distance (in Mpc). Ω_{s*b} is the solid angle of the source convolved with the beam,

$$\Omega_{s*b} = \frac{\pi(\theta_s^2 + \theta_b^2)}{4\ln 2}, \tag{2.3}$$

where θ_s and θ_b are the half power beam widths of the source and beam, respectively. Because the CO emitting size estimates (see §2.4.2) are not available for all the sources, we adopt a simple approximation such that the beam is much larger than the source, so $\Omega_{s*b} \approx \Omega_b$. Note that depending on the actual size estimates in §2.4.2, we could be underestimating $L'_{\rm CO}$ by $\sim 1.1 - 2.2\times$, with a median of 1.4, but this does not affect our conclusions throughout the paper.

The molecular gas mass can be calculated from $L'_{\rm CO}$ by assuming a conversion factor $\alpha_{\rm CO}$, as

$$M({\rm H_2}) = \alpha_{\rm CO} L'_{\rm CO}. \tag{2.4}$$

For now, we assume an $\alpha_{\rm CO}$ comparable to that in Galactic molecular clouds and the Local Group (aside from the SMC; see recent reviews by Bolatto et al., 2013;

Carilli & Walter, 2013; Casey et al., 2014): $\alpha_{\rm CO} = 4$ $M_\odot$ $({\rm K\,km\,s^{-1}\,pc^2})^{-1}$ (units omitted hereafter). This choice is examined below and in §2.4.3.

Molecular gas masses for the post-starburst sample span a broad range, from 3.4×10^8 to $6.9 \times 10^9 M_\odot$, with a mean value of $3.0 \times 10^9 M_\odot$ among the detected sample. We measure upper limits for the remaining 15 galaxies, with 3σ limits ranging from 4.6×10^7 to $5.2 \times 10^9 M_\odot$. Molecular gas masses and upper limits are listed in Table 2.5. Optical postage stamps of the galaxies with and without molecular gas detections are shown in Figures 2.2 and 2.3, respectively.

Next, we compare the molecular gas masses measured here to those from surveys of other galaxy types. CO (1–0) measurements have been compiled for the Atlas-3D sample of early type galaxies (Young et al., 2011). The COLD GASS (Saintonge et al., 2011) sample is a stellar mass-limited sample of galaxies, selected from the SDSS independent of galaxy type. We divide the COLD GASS sample up by galaxy type assigned by the SDSS based on the optical spectra (galspec `bptclass`). For now, we only use galaxies classified as star-forming or low signal-to-noise star-forming. We assume $\alpha_{\rm CO} = 4$ to calculate molecular gas mass for the early type and COLD GASS star-forming samples.

We compare the total molecular gas masses of these samples in Figure 2.4, seeing significant overlap between the star-forming and post-starburst samples. This overlap is surprising, because of the lack of equivalent levels of current star formation in the post-starburst sample. The lower mass end, as well as the upper limits, of the post-starburst sample are consistent with the early type sample.

In addition to comparing $M({\rm H_2})$, we also compare molecular gas fraction $f_{\rm gas} \equiv M({\rm H_2})/{\rm M_\star}$ normalized by stellar mass $M_\star$. We use $M_\star$ calculated from the SDSS spectra, as discussed in §2.2.4, for both the post-starburst and COLD GASS samples. We calculate stellar masses for the early type galaxies in the same way as Atlas-3D, using K-band measurements (Cappellari et al., 2011).

As with the $M({\rm H_2})$ comparison, we see considerable overlap in $f_{\rm gas}$ between the

post-starburst and star-forming samples. These comparisons are shown in the right-hand panels of Figure 2.4. The molecular gas fractions for the post-starburst sample are primarily above those of the early type sample, while some of the upper limits are more consistent with early types.

The CO to H_2 conversion factor (α_{CO}) is a known source of uncertainty in observations of molecular gas (see recent review by Bolatto et al., 2013). Traditionally, a bimodel model has been used, with normal star-forming galaxies assigned a Milky Way-like value of $\alpha_{CO} \sim 4$, and ULIRGs or starbursting galaxies assigned $\alpha_{CO} \sim 0.8$. This approach was initially motivated by the fact that a high α_{CO} applied to ULIRGs produced gas masses higher than the dynamical masses. In Figure 2.5, we plot $M(H_2)$ and f_{gas} for the post-starbursts and comparison galaxies for different α_{CO} assumptions. We also compare to the sample of LIRGs and ULIRGs from Gao & Solomon (2004). Even if a low, ULIRG-like value of $\alpha_{CO} = 0.8$ is used for the post-starburst sample, we still see significant overlap with the star-forming sample (at $\alpha_{CO} = 4$), and even some overlap with the LIRG and ULIRG sample (at $\alpha_{CO} = 0.8$). We expect $\alpha_{CO} = 0.8$ and $\alpha_{CO} = 4$ to span the range of possible values of α_{CO} in post-starburst galaxies, because recently ended starbursts may reflect ISM physical conditions between ULIRGs and quiescent disk galaxies. However, the appropriate value of α_{CO} for post-starbursts remains largely unconstrained. We discuss the effects of this uncertainty on our results in §2.4.3.

2.3.2   High Molecular Gas Mass for Given SFR

We compare the molecular gas masses measured here to upper limits on SFR derived from Hα and $D_n(4000)$ in Figure 2.6. We use several comparison datasets: star-forming galaxies selected from the COLD GASS (Saintonge et al., 2011, 2012), the star-forming and starburst sample from Gao & Solomon (2004), and early type galaxies (with Hα+PAH SFRs) from Young et al. (2011); Davis et al. (2014). The post-starburst sample lies at higher $M(H_2)$ for their SFRs than early-types, star-
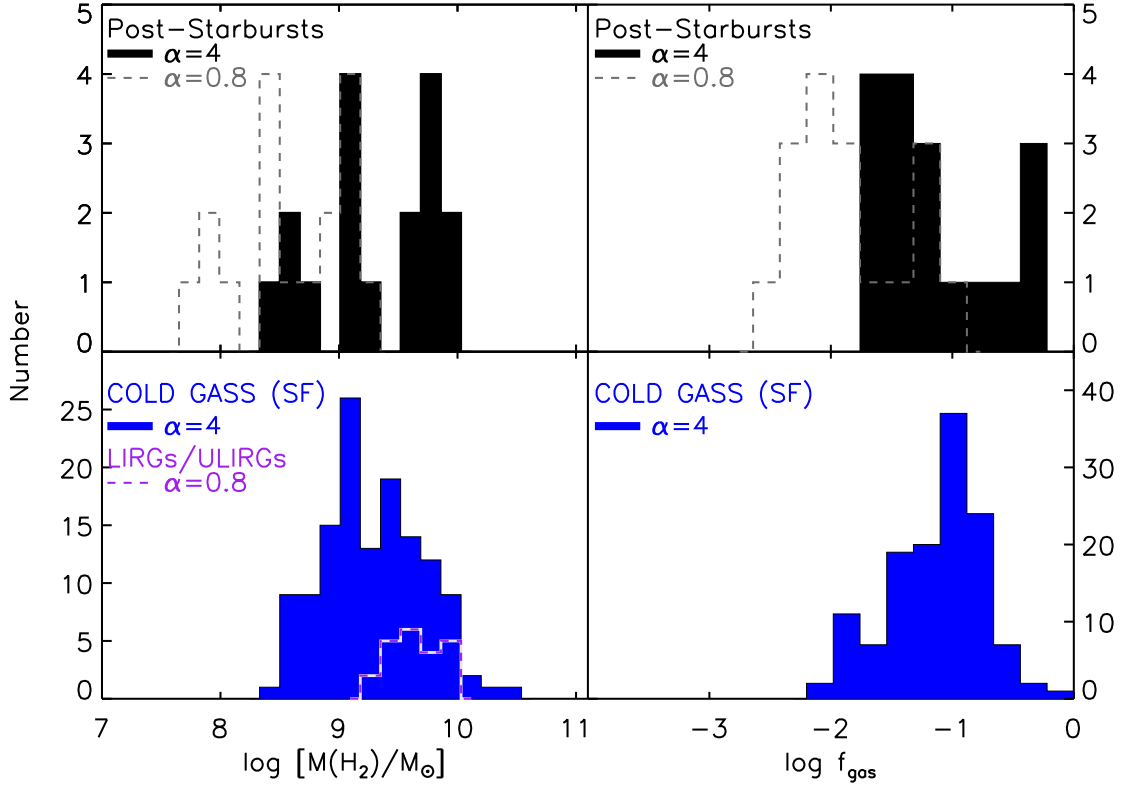
Figure 2.5: Left: Histograms of derived molecular gas masses $M(H_2)$ for a variety of galaxy types: star-forming (bottom, from COLD GASS; Saintonge et al., 2011), LIRGs and ULIRGs (bottom, from Gao & Solomon, 2004), and our post-starburst sample (top). $\alpha_{CO} = 4M_\odot$ $(K\,km\,s^{-1}\,pc^2)^{-1}$ is assumed where data are plotted as solid histograms, and $\alpha_{CO} = 0.8M_\odot$ $(K\,km\,s^{-1}\,pc^2)^{-1}$ where histograms are dashed lines. Bin size represents the mean error in the post-starburst sample. Right: Histograms of molecular gas normalized to stellar mass (f_{gas}) for the same samples (except for Gao & Solomon, 2004). Even if a low, ULIRG-like value of α_{CO} is used for the post-starburst sample, we still see significant overlap with the star-forming sample, and even some overlap with the LIRG and ULIRG samples.
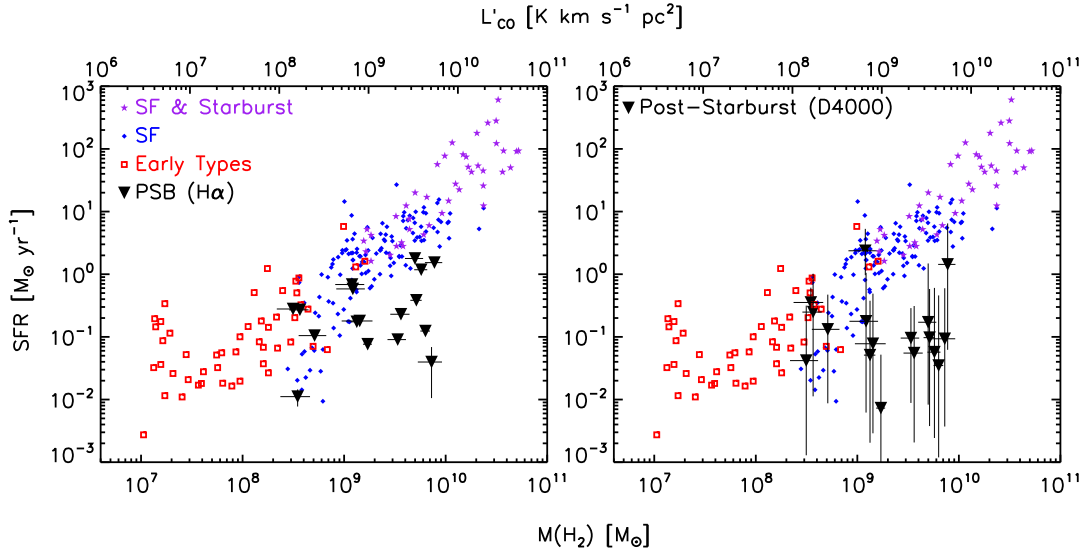
Figure 2.6: Molecular gas mass vs. SFR for post-starburst (PSB) galaxies and comparisons. Whether Hα (left) or $D_n(4000)$ (right) SFR upper limits are used for the post-starburst sample, these galaxies fall systematically below the comparison galaxies from the COLD GASS sample classed by the SDSS as star-forming (Saintonge et al., 2011, 2012), star-forming, LIRG, and ULIRG galaxies from the Gao & Solomon (2004) sample, and early type galaxies from Young et al. (2011). Both $D_n(4000)$ and Hα are expected to overestimate the SFR in the post-starburst sample, so these galaxies may lie at even lower SFRs. All galaxies have been normalized to the same value of $\alpha_{\mathrm{CO}} = 4$.
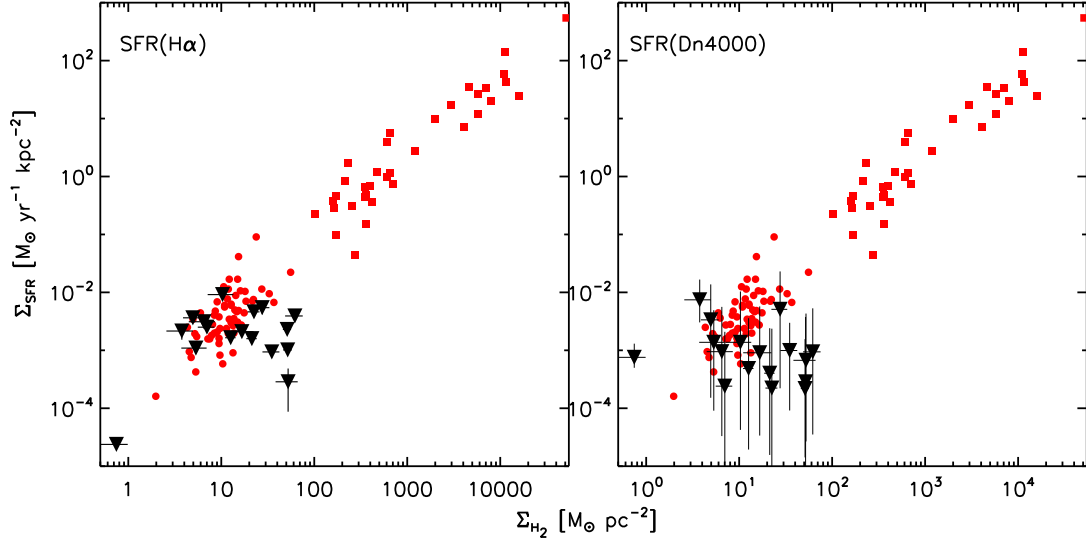
Figure 2.7: Molecular gas surface density vs. SFR surface density from Hα (left) and $D_n(4000)$ (right) SFR upper limits. The post-starburst sample is shown in black, with other local galaxies (Kennicutt, 1998) shown in red. Red circles are normal star-forming galaxies and red squares indicate local starbursts. Both SFR indicators are upper limits to the true current SFRs for the post-starburst sample. Hα has a contribution from the LINER, and $D_n(4000)$ has a contribution from the intermediate age stars produced in the burst. Our post-starburst galaxies are biased low on this relation. For the post-starburst sample, we assume the CO is distributed in the same way as the star formation regions, using the Petrosian 90% radius R_{90} to calculate the surface densities, $\Sigma_{\mathrm{SFR}} = SFR/\pi R_{90}^2$ and $\Sigma_{\mathrm{H_2}} = M(H_2)/\pi R_{90}^2$. Here, $M(\mathrm{H_2})$ includes all the CO detected in the IRAM 30m beam. We use the same value of $\alpha_{\mathrm{CO}} = 4$ for all galaxies. This plot is the most appropriate comparison to the K98 dataset, although we test our assumption that CO and star formation are distributed like the optical light in §2.4.2, and that $\alpha_{\mathrm{CO}} = 4$ in §2.4.3.

forming galaxies, and (U)LIRGs. The median Hα-derived SFR upper-limit for the post-starburst sample is $\sim 10\times$ lower than the median SFR for the COLD GASS star-forming sample across the same $M(\text{H}_2)$ range. This offset persists for the median of the $D_n(4000)$-derived SFR upper limits, which is $\sim 20\times$ lower than expected given $M(\text{H}_2)$.

Is it possible that our post-starburst selection criteria have generated the observed offset in SFR? Because we selected the post-starburst sample to have low Hα equivalent widths, it may include star-forming galaxies whose EW(Hα) measurement errors have scattered them low. This does not appear to be the case, as star-forming galaxies (classified using `bptclass=1`) that pass our Hδ absorption cut typically have EW(Hα)$\gg$ 3Å, the limit for our post-starburst sample. A Monte-Carlo analysis predicts a 0.004% contamination rate, and even if the Hα equivalent widths had systematic errors $3\times$ as large as their measurement errors, we still expect $\ll 1$ contaminant in the complete SDSS post-starburst sample of 1207 galaxies. Thus, the KS offset does not arise from contamination from normal star-forming galaxies.

The large molecular gas reservoirs in post-starburst galaxies are inconsistent with their SFRs when compared to a broad sample of galaxy types. Thus, the cessation of star formation after the starbust cannot be due to a lack of gas in the nearly half of our sample with detected CO. The question remains: why are these galaxies no longer forming stars at significant rates? One possibility is that the molecular gas is spread out over a larger area, dropping its surface density to be consistent with SFR density on the Kennicutt-Schmidt (KS) relation (Kennicutt, 1998, hereafter K98). We examine the KS relation below.

2.3.3 Offset from the Kennicutt-Schmidt Relation

While there are clear trends of SFR with molecular gas mass, tighter correlations exist when comparing the surface densities of these quantities for normal star-forming

and starburst galaxies.

We determine the molecular gas surface density Σ_{H_2} and SFR surface density Σ_{SFR} for the post-starburst sample, using the SDSS r-band Petrosian 90% radius to calculate the area as

$$\Sigma_{\mathrm{H}_2} = \alpha_{\mathrm{CO}} L'_{\mathrm{CO}}/(\pi R_{90}^2); \ \ \Sigma_{\mathrm{SFR}} = SFR/(\pi R_{90}^2). \tag{2.5}$$

We place the post-starburst sample on a KS plot in Figure 2.7. Other local galaxies are shown for comparison, including both normal star-forming galaxies and starbursts from the canonical K98 sample. For now, we apply the same value of α_{CO} = 4 to the post-starburst sample, and the entirety of the K98 sample. Many of the post-starburst galaxies lie below the relation defined by the other galaxies: the Hα-derived SFR limits exclude consistency with the relation for all but 4-5 galaxies. The $D_n(4000)$ based SFR limits also lie mostly below the relation.

The median locus of the 17 post-starburst galaxies lies $4^{+2}_{-1.5}\times$ lower than the $n = 1.4$ power law fit to the K98 galaxies. We perform a Monte Carlo analysis to assess the significance of this result by choosing random sets of 17 galaxies from the K98 disk sample, finding a 5σ significant offset for the post-starburst locus. This offset is more extreme than that found by Davis et al. (2014) for their sample of gas-rich early type galaxies. The relationship between the two datasets is unclear.

We see no obvious differences between the properties of our galaxies that are roughly consistent and most discrepant with the KS relation. It is not clear if the post-starbursts are single population of galaxies, or several different families.

The optical size used by K98 to calculate the surface densities is the isophotal radius, where the B-band surface brightness drops to 25 mag arcmin^{-2} and which is comparable to the Hα emitting region for normal spiral galaxies (K98, although we test this assumption for our sample in §2.4.2). This isophotal radius should be a good estimate of the size if the CO emission is coming from the same region as the optical light from star formation. Here, we use the Petrosian 90% radius for our

post-starbursts, because the isophotal sizes in SDSS are not considered reliable and are not included in the photometric catalogs after DR8. However, the significant offset from the K98 sample remains if we use the r-band isophotal radii instead.

There are several other observational uncertainties that could affect our results, which we consider in the Section 2.4. We discuss the effect of our sample selection criteria in §2.4.1. Like K98, we assume that the optical size of the galaxies is a good proxy for the spatial extent of both star formation and molecular gas. This assumption may not be valid for post-starburst galaxies. In §2.4.2, we test the possibilities that the CO is distributed differently from the optical light and that the star formation is distributed differently from both the optical light and most of the H_2, as traced by CO. We also consider how our sampling of the CO region (aperture bias) might affect our results. In §2.4.3, we test for the possibility that the measured CO is not tracing the H_2 as we expect, resulting in a different α_{CO}.

2.4 Discussion

2.4.1 Possible Sample Selection Biases

Given the way we selected our CO targets, the sample observed here might not represent the gas properties of the overall post-starburst sample. To study any biases that may occur within our sample, we test whether the galaxies with CO (1–0) detections lie at the extremes of our selection criteria.

The two parts of our sample (labeled "H" and "S") were selected from the parent sample of SDSS post-starbursts using different criteria (more details in Smercina et al., in prep). The "H" sample was selected based on post-starburst galaxies bright in the WISE 12μm band. One might expect these galaxies to have more gas if the 12μm band is a proxy for hot dust content and their dust traces their gas. However, we see no mean offset in 12μm luminosity between the galaxies detected and not detected in CO.

Both samples were selected to have a variety of times elapsed since the starburst (post-burst age). If the molecular gas is depleted over time, younger post-starbursts may be easier to detect in CO. While there is a shift towards detections with younger post-starburst ages, it is not statistically significant. The relation between molecular gas content and age since the burst is not straightforward, and is heavily dependent on the pre-burst gas mass of the galaxy and on the mechanics of the burst itself.

Because no statistically significant boost in CO detections occurs with either younger post-burst age or higher 12μm luminosity, the molecular gas properties of our sample here are not significantly biased by the selection criteria. Therefore, our sample is likely to have a molecular gas detection rate representative of the overall post-starburst population.

2.4.2   Effect of Spatial Distributions of Gas and Stars

In §2.3.3, we made the assumptions that both the CO and current star formation were well-traced by the optical light, in order to calculate their surface densities. This is a good assumption for star-forming galaxies (Regan et al., 2001; Leroy et al., 2008; Schruba et al., 2011), but may not apply to our sample, especially if the reason for the end of the starburst is a disruption of the gas. Additionally, the spatial extent of any residual star formation is unknown and may not overlap with the optical light, which is dominated ($\sim 60 - 90\%$) by the A stars formed in the recent burst. Without resolved observations, we are limited in how accurately we can know the distributions of gas and current star formation. If the CO emission or any currently star forming regions have sizes different than the optical size, it might be possible to resolve the observed offset from the KS relation. First, we test these assumptions for the post-starburst sample by estimating the CO emitting size with a model for the CO emission. We continue here to assume that CO traces H_2 well, with a conversion factor of $\alpha_{CO} = 4$. Second, we use our estimate of the CO emitting size to compare the scaled amount of CO near the center of the galaxy to

the SDSS fiber-based SFRs.

By comparing the CO emission in two differently sized beams, we can roughly constrain the CO emitting size by assuming a Gaussian model for the shape of the emitting region. We estimate the source size for each galaxy by combining the CO (2–1) line measurements from IRAM 30m and SMT 10m, using the method from Lavezzi et al. (1999). I_{CO}, the integrated line intensity, is related to the surface brightness, so it should scale with the convolved size of the beam and the source as

$$\frac{I_{SMT}}{I_{IRAM}} = \frac{\theta_s^2 + \theta_{b,IRAM}^2}{\theta_s^2 + \theta_{b,SMT}^2} \tag{2.6}$$

for the same line, assuming a Gaussian distribution of the CO emission, where θ_b are the different beam sizes for IRAM 30m and SMT, $\theta_{b,SMT} = 1.2\lambda/D \approx 33$ arcsec, and $\theta_{b,IRAM} = 1.166\lambda/D \approx 11$ arcsec, with the different coefficients due to the taper of each telescope. The source size θ_s is then given by,

$$\theta_s = \sqrt{\frac{I_{IRAM}\,\theta_{b,IRAM}^2 - I_{SMT}\,\theta_{b,SMT}^2}{I_{SMT} - I_{IRAM}}} \tag{2.7}$$

for a Gaussian source

We estimate source sizes for the 6 galaxies with IRAM 30m CO (1–0), CO (2–1) and SMT CO (2–1) detections. Because the measurement errors propagate non-linearly, we use a Monte Carlo technique to estimate the formal error on the size estimates, excluding any systematic error from the Gaussian model assumption. Sizes are listed in Table 2.3, and plotted over SDSS postage stamp images in Figure 2.8.

Previous studies of star-forming galaxies have found comparable exponential scale lengths of the CO emission and optical emission using resolved data (Regan et al., 2001; Leroy et al., 2008; Schruba et al., 2011). However, the CO to optical sizes are on average $\sim 2\times$ larger for our post-starburst sample, using either the optical half-light radii from an exponential fit or the Petrosian half-light radii. Because of the centrally peaked distribution of A stars in the post-starburst sample, this

difference is due to the concentrated optical light, rather than extended CO emission. Concentrations measured for post-starburst galaxies (Yang et al., 2008) are high, consistent with the half light radii being smaller than for galaxies with an exponential profile.

To test the effect of assuming a Gaussian model, we perform a similar calculation for each galaxy, but for a uniform disk emitting region instead of a Gaussian. The half-light sizes for each source model are consistent within the measurement errors except for EAS06, where the uniform disk model predicts a size smaller than the Gaussian prediction ($20''$ vs. $25''$).

The systematic errors associated with this method may be significant, especially as several of the estimated sizes are larger than the CO (2–1) IRAM 30-m beamsize. Thus, we use these sizes only to roughly estimate aperture bias in the CO observations, and to test whether use of this alternate size measure can eliminate the offset in the observed KS relation. The CO size estimates play no role in our main conclusions.

We use the CO emitting size estimates to model the effect of aperture bias in our CO (1–0) observations taken with the IRAM 30-m $\approx 22''$ beam. Given that the CO-emitting region is not a point source, the CO line luminosity calculated in §3.1 is likely an underestimate by a factor of $(\theta_s^2 + \theta_b^2)/\theta_b^2$, where θ_s and θ_b are the source and beam sizes, respectively. If we assume the mean CO source size of 9.2 kpc from our estimates above, then the corrections needed for the CO line luminosity, thus also $M(\text{H}_2)$ are $\sim$1.1-2.2$\times$. The mean correction is an increase of 1.4$\times$ from the original calculation, indicating that the molecular gas masses reported here may be conservative, with even higher amounts of molecular gas present.

Using the models of the CO emitting region that we construct from the size estimates and Gaussian assumption, we test the possibility that some of the observed CO does not participate in star formation. In §2.3.3, and in Figure 2.7, we assumed that all of the observed CO lay within the optical size R_{90}, which is always smaller
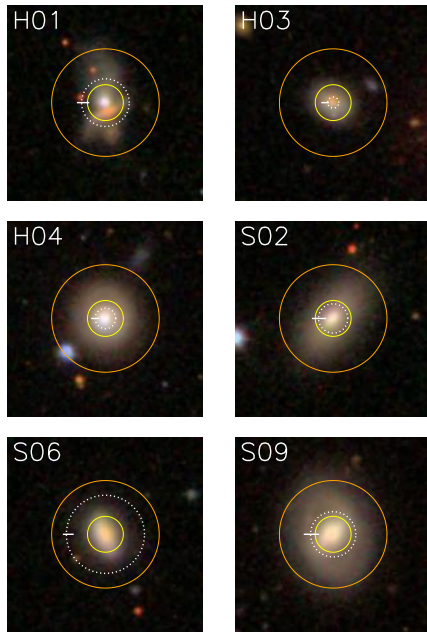
Figure 2.8: Estimated Gaussian half-light sizes of CO emitting regions (white dotted circles), with horizontal lines representing the Monte Carlo estimated error. FWHM beam sizes are shown for comparison: the inner yellow circle represents the IRAM 30m CO (2–1) $\approx 11''$ beamsize, and the outer orange circle is the SMT CO (2–1) $\approx 33''$ beamsize. Optical images are from SDSS, and are $60'' \times 60''$. These CO sizes are $\sim 2\times$ the optical half-light sizes (not shown), due to the concentrated optical profile from the stars produced during the burst.
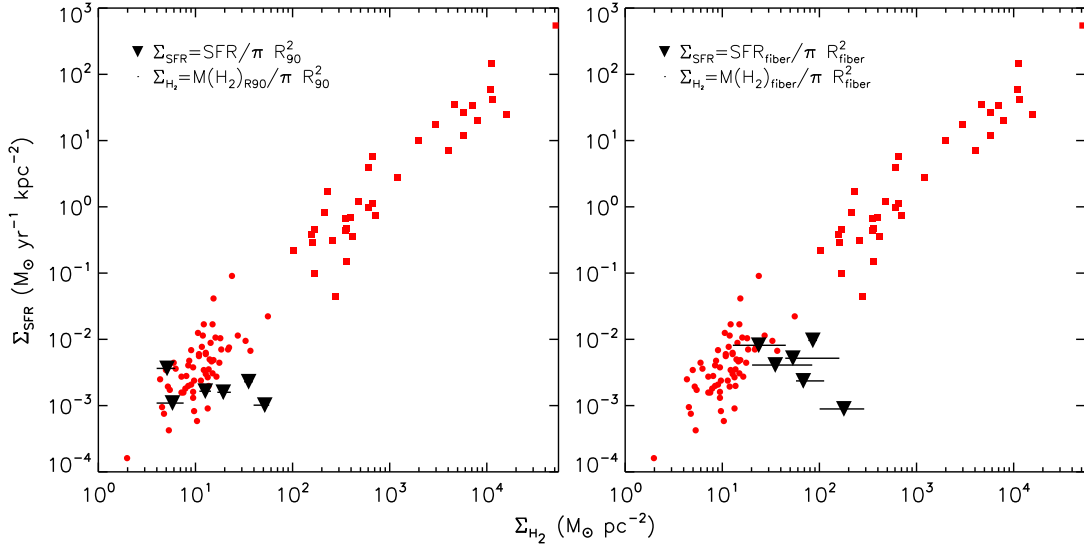
Figure 2.9: Alternative KS plots (red comparison points same as in Figure 2.7), accounting for possible spatial differences between molecular gas, star formation, and optical light. Left: Σ_{SFR} (from Hα) and Σ_{H_2} are both calculated within the optical radius R_{90} for the post-starburst sample. We use the CO size estimate from §2.4.2 and assume a Gaussian distribution to rescale $M(\mathrm{H_2})$ to that within R_{90} instead of within the larger IRAM 30m 22$''$ beam as in Figure 2.7. Despite this rescaling, which allows for the possibility that the optical light and CO are distributed differently, we still observe an offset of the post-starbust galaxies from the K98 sample. Right: Σ_{SFR} and $\Sigma_{\mathrm{H_2}}$ are both calculated within the 3$''$ SDSS fiber. We rescale $M(\mathrm{H_2})$ to within this radius. SFR is calculated using only the Hα flux from the fiber, without rescaling. This is a test of whether the star formation is distributed differently than either the optical light or CO, and the continued offset shows that this possibility is unlikely unless the Gaussian assumption for the CO distribution is poor, or the star formation is even more concentrated within the fiber size.

than the IRAM 30m CO (1–0) beamsize. Our CO size estimates, however, indicate that CO may extend beyond this aperture. We now estimate Σ_{H_2} within R_{90} by rescaling $M(\mathrm{H}_2)$ using the Gaussian model to include only the gas mass within R_{90} (Figure 2.9a). While still assuming that the current star formation is distributed like the optical light, this method allows us to compare the surface densities within the same aperture. In §2.3.1, we assumed that the source sizes were much smaller than the beam sizes to calculate $L'_{CO(1-0)}$, but we now calculate Ω_{s*b} explicitly in Equation 1. Despite the decrease in $M(\mathrm{H}_2)$ (and Σ_{H_2}), the post-starburst sample is still significantly ($> 4\sigma$) offset from the K98 galaxies. Allowing for the optical light and CO to be distributed differently does not change our results.

Next, we study the effect of allowing the spatial extent of any current star formation to differ from both the CO and optical light distributions. Swinbank et al. (2012) use resolved IFU observations of post-starburst galaxies, and find the nebular emission lines [O II] and [O III] to be spatially offset from the A star population in some cases, although these lines are particularly contaminated by LINER emission. If the current star formation is even more concentrated than the optical light, this could drive the observed offset of the post-starbursts on the KS relation. If this is the case, our assumptions about the aperture correction in the SFRs in §2.2.5 are not valid, and the SFRs are even more of an over-estimate. We consider now the case where the star formation is restricted to the optical fiber.

Using the CO sizes estimates and Gaussian model, we rescale $M(\mathrm{H}_2)$ to that within the 3″ SDSS optical fiber, again with a Monte-Carlo method to estimate the errors. We then estimate Σ_{H_2} inside the fiber aperture by scaling the CO luminosity, assuming a Gaussian profile with the CO size estimate. To calculate Σ_{SFR} , we use only the Hα flux from the fiber, not the aperture-corrected flux used elsewhere throughout this paper. We plot the resulting surface densities within the fiber apertures in Figure 2.9b. The post-starburst galaxies are still significantly offset from the K98 comparison galaxies. Thus, even if we allow for the possibility that

some of the CO in the outer regions of the galaxy does not participate in star formation, or that the current star formation is more compact than the optical light, the offset from the K98 galaxies remains.

Even if the CO in the post-starburst sample and the K98 sample is distributed in the same way with respect to the optical light, aperture bias in the datasets could generate an apparent offset. We do not see evidence of severe aperture bias in the post-starburst sample. Although we do observe higher molecular gas masses at higher redshifts, this is due to a combination of our decreased sensitivity and the higher stellar mass SDSS-selection at higher redshifts. We see no statistically significant trends with redshift of f_{gas}, or in the offset from the $n = 1.4$ power law KS relation from K98. If aperture bias only affected the post-starburst sample, it would result in an under-estimation of the offset.

An offset could be generated, however, if the K98 sample was not measured out to the same physical radii as in the post-starburst sample. The CO isophotal sizes in the K98 star-forming sample are at most 60% of the optical isophotal sizes, and often much smaller. Galaxies with CO measured out to at least half the isophotal radii are the only ones included in the K98 sample. Assuming a worst-case, uniform disk distribution, the actual CO flux could be up to 70% higher than measured, which is not enough to resolve the observed offset of $\sim 400\%$.

The offset observed in Figure 2.6, that the post-starburst sample lies at lower SFR for a given $M(\mathrm{H}_2)$ than other galaxies, and the similar robust offset in the KS relation (Figures 2.7 and 2.9), suggest that 1) the CO does not trace the H_2 as in our comparison galaxies or 2) the H_2 is not turning into stars in the same manner as our comparison galaxies (i.e., the star formation efficiency (SFE) is lower or the IMF is bottom-heavy). We explore 1) in Section 2.4.3 and 2) in Section 2.4.4. For now we note that suppressing the SFE by allowing CO to extend beyond any current star formation region does not resolve the KS offset. Ultimately, interferometric CO observations will be required to test the spatial distribution of CO.

2.4.3 Effect of $\alpha_{\rm CO}$ Choice

As discussed in §3, the CO to H$_2$ conversion factor ($\alpha_{\rm CO}$) is a known source of uncertainty in measuring molecular gas masses from CO observations. Here, we assume that H$_2$ traces the current star formation as expected for other galaxies, and explore variations in how CO traces the H$_2$.

So far, in plotting the KS relation we have assumed a single value of $\alpha_{\rm CO} = 4$ for all samples. Now assuming a bimodel $\alpha_{\rm CO}$ model instead, we apply a ULIRG-like value of $\alpha_{\rm CO} = 0.8$ to the K98 starbursts and to our post-starburst sample, and leave the K98 star-forming galaxies with $\alpha_{\rm CO} = 4$. We obtain the results in Figure 2.10a. This low value of $\alpha_{\rm CO}$ applied to the post-starburst sample can remove their observed offset from the modified KS relation.

We can understand why starbursting galaxies may require a lower value of $\alpha_{\rm CO}$ using the following toy model. $\alpha_{\rm CO}$ is proportional to the column density of molecular gas $N(H_2)$ over the CO line intensity, as

$$\alpha_{CO} \propto \frac{N(H_2)}{I_{CO}} \propto \frac{N(H_2)}{T \times \sigma} \qquad (2.8)$$

(Narayanan et al., 2011). In a merger, the column density is increased. However, the line intensity goes as the temperature T times the velocity dispersion σ, which both increase during the merger. In total, these factors result in a lower value of $\alpha_{\rm CO}$. After the merger, the gas kinetic temperature may decline to match conditions in early-type galaxies, but it is not clear what this simple model predicts for the post-starburst sample.

We cannot assume the post-starbursts will have a similar value of $\alpha_{\rm CO}$ as ULIRGs or starbursts simply because they are the likely progenitors. We expect the physical state of the gas to have changed significantly in the 0.3-1 Gyr since the burst, as the dynamical timescales for ULIRGs are of order $10^6 - 10^{7.5}$ yr (Genzel et al., 2010). However, if the state of the gas after the merger changes in such a way as to keep the gas heated, but as to lower the column density of molecular gas, $\alpha_{\rm CO}$ may have

a low value. Additionally, if an AGN heated the bulk of the molecular gas, the CO brightness temperature could increase for a given H_2 mass, lowering α_{CO}.

If much of the CO emission comes from outside of GMCs, the CO (1–0) linewidth could be strongly affected by the gravitational potential in the galaxy, instead of just by its own turbulence (Downes & Solomon, 1998). The fact that starbursts have more diffuse gas, and less gas bound in molecular clouds, has been used as justification for their low values of α_{CO}. We can estimate the influence of the stellar potential on α_{CO} using the prescription from Bolatto et al. (2013). They suggest that α_{CO} scales down from the Galactic value as $\alpha_{CO}/\alpha_{CO,MW} = (\Sigma_{\text{total}}/100 \ M_{\odot}\text{pc}^{-2})^{-0.5}$, where Σ_{total} is the combined surface density of stars and gas. Adding the stellar mass to the molecular gas mass, and calculating the surface density within the optical radius R_{90}, our post-starbursts have total surface densities of 130-460 $M_{\odot}\text{pc}^{-2}$, predicting $\alpha_{CO} = 1.9 - 3.5$, scaled down from the Galactic value of $\alpha_{CO} = 4$. This difference between the assumed α_{CO} for comparison star-forming galaxies and the post-starburst sample is not enough to resolve their observed offset. However, this relation is subject to scatter, and there may be significant variation in the influence of diffuse gas on α_{CO} (Liszt & Pety, 2012).

The use of a bimodel α_{CO} is not necessarily physical (although see, e.g., Tacconi et al., 2008; Daddi et al., 2009), because a variety of ISM conditions should exist, resulting in a continuum of α_{CO} values. In particular, because post-starburst galaxies may be at an intermediate stage between being dynamically hot and more relaxed, the appropriate α_{CO} for these systems may lie between the Galactic average and the typical value used for ULIRGs. The Narayanan et al. (2012) formulation suggests that α_{CO} varies smoothly with galaxy physical properties, and may be parametrized in terms of the gas phase metallicity and the CO surface brightness. Our galaxies do not have abnormal metallicities. Goto (2007) study the metallicities of post-starburst galaxies and do not find them to be anomalous. The mass-metallicity relation (Tremonti et al., 2004) also predicts metallicities that are similar to the

comparison galaxies, so we vary α_{CO} only with CO brightness. The result of applying this variable α_{CO} model to both the post-starburst and K98 samples can be seen in Figure 2.10b. The variable α_{CO} model does not remove the offset.

We are unable to rule out a low value of $\alpha_{CO} = 0.8$ as a potential explanation for the offset from the KS relation. We can resolve this question observationally using higher J_{up} lines of CO to constrain the temperature and density of the gas, as well as with denser gas tracers such as HCN to probe denser regions of the gas, bypassing the uncertainties arising from any CO outside of GMCs.

2.4.4 Implications for Galaxy Evolution

Our findings that post-starburst galaxies can have large gas reservoirs, and that they are offset low from the KS relation, help to discriminate among the physical processes proposed to end the burst. Clearly, scenarios that require the molecular gas to be absent, such as the complete 1) expulsion or removal of the gas (e.g., in outflows or some environmental mechanisms; Feruglio et al., 2010; Rupke & Veilleux, 2011; Boselli & Gavazzi, 2006), 2) consumption of the gas in the burst, and 3) prevention of gas infall into the galaxy and of the subsequent formation of new GMCs ("starvation"; Larson et al., 1980), are now excluded, at least in the half of our sample with detected molecular gas. Alternatively, the molecular gas within the galaxies could be 4) heated (Nesvadba et al., 2010), 5) kinematically prevented from collapsing into GMCs ("morphological quenching"; Martig et al., 2009), or 6) dispersed. Here, we comment on the implications of our results for these latter scenarios, and on what data are needed to complete the picture.

The offset observed in both Figures 2.6 and 2.7 could be caused by either a breakdown in the relation between CO and H_2 (a different value of α_{CO}), or between H_2 and the SFR (a different star formation efficiency), such that either is different than for the comparison galaxies. The burst-ending mechanisms of molecular gas heating (scenario 4) or morphological quenching (scenario 5) might alter the state
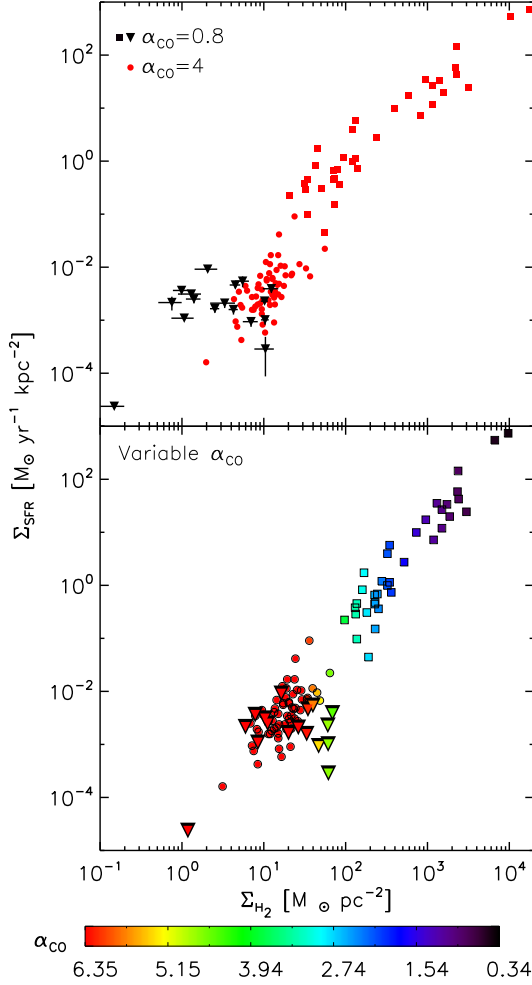
Figure 2.10: Top: Same as Figure 2.7a (see description in §2.3.3), but assuming α_{CO} = 4 for the K98 star-forming galaxies, and α_{CO} = 0.8 for the K98 starbursts and our post-starburst sample. Here, the offset previously observed can be reconciled by assuming a ULIRG-type value of α_{CO} = 0.8 for the post-starburst sample. Bottom: Same as Figure 2.7, but now assuming the variable α_{CO} for the K98 sample and post-starburst sample using the formula from Narayanan et al. (2012). As before, triangles, circles, and squares represent the post-starburst sample, K98 star-forming galaxies, and K98 starbursts, respectively. We still observe a systematic shift low on the Kennicutt-Schmidt relation, which suggests that the variable α_{CO} model does not resolve the differences between the post-starbursts and other galaxies.

of the gas relative to normal star-forming galaxies, acting to lower α_{CO} (see Eqn. 5) or to reduce the SFE for a given $M(H_2)$. In the case where α_{CO} is low, dispersal of the gas (scenario 6) would drive the post-starbursts down along the KS relation.

Analyzing the gas state is outside the scope of this paper, as we cannot constrain the temperature or density of the CO emitting region using only the CO (1-0) and (2-1) lines (e.g., Carilli & Walter, 2013). We need higher J_{up} lines and denser gas tracers to do so. Determining if the galaxy is undergoing morphological quenching requires resolved kinematics of the molecular gas. If the offset from the KS relation is not due to incorrect assumptions about α_{CO} (see §2.4.3), the SFR (§2.2.5), or the relative spatial distribution of H_2, optical light, and star formation (§2.4.2, assuming CO traces H_2), the intriguing possibility of a lower star formation efficiency in post-starbursts remains.

Another potential explanation for the offset is that our galaxies are still forming stars, but with a bottom-heavy IMF dominated by low mass stars that are not detectable by our SFR indicators. Regardless of the IMF during the burst, any subsequent star formation in our sample might be expected to track that of early types, for which bottom-heavy IMFs have been suggested (e.g., van Dokkum & Conroy, 2010). We test this hypothesis by estimating the change in the Hα-derived SFRs with IMF slope. For consistency, so far we have used the same conversion factor from $L(H\alpha)$ to SFR as K98, who employed a Salpeter IMF ($x = 2.35$ slope). However, van Dokkum & Conroy (2010) favor a steeper, more bottom heavy slope of $x = 3$. We use Starburst 99 v7.0.0 (Leitherer et al., 2014) models with a variety of IMF slopes over the range $0.1 - 1 M_\odot$. For a bottom heavy IMF slope of $x = 3$, we would underestimate the SFR significantly (by $\sim 20\times$), more than enough to explain the offset of our galaxies from the KS relation.

2.5   Conclusions

We study molecular gas in a sample of 32 nearby ($0.01 < z < 0.12$) post-starburst (aka "E+A") galaxies, whose optical spectra indicate a recent starburst that ended within the last $\sim$Gyr. We target the CO lines (1–0) and (2–1) with the IRAM 30m and SMT 10m telescopes, constraining the molecular gas mass remaining in these galaxies after the starburst. Our conclusions are as follows:

- Molecular gas is detected in 17 (53%) galaxies with CO (1-0) observations from the IRAM 30m. We obtain molecular gas masses of $M(H_2) = 10^{8.6}$-$10^{9.8} M_\odot$ ($\alpha_{CO}/4 M_\odot$ (K km s^{-1} pc^2)$^{-1}$), and molecular gas to stellar mass fractions of $f_{gas} \sim 10^{-2}$-$10^{-0.5}$ ($\alpha_{CO}/4 M_\odot$ (K km s^{-1} pc^2)$^{-1}$), roughly comparable to those of star-forming galaxies and generally larger than for early types, for a range of likely CO-to-H$_2$ conversion factors (α_{CO}). The upper limits on $M(H_2)$ for the 15 non-detected galaxies range from $10^{7.7} M_\odot$ to $10^{9.7} M_\odot$, with the median more consistent with early-type galaxies than with star-forming galaxies.

- We compare $M(H_2)$ to the star formation rate (SFR), using Hα and $D_n(4000)$ to calculate upper limits on the current SFR in this sample. When compared to other star-forming, starbursting, and early type galaxies, the post-starbursts have $\sim 10 - 20\times$ lower SFRs for a given $M(H_2)$.

- The post-starburst sample falls $\sim 4\times$ below other local galaxies on the Kennicutt-Schmidt relation (Kennicutt, 1998) of SFR surface density vs. $M(H_2)$ surface density. The median locus of the post-starburst galaxies is offset from the relation defined by normal star-forming galaxies (K98) at 5σ significance. After considering sample selection effects, aperture bias, varying spatial extents of current star formation, optical light and H$_2$, CO not tracing H$_2$ (a different α_{CO}), and the effect of IMF assumptions, we conclude the observed offset is likely due to suppressed SFE, a low value of α_{CO} consistent

with ULIRGs, and/or a bottom-heavy IMF.

Our results show that the end of the starburst in these galaxies cannot be attributed to the complete consumption, expulsion, or starvation of the molecular gas reservoirs. Resolved interferometric CO maps of these galaxies, higher J_{up} lines of CO for density-temperature constraints, denser gas tracers such as HCN, and resolved star formation maps are necessary to more thoroughly study the current state of gas in post-starbursts, and to more accurately compare to the residual star formation. Understanding this possibly common phase in galaxy evolution will help reveal the physics of star formation in galaxies as well as their evolution through mergers.

Table 2.1.   Post-Starburst Targets

Target	R.A. (deg)	decl. (deg)	z	PlateID [a]	MJD [a]	FiberID [a]	$\log(M_*/M_\odot)$ [b]	$D_n(4000)$ [c]	R_{90} [d] arcsec	$SFR_{lim}(\mathrm{H}\alpha)$ [e] $M_\odot\ \mathrm{yr}^{-1}$	$SFR_{lim}(D_n(4000))$ [f] $M_\odot\ \mathrm{yr}^{-1}$	ap. corr. [g]
EAH01	128.640457	17.346207	0.0478	2276	53712	444	10.45	1.4122	9.35	0.0586	0.0149	6.5416
EAH02	141.580383	18.678055	0.0541	2360	53728	167	9.96	1.3798	5.26	0.0256	0.0271	3.5339
EAH03	222.066864	17.551651	0.0449	2777	54554	258	10.34	1.4227	7.06	0.0196	0.0055	6.3128
EAH04	318.502258	0.535107	0.0269	986	52443	468	10.18	1.2445	8.98	0.0674	0.0621	4.0061
EAH05	184.260117	39.077038	0.0653	2001	53493	473	10.00	1.4148	3.44	0.0625	0.0150	3.6750
EAH06	116.456268	31.378378	0.0441	755	52235	42	10.53	1.4477	5.52	0.3737	0.0221	2.8889
EAH07	167.824844	11.554388	0.0380	1604	53078	161	10.65	1.3226	12.50	0.2206	0.0292	9.8156
EAH08	147.077820	2.501155	0.0604	480	51989	580	10.41	1.3765	4.48	0.0407	0.0176	4.4127
EAH09	227.229538	37.558273	0.0291	1352	52819	610	10.21	1.3668	5.34	0.0572	0.0086	4.8709
EAH10	158.427979	21.127987	0.1053	2376	53770	454	10.24	1.4019	3.44	0.0419	0.0985	0.9470
EAH11	166.419617	5.998405	0.0542	1003	52641	87	10.61	1.4173	4.67	0.1690	0.0271	1.8951
EAH12	223.772690	13.281012	0.0826	2750	54242	18	10.55	1.4002	2.83	0.1834	0.0217	1.5728
EAH13	155.503281	22.163177	0.1129	2365	53739	624	11.00	1.2897	4.61	0.6212	0.5817	2.4663
EAH14	178.276855	64.299026	0.0622	598	52316	170	10.04	1.2878	3.15	0.1005	0.0272	2.1201
EAH15	163.085205	5.828218	0.0411	1001	52670	48	10.40	1.4178	4.72	0.0596	0.0258	5.6546
EAH16	141.740372	42.526840	0.1113	870	52325	208	10.74	1.1959	4.52	0.5076	5.2118	1.5974
EAH17	191.215393	-1.759901	0.0481	336	51999	469	10.05	1.4225	4.67	0.0479	0.0634	1.6746
EAS01	11.246839	-8.889684	0.0196	656	52148	404	10.24	1.4919	13.08	0.0130	0.0255	5.0585
EAS02	49.228809	-0.041979	0.0231	413	51929	238	10.08	1.4068	11.83	0.0253	0.0318	4.1478
EAS03	117.809624	34.418201	0.0628	756	52577	424	10.86	1.4849	7.46	0.1710	0.0083	6.8937
EAS04	126.755821	21.706779	0.0153	1927	53321	584	9.99	1.4244	8.84	0.0140	0.0091	45.2321
EAS05	146.112335	4.499120	0.0467	570	52266	537	10.57	1.3109	8.42	0.1078	0.0328	5.4079
EAS06	159.488983	46.244514	0.0227	962	52620	212	10.14	1.4450	7.10	0.0575	0.0055	1.3282
EAS07	169.781738	58.053974	0.0325	951	52398	128	10.54	1.4897	7.23	0.0447	0.1355	2.7343

Table 2.1 (cont'd)

Target	R.A. (deg)	decl. (deg)	z	PlateID [a]	MJD [a]	FiberID [a]	log$(M_*/M_\odot)$ [b]	$D_n(4000)$ [c]	R_{90} [d] arcsec	$SFR_{lim}(H\alpha)$ [e] $M_\odot$ yr^{-1}	$SFR_{lim}(D_n(4000))$ [f] $M_\odot$ yr^{-1}	ap. corr. [g]
EAS08	189.900208	12.438888	0.0408	1616	53169	71	10.67	1.3406	13.55	0.0550	0.1720	6.2527
EAS09	191.611816	50.792061	0.0270	1279	52736	362	10.56	1.5223	10.68	0.0432	0.0127	4.0306
EAS10	196.357605	53.591759	0.0381	1039	52707	42	10.53	1.5089	6.44	0.0189	0.0397	2.5848
EAS11	242.585358	41.854881	0.0395	1170	52756	189	10.74	1.5299	10.55	0.0765	0.0583	6.6460
EAS12	243.375778	51.059879	0.0336	623	52051	209	10.01	1.1354	18.20	0.0314	0.2572	1.3772
EAS13	246.760666	43.476093	0.0462	815	52374	586	10.95	1.4548	11.41	0.0860	0.0101	7.2333
EAS14	316.286133	-5.399832	0.0826	637	52174	584	11.31	1.5036	9.68	0.4120	0.0396	4.3280
EAS15	343.778320	0.977756	0.0533	379	51789	579	10.83	1.3498	9.70	0.1697	0.5866	4.0352

[a]SDSS Spectra Identification from DR7 (Abazajian et al., 2009).

[b]MPA-JHU Stellar Masses, method described in Brinchmann et al. (2004).

[c]$D_n(4000)$ from SDSS spectra.

[d]Petrosian 90% size in r band, from SDSS photometry.

[e]Limit on SFR from Hα measurements, before aperture correction. Conversion from Kennicutt et al. (1994), line fluxes from MPA-JHU catalogs (Aihara et al., 2011). See §2.2.4.

[f]Limit on SFR from $D_n(4000)$ measurements, from MPA-JHU catalogs (Brinchmann et al., 2004), before aperture correction. See §2.2.5.

[g]Aperture correction to convert fiber-based SFRs to global SFRs, from MPA-JHU catalogs (Brinchmann et al., 2004). See §2.2.5.

Table 2.2.   IRAM 30m CO (1-0) observations

Target [a]	t_{obs} (hours)	I_{CO} [b] (K km s^{-1})	$L'_{\rm CO}$ [c] (10^7 K km s^{-1} pc^2)	$M({\rm H_2})$ [d] (10^7 $M_\odot$)	FWHM [e] (km s^{-1})
EAH01	0.30	2.58± 0.33	128.6± 16.4	514.5± 65.7	309.8± 18.4
EAH02	0.31	1.32± 0.27	84.3± 17.4	337.0± 69.7	172.9± 29.8
EAH03	0.20	3.60± 0.39	158.0± 17.2	632.1± 68.9	158.7± 8.6
EAH04	0.51	0.59± 0.13	9.2± 2.0	36.7± 7.9	106.7± 20.3
EAH05	0.60	0.97± 0.21	90.7± 19.5	362.7± 77.9	278.7± 44.8
EAH06	0.71	< 0.59	< 24.84	< 99.34	...
EAH07	1.02	< 0.33	< 10.31	< 41.25	...
EAH08	0.83	0.45± 0.15	35.6± 12.0	142.5± 47.8	233.7± 56.9
EAH09	0.61	0.43± 0.13	7.8± 2.4	31.4± 9.7	119.5± 28.5
EAH10	0.43	0.73± 0.20	181.5± 48.6	726.1± 194.3	275.1± 58.8
EAH11	0.40	< 0.60	< 38.53	< 154.12	...
EAH12	0.70	< 0.44	< 65.87	< 263.47	...
EAH13	0.94	0.68± 0.13	193.8± 37.6	775.2± 150.3	190.1± 27.8
EAH14	0.80	< 0.53	< 44.96	< 179.85	...
EAH15	0.60	< 0.75	< 27.57	< 110.27	...
EAH16	0.30	< 0.56	< 155.85	< 623.40	...
EAH17	0.43	< 0.51	< 25.67	< 102.66	...
EAS01	0.33	< 0.76	< 6.23	< 24.93	...
EAS02	0.40	1.11± 0.34	12.8± 3.9	51.2± 15.5	162.7± 44.0
EAS03	0.47	1.66± 0.24	143.6± 21.1	574.4± 84.5	270.5± 30.3
EAS04	1.56	< 0.28	< 1.38	< 5.51	...
EAS05	0.74	0.64± 0.20	30.5± 9.5	121.8± 38.2	346.9± 82.0
EAS06	0.31	3.83± 0.39	42.6± 4.3	170.6± 17.2	112.9± 4.0
EAS07	0.61	< 0.47	< 10.82	< 43.27	...
EAS08	1.14	< 0.28	< 10.06	< 40.24	...
EAS09	0.54	2.12± 0.27	33.3± 4.3	133.3± 17.2	267.8± 20.5
EAS10	0.80	< 0.49	< 15.53	< 62.12	...
EAS11	0.40	< 0.51	< 17.20	< 68.80	...
EAS12	1.10	0.36± 0.12	8.7± 2.8	34.9± 11.3	141.7± 29.1
EAS13	0.39	< 0.70	< 32.75	< 131.01	...
EAS14	1.61	0.83± 0.17	124.6± 25.3	498.5± 101.1	428.7± 73.4
EAS15	0.74	0.48± 0.15	29.9± 9.5	119.8± 38.0	166.2± 57.2

[a]Lines in **bold** represent $> 3\sigma$ detections in IRAM 30m CO (1–0) observations.

[b]Upper limits are shown at the 3σ level.

[c]Calculated using $L'_{\rm CO} = 23.5\,\Omega_b\,D_L^2\,I_{CO}\,(1+z)^{-3}$.

[d]Masses calculated assuming $\alpha_{\rm CO} = 4 M_\odot$ (K km s^{-1} pc^2)$^{-1}$, $M({\rm H_2}) = \alpha_{\rm CO} L'_{\rm CO}$.

[e]FWHM from Gaussian fit to data.

Table 2.3.   IRAM 30m and SMT CO (2-1) observations

Target	t_{obs} [a] (hours)	I^{2-1}_{IRAM} [b] (K km s^{-1})	IRAM 30m FWHM [c] (km s^{-1})	t_{obs} [d] (hours)	I^{2-1}_{SMT} [b] (K km s^{-1})	SMT FWHM [5][c] (km s^{-1})	θ_s [e] (arcsec)
EAH01	0.30	4.67±0.57	337.7±18.4	3.10	1.12±0.27	275.7±31.2	$14.6^{+2.9}_{-4.7}$
EAH02	0.26	1.39±0.46	81.6±18.2	...	...	...	...
EAH03	0.20	5.60±0.61	144.0±6.3	2.85	0.64±0.15	149.5±25.2	$3.4^{+3.9}_{-0.7}$
EAH04	0.41	1.51±0.23	125.3±17.0	6.60	0.20±0.03	126.5±16.9	$6.3^{+2.4}_{-2.6}$
EAH05	0.54	1.21±0.30	266.4±54.0	6.00	<0.72	...	...
EAH06	0.71	<1.53	...	...	...	...	...
EAH07	1.03	<0.48	...	...	...	...	...
EAH08	0.76	<1.06	...	3.80	<0.18	...	...
EAH09	0.61	0.78±0.18	127.0±24.2	9.50	<0.20	...	...
EAH10	0.43	<1.83	...	...	...	...	...
EAH11	0.40	<0.66	...	...	...	...	...
EAH12	0.70	<1.15	...	...	...	...	...
EAH13	0.94	<1.17	...	...	...	...	...
EAH14	0.80	<0.98	...	...	...	...	...
EAH15	0.60	<1.14	...	...	...	...	...
EAH16	0.32	<2.05	...	...	...	...	...
EAH17	0.43	<1.69	...	...	...	...	...
EAS01	0.34	<0.81	...	...	...	...	...
EAS02	0.40	2.31±0.70	202.2±62.5	4.60	0.38±0.09	131.2±16.9	$9.0^{+4.1}_{-4.7}$
EAS03	0.47	1.84±0.43	71.0±18.0	6.80	<0.28	...	...
EAS04	1.61	<0.47	...	...	...	...	...
EAS05	0.75	<0.81	...	4.60	<0.77	...	...
EAS06	0.31	5.19±0.54	117.6±3.6	1.50	2.10±0.21	111.7±8.0	$24.0^{+2.1}_{-4.5}$
EAS07	0.61	<0.74	...	...	...	...	...

Table 2.3 (cont'd)

Target	t_{obs} [a] (hours)	I^{2-1}_{IRAM} [b] (K km s^{-1})	IRAM 30m FWHM [c] (km s^{-1})	t_{obs} [d] (hours)	I^{2-1}_{SMT} [b] (K km s^{-1})	SMT FWHM [6c] (km s^{-1})	θ_s [e] (arcsec)
EAS08	1.00	<0.61	...	...	...	...	...
EAS09	0.55	3.39±0.39	276.1±13.8	2.60	0.79±0.26	234.6±46.3	$13.9^{+4.2}_{-5.2}$
EAS10	0.80	<0.82	...	...	...	...	...
EAS11	0.39	<0.52	...	...	...	...	...
EAS12	1.10	0.62±0.14	...	5.55	<0.27	...	...
EAS13	0.44	<0.81	...	...	...	...	...
EAS14	1.61	1.15±0.30	598.1±199.7	...	...	...	...
EAS15	0.70	1.04±0.22	299.0±58.1	4.50	<0.16	...	...

[a]Time on source (hours) IRAM 30m.

[b]Upper limits are shown at the 3σ level.

[c]FWHM from Gaussian fit to data.

[d]Time on source (hours) SMT.

[e]Approximate Gaussian source size (FWHM) of CO emitting region, see text (§2.4.2) for details
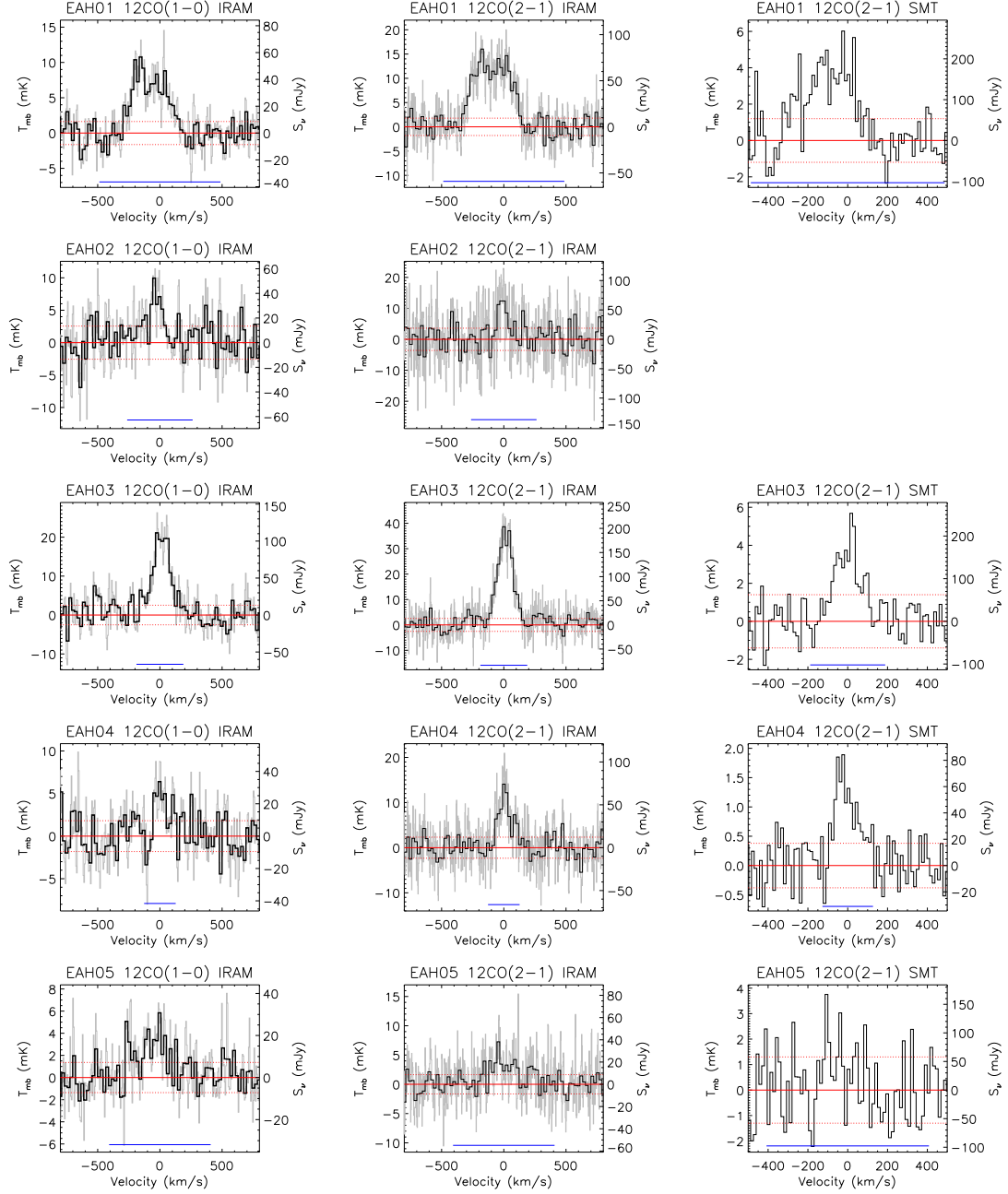
Figure 2.11: CO(1-0) and CO(2-1) spectra from IRAM and SMT for galaxies with IRAM-30m CO (1–0) detections ($> 3\sigma$) in our post-starburst sample. Spectra are shown in units of both main beam temperature T_{mb} [mK] and S_ν [Jy]. Grey lines show the unbinned IRAM data for 5 km/s channels, and black lines show the data binned to 20 km/s. Dashed red lines represent the rms of the binned data. SMT data are shown in 13 km/s bins. Blue horizontal lines at bottom represent the integration intervals, as described in the text.
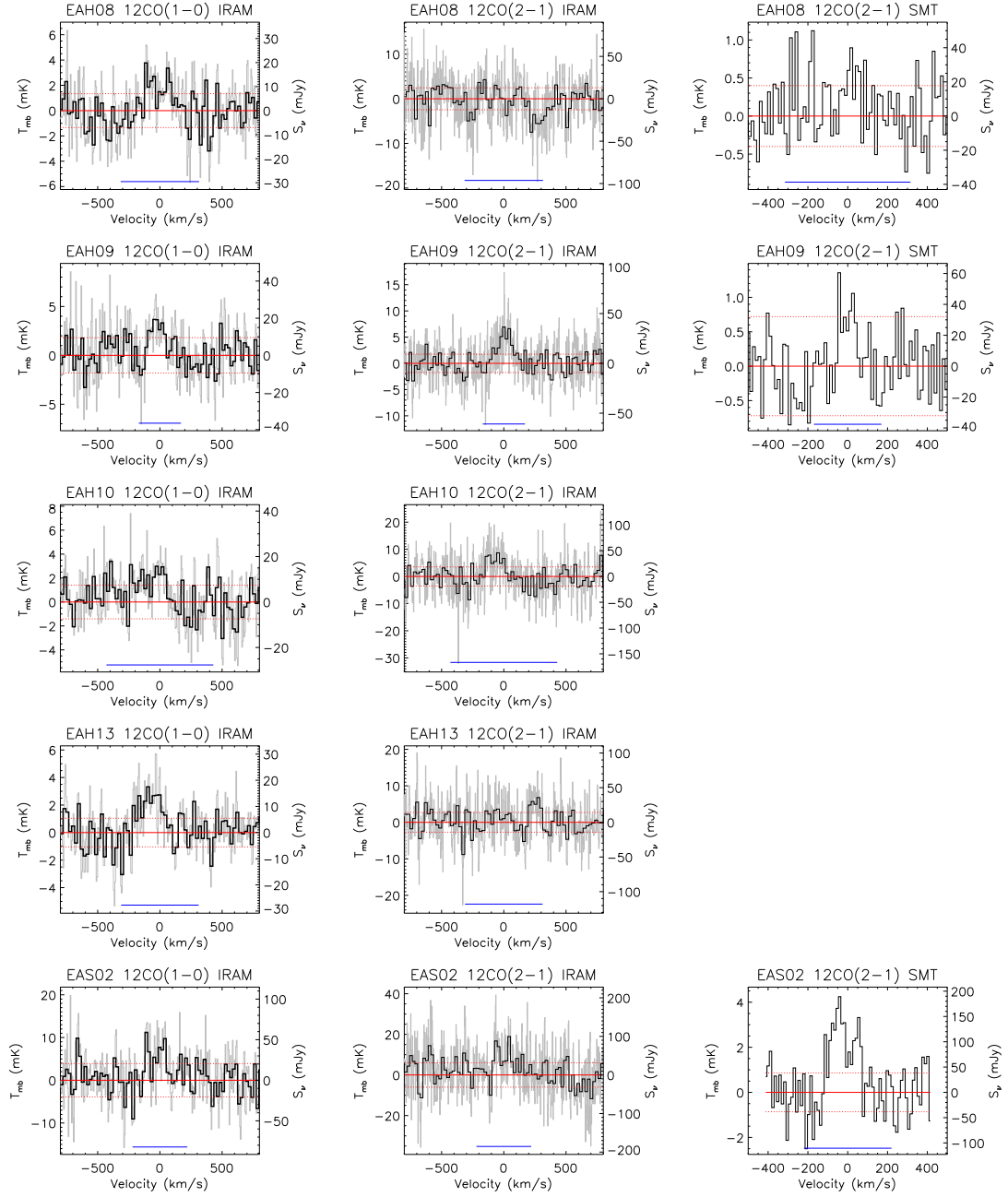
Figure 2.11: continued
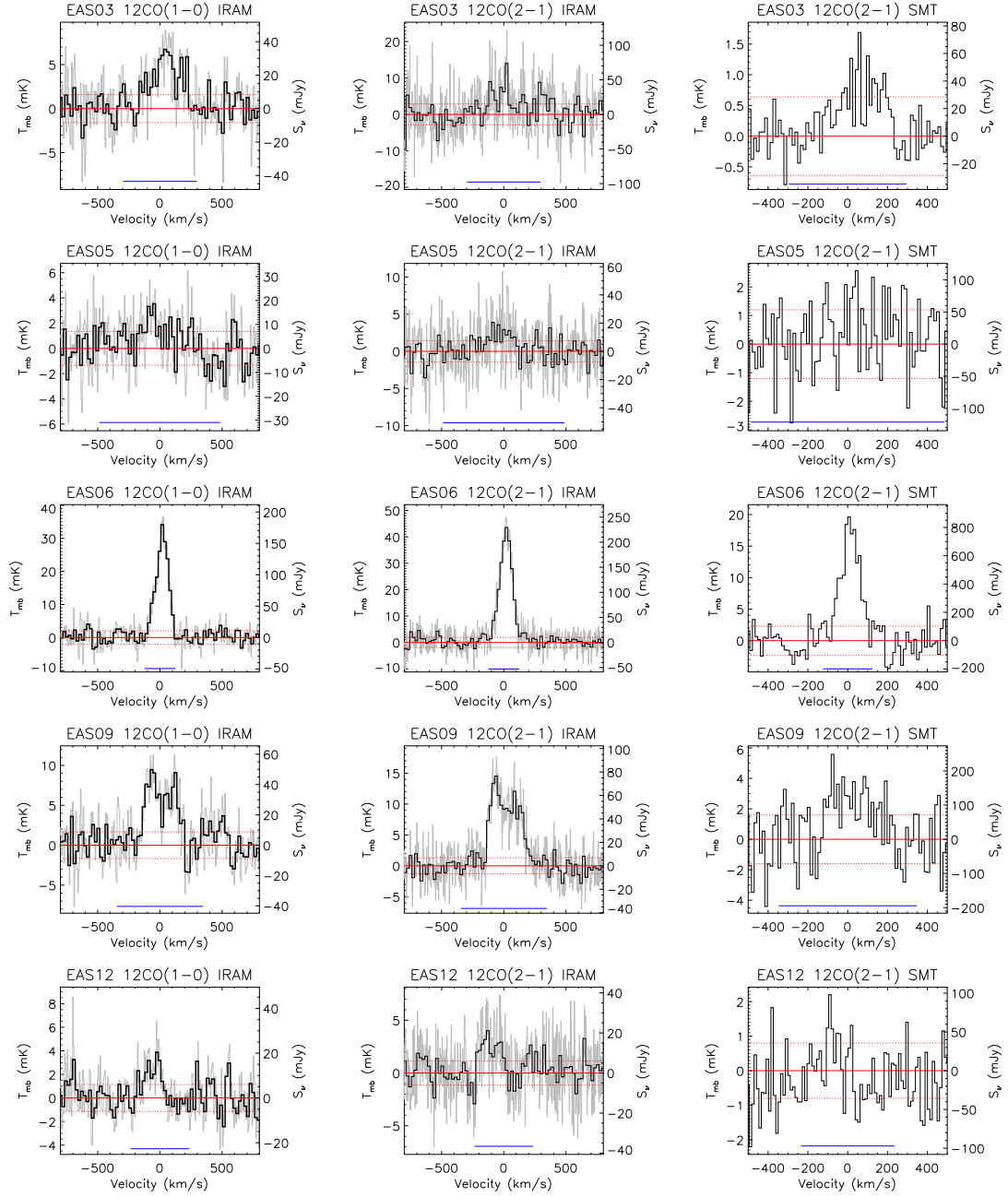
Figure 2.11: continued
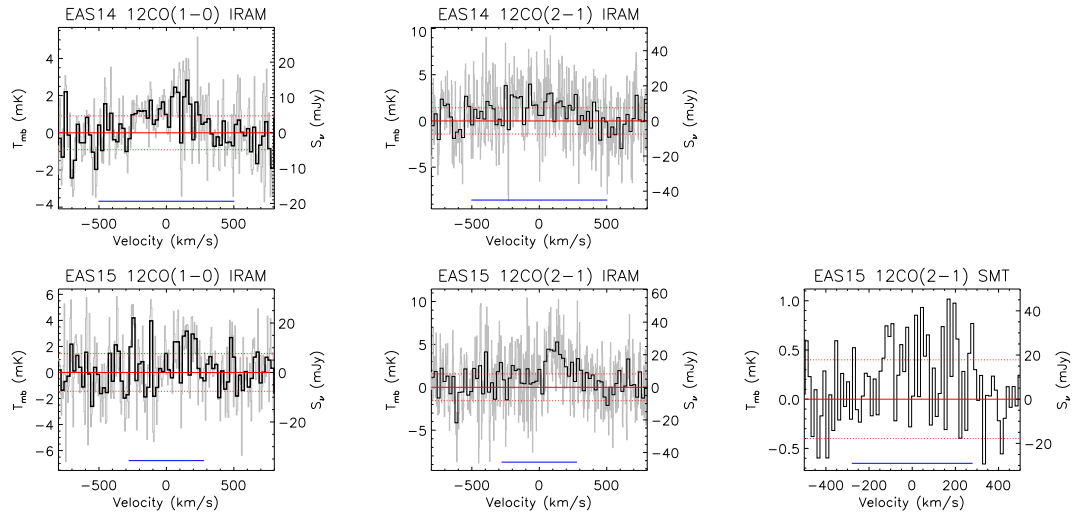
Figure 2.11: continued
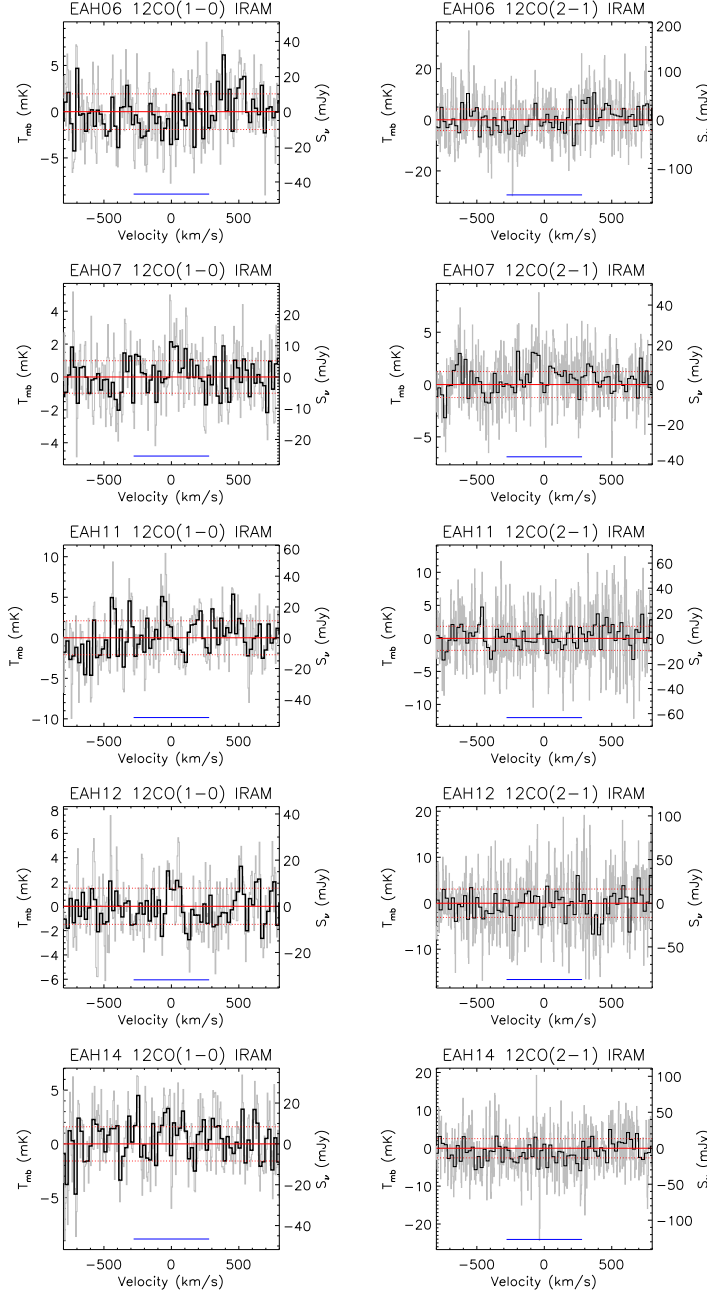
Figure 2.12: CO(1-0) and CO(2-1) spectra from IRAM and SMT for galaxies with CO (1–0) not detected with the IRAM 30m. Spectra are shown in units of both main beam temperature T_{mb} [mK] and S_ν [Jy]. Grey lines show the unbinned IRAM data for 5 km/s channels, and black lines show the data binned to 20 km/s. Dashed red lines represent the rms of the binned data. SMT data are shown in 13 km/s bins. Blue horizontal lines at bottom represent the integration intervals, as described in the text.
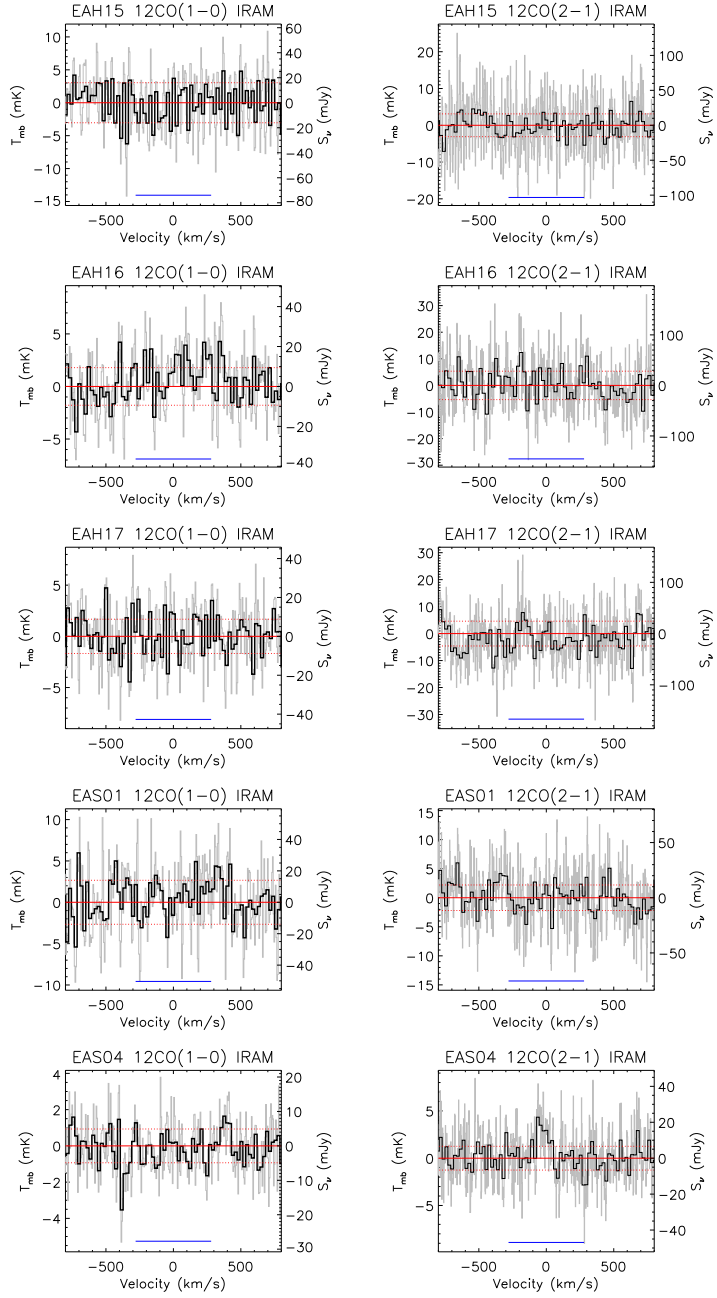
Figure 2.12: continued
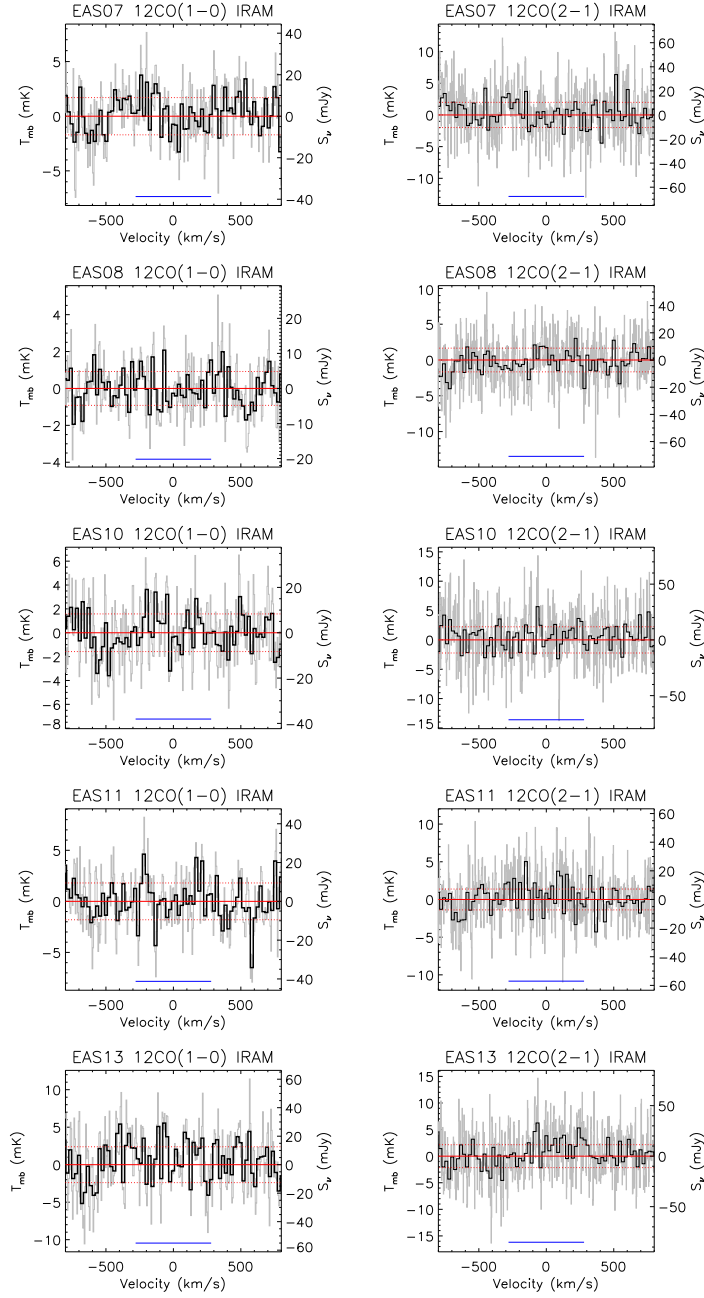
Figure 2.12: continued

CHAPTER 3

Clocking the Evolution of Post-Starburst Galaxies: Methods and First Results

Detailed modeling of the recent star formation histories (SFHs) of post-starburst (or "E+A") galaxies is impeded by the degeneracy between the time elapsed since the starburst ended (post-burst age), the fraction of stellar mass produced in the burst (burst strength), and the burst duration. To resolve this issue, we combine *GALEX* ultraviolet photometry, SDSS photometry and spectra, and new stellar population synthesis models to fit the SFHs of 535 post-starburst galaxies. This method is a significant improvement over using $D_n(4000)$-Hδ; when $D_n(4000) >$ 1.4, the measured $D_n(4000)$ is not significantly correlated with our derived post-burst ages for the sample studied here. For our post-starburst sample, 68% of the burst mass fractions are within 7.0%–69%, and 68% of the post-burst ages are within 240–680 Myr. 50% of the post-starbursts are best fit by a single recent burst and an older stellar population, and 48% have a young and an intermediate age stellar population consistent with two recent bursts in addition to the older stellar population. Lower stellar mass galaxies (log M$_\star$ < 10.5) are more likely to experience two recent bursts, and the fraction of their young stellar mass is more strongly anti-correlated with their total stellar mass. Applying our methodology to other, younger post-starburst samples, we identify likely progenitors to our sample and examine the evolutionary trends of molecular gas and dust content with post-burst age. We discover a significant (4σ) decline, with a 90 Myr characteristic depletion time, in the molecular gas to stellar mass fraction with the post-burst age. The implied rapid gas depletion rate of $5 - 200$ M$_\odot$yr^{-1} cannot be due to current star formation, given the upper limits on the current SFRs in these post-starbursts. Nor are stellar winds or SNe feedback likely to explain this decline. Instead, the

decline points to the expulsion or destruction of molecular gas in outflows, a possible smoking gun for AGN feedback. We also observe significant anti-correlations in the WISE [4.6]-[12] and [3.4]-[4.6] μm colors with post-burst age; the dust mass and/or the sources of dust heating are declining over time. [1]

3.1 Introduction

Post-starburst (or "E+A") galaxies have been caught in the midst of a rapid transition from star-forming to quiescent. They are not currently forming stars, as indicated by their lack of significant nebular emission lines. Yet, their strong Balmer absorption lines reveal a substantial population of A stars, indicating these galaxies have experienced a burst of star formation sometime in the past billion years (Dressler & Gunn, 1983; Couch & Sharples, 1987). Post-starburst galaxies show disturbed morphologies and tidal features in at least half of the studied cases, providing evidence that mergers and interactions can drive this transition (Zabludoff et al., 1996; Yang et al., 2004, 2008). Their range of angular momentum properties is likewise consistent with a variety of possible merger histories (Pracy et al., 2009; Swinbank et al., 2012; Pracy et al., 2013).

Post-starburst galaxies represent our best candidates for the rapid, non-secular, mode of galaxy evolution (Schawinski et al., 2014; Smethurst et al., 2015) that half to all red sequence galaxies are expected to experience (Martin et al., 2007; Wild et al., 2016). Post-starburst galaxies are generally found in the "green valley" (Wong et al., 2012) of the optical color-magnitude diagram, indicating stellar populations that could redden and evolve passively onto the red sequence. Post-starburst galaxy morphologies (Yang et al., 2004, 2008) and spatially resolved kinematics (Norton et al., 2001; Swinbank et al., 2012) are also consistent with evolution into early-type

[1]A version of this chapter has been submitted to the Astrophysical Journal. All of the work described below was carried out by me, with help from co-authors Yujin Yang, Ann Zabludoff, and Christy Tremonti.

galaxies.

Large spectroscopic surveys have allowed for the study of post-starburst galaxies as a population (Zabludoff et al., 1996; Goto et al., 2003). By studying galaxies after their starbursts are complete, and with data sensitive to the newly-formed stellar populations, we can obtain detailed information on the time elapsed since the burst, the mass produced in the burst, the overall burst duration, and whether more than one burst occurred. Previous approaches to age-dating post-starburst galaxies have often been too coarse, suffered from degeneracies between the post-burst age and burst strength, or used uncertain stelar population models.

Simple indices, such as the Ca II H+Hϵ vs. Ca II K lines (Leonardi & Rose, 1996), or D_{4000} vs. Hδ_{A} (Yagi et al., 2006) only crudely constrain the post-burst ages and burst mass fractions, and are only useful for galaxies with very high burst strengths or very young ages.

The post-burst age and burst strength can be determined by fitting the SEDs of post-starburst galaxies with templates from stellar population synthesis (SPS) models (Liu & Green, 1996; Barger et al., 1996; Shioya et al., 2002; Falkenberg et al., 2009; Du et al., 2010; Bergvall et al., 2016). While this technique benefits directly from the wide wavelength coverage and the spectral resolution of both the models and data, the optical SED cannot suitably break the degeneracy between the post-burst age, burst strength, and burst duration in many cases, and the covariance in adjacent spectral pixels must be considered to produce meaningful errors on the fit parameters. Several studies have used PCA methods on the data surrounding 4000Å (Wild et al., 2007, 2009, 2010; Rowlands et al., 2015; Pawlik et al., 2015) to both select and age-date post-starburst galaxies, but these methods result in a biased sample of recent SFHs (see §3.3.11).

Rest-frame UV photometry is essential in breaking the degeneracies. Several studies have employed UV+optical photometry to age-date post-starburst galaxies (Kaviraj et al., 2007; Kriek et al., 2010; Crockett et al., 2011; Melnick & De Propris,

2013; Yesuf et al., 2014; Ciesla et al., 2016), but are limited by small sample sizes, lack of spectral line information, or poorly resolved time steps or mass fraction/ burst timescale bins.

The properties of the recent starburst are connected to the physical conditions in the galaxy during the starburst, and to the mechanism that ends ("quenches") the burst. The duration of the burst is related to the quenching physics. The amount of mass produced in the starburst is related to how much gas is available and how efficiently it is funneled to the center and forms stars. The number of bursts experienced during the merger is related to the merger progenitors. These burst properties may both drive and be affected by feedback processes, whose impact may depend on the stellar mass of the galaxy (Kauffmann, 2014; Sparre et al., 2015).

Characterizing the starburst properties of a galaxy is also useful in connecting the starburst progenitors of these systems to their quiescent descendants. There are several proposed methods for selecting such age sequences (Yesuf et al., 2014; Rowlands et al., 2015; Alatalo et al., 2016c), each with their own set of efficiencies and biases. Connecting these galaxies using their detailed SFHs can more finely select sets of galaxies that represent evolutionary sequences, and can be used to track galaxies onto the red sequence of quiescent early-type galaxies.

The ability to connect time sequences of starbursting and post-starburst galaxies is important to understand the physics of how star formation shuts down, by identifying the likely timescales for various physical mechanisms. While simulations often assume the molecular gas reservoirs are depleted via star formation, stellar feedback, and AGN feedback, ending the starburst (e.g., Hopkins et al., 2006), recent evidence has emerged that AGN activity may be delayed after the end of the starburst. Large molecular gas reservoirs remain in post-starburst galaxies (French et al., 2015), which are otherwise consistent with evolving to early types in several Gyr. Something else must happen — another epoch of star-formation or AGN activity — to deplete the gas reservoirs to match those seen in early type galaxies.

QSOs with post-starburst signatures have older stellar populations than some samples of post-starburst galaxies (Cales & Brotherton, 2015), which similarly indicates a delay between the end of the starburst and the period of QSO activity. Studies of AGN activity in galaxies with ongoing and recent starbursts (Davies et al., 2007; Wild et al., 2010) indicate a delay of 50-300 Myr between the onset of star-formation and the onset of AGN activity. The intermediate stellar ages of Seyfert and LINER galaxies (Schawinski et al., 2009) also suggest such a delay. In simulations, the delay between the starburst or merger, and the peak of AGN activity or feedback, depends on the details of how AGN feedback is implemented (see e.g., Pontzen et al., 2016; Sparre & Springel, 2016). To make progress, we need to compare the gas reservoirs of post-starburst evolutionary sequences. Identifying the period over which they lose their gas, and determining whether the loss can be explained by consumption by residual star formation is critical.

Because of the recent sharp end to their star-formation, the details of how star formation progressed and ended can be better constrained in post-starburst galaxies than in galaxies with less eventful star-formation histories, older galaxies, and galaxies still undergoing such a starburst. Here, we present a catalog of 535 galaxies for which we determine details of recent SFHs: post-starburst ages, burst strengths, evidence for multiple bursts, and burst durations. We discuss the data used and post-starburst selection in §2, the age-dating technique and discussion of biases and sources of systematic error in §3, results relating to constraints on the recent SFHs in §4, and results relating to the evolution of gas and dust in the post-starburst phase in §5.

Figure 3.1: Hδ absorption vs. Hα emission equivalent width for our parent sample of 595,268 galaxies in the SDSS DR10. The region outlined in black shows our post-starburst selection criteria. To select galaxies with little-to-no current star formation, we require Hα EW < 3 Å. To select galaxies with a recent ($\lesssim$ Gyr) starburst population indicated by strong Balmer absorption lines, we require Hδ_A $- \sigma(H\delta_A) > 4$ Å, where $\sigma(H\delta_A)$ is the measurement error of the Hδ_A index. Post-starburst galaxies are located on this spur of the distribution of blue cloud and red sequence galaxies. We show two example tracks of a 100 Myr burst added to an old stellar population, with a mass fraction of 5 or 10%. A starburst must form a substantial fraction of the galaxy's stars, and be over a short duration, in order to go through the post-starburst spur. Star-forming galaxies in the parent sample are at higher Hα absorption, and moderate Hδ_A (the turnover in Hδ_A at high Hα is due to absorption line filling). Quiescent galaxies have little Hα emission and little Hδ absorption. Due to our use of the A-star optimized Hδ_A index, these galaxies extend to negative values.

3.2 Sample Selection and Data

3.2.1 Post-Starburst Galaxy Sample

Our parent sample is drawn from the DR8 SDSS main galaxy spectroscopic sample (Strauss et al., 2002; Aihara et al., 2011), using the galaxy properties from the MPA-JHU catalogs (Brinchmann et al., 2004; Tremonti et al., 2004). We exclude galaxies with $z < 0.01$ to eliminate those that are much larger than the the $3''$ diameter of the SDSS fibers (we explore aperture bias §3.3.8). We also exclude galaxies with unreliable Hα equivalent widths (we require `h_alpha_eqw_err > -1`) or median (over the whole wavelength range) signal-to-noise values of less than 10 per pixel. These cuts ensure that the line index measurements are reliable. Our final parent sample from DR8 is composed of 595,268 galaxies.

We select post-starburst galaxies from our parent sample by identifying galaxies with strong stellar Balmer absorption lines, characteristic of a recent ($\lesssim$ Gyr) starburst, and little nebular emission, indicating a lack of significant on-going star formation (Figure 3.1). We use the Lick Hδ_A index (Worthey & Ottaviani, 1997) to characterize the stellar Balmer absorption. We do not correct the index for filling due to nebular emission. This effect is negligible for our post-starburst galaxies given that they have weak nebular lines by definition and Hδ will be at most $\sim$8% of the Hα emission line. We require H$\delta_A - \sigma(\mathrm{H}\delta_A) > 4\,$Å, where $\sigma(\mathrm{H}\delta_A)$ is the measurement error of the Hδ_A index. We include $\sigma(\mathrm{H}\delta_A)$ in our selection criteria to elliminate spurious objects because Hδ_A measurements can be noisy (median $\sigma(\mathrm{H}\delta_A)$ ~ 0.48 in the parent sample). We select for galaxies that have little on-going star formation by requiring Hα EW $< 3\,$Å in the rest frame. We require that the SDSS spectra have no gaps over Hα or Hδ in the rest frame. These selection criteria result in a sub-sample of 1132 galaxies from the parent sample (0.2%). We discuss the biases that result from this sample selection in §3.3.11.

Figure 3.1 shows the distribution of Hα EW and Hδ_A in our parent sample.

The region delineated by the black lines represents our selection criteria for post-starburst galaxies. Star-forming galaxies in the parent sample are at higher Hα emission and moderate Hδ_{A} absorption. For star-forming galaxies with more Hα emission, the Lick Hδ_{A} index will be partially filled, resulting in the "turnover" in Hδ_{A} at high Hα seen in Figure 3.1. Quiescent galaxies have little Hα emission and little Hδ absorption. Due to our use of the A-star optimized Hδ_{A} index, these galaxies extend to negative values. This correlation is expected for galaxies forming stars roughly continuously, because Hα emission and Hδ absorption both trace star formation, but on different timescales: Hα emission is powered by O stars which have lifetimes shorter than 10 Myr, whereas stellar Balmer absorption is produced by A stars with lifetimes of 0.3 - 1.3 Gyr. Post-starburst galaxies are visible as a distinct spur of points with small Hα EW and large Hδ_{A}, well-separated from the populations of passively-evolving red galaxies and actively star forming galaxies. We also show two example tracks of a 100 Myr burst, with 5% (or 10%) of the current stellar mass produced in the recent burst and 95% (or 90%) from an old stellar population. A starburst must form a substantial fraction of the galaxy's stars over a short duration to go through the post-starburst spur.

3.2.2 Optical Photometry and Spectroscopy

We use the *ugriz* magnitudes and Lick indices[2] from the SDSS in our age-dating procedure. The emission line and absorption line index measurements are described in Tremonti et al. (2004) and Brinchmann et al. (2004). For the photometric data, we adopt the `modelmag` magnitudes, which provide stable colors while containing most of the galaxy light (Abazajian et al., 2004). We make small corrections to the u and

---

[2]We use the following Lick indices: `D4000_Narrow`, `Lick_CN2`, `Lick_Ca4227`, `Lick_G4300`, `Lick_Fe4383`, `Lick_Ca4455`, `Lick_Fe4531`, `Lick_C4668`, `Lick_Hb`, `Lick_Fe5015`, `Lick_Mg1`, `Lick_Mg2`, `Lick_Mgb`, `Lick_Fe5270`, `Lick_Fe5335`, `Lick_Fe5406`, `Lick_Fe5709`, `Lick_Fe5782`, `Lick_TiO1`, `Lick_TiO2`, `Lick_Hd_A`, `Lick_Hg_A`

z bands (-0.04 and 0.02 mag) to put them on the correct AB magnitude system[3]. In addition to photometry errors given in the SDSS catalog, we add the magnitude zero-point errors (5%, 2%, 2%, 2%, and 3% in $ugriz$, respectively) in quadrature to ensure that we obtain a realistic χ^2 values in the SED fitting (Blanton & Roweis, 2007)[4].

3.2.3   UV Photometry

For each of the post-starburst galaxies selected from the SDSS, we search for matching $GALEX$ (Galaxy Evolution Explorer; Martin et al., 2004) NUV and FUV detections using the $GALEX$ GCAT All-Sky Survey Source Catalog (GASC) and GALEX Medium Imaging Survey Catalog (GMSC) catalogs[5]. We search for galaxies within $4''$ of the SDSS positions. This radius is similar to the FWHM of the NUV PSFs and much larger than the $GALEX$ astrometric uncertainties ($0.59''$ in FUV). In the GCAT catalog, we find 729 galaxies (64%) with NUV detections of at least 3σ, and 535 galaxies (47%) with additional FUV detections. In this paper, we use only the galaxies with both NUV and FUV detections, as the UV data is essential for breaking the age-burst strength-burst duration degeneracy.

We use the `MAG_FUV` and `MAG_NUV` magnitudes from the GCAT catalogs, which were determined from the SExtractor `AUTO` magnitudes. These magnitudes should represent the total galaxy light, and thus are comparable to the SDSS `modelmag` magnitudes (Abazajian et al., 2004). The zero-point calibration errors of 0.052 and 0.026 mag (Morrissey et al., 2007) are added to the FUV and NUV photometry errors respectively to reflect the uncertainties in photometric uniformity. The addition of these zero-point errors to the formal photometric errors is critical in our study, because we combine photometric measurements from different databases to construct

---

[3]`http://www.sdss3.org/dr8/algorithms/fluxcal.php`

[4]`kcorrect.org`

[5]`https://archive.stsci.edu/prepds/gcat/`

SEDs. Under-estimated errors could lead us to inflated χ^2 values and therefore to unrealistic uncertainties in the post-burst ages and the burst mass fractions derived from our SED fitting procedure.

We test whether the *GALEX* photometry is affected by a lack of deblending, by comparing the SDSS and *GALEX* centroids. The mean difference is $1.1''$, and only 3% have centroids more than $3''$apart. The lack of cases where the centroids are more offset than expected from the PSFs indicates that blending from other sources is not a significant effect.

3.3   Age Dating Technique

3.3.1   Stellar Population Synthesis Models

The details of the SPS models used in our analysis are especially important given the presence of evolving low to intermediate mass stars after the end of the starburst. The thermally pulsing asymptotic giant branch (TP-AGB) phase is especially uncertain, so different SPS model treatments of the TP-AGB phase can have large impacts on the predicted post-starburst SEDs. Specifically, the Bruzual & Charlot (2003) models feature a less prominent contribution from this phase than the Maraston (2005) models. The Maraston (2005) models predict younger ages than the BC03 models (Maraston et al., 2006).

Analyses of post-starburst galaxies (Kriek et al., 2010) have found that the Maraston (2005) models generally overpredict the TP-AGB luminosity. Similar results are found by Zibetti et al. (2012) and Melnick & De Propris (2013). Thus, previous studies of the ages of recently quenched galaxies (Schawinski et al., 2007) that use the Maraston (2005) models may be subject to error. The FSPS (Flexible Stellar Population Synthesis) set of SPS models (Conroy et al., 2009; Conroy & Gunn, 2010) includes two parameters to tune the shift in T_{eff} and L_{bol} of the TP-AGB track on the HR diagram, from the tracks predicted by Marigo et al. (2008).

These models include a best fit of ΔT_{eff} and ΔL_{bol} to data from the SDSS and 2MASS (2 Micron All Sky Survey Skrutskie et al., 2006).

We age-date our sample of post-starburst galaxies using both the BC03 and FSPS models and do not find a difference in the resulting ages above the statistical error. This is likely due to the greater influence of age on the *GALEX* UV data points, as the TP-AGB contribution is primarily in the NIR, which is less sensitive to the details of the recent star formation histories. The remainder of this work uses only the FSPS models.

Here, we use the FSPS models to generate stellar population synthesis models for several families of physically-motivated SFHs for post-starburst galaxies. We consider several possibilities for a younger stellar population from the recent starburst (§3.3.2) on top of and older, pre-starburst, stellar population (§3.3.4).

3.3.2 Recent Star Formation Histories

Post-starburst galaxies are likely the result of recent major mergers (e.g. Zabludoff et al., 1996; Yang et al., 2004, 2008; Pawlik et al., 2015), showing evidence of disturbed morphologies and the young stellar populations we are interested in here. We motivate the details of our assumed SFHs using simulations of gas-rich major mergers. Simulations of merging galaxies predict the triggering of a starburst, with one (e.g. Snyder et al., 2011; Hayward et al., 2014) or two (e.g. Mihos & Hernquist, 1994; Cox et al., 2008; Renaud et al., 2015) exponentially declining starburst events. In a merger, gas is funneled into the center of the galaxy, causing an initial burst during the first galaxy-galaxy tidal passage, and another upon coalescence. If the galaxies already have a bulge in place, it acts to stabilize the gas from collapse, and most of the new stars will be formed in a single burst. If the bulge is not in place, some of the gas forms stars during the first passage, resulting in two bursts of star formation. The timescale of the separation between bursts depends on the initial conditions of the galaxies' relative positions and velocities before the merger.
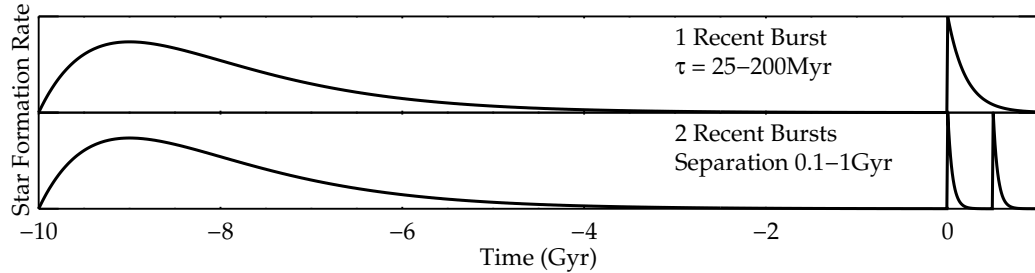
Figure 3.2: Star Formation History (SFH) models used here in fitting the post-starburst SFHs. The old stellar population is modeled by a linear exponential. The young stellar population is fit to two different classes of SFHs, those with 1 recent burst, varying the burst duration, and those with 2 recent bursts, varying the separation between bursts. Post-starburst galaxies are likely post-merger, so we use simulations of gas-rich major mergers to motivate the range of recent SFH used (see §3.3.2). The burst durations range from 25 Myr to 200 Myr for the single burst models. We do not have the sensitivity to distinguish the burst mass fractions or durations of the individual bursts in the double recent burst model, so we assume the bursts are each 25 Myr exponentially declining models, and form equal stellar masses. We instead vary the separation between each burst, from 100 Myr to 1 Gyr.

Multiple starburst episodes can also occur when stellar feedback is important (e.g., Muratov et al., 2015). Galactic outflows observed in post-starburst galaxies (Tremonti et al., 2007) have been proposed to arise from stellar feedback (Diamond-Stanic et al., 2012). Multiple episodes of star-formation are expected to occur in low mass galaxies, with observations constraining the duty cycles of these "bursty" star formation histories (Lee et al., 2009; Geha et al., 2012). However, some observations of long duration starbursts in low mass galaxies have shed doubt on whether these bursty SFHs can be explained with stellar feedback alone (McQuinn et al., 2010).

Because post-starburst galaxies are primarily found in poor groups (Zabludoff et al., 1996; Hogg et al., 2006), we do not include "truncated" SFHs in our stellar population fitting method, as in Ciesla et al. (2016), as such models are motivated by processes unique to dense cluster environments, such as ram pressure stripping.

We test several different models for the recent SFH (Figure 3.2). Motivated by

the simulations described above, we choose two different classes of SFHs: one or two recent bursts, with an early period of star formation at high redshift. We then vary the duration of the exponentially declining burst in the former and the separation between the bursts in the latter. Exponentially declining ("τ") bursts are seen in simulations, but we also test a gaussian-shaped recent burst, at different durations. The post-burst ages fit using the two models are consistent, using the definition below. The τ model bursts produce better fits to the data than the gaussian shaped bursts, so we use these in all cases.

For the two recent burst model, we do not have the sensitivity to fit separate ages, burst strengths, durations, and the time between bursts, due to degeneracies in the spectra. We choose five burst separations between 100 Myr and 1 Gyr, typical of those seen in the simulation results discussed above. We set the burst durations to $\tau =25$ Myr and require the mass fractions to be equal between the two recent bursts.

To properly compare the post-burst ages from different SFH fits, we define the "post-burst" age to be the time elapsed since the burst was complete, instead of the time elapsed since the burst began. Because the SFHs we consider have different burst durations and numbers of recent bursts, this convention allows the post-burst ages to be compared in a physically meaningful way. While we are interested in the post-burst age for studying how post-starburst galaxies evolve through this phase, a different convention may be desirable for other purposes, such as timing the onset of various evolved stellar populations. We include both the age since the starburst began and the post-burst age in Table 3.1.

We define the "post-burst age" to be the time elapsed since the majority (90%) of the stars formed in the recent burst(s). We choose this convention by fitting single population recent bursts + a 10 Gyr old single stellar population to synthetic UV-optical SEDs for the single and double burst SFHs described above, with typical uncertainties added, then comparing the age of the single stellar population model

to that of the single or double exponentially declining bursts. The age since 90% of the stars formed, or "post-burst age", is most consistent with the age obtained by using a single stellar population to model the recent burst. This definition is thus comparable to a light-weighted young stellar population age, as derived using a "K+A" model (e.g., Quintero et al., 2004); it also allows comparisons between post-starbursts with single vs. double burst recent SFHs, to explore how the galaxies evolve after the burst has ended (see §5).

We demonstrate how the double burst model is a better fit to many of the galaxies, by plotting the fitting residuals for the *FUV* flux, $D_n(4000)$ index, and Lick $H\delta_A$ index in Figure 3.3. For galaxies that strongly prefer the double recent burst model, the fitting residuals are narrower and less biased than the single burst model fitting residuals for the same galaxies. The addition of an intermediate F star population allows for these indices, as well as many of the iron-influenced Lick indices, to be better fit, while still providing a good fit to the UV colors and Balmer absorption indices. We ultimately find that 50% of the galaxies prefer the single burst model, and 48% prefer the double burst model. Only 11 galaxies (2%) do not show a statistical preference given the error in χ^2. For these galaxies, we nonetheless assign the model with the lower χ^2, although this does not affect our conclusions.

3.3.3 SED fitting

To determine the time elapsed since the starburst ended, what fraction of the stellar mass was produced during the burst, the duration of the recent burst, and whether there was more than one burst, we model the SEDs of post-starburst galaxies as a combination of old and new stellar population. The old stellar population is modeled as a linear-exponential star formation rate over time t_{old}:

$$\Psi \propto t_{old}e^{-t_{old}/\tau_{old}} \tag{3.1}$$
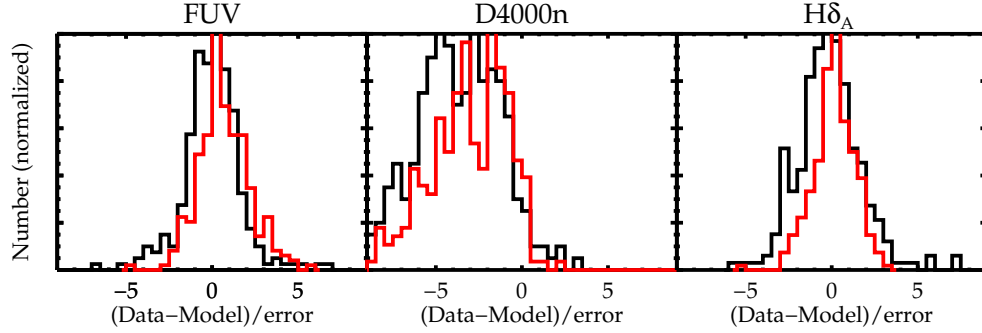
Figure 3.3: Histograms of fitting residuals for the FUV flux, $D_n(4000)$ index, and Lick $H\delta_A$ index, for galaxies best fit by a double recent burst. The double burst model fit residuals are shown in red, and the (not preferred) single burst model fit residuals are shown in black. For galaxies that strongly prefer the double recent burst model, the fitting residuals are narrower, and less biased than the single burst model fitting residuals for the same galaxies.

beginning 10 Gyr ago and characterized by the timescale $\tau_{old} = 1$ Gyr. The young stellar population's star formation history is modeled as either one or two exponential declining components in the star formation rate over time t_{young}. For one recent burst:

$$\Psi \propto e^{-t_{young}/\tau}. \tag{3.2}$$

We vary the time t_{SB} since this recent period of star formation began[6] as well as the characteristic timescale τ.

For two recent bursts,

$$\Psi \propto e^{-t_{SB}/\tau} + e^{-(t_{SB}+\Delta t)/\tau}, \tag{3.3}$$

where $\tau = 25$ Myr for each, and the separation Δt between the two recent bursts is 0.1-1 Gyr.

We use the flexible stellar population synthesis (FSPS) models of Conroy et al. (2009); Conroy & Gunn (2010) to construct model template spectra. We assume a

---

[6]Equations 6.1 and 6.2 are related by $t_{old} - t_{young} = 10$ Gyr $-t_{SB}$.

metallicity Z using a stellar mass prior (§3.3.5), a Calzetti reddening curve, and a Chabrier IMF. The effects of these assumptions, as well as the assumed SFHs, are discussed below (§3.3.5, §3.3.6, §3.3.7).

The observed spectrum is modeled as a linear combination of the young and old stellar templates:

$$f_{model} = [y f_{young} + (1 - y) f_{old}] \times 10^{-0.4k(\lambda)A_V}, \tag{3.4}$$

where $k(\lambda)$ is the reddening curve as a function of the wavelength λ, A_V is the amount of extinction expressed in magnitudes of V-band absorption, $f_{young}(\lambda; t_{SB}, \tau/\Delta t, Z)$ is the young stellar population spectrum (arising from Eq. 6.2) with an SFR decay rate of τ (or the separation Δt between 2 recent bursts), and $f_{old}(\lambda; Z)$ is the old stellar population spectrum (arising from Eq. 6.1). Z is the stellar metallicity assumed, using the priors described below (§3.3.5. Each spectrum is normalized within the 5200–5800 Å wavelength window, and y represents the fraction of the total galaxy light in the young stellar template. The mass fraction of new stars m_f is derived from y and t_{SB}. Thus, we parameterize the spectrum using four free parameters, t_{SB}, A_V, y, and τ.

The priors on these four parameters are as follows. A_V: [0,2] magnitudes, spaced linearly, t_{SB} (age since starburst began): [30, 2000] Myr, space logarithmically, y: [0.01, 1], spaced logarithmically, $\tau = [25,50,100,150,200]$ Myr [7] or $\Delta t = [100,200,300,500,1000]$ Myr. The priors on A_V were set by the typical dust attenuation seen in SDSS galaxies (Brinchmann et al., 2004). The minimum age prior is set to be smaller than the minimum time any galaxy would take to enter the post-starburst selection criteria. The maximum age prior is set to be well after all galaxies would have exited the post-starburst selection critera. Similarly, starbursts with $y < 0.01$, or $\tau > 200$ Myr will never be selected as post-starbursts. We tested

---

[7]We find that we cannot distinguish statistically between $\tau = 150$ Myr and $\tau = 200$ Myr, so this last option is not used in the following analysis.

smaller values of τ, but found this method cannot distinguish statistically amongst burst durations shorter than 25 Myr.

We compare the SDSS *ugriz* and *GALEX FUV, NUV* photometry, and 22 Lick indices[8] (29 total data points) to synthetic photometry and Lick indices calculated from the model spectra. While we would ideally make use of every spectral data point available, the use of the full SDSS spectra is complicated by the covariance in the spectral data points. Thus, we extract information from the SDSS spectra using the Lick indices alone (Worthey et al., 1994; Worthey & Ottaviani, 1997). While these data points are not truly independent due to the astrophysical processes underlying their relative strengths, we avoid instrumental and calibration uncertainties in interpreting the spectra. We determine the best fit model using χ^2 minimization and marginalize over all other parameters to determine the 68% likelihoods for each parameter. The errors on the data and Lick indices are taken from the SDSS catalogs described above, and we assume the error distributions are Gaussian. In Table 3.5 we show the mean and rms of the fit residuals, and in Table 3.7 we show the full covariance matrix of the fit residuals.

3.3.4   Early Star Formation History

The overall star formation history of galaxies can be approximated as a linear-exponential, $\Psi_{old} \propto te^{-t/\tau}$ (Simha et al., 2014). We use this model for the old stellar population in our stellar population fitting, with 1 Gyr as the characteristic duration τ (see Figure 3.2). To test how this choice of old stellar population model affects our results, we replace the linear-exponential model with a single-age stellar population, placed at different times 10 Gyr to 1 Gyr before the starburst. We find that the post-burst ages derived do not change by more than the formal fit error, so long as the old stellar population is > 4 Gyr before the starburst. Thus, the linear-exponential model with τ=1 Gyr is indistinguishable from a single stellar

---

[8]We eliminate NaD due to concerns about possible contamination from interstellar absorption.

population at any time >4 Gyr before the starburst, in terms of its effects on our results. Old SFHs with substantial star-formation extending to the present produce poor fits to the data, as they are not flexible in varying the amount of light from old vs. intermediate vs. young stars.

However, the SFR before the burst is expected to be non-zero, and typical of gas-rich disk galaxies. We test the effect of adding an additional SFH component, with at a constant SFR over the 10 Gyr prior to the starburst. For consistency with the prior analysis, we define the post-burst age as the age since 90% of the A stars were formed. As long as the constant SFR component does not dominate the light ($y_{constant} < 0.5$), the difference in derived post-burst age is less than the statistical + systematic error.

3.3.5   Metallicity

To fit the post-starburst data to SPS models, we must assume or fit stellar metallicities. The choice of metallicity is important in determining the post-burst ages, as changes in Z will result in systematic differences in the post-burst ages. Traditionally, the age-metallicity degeneracy can be broken using the Lick index system (Worthey et al., 1994; Worthey & Ottaviani, 1997), which we make use of in our fitting procedure. However, we cannot simultaneously break the age-burst strength-burst duration degeneracy and the age-metallicity degeneracy to the age precision required to track galaxies across the post-starburst stage. The photometry of these galaxies is unhelpful in fitting the stellar metallicities, as the extremely blue colors bias the metallicities low. Ignoring the photometry and fitting the models only to the Lick indices is not sufficient, as the difference in ages in our fitting grid is small compared to the range of metallicities allowed.

We test two priors on metallicity in our method: a constant solar value or a stellar-mass dependent value using the Gallazzi et al. (2005) mass-metallicity relation. We use the second case throughout, as it is more physically motivated, and

produces smaller average χ^2 values. To estimate the systematic error in post-burst age, we propagate the range in likely metallicities for each stellar mass from Gallazzi et al. (2005) through the SED fits. We draw 10 randomly-selected metallicities from the mass-metallicity relationship, using the error bounds in Gallazzi et al. (2005), assuming a Gaussian distribution, and using the stellar masses from the SDSS MPA-JHU catalogs (Brinchmann et al., 2004; Tremonti et al., 2004). We determine the median scatter in the age and burst mass fraction in these 10 trials for each post-starburst galaxy in the sample. The median error resulting from this analysis is 14% of the post-burst ages and 23% of the burst mass fractions. We discuss the treatment of these systematic errors in §3.3.9. We note that the stellar masses predicted at the end of this process are within the fit errors of those by the MPA-JHU group (~ 0.15 dex for this sample).

Should post-starburst galaxies lie on the mass-metallicity relation generated from all SDSS absorption line galaxies? If post-starburst galaxies are to evolve to the early-type galaxies that lie on this relation, without further episodes of star formation, they should experience no evolution on it. Short bursts of star formation can increase the stellar mass before the ISM is enriched for further star formation, resulting in a bias low in the M-Z relation. However, galaxies with longer duration bursts, multiple bursts, or those that start out at a higher Z for their stellar mass, will compensate for this effect.

3.3.6   Dust Extinction

We have assumed a Calzetti et al. (2000) extinction law in our model fits so far. The characteristic extinction in this model has uncertainty $R_V = 4.05 \pm 0.80$, but because we fit A_V directly, only A_V is sensitive to a change in R_V. Assuming the reddening curves of Charlot & Fall (Charlot & Fall, 2000) or O'Donnell (O'Donnell, 1994), we do not find significant changes in the extinction (E(B-V)) or post-burst ages or burst mass fractions measured. The results of these tests are plotted in

Figure 3.4.

We have an independent constraint on A_V through the Balmer decrement. We examine the Hα and Hβ fluxes from the MPA-JHU dataset (Aihara et al., 2011). We assume the standard case B recombination at T=10^4 K and an intrinsic value of 2.86. In general, the extinction fit from the SPS models is less than that derived from the Balmer decrement, although consistent with the errors propagated from uncertainties in the emission line fluxes. This is not unexpected (Hemmati et al., 2015), as the dust surrounding the A star population (measured in our SED fits) may cause less extinction that the dust surrounding the nebular line emission regions.

3.3.7 IMF

In our analysis, we have assumed a Chabrier IMF (Chabrier, 2003). However, there is some evidence that the IMF varies between galaxies, especially in early-types (Cappellari et al., 2012; van Dokkum & Conroy, 2012). We test the effect on the age-dating fits if we assume instead a bottom-heavy IMF, with slope $x = -3$ from stellar masses $0.1 - 100 M_\odot$. The change in IMF primarily affects the light or mass fraction measured, as the IMF effectively re-weights the old and young stellar contributions in each burst. The results of this test are plotted in Figure 3.5. We compare the difference in fit results to the fit errors estimated using each IMF. While a bottom heavy IMF would lead to measuring systematically younger ages and lower light fractions, the difference in derived ages is greater than the fit errors in only 29% of cases, and the difference in derived light fractions greater than the fit errors in 18% of cases, both within the expected number for the 68% error ranges.

3.3.8 Aperture Bias

Because the post-starburst galaxies have larger angular sizes than the 3″ fibers with which they are selected and characterized, these methods may suffer from aperture bias. A key concern in post-starburst selection is to select only truly post-starburst
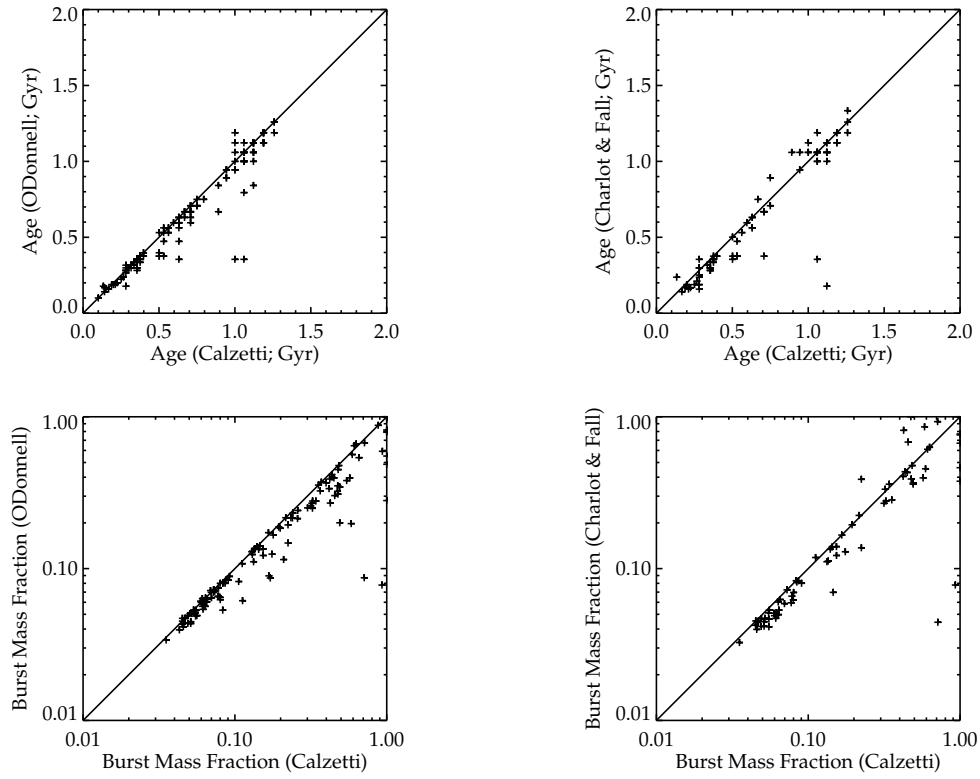
Figure 3.4: Ages and burst mass fractions fit using either Calzetti (Calzetti et al., 2000), Charlot & Fall (Charlot & Fall, 2000), or O'Donnell (O'Donnell, 1994) extinction laws, for a test of 100 post-starburst galaxies. Our derived parameters are robust to the choice of extinction law, and the only significant outliers are those with large fit errors on the derived parameters.
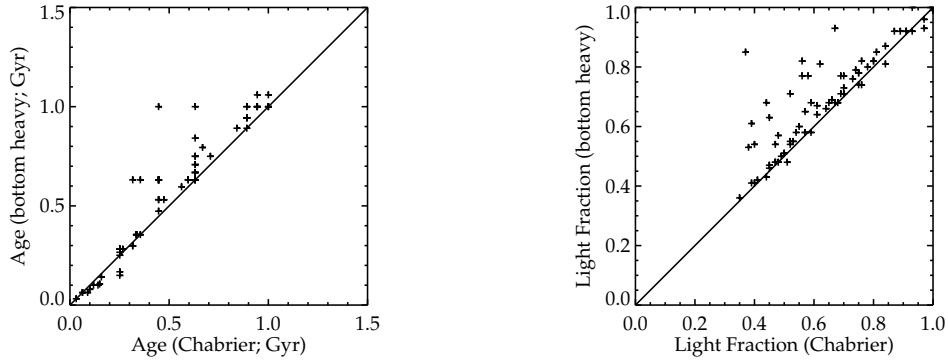
Figure 3.5: Ages and burst light fractions when assuming a Chabrier IMF vs. a bottom-heavy IMF with slope $x = -3$ from stellar masses $0.1 - 100 M_\odot$, for a test of 100 post-starburst galaxies. The change in IMF primarily affects the light or mass fraction inferred, as the IMF effectively re-weights the old and young stellar contributions in each burst. A more bottom-heavy IMF (fewer bluer high-mass stars) looks similar to a lower burst mass fraction (which would also have fewer bluer high-mass stars). The difference in derived ages is greater than the fit errors in only 29% of cases, and the difference in derived light fractions greater than the fit errors in 18% of cases, both within the expected number for the 68% error ranges.

galaxies, excluding post-starburst nuclei surrounded by a star forming disk. We select only galaxies with $z > 0.01$ to avoid this case. Indeed, IFU observations of more local post-starbursts (Pracy et al., 2014) have found pockets of star formation outside of the post-starburst nucleus of galaxies. However, these star forming regions are only ~ 500 pc from the center, and would have been included inside a $3''$ diameter fiber for galaxies with $z > 0.017$ (or 99% of our sample).

Fiber-based estimates of global galaxy properties are known to have large errors due to aperture bias when the total flux gathered by the fiber is less than 20% of the total flux (Kewley et al., 2005). In Figure 3.6 we plot the fraction of the r-band flux captured by the SDSS fiber for our post-starburst sample. Only 5% have $< 20\%$ of the total flux within the SDSS fiber (for any band), and we do not observe trends in any of the derived galaxy properties with the fraction of flux inside the fiber. The centrally concentrated light in post-starbursts results in less aperture bias than in our parent sample of SDSS galaxies: the median flux within the fiber is 43% for our post-starburst sample. For the parent sample of SDSS galaxies described above (selected to have $z > 0.01$), the median flux within the fiber is 30%, and 25% have $<20\%$ of the total flux captured by the SDSS fiber.

One concern is the dilution of the burst signatures, when the fiber samples an area greater than the extent of the starburst (Snyder et al., 2011). This effect acts to decrease the Hδ index, such that higher redshift galaxies will have weaker Balmer absorption lines. We thus caution that the parameters fit here represent the area of the fiber sampled. The area over which the starburst took place is both observed (Swinbank et al., 2012) and predicted (Snyder et al., 2011) to vary, depending on the progenitors and configuration of the triggering merger. To fully resolve the issue of how aperture affects measurements of the post-starburst properties of galaxies, spatially resolved spectra are needed. Future IFU surveys such as MANGA (Drory et al., 2015) will contribute to the growing number of post-starburst galaxies with resolved spectroscopy.
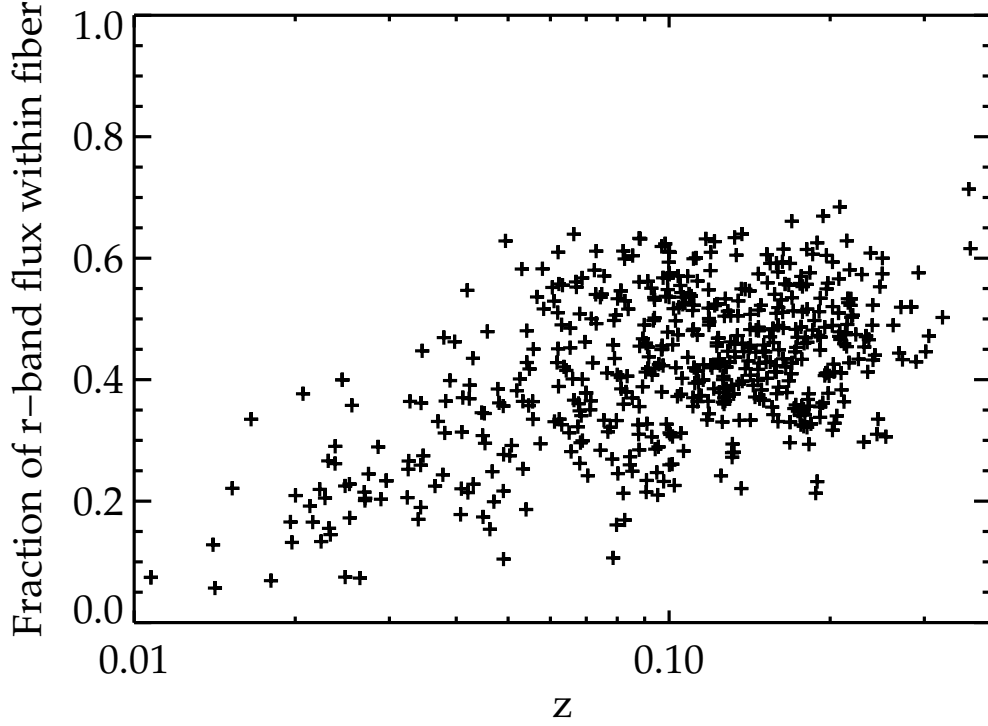
Figure 3.6: Fraction of r-band flux that falls within the $3''$ SDSS fiber vs. redshift. Only 5% of the sample has $< 20\%$ of its total flux within the SDSS fiber, where errors in determining global galaxy properties become large (Kewley et al., 2005). We do not remove these galaxies from our sample, as they do not have different distributions in any of the derived properties.

Another concern is that a mismatch between the vital *GALEX* photometry and SDSS fiber may bias the results. The FWHM of the *GALEX* PSFs are $4.9''$ and $4.2''$ for the *NUV* and *FUV* bands respectively, making it difficult to determine whether the flux is as centrally concentrated as the optical light. We estimate the effect this may have by comparing the $u - r$ colors from the `modelmag` and `fibermag` magnitudes. The difference between these colors is on average only 34% of the uncertainty in these colors, so the mismatch in apertures is unlikely to have a severe impact on the quantities derived from the SED fitting.

3.3.9 Error Estimation

We test whether the derived parameter errors are reasonable, despite the high χ^2 values (median reduced $\chi^2/\nu \sim 2.5$) by performing a jackknife test as an additional way to calculate the parameter errors. We fit each galaxy many times, removing one datapoint each time, then compare the mean and variance of the derived parameters to the original. The mean of the ratio of the initial errors to the jackknife-derived errors is consistent with 1. This indicates that the derived parameter errors are meaningful, and not severely over- or under-estimated.

We test the effects of any additional parameters outside of the SFH that could influence the quality of our fits (IMF, dust law, metallicity, SPS model, recent SF, the shape of the old stellar population), as described in the preceding sections. Our primary goal in this modeling and fitting procedure is to determine parameterized quantities relating to the time elapsed since a starburst and the nature of that starburst. While better χ^2 fits would be obtained by adding more parameters to the SFH descriptions, the results would be less useful. That approach would be valuable if the goal were accurate stellar masses (for example). Nonetheless, our derived stellar masses are within the fit errors of those by the MPA-JHU group.

While we parameterize our models using the light fraction of the recent burst(s) compared to the old population, we are interested in the burst mass fraction, which we derive from the light fraction. The conversion from light fraction to mass fraction depends on the post-burst age and burst duration (τ or Δt), as younger populations will have lower mass to light ratios. The error in the burst mass fraction is calculated by determining the likelihood function from the light fraction and age likelihood grid. We plot the light fraction vs. mass fraction for several post-burst ages for the single burst models (Figure 3.7). At very young post-burst ages, the light from the young stellar population dominates the total light for any mass fraction $> 10\%$. As a result, large uncertainties exist in many of the burst mass fractions, especially for short post-burst ages.

We consider three main sources of error in our derived properties: the fit uncertainty (including errors on the data propagated through), our metallicity assumption, the SFH uncertainty. The errors from the fit uncertainty are shown in Figure 3.8 (left). The median errors on the age are 10%, and the median errors on the burst mass fraction are 12%. The systematic errors due to our metallicity assumption, as described in §3.3.5, are shown in Figure 3.8 (middle). The median errors on the ages due to the metallicity uncertainties are 14%, and the median error on the mass fractions is 23%. Histograms of combined errors are shown in Figure 3.8 (right). The median combined errors on the ages are 22%, and the median combined errors on the burst mass fractions are 38%. These trends are not significant functions of either the post-burst age or burst mass fraction.

We have two physically motivated classes of SFHs: one or two recent bursts. The data available are not sensitive enough to discern among more complex models of the recent SFH, such as varying the relative contributions or durations of the two recent bursts, thus we do not consider external estimates of the systematic error caused by the assumed SFH history.

3.3.10   Breaking the Age-Burst Fraction-Burst Duration Degeneracy

A key feature in our method is breaking the degeneracies of the post-burst age with the burst mass and burst duration. Doing so relies on the UV photometry from *GALEX*. In Figure 3.9, we demonstrate the effect of the UV photometry and optical lines on decreasing the fit parameter uncertainties and their degeneracies by age-dating a galaxy with and without these data. The post-burst age, burst fraction, and burst duration have highly correlated errors, and higher uncertainties result. Including the UV photometry and optical lines successfully breaks these degeneracies, reducing the uncertainties in the fit parameters.

To test that our method successfully breaks these degeneracies, we add noise to simulated data and apply the age-dating method to recover the input parameters.
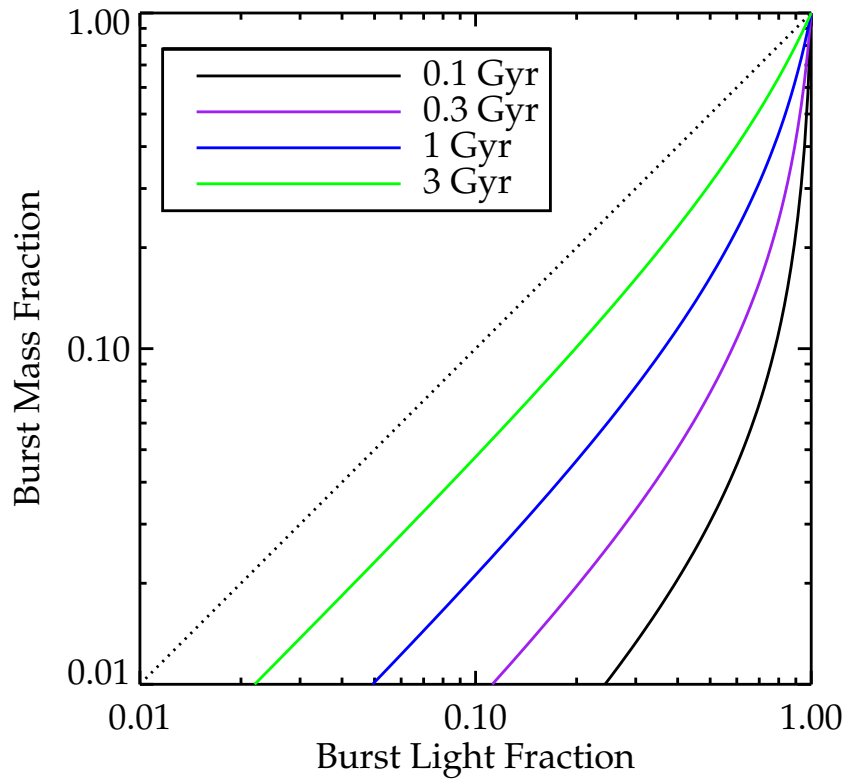
Figure 3.7: Burst light fractions vs. burst mass fractions for four post-burst ages, for a single recent burst with $\tau = 25$ Myr. At very young post-burst ages, the light from the young stellar population will dominate the total light for any mass fraction $> 10\%$. As a result, large uncertainties exists in many of the burst mass fractions, especially for short post-burst ages.
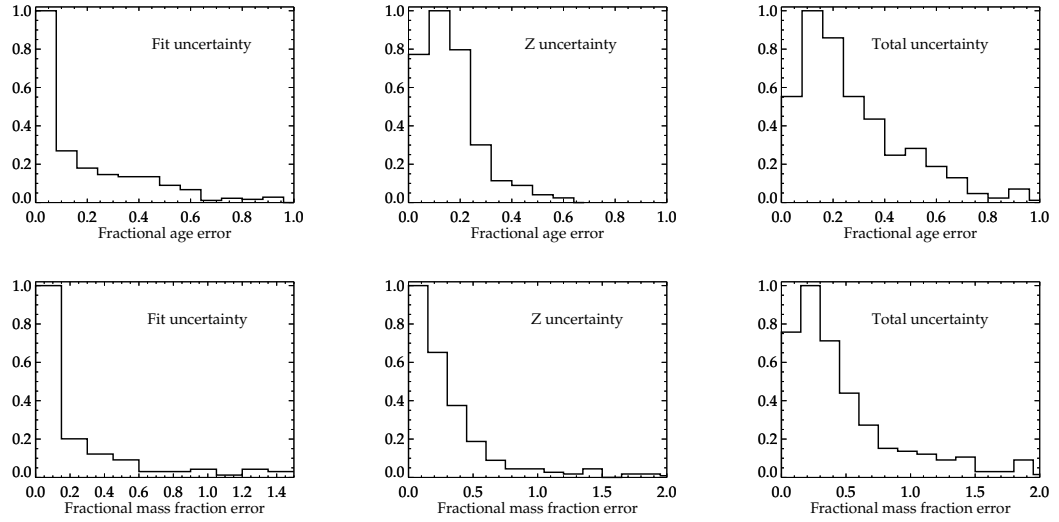
Figure 3.8: Normalized histograms of fractional errors on age and burst mass fraction (see §3.3.9). **Left**: fit error, with data uncertainties propagated through. The median errors on the ages are 10%, and the median errors on the burst mass fractions are 13%. **Middle:** systematic errors due to metallicity uncertainties. The median errors on the ages are 14%, and the median errors on the burst mass fractions are 23%. **Right:** combined errors. The median errors on the ages are 22%, and the median errors on the burst mass fractions are 38%. These trends are not significant functions of either the post-burst age or burst mass fraction.

We draw randomly from the fit grid in age, burst light fraction, and burst duration, keeping a constant A_V and metallicity. Random errors are drawn from the distribution of uncertainties of the real data, and applied to these simulated data. We apply the age-dating method to these synthetic data, testing whether the method recovers the original parameters or adds any systematic biases. The fit ages are within the fit errors of the input ages 80% of the time, and the fit mass fractions are within the 1σ fit errors of the input mass fractions 90% of the time. From the uncorrelated initial set of ages and burst light fractions, no correlation is introduced during the fitting process, and there is no significant ($> 3\sigma$) correlation between the recovered ages and burst light fractions.

3.3.11 Star Formation History Selection Effects

By selecting against galaxies with significant Hα emission, we select only galaxies that are truly *post*-starburst. However, galaxies with different burst durations and burst mass fractions will go through our post-starburst selection criteria at different post-burst ages. In Figure 3.10, we plot the regions of the burst parameter space that we expect our sample of post-starbursts to occupy, as they evolve in and out of the post-starburst selection criteria. The Lick Hδ_A limits are obtained from the FSPS models. The Hα EW limits are obtained by converting the model SFR to an Hα flux using the Kennicutt et al. (1994) relation and by comparing to the continuum level from the FSPS models. For each burst duration and burst mass fraction, it will take some time before the Hα EW has subsided enough for these galaxies to enter our selection criterion, even after waiting for all but 10% of the stars to be made in the burst. Similarly, the post-burst age at which the strong Hδ absorption fades out of our selection criterion will differ, depending on the burst mass fraction. It is clear from this plot that we are more sensitive to weaker bursts (lower burst mass fraction) at younger ages, for shorter bursts. The effects of our selection must be taken into consideration when examining the statistical properties
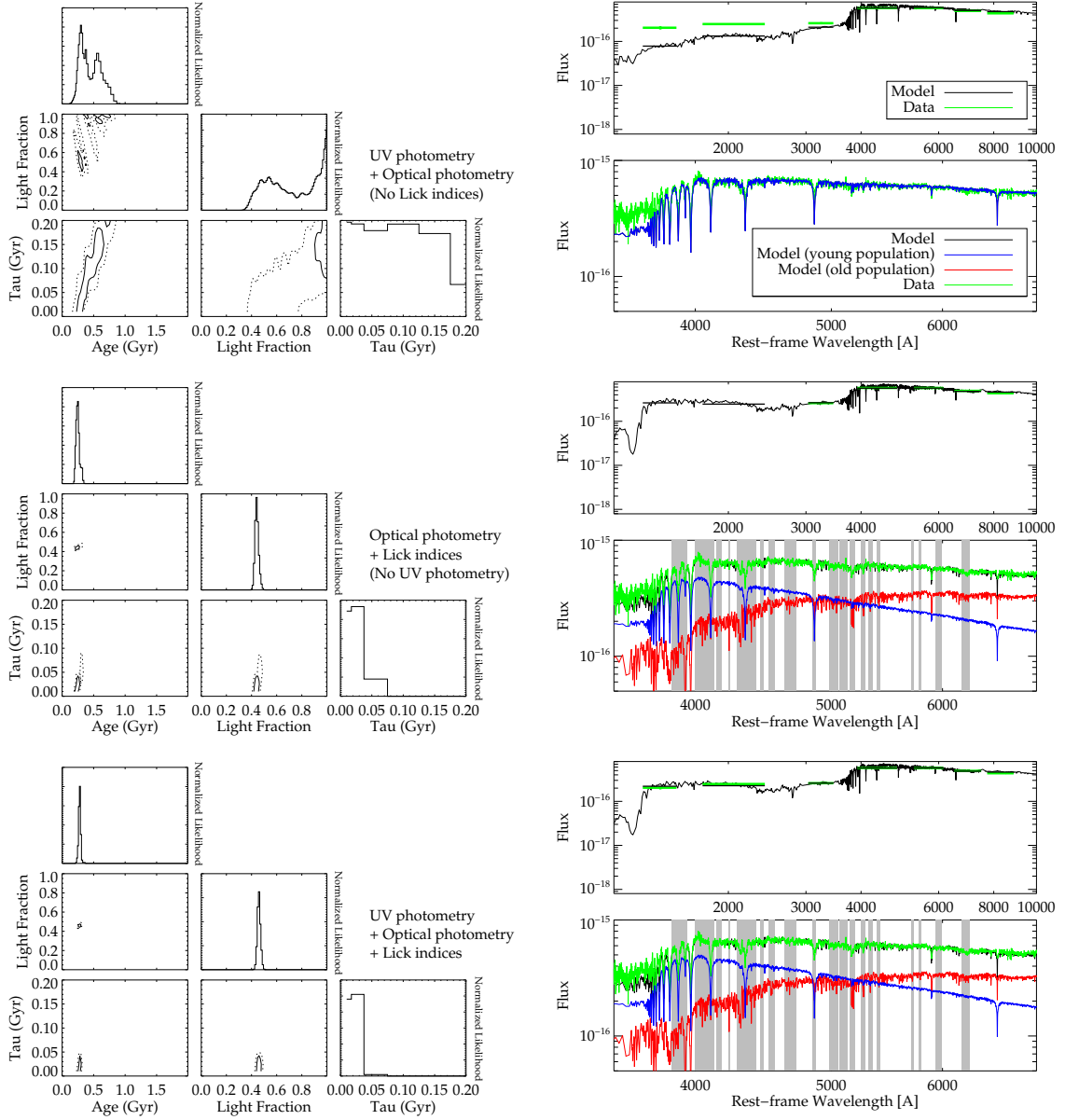
Figure 3.9: Example likelihood contours of model parameters from this age-dating method (left column), and comparisons of the data and model spectra (right column). This case shows the derived properties for the single recent burst SFH model. We marginalize over A_V, then plot the 68% (solid lines) and 95% (dotted lines) likelihood contours for the remaining parameter pairs, marginalizing over the third parameter. Normalized likelihoods for each parameter are shown at the top of each column. In the right hand column, we plot the associated model and data spectra and photometry for the best fit given each set of data. The grey bars indicate the location of the Lick indices used to parameterize the spectra. The bottom row shows the results for a galaxy, using the full set of UV-optical photometry and optical line indices. The middle row shows the consequently worse parameter degeneracies and uncertainties, if the UV photometry is not included in the fit, and the top row, if the optical lines are not included in the fit. The redshift of this example galaxy is

of post-starbursts.

From the way the post-burst age, burst mass fraction, and burst duration map to the observed post-starburst signatures, it is clear that different selection methods can produce different populations of post-starbursts. The method by Wild et al. (2007, 2009), used for example by Yesuf et al. (2014) and Rowlands et al. (2015), aims to select post-starburst galaxies with the strongest (i.e., highest burst mass fraction) bursts, using a PCA analysis of spectra around the 4000Å region, especially the $D_n(4000)$ index, excess Balmer absorption, and excess Hϵ vs. Ca II H+K absorption. By selecting only the strongest bursts, this method selects *only* post-starburst galaxies with burst durations of $\gtrsim 150$ Myr, not the population with shorter durations. Figure 3.10 demonstrates that for shorter starbursts, lower burst mass fractions produce similarly strong post-starburst signatures, because the SFRs and sSFRs during the burst are similarly high. Although this method has other strengths, such as identifying galaxies transitioning from starbursting to post-starburst (Rowlands et al., 2015), it neglects a significant number of post-starburst galaxies.

3.3.12 Effects of Magnitude-Limited Parent Sample

Our sample is subject to potential biases from magnitude limits in two ways. The first is the magnitude-limited nature of the SDSS parent sample. The second is the requirement that the galaxies be detected in both the *GALEX FUV* and *NUV* bands.

As detailed in Section 3.3.11, the selection on Hα emission and Hδ absorption has a strong influence on the distribution of the properties mentioned (especially age since starburst, and the strength and duration of the starburst). This selection biases the distributions of these quantities much more significantly than the magnitude cuts (this can be seen in the predicted vs observed distributions given the selection cuts alone), and as such we caution against making claims about the distributions of
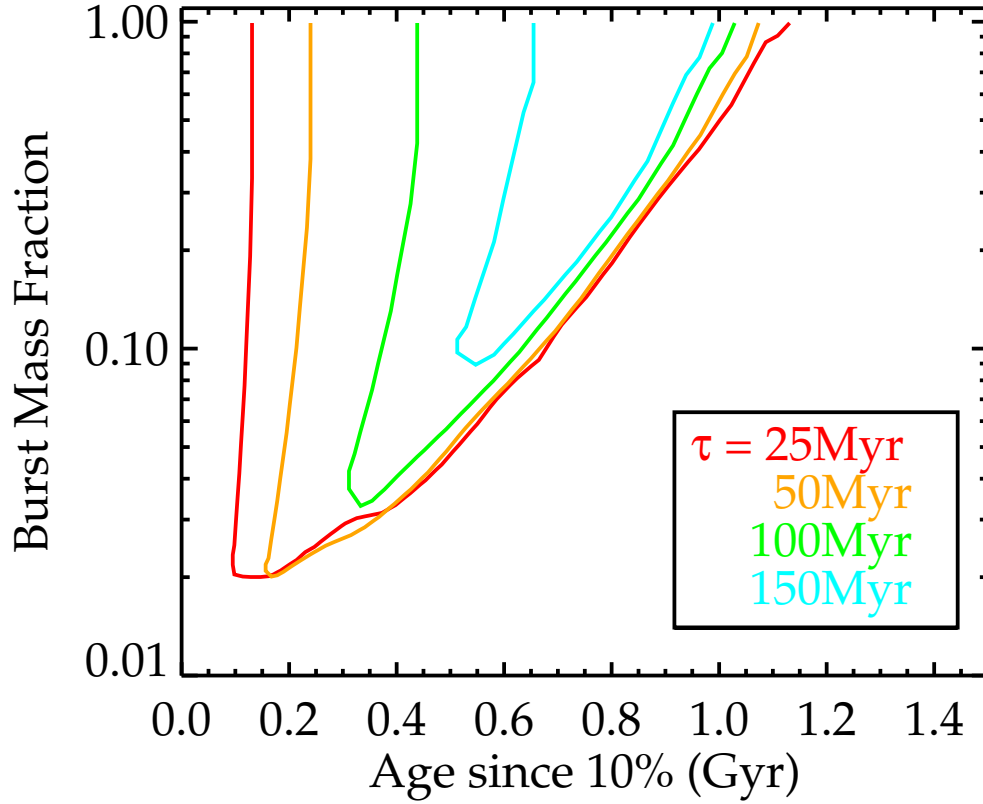
Figure 3.10: Burst mass fraction and post-burst age space for post-starburst galaxies selected with the Hα-Hδ method described in §3.2.1, divided up by the burst duration, τ. Colored contours mark where galaxies enter and leave the post-starburst Hα emission and Hδ absorption criteria. After the starburst ends, the post-burst age at which the Hα emission EW is low enough to enter the post-starburst phase will depend on how much stellar mass is produced in the recent starburst, and the burst duration. As the stellar populations age, the $H\delta_A$ absorption will decrease, and galaxies will leave the post-starburst phase at different post-burst ages depending on burst fraction of the starburst. As a result, the descendants of starbursts with longer durations will only be seen at older post-burst ages, and only if the burst fraction is high. This selection must be understood in order to asses physical features in the distribution of starburst properties.

these properties independent of their selection.

We test whether the distribution of derived ages is subject to bias from the magnitude limit. The distribution of ages is the same (passes a KS test) for different bins of stellar mass. If a large number of galaxies were brightened in FUV into our sample, we would have expected (given that the FUV flux should fade with time) that the lower mass galaxies should have younger age distributions.

We test whether the main difference in the galaxies with FUV detections and those without is stellar mass or redshift. The distribution in redshift between these samples is different (fails a KS test), but the distribution of stellar masses is the same (passes a KS test). Thus, we do not expect the FUV-limited nature of the sample to bias the sample, except to exclude farther away galaxies in the SDSS parent sample.

Nonetheless, we test whether our stellar-mass dependent conclusions might be affected by the magnitude-limited nature of the sample. We define a volume-limited subset, and find that much of the power in our conclusions is driven by the intermediate mass galaxies, rather than a small number of low mass galaxies. More detail is presented in the relevant section: §3.4.2.

3.3.13 Comparison to $D_n(4000)$-Hδ Method

In the absence of detailed modeling, the indices $D_n(4000)$ and Hδ are sometimes used as proxies for the post-burst age and burst mass fraction (e.g., Yagi et al., 2006). Using the results of our stellar population fits, we evaluate how accurate this method is in assessing the recent SFHs of post-starbursts. We show the standard plot of $D_n(4000)$ vs. Lick Hδ_A, colored by post-burst age and burst mass fraction (Figure 3.11).

In Figure 3.12 we plot the post-burst age and burst mass fraction vs. $D_n(4000)$ and Lick Hδ_A, for galaxies in our sample best fit by a single recent burst. The relation between $D_n(4000)$ and the post-burst age suffers from a degeneracy with the

burst mass fraction and burst duration. For post-starbursts with $D_n(4000) < 1.3$, where post-starburst ages are typically younger than 300 Myr, the degeneracy is lessened, and $D_n(4000)$ is highly correlated with the post-burst age. However, if $D_n(4000) > 1.42$, where post-starburst ages typically range from 300-1500 Myr, $D_n(4000)$ is no longer significantly ($> 3\sigma$) correlated with the post-burst age or the age since the starburst began. We caution that these results depend on our post-starburst selection method. For the youngest post-burst ages, we only can select short-duration, low burst mass fraction starbursts. Selection methods that do not make the same Hα-Hδ cuts may find increased scatter in the $D_n(4000)$-age at younger ages, where it currently appears more robust, if longer duration starbursts are allowed into the sample. For the Lick Hδ_A index, we see that the post-starbursts with the highest values of Hδ_A are not those with the strongest bursts, but those with short duration bursts of $m_\mathrm{burst} \sim 0.1$ observed within 500 Myr post-burst.

3.4   Results: Constraints on Star Formation Histories

3.4.1   Derived Starburst Properties

We plot the post-burst ages and burst mass fractions for the post-starburst galaxies best fit by a single recent burst in Figure 3.13. 68% of the burst mass fractions are within 7.0%–69%, and 68% of the post-burst ages are within 240–680 Myr. The ages appear correlated with the burst mass fractions, although this is due to our selection of the post-starburst galaxies, rather than fitting degeneracies.

To illustrate how the selection of post-starburst galaxies influences the ages, burst mass fractions, and burst durations, we outline the parameter space in post-burst age, burst fraction, and burst duration where the a hypothetical galaxy would meet our post-starburst selection criteria after the starburst, as in §3.3.11. For each burst duration, the remaining panels in Figure 3.13 plot these outlines. The absence of post-starburst galaxies at old age and low mass fraction is due to a lack of strong
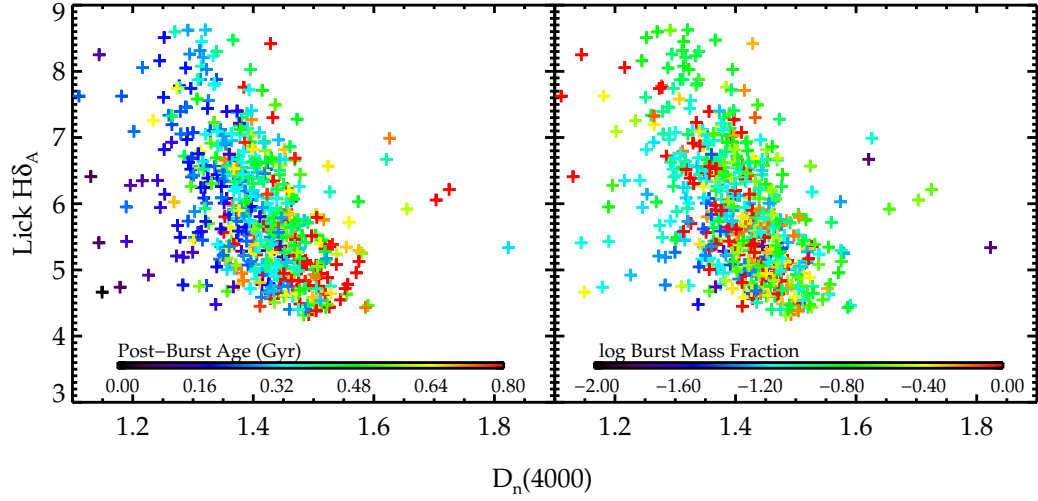
Figure 3.11: $D_n(4000)$ vs. Lick Hδ_A, colored by post-burst age (left) and burst mass fraction (right). $D_n(4000)$ and Lick Hδ_A are from the SDSS catalogs described in the text, not the best-fit values. This parameter space has been used a a proxy for the post-burst age and burst mass fraction (e.g., Yagi et al., 2006). Here, and in the next figure, we demonstrate that there is significant scatter in where post-starburst galaxies with a certain post-burst age and burst mass fraction lie.
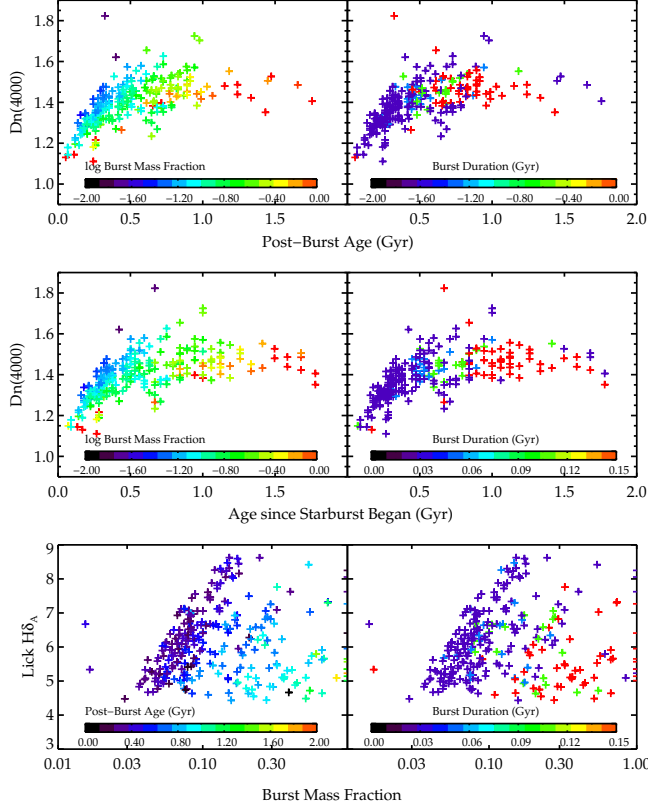
Figure 3.12: Comparison of post-burst age, age since starburst began, and burst mass fraction to the indices $D_n(4000)$ and Hδ, which are sometimes used as proxies for the post-burst age and burst mass fraction. $D_n(4000)$ is from the SDSS catalogs described in the text, not the best-fit values. We plot only galaxies best fit by a single recent burst, and color code by the additional SFH parameters (post-burst age, burst mass fraction, or burst duration). The relation between $D_n(4000)$ and the post-burst age suffers from a degeneracy with the burst mass fraction and burst duration. For post-starbursts with $D_n(4000) < 1.3$, where post-starburst ages are typically younger than 300 Myr, the degeneracy is lessened, and $D_n(4000)$ is highly correlated with the post-burst age. However, if $D_n(4000) > 1.42$, where post-starburst ages typically range from 300-1500 Myr, $D_n(4000)$ is no longer significantly ($> 3\sigma$) correlated with either the post-burst age or the age since the starburst began. We caution that these results depend on our post-starburst selection method. For the youngest post-burst ages, we only can select short-duration, low burst mass fraction starbursts. Selection methods that do not make the same Hα-Hδ cuts may find increased scatter in the $D_n(4000)$-age at younger ages, where it currently appears more robust, if longer duration starbursts are allowed into the sample. For the Lick Hδ_A index, we see that the post-starbursts with the highest values of Hδ_A are not those with the strongest bursts, but those with short duration bursts of $m_{\mathrm{burst}} \sim 0.1$ observed within 500 Myr post-burst.

Hδ absorption. The dearth of post-starburst galaxies at short τ and high mass fraction is real, arising from the too high burst sSFRs ($> 1 \times 10^8$ yr^{-1}) required to produce such a high fraction of the stellar mass in such a short time. For the median stellar mass of our sample, $3 \times 10^{10} M_\odot$, this corresponds to an absence of starbursts with SFRs (> 300 M$_\odot$ yr^{-1}). This is the reason the burst fractions appear to be correlated with the burst durations. If such galaxies were common in the local universe, we would have selected their descendants as members of the post-starburst sample. The post-starburst galaxies uniformly fill the space within their selection criteria to within the formal fit errors, when considering the lack of starburst progenitors with exceptionally high sSFRs.

The fitted burst durations and mass produced in the burst provide an estimate of the maximum sSFR during the starburst. In Figure 3.14, we plot the max sSFRs from the recent starburst and stellar masses in comparison to the star-forming Main Sequence fit from Schiminovich et al. (2007). The starbursts experienced by our sample of post-starburst galaxies lie 10-100$\times$ above the Main Sequence and are typical of starbursting galaxies.

In Figure 3.13, we also plot the ages and burst mass fractions for post-starburst galaxies best fit by two recent bursts. Again, the galaxies fall within the bounds expected from the Hα and Hδ selection criteria. However, we do not have the sensitivity to fit the individual durations or mass fractions of each burst. Because of this, we cannot accurately estimate the maximum SFR for these galaxies.

3.4.2 Single or Double Recent Burst?

In Section 3.3.2 we discussed two classes of recent SFHs for the post-starburst galaxies: one or two recent bursts. Now, we constrain the implications of which galaxies prefer each model. In Figure 3.15, we show the distribution of stellar mass for galaxies preferring each model. Recent double burst galaxies are at systematically lower stellar mass than single recent burst galaxies. The separation in the median values
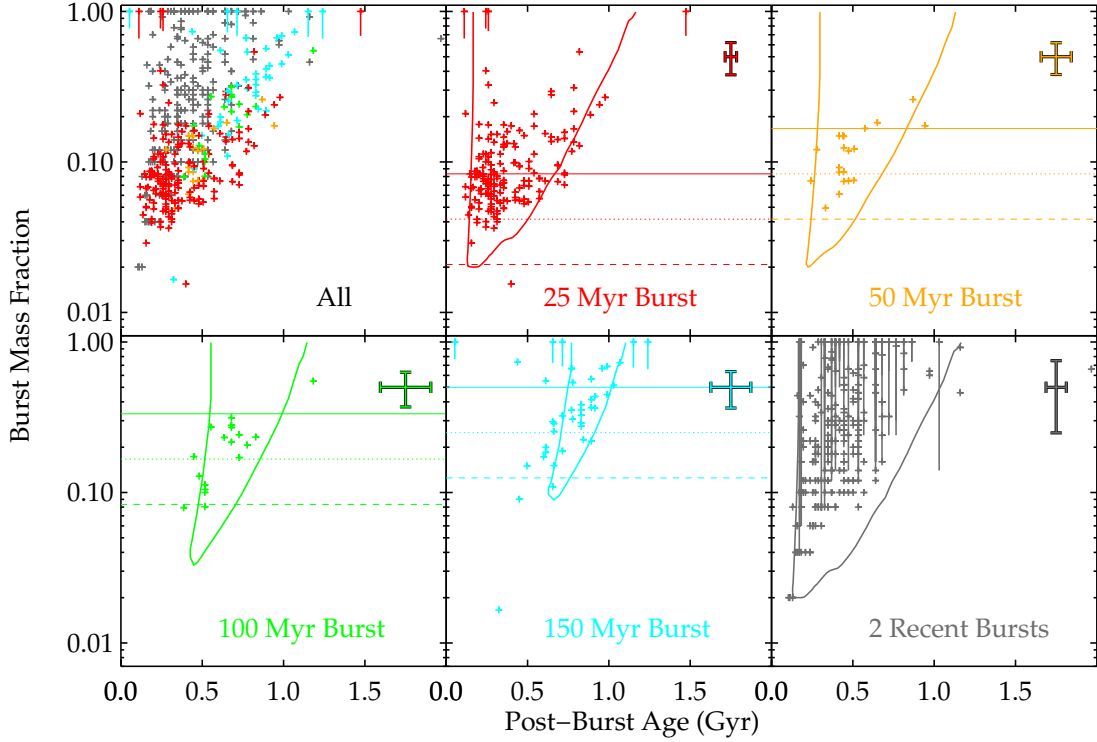
Figure 3.13: Burst mass fraction and post-burst age for post-starburst galaxies, divided up by SFH. For galaxies which strongly prefer a single recent burst, we show only those with prefer a value for τ. The final panel shows the galaxies best fit by two recent bursts. Colored contours mark where galaxies enter and leave the post-starburst Hα EW and Hδ absorption criteria. The observed lack of post-starburst galaxies at old age and low mass fraction is due to their lack of strong Hδ absorption. The dearth of post-starburst galaxies at short τ and high mass fraction is due to the high burst (maximum) SFRs that would be required to produce so much mass in such a short time. Overplotted as solid, dotted, and dashed lines are the burst SFRs for a 1e10 $M_\odot$ galaxy at SFR=25, 50, and 100 $M_\odot$ yr^{-1} respectively. The post-starburst galaxies uniformly fill the space within their selection criteria and constraints on the burst SFR, to within the formal fit errors. Characteristic error bars reflecting the fit uncertainties are shown in each panel, and we plot individual error bars for galaxies with unphysical burst mass fractions of 1, to show that the error bars extend down to much lower mass fractions. For galaxies best fit by the two recent burst model, we do not have the sensitivity to fit the individual durations or mass fractions of each burst. Because of this, we cannot accurately estimate the maximum SFR for these galaxies.
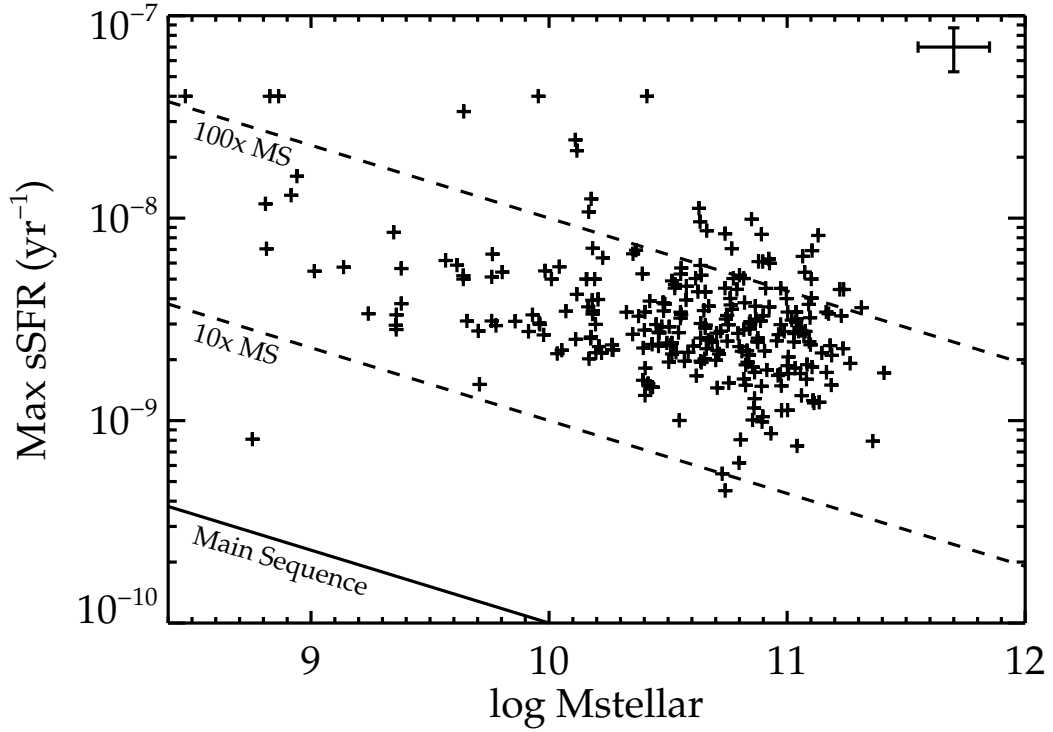
Figure 3.14: Stellar mass vs. maximum sSFR (m_{burst}/τ) during the burst. The Main Sequence as fit by Schiminovich et al. (2007) is shown, along with multiples of 10-100×, as is common for starbursting galaxies. A characteristic error bar is shown in the upper right. We plot sSFR (derived from the burst mass fraction m_{burst} and the burst duration τ from the stellar population fits) instead of SFR to avoid correlated errors. We only plot galaxies which strongly prefer a single recent burst, and prefer a value for τ. The expected progenitors of the post-starburst sample have similar ranges of sSFRs.

is significant (3.0σ).

In Figure 3.16, we compare the burst mass fractions to stellar mass for galaxies with either one or two recent bursts. Lower mass galaxies have on average higher burst mass fractions (see also Bergvall et al. 2016). This trend is strongly dependent on the number of recent bursts, considering both the fit error and systematic error due to the metallicity uncertainty. For galaxies with one recent burst, there is an (Spearman $\rho = -0.19$, 3.1σ) anti-correlation. For galaxies with two recent bursts, there is a stronger (Spearman $\rho = -0.45$, 7.2σ) anti-correlation. At a single stellar mass, the scatter in burst mass fraction is physical among the galaxies with well-determined mass fractions (i.e., fit errors less than 33%).

Many of the galaxies at the highest burst mass fractions show a best-fit burst mass fraction of 1, which is unphysical. This is due to the effect discussed in Figure 3.7, where small changes in light fraction can lead to large changes in burst mass fractions, especially at the highest burst mass fractions, leading to higher fit errors. The lower bounds of the fit errors on the mass fraction extend to lower burst mass fractions, which are more physical. Nonetheless, we also consider the strength of the anti-correlations with stellar mass excluding the galaxies with best-fit burst mass fractions of 1. The anti-correlation for the sample with two recent bursts remains significant (Spearman $\rho = -0.42$, 5.9σ), while the anti-correlation for the sample with single recent bursts drops below our significance threshold (Spearman $\rho = -0.13$, 2.0σ).

Why do the lower mass galaxies experience a greater number of recent bursts, with a greater fraction of their stellar mass created? There are two possibilities. First, if the lower mass galaxies are more susceptible to stellar feedback, and the first burst was interrupted by the expulsion and re-accretion of gas in the galaxy. Lee et al. (2009) study the duty cycle of starbursts in dwarf galaxies and find the typical burst duration is ~ 100 Myr, with such events happening every $1 - 2$ Gyr. This frequency is consistent with the burst durations and separations fit here for

the low mass post-starburst galaxies.

Another possibility is that the lower mass galaxies could have had progenitors with smaller bulge components, as discussed in our initial motivation of these models (see §3.3.2). As galactic bulges can act to stabilize the gas, bulge-less progenitors can experience a burst of star formation during the first pericenter passage of the two galaxies, in addition to a burst upon final coalescence (Mihos & Hernquist, 1994; Cox et al., 2008; Renaud et al., 2015). We compare the stellar mass produced in the recent burst to estimates of the current bulge mass by Mendel et al. (2014). The stellar mass produced in the recent burst is typically 10-100% of the bulge mass. This implies that the bulges are not formed entirely by the new stars produced in the starburst and that the progenitors had pre-existing bulges. However, there are significant uncertainties in performing a bulge-disk decomposition on post-starburst galaxies using photometry alone. The high concentration of the newly formed stars can result in a smaller bulge radius (Yang et al., 2006, 2008), or the mass of the bulge can be underestimated if the SED fitting does not account for the extreme recent star formation history. Additionally, it is uncertain what fraction of the newly formed stars reside in the bulge. Spatially resolved spectroscopy is needed to determine the age of the bulge stellar populations.

We test whether these results could be driven by the magnitude-limited nature of this sample (see §3.3.12). We define a volume-limited subset, which has $z < 0.15$ and $M_{stellar} > 10^{10.2}$. In this volume-limited subset, we still find a significant difference between the stellar masses of galaxies preferring one vs. two recent bursts, and a significant trend in stellar mass vs. burst mass fraction for the galaxies with two recent bursts. Thus, our results are not likely to be driven by a scenario where only the lower stellar mass galaxies with the strongest bursts have been included in our sample.
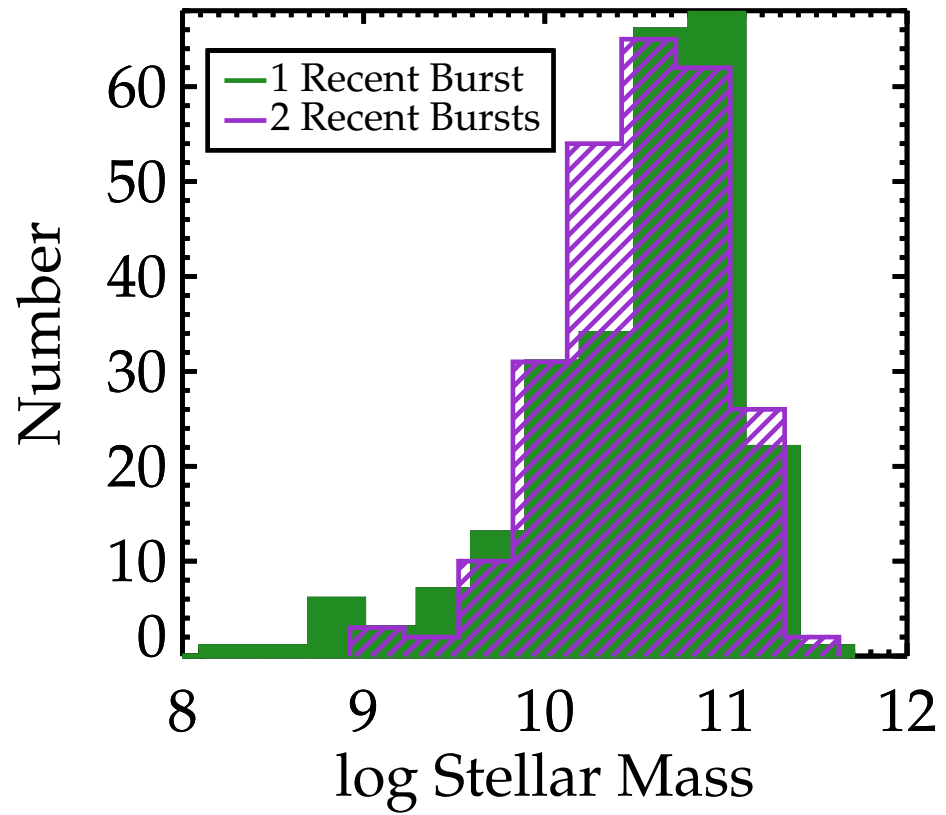
Figure 3.15: Histograms of stellar masses for post-starburst galaxies preferring a single or double recent burst SFH. There is a significant shift toward lower stellar mass for galaxies preferring two recent bursts, compared to those best fit by one recent burst.
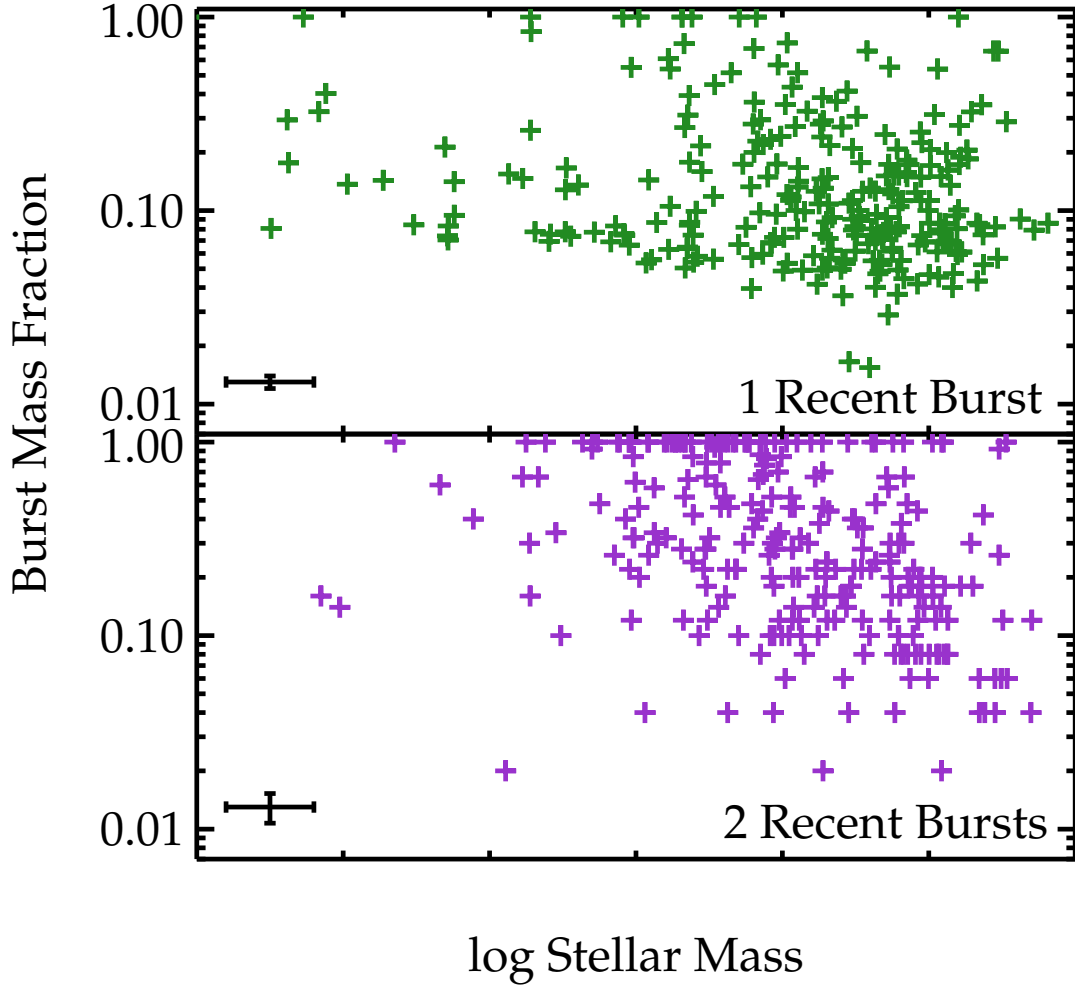
Figure 3.16: Stellar mass vs. burst mass fraction, with galaxies color coded by best-fit SFH. A representative error bar reflecting the fit uncertainty and metallicity uncertainty is also shown. For galaxies which have experienced one recent burst, there is a weak (Spearman $\rho = -0.17$, 2.4σ) anti-correlation. For galaxies which have experienced two recent bursts, there is a stronger (Spearman $\rho = -0.48$, 6.8σ) anti-correlation.

3.4.3 Comparison to Shocked Post-Starburst Galaxies

Our selection of post-starburst galaxies selects against all Hα emission, regardless of the source. This biases us against post-starburst galaxies with Seyfert activity (Yesuf et al., 2014) or strong shocks (Alatalo et al., 2016c). Additionally, we only select galaxies which are truly *post*-starburst. Galaxies with ongoing starbursts are excluded, as seen by the left hand limits in Figure 3.10. Identifying these galaxies before they enter the post-starburst criterion is of considerable interest, but requires more sophisticated selection methods.

The age-dating method described here can be applied to both galaxies before they enter the post-starburst phase and to post-starburst galaxies with AGN activity. Our tests on galaxies with strong Balmer absorption and no cut on Hα place the galaxies still within their burst (i.e., the post-burst age is negative), with similar burst mass fractions as the post-starburst sample. Our method is useful in matching progenitor starbursting galaxies to their likely post-starburst descendants. Galaxies with suspected AGN activity may benefit from an additional AGN template added to the SPS modeling to account for any contribution to the continuum light.

We use the age-dating method described here to test how a sample of post-starburst galaxies selected to allow emission lines from shocks (SPOGs; Alatalo et al., 2016c) compares with the sample identified using our Hα-Hδ cuts. If the emission lines allowed by the SPOG selection are due to star formation, and the starburst has not truly ended, our best-fit model will show a starburst age t_{sb} shorter than the duration τ of the most recent burst of star formation, resulting in a "negative" post-burst age (i.e., the burst is still on-going). However, emission lines from star formation or other sources could impact the optical spectral indices using in these fits. We must correct the Lick Hβ, Hγ and Hδ indices for emission filling. We estimate the emission in these lines, using the Hα line flux from the MPA-JHU line catalogs (Brinchmann et al., 2004), the intrinsic line ratios Hα/Hβ = 2.86, Hα/Hγ = 6.11, and Hα/Hδ = 11.1, assuming case B recombination at T= 10^4 K (Osterbrock,

1974) . We use the average reddening from the SPOGs fit without this correction, $A_V = 0.8$ mag, and a Calzetti extinction law as before. The Lick index corrections are thus:

$$\Delta H\beta = \frac{f(H\alpha)10^{-0.4A_V/R_V(k_\lambda(H\beta)-k_\lambda(H\alpha))}}{2.86f(H\beta)_{cont}} \qquad (3.5)$$

$$\Delta H\gamma = \frac{f(H\alpha)10^{-0.4A_V/R_V(k_\lambda(H\gamma)-k_\lambda(H\alpha))}}{6.11f(H\gamma)_{cont}} \qquad (3.6)$$

$$\Delta H\delta = \frac{f(H\alpha)10^{-0.4A_V/R_V(k_\lambda(H\delta)-k_\lambda(H\alpha))}}{11.1f(H\delta)_{cont}}, \qquad (3.7)$$

where f_{cont} is the continuum flux at each line. These corrections are large compared to the average error on the indices. For our post-starburst sample, $\langle \Delta H\beta \rangle = 0.25$ Å, lower than the uncertainty $\sigma(\text{Lick } H\beta) = 0.40$ Å. However, for the SPOGs sample, $\langle \Delta H\beta \rangle = 2.71$ Å, much higher than the uncertainty $\sigma(\text{Lick } H\beta) = 0.64$ Å. Additionally, we exclude the Fe5015 Lick index, as it is contaminated by the [OIII]λ5007Å line in the SPOGs sample.

If the emission lines in the SPOGs sample are due to type II AGN activity, this emission line treatment is sufficient, and the addition of an AGN component to fit the UV/optical photometry is not required. Except in the case of QSOs, the AGN contribution to the NUV photometry is small, at $\lesssim 15\%$ (Salim et al., 2007), similar to the typical errors in our NUV photometry. The observed UV emission from type II AGN is observed to be extended (Kauffmann et al., 2007) and thus not originating from the AGN.

Post-starburst ages and starburst properties for the SPOGs are shown in Table 3.3. We plot the post-burst ages, mass fractions, and durations in Figure 3.17. The SPOGs are generally younger than the post-starburst galaxies, with 60% too young to have been selected by our post-starburst criteria, as they lay outside the selection contour lines from Figure 3.13. SPOGs with similar mass fractions and

durations as the post-starbursts may represent an evolutionary sequence. However, an additional population of SPOGs (10% of the total SPOGs sample) exists at long duration (> 100 Myr) and small burst fraction ($< 10\%$), not consistent with our post-starburst selection criteria.

3.5 Results: Discovery of Gas and Dust Evolution

3.5.1 Molecular Gas Evolution

Determining the post-burst ages of post-starburst galaxies, and identifying evolutionary sequences, is important in studying the mechanisms by which star formation shuts down and stays dormant in these galaxies. In this section, we combine molecular gas (CO $J=$ 1–0 and CO $J=$ 2–1) measurements of post-starburst galaxies to piece together the likely history of molecular gas depletion after the starburst. We combine three samples to extend our time baseline[9]. The first sample we consider, from French et al. (2015), uses the selection method discussed in §3.2.1. These galaxies are contained within our parent sample of post-starburst galaxies, and have stellar masses $10^{9.96} - 10^{11.31}$ and redshifts $z = 0.0196 - 0.1129$. For those without *GALEX* photometry, we use upper limits when available. The second sample, by Rowlands et al. (2015), uses the selection method by Wild et al. (2009), which selects high burst mass fraction, long duration starbursts and post-starbursts. The third sample is the shocked post-starburst galaxy sample by Alatalo et al. (2016c) described in §3.4.3, with molecular gas measurements presented in Alatalo et al. (2016b).

We exclude the French et al. (2015) galaxy labeled H01, as resolved CO (2–1) imaging with ALMA has shown that the gas is associated with a companion, non-post-starburst galaxy. The resolved CO is coincident with a 1.4 GHz FIRST (Becker

---

[9] We note that during the refereeing process, another paper with several CO observations of post-starburst galaxies was submitted to MNRAS by Yesuf et al.
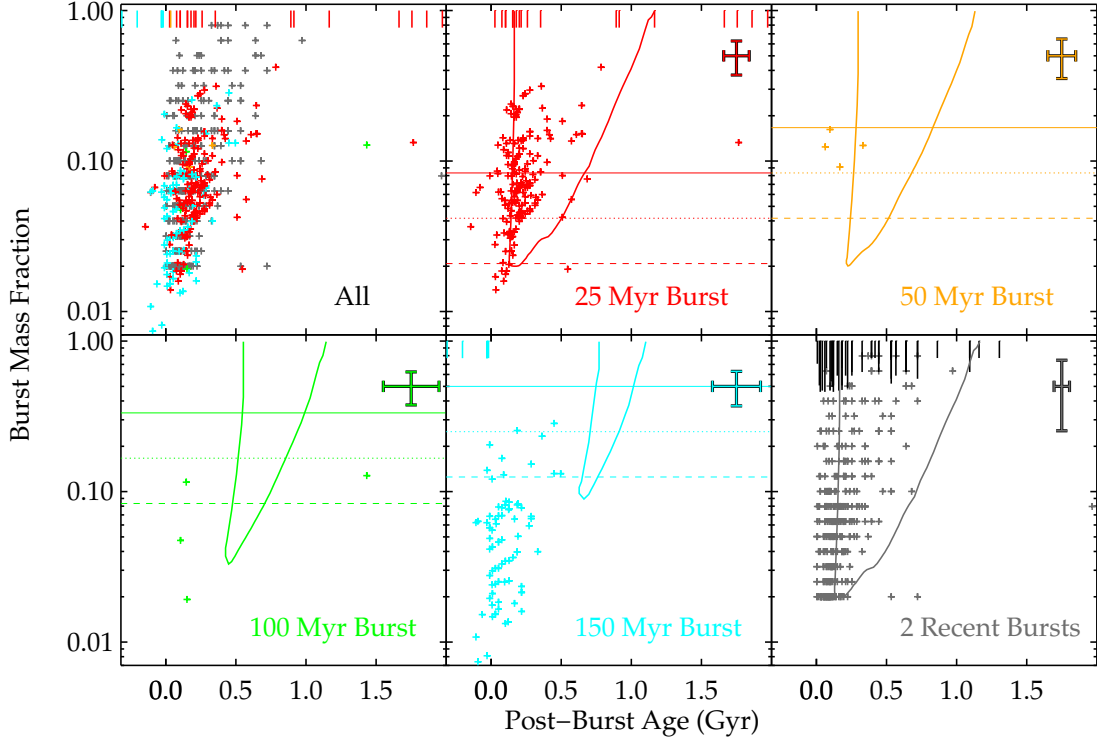
Figure 3.17: Same as Figure 3.13, but for shocked post-starburst galaxies (SPOGs; Alatalo et al., 2016c). We plot characteristic error bars representing the fit uncertainties, and we plot individual error bars for galaxies with unphysical burst mass fractions of 1. The contours represent the post-starburst selection contours for the traditionally-selected sample. The SPOGs are generally younger than the post-starburst galaxies, with 60% too young to have been selected into our post-starburst criterion. SPOGs with similar mass fractions and durations as the post-starbursts may represent an evolutionary sequence. However, an additional population of SPOGs exists at long duration (> 100 Myr) and small burst fraction ($< 10\%$), which will not enter our post-starburst selection criteria.

et al., 1995) detection, while the post-starburst component has no corresponding detection. Including this galaxy would not significantly change our results. Unlike H01, none of the other post-starbursts with multiple components inside the observed beam have possible star-forming companions, based on FIRST 1.4 GHz data.

How does the molecular gas and dust content of a galaxy evolve after the starburst ends? We would like to trace the evolution of a similar galaxy through time, although how finely we can divide the sample is limited by the number of post-starburst galaxies with molecular gas measurements in how finely we can divide the sample and by the fact that the measurements are from three differently-selected post-starburst samples. The galaxies considered here span a range of stellar masses from $10^{9.50} - 10^{11.31}$, with 68% within $10^{10.04} - 10^{10.88}$. There is no significant difference amongst the median stellar masses of the three samples. Similarly, the range in redshifts is small, with all at $z > 0.01$ to avoid issues of serious aperture bias, and no significant redshift evolution expected within the sample to $z \sim 0.2$.

One of the main sources of scatter in tracing the molecular gas content with age is how much molecular gas was used up in the starburst. If the progenitors of the galaxies studied here had similar initial gas fractions, we should reduce the scatter caused by varying starburst efficiencies by dividing the sample by burst mass fraction. We split the samples into 2 classes of SFHs: those with burst mass fractions ≤ 0.2 and > 0.2. The two classes have a mix of single and double recent bursts, although the first class has primarily short-duration bursts, and the second long-duration bursts (see §3.3.11 and §3.4.1). We plot the molecular gas to stellar mass fractions vs. post-burst age for each class (Figure 3.18). We observe a significant decline in the molecular gas fraction ($M(H_2)/M_\star$) with increasing post-burst age (Spearman $\rho = -0.50$ at 4.0σ significance). Split up into the two burst fraction bins, the significance drops to 3.7σ (Spearman $\rho = -0.61$) for the low burst fraction sample, and 2.8σ (Spearman $\rho = -0.49$) for the high burst fraction sample.

We do not expect a selection bias in the Rowlands et al. (2015) sample against

galaxies with low gas fractions. The Alatalo et al. (2016b) sample measured molecular gas content in only galaxies with SNR> 3 in WISE 22μm, which would result in higher gas fractions if the dust traces the gas. However, in the French et al. (2015) sample, only 2/32 galaxies do not have WISE 22μm detections with SNR> 3; neither has a molecular gas detection. Removing these two galaxies has no effect on the anti-correlations described, so the selection cut made by Alatalo et al. (2016b) should not affect the trend seen in these gas fractions with post-burst age. The French et al. (2015) sample was chosen with a cut on the median SNR of the SDSS spectra, while the Alatalo et al. (2016b) sample was not. However, only two of the Alatalo et al. (2016b) sample would not pass our cut of median SNR >10.

All three post-starburst samples are affected by the magnitude limit of their SDSS parent sample. There is no additional limit imposed on their *GALEX* magnitudes, as we fit their stellar populations regardless of the presence of *GALEX* detections, unlike in the sample of post-starburst galaxies discussed earlier in this work. The lack of the *GALEX* information is reflected in the significantly larger errors in age in these cases. We established earlier (§3.3.12) that the derived ages are not affected by biases in the SDSS parent sample. In combination with our normalization by stellar mass, our result is thus not due to the magnitude-limited nature of the SDSS parent sample. We caution that these results may differ for samples at dramatically different stellar masses or redshifts, or with differing star formation histories.

3.5.2 Molecular Gas Depletion Mechanisms

What processes could deplete the molecular gas reservoirs after the starburst has ended? We fit the observed trend, plotting the range of best fits in Figure 3.19, using a linear least-squares fit to $log(M(H_2)/M_{\text{stellar}})$ and the post-burst age, taking errors in both quantities into account. The best fit exponentially declining timescale is 90$\pm$10 Myr, with a best fit molecular gas fraction $0.5 - 1$ at zero post-burst age

(when 90% of the stars in the recent starburst had formed).

Mechanisms related to star formation or AGN activity could act to deplete the molecular gas. Star formation not only consumes gas, but could also expel or heat the gas through stellar feedback (from stellar winds and supernovae). Black holes could also consume some of the gas, and expel or heat the rest via AGN feedback. In some cases, strong outflows have been observed, but without sufficient energy to become unbound from the galaxy (Alatalo et al., 2015). Feedback processes could also result in a change of state in the gas, to atomic or hot ionized gas, removing the observed molecular gas signatures.

We test these possibilities by comparing the timescales for gas depletion. Depletion this rapid cannot be due to star formation, given the upper limits on the current SFRs in these post-starbursts. Depleting a gas reservoir of gas fraction $0.1 - 1$, typical of starburst galaxies and consistent with the start of the observed post-starburst trend, in 100 Myr would require sSFR$\sim 10^{-9} - 10^{-8}$yr^{-1}. These sSFRs are as high as they were during the starburst (see Figure 3.14). The sSFRs of the post-starburst galaxies are much lower, sSFR$\leq 5 \times 10^{-13} - 2 \times 10^{-10}$, even considering estimates from $D_n(4000)$, which are sensitive to star formation over several hundred Myr. The current sSFRs of the Alatalo et al. (2016b) sample are also too low to account for the rapid gas depletion, with sSFR$= 1 \times 10^{-12} - 4 \times 10^{-10}$.

We consider two pathological cases that would affect our gas depletion time estimates by affecting our inferred rate of gas consumption by stars: a bottom-heavy IMF or an unusual dust geometry. For an extremely bottom-heavy IMF (see French et al. 2015), the SFRs would only differ by $\sim 20\times$, not the $\sim 400\times$ required to account for the molecular gas depletion. In the case of an unusual dust geometry, we can estimate the SFRs using the 1.4 GHz emission. As discussed in French et al. (2015), 1.4 GHz emission is sensitive to dust-obscured star formation, but may be enhanced by the LINER (LINER-like emission is commonly seen in post-starbursts, Yan et al. 2006; Yang et al. 2006) or by the recent starburst. For the French et al.

(2015) galaxies with FIRST (Becker et al., 1995) detections, the predicted median molecular gas depletion time is still only 1 Gyr, not enough to explain the observed rapid depletion.

The molecular gas depletion cannot be due to stellar feedback either, as the mass loading factors (mass outflow / SFR) from stellar feedback are expected to be 1-5 for the stellar mass range of this sample (Muratov et al., 2015), so the addition of stellar feedback is not sufficient to resolve this deficiency.

Direct accretion of gas by the black hole is unlikely to be a significant cause of the observed decline, as the black hole masses are expected to be of order $10^7 - 10^8$ M$_\odot$ for this sample, given bulge mass estimates from Mendel et al. (2014) and the best-fit black hole - bulge relation from McConnell & Ma (2013), and of order $10^9 - 10^{10}$ M$_\odot$ of molecular gas is lost.

The molecular gas reservoirs could be expelled or destroyed after the starburst has ended through AGN-driven outflows. The delay between the decline in star-formation and the onset of AGN feeding is expected to be ∼10-300 Myr (Davies et al., 2007; Schawinski et al., 2009; Wild et al., 2010; Cales & Brotherton, 2015), consistent with the durations of the starbursts observed here, such that the observed depletion of the gas takes place with similar delay times after the starburst began. Longer delays of several Gyr (Curtis & Sijacki, 2016) may also occur, but none of the post-starburst sample selection methods would have selected such galaxies. We note that there may exist an additional time delay between AGN feeding and the loss of the molecular gas detection. The median rate of gas depletion required, given the $M(H_2)$ measurements and 90 Myr depletion time, is 40 M$_\odot$yr^{-1} with a 68% likelihood range of $5 - 200$M$_\odot$yr^{-1}. This rate is consistent with observed outflow rates driven by AGN, although the depletion timescales observed are much shorter, of only a few Myr (Cicone et al., 2014). If depletion times are this rapid, scatter in the time between the starburst and the onset of gas depletion could result in the observed 90 Myr average depletion time. Thus, the observed decline in molecular gas

fraction during the post-starburst phase may be a smoking gun for AGN feedback in transitioning galaxies.

Post-starburst galaxies have stellar populations, color gradients, morphologies, and kinematics consistent with reaching the red sequence of early type galaxies in (Norton et al., 2001; Yang et al., 2004, 2008; Pracy et al., 2013; Pawlik et al., 2015) in a few Gyr. Early type galaxies are typically gas-poor, with molecular gas fractions of $\lesssim 10^{-3}$ (Young et al., 2011). With the observed molecular gas depletion rate, the post-starburst galaxies should reach early-type levels of molecular gas in $600-800$ Myr, thus becoming gas-poor when their other properties start to resemble early-types.

3.5.3 Dust Evolution

We test for dust evolution with post-burst age, using the WISE [3.4]-[4.6] and [4.6]-[12] colors. We take the SDSS DR12 - WISE all-sky matched catalog, and select the `wxmpro` profile-fit magnitudes for the Rowlands et al. (2015) sample, the whole Alatalo et al. (2016c) SPOGs sample, and for our entire post-starburst sample presented here. We plot each color against the post-burst age in Figure 3.18, broken up into the same burst mass fraction categories as for the previous molecular gas analysis. For the WISE [4.6]-[12] color, there is a significant (Spearman $\rho = -0.55$, 16σ) anti-correlation with the post-burst age that remains significant for the low and high burst mass fraction bins (Spearman $\rho = -0.55, -0.55, 12\sigma, 10\sigma$, respectively). For the WISE [3.4]-[4.6] color, there is a weaker, but still significant (Spearman $\rho = -0.31$, 10σ) anti-correlation with the post-burst age that remains significant for the low and high burst mass fraction bins (Spearman $\rho = -0.30, -0.27, 7\sigma$, 5σ respectively). However, the anti-correlation between post-burst age and WISE [3.4]-[4.6] color may be driven by increased scatter in WISE [3.4]-[4.6] color for the SPOGs sample compared to the older post-starburst sample.

These WISE colors represent a combination of the dust mass and dust heating.

Various heating sources can act to change them: star-formation, young (A) stars, evolved stars (post-AGB or TP-AGB), or AGN. PAH features can also potentially influence these colors. Starbursts, star-forming galaxies, and early type galaxies separate in the color-color space of WISE [4.6]-[12] vs. [3.4]-[4.6] (Wright et al., 2010; Yesuf et al., 2014; Alatalo et al., 2014), with post-starburst galaxies lying near the infrared "green valley" and star-forming regions in WISE [4.6]-[12] color and near star-forming galaxies in WISE [3.4]-[4.6] color (Alatalo et al., 2016d). Given the anti-correlations of bluer WISE colors with post-burst age, either the dust mass or sources of dust heating could be declining over time.

Rowlands et al. (2015) use additional observations from *Herschel* PACS and SPIRE of their sample of starbursts and post-starbursts to show that both the dust-to-stellar mass ratio and cold dust temperature declines with post-burst age. However, it is not clear if the observed trends in WISE [3.4]-[4.6] and [4.6]-[12] are driven by the same effects, as these colors are sensitive to hotter dust. Additionally, many of the shocked post-starbursts have higher WISE [3.4]-[4.6] colors than the Rowlands et al. (2015) sample and may be subject to additional sources of dust heating. The lack of a significant anti-correlation in the molecular gas mass with post-burst age in the Rowlands et al. (2015) sample alone may be due to small numbers, or a narrower post-burst age baseline. Rowlands et al. (2015) do see a trend in the dust-to-gas ratio with age, but only when excluding the galaxy with the longest post-burst age, one of only two from that sample with a sSFR consistent with our post-starburst selection. Further work studying the full MIR-FIR SED of post-starburst galaxies as they evolve through the post-starburst phase will be needed to disentangle the dust mass and various possible heating sources.

Early type galaxies have narrow ranges of WISE [3.4]-[4.6] colors of −0.1 to 0, and [4.6]-[12] colors of 0 to 1. If the WISE [4.6]-[12] colors decline linearly with post-burst age, they should reach colors typical of early types at ∼1 Gyr post-burst. The WISE [3.4]-[4.6] colors have significantly more scatter, and it is not clear when

the scatter decreases after the burst.
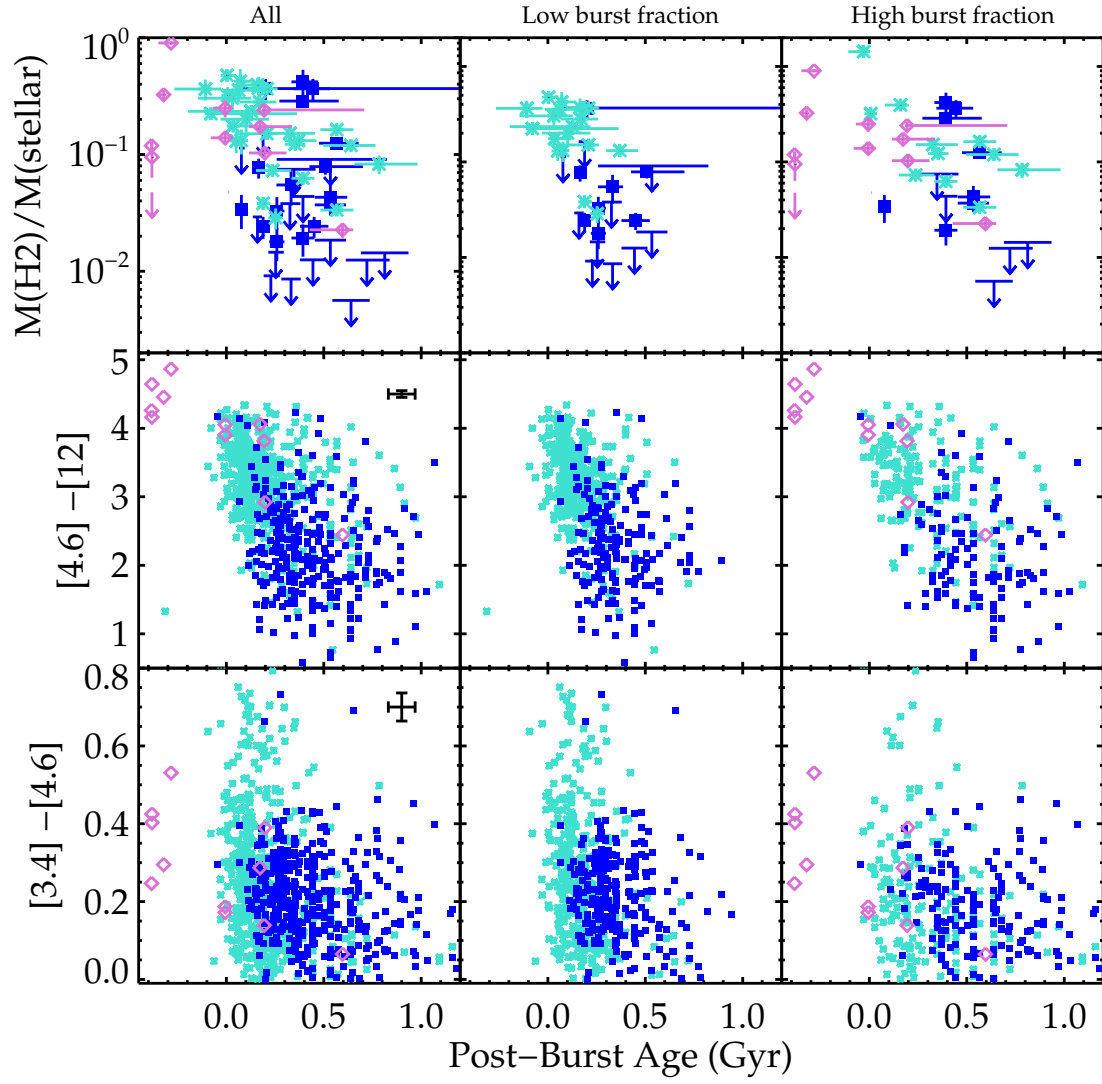
Figure 3.18: (Caption next page.)

Figure 3.18: (Previous page.) Post-burst ages vs. molecular gas fractions and WISE colors for three samples of starburst/post-starburst galaxies. The left panels show the full set of galaxies, broken down into those with burst mass fractions $\leq 20\%$ (middle panel) and $> 20\%$ (right panel). The top panels show molecular gas mass fractions vs. post-burst age for three samples: post-starburst galaxies (blue squares) from French et al. (2015), shocked post-starbursts (teal stars) from Alatalo et al. (2016b), and starburst/post-starbursts (pink diamonds) from Rowlands et al. (2015). We observe a significant trend in the molecular gas fraction with the post-burst age, at 4σ significance. Split up into the two burst fraction bins, the significance drops to 2.7σ in each bin. Early type galaxies are typically gas-poor, with molecular gas fractions of $\lesssim 10^{-3}$ (Young et al., 2011). With the observed molecular gas depletion rate, the post-starburst galaxies should reach early-type levels of molecular gas in $600 - 800$ Myr. The middle panels show the WISE [4.6]-[12] μm colors vs. post-burst age for the post-starburst galaxies studied in this work, shocked post-starbursts from Alatalo et al. (2016c), and starburst/post-starbursts from Rowlands et al. (2015). The bottom panels show the WISE [3.4]-[4.6] μm colors vs. post-burst age for the same samples. We see significant ($> 3\sigma$) anti-correlations for each of the WISE colors with post-burst age, and for all of the burst mass fraction bins. These WISE colors represent a combination of the dust mass and dust heating. Various heating sources can act to change the WISE colors: star-formation, young (A) stars, evolved stars (post-AGB or TP-AGB), or AGN. Given the anti-correlations of bluer WISE colors with post-burst age, either the dust mass could be declining with the gas mass, and/or the sources of dust heating could be declining. Early type galaxies have WISE [3.4]-[4.6] colors of $-0.1-0$, and [4.6]-[12] colors of $0 - 1$. If the WISE [4.6]-[12] colors decline linearly with post-burst age, they should reach colors typical of early types at ~ 1 Gyr post-burst. The WISE [3.4]-[4.6] colors have significantly more scatter, and it is not clear when post-burst the scatter decreases.

3.6 Conclusions

We fit stellar population models to 535 post-starburst galaxies, breaking the age - burst strength - burst duration degeneracy using a combination of UV photometry from *GALEX* (Martin et al., 2004) and optical photometry and spectroscopy from SDSS (Strauss et al., 2002; Ahn et al., 2014). We present a catalog of post burst ages, burst mass fractions, and burst durations. We conclude the following:
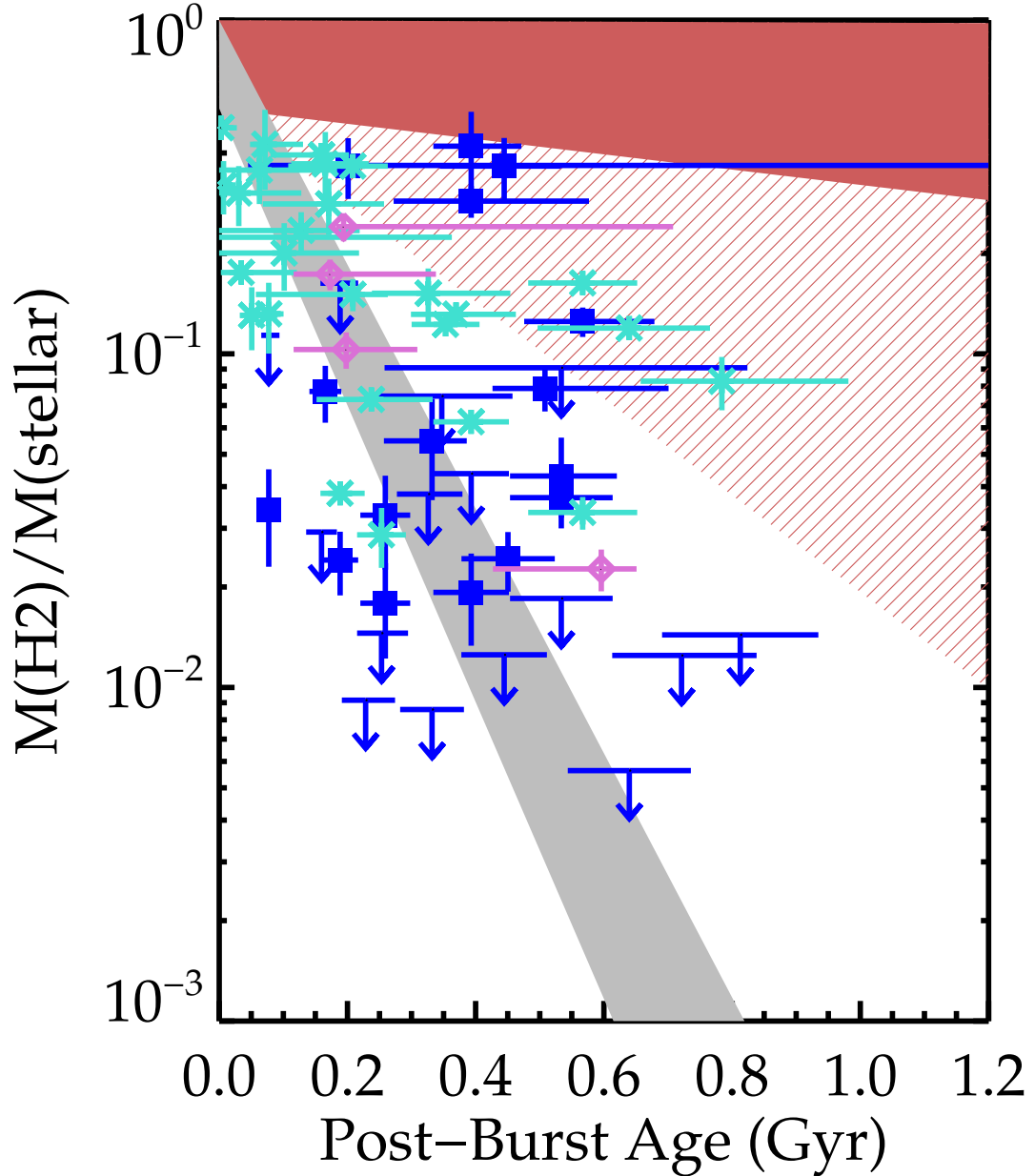
Figure 3.19: Post-burst ages vs. molecular gas fractions for the same samples as in Figure 3.18. The best-fit line for an exponential depletion of the molecular gas reservoirs (grey region) has a timescale of 90 ± 10 Myr. The post-burst age is the time since 90% of the stars from the recent starburst were formed. The gas depletion cannot be due to on-going star formation or stellar feedback, which would have a much longer allowed depletion time (solid red region), even allowing for an unusual IMF or dust geometry (hashed red region). Early type galaxies are typically gas-poor, with molecular gas fractions of $\lesssim 10^{-3}$ (Young et al., 2011). With the observed molecular gas depletion rate, the post-starburst galaxies should reach early-type

1. We derive post-burst ages and burst mass fractions, with median errors of 22% and 42%, respectively. 68% of the burst mass fractions are within 7.0%–69%, and 68% of the post-burst ages are within 240–680 Myr. We define the "post-burst" ages to be the time elapsed since 90% of the stars from the recent starburst(s) formed.

2. This method is more accurate than using the $D_n(4000)$ - Hδ parameter space to derive post-burst ages and burst mass fractions. The relation between $D_n(4000)$ and the post-burst age suffers from a degeneracy with the burst mass fraction and burst duration. For post-starbursts with $D_n(4000) < 1.3$, where post-starburst ages are typically younger than 300 Myr, the degeneracy is lessened, and $D_n(4000)$ is highly correlated with the post-burst age. However, if $D_n(4000) > 1.42$, where post-starburst ages typically range from 300-1500 Myr, $D_n(4000)$ is no longer significantly ($> 3\sigma$) correlated with the post-burst age.

3. The star formation rates experienced during the starburst were $\sim$10-100$\times$ above the stellar mass - specific star formation rate relation, consistent with those in starbursting galaxies (Schiminovich et al., 2007).

4. Starbursts with specific star formation rates $> 10^{-8}$ yr^{-1} are rare ($< 1\%$ of the sample). As a consequence, those post-starburst galaxies with short duration (25 Myr) bursts generate 1-10% of their stellar mass in the burst, whereas galaxies with longer duration (>150 Myr) bursts produce 10-50% of their stellar mass in the burst.

5. Many post-starbursts show signs of intermediate mass ($\sim$F) stellar populations; 50% of the post-starbursts are best fit by a single recent burst, 48% prefer a double recent burst, and 2% do not have a statistical preference. Lower stellar mass galaxies are more likely to experience two recent bursts,

and the fraction of mass produced in their recent burst(s) is more strongly anti-correlated with their stellar mass.

6. We compare the SFHs selected via our selection criteria with those from other, differently-selected post-starburst samples. Rowlands et al. (2015) use the approach of Wild et al. (2007, 2009) to select longer duration (>150 Myr) starbursts, at a wider range of post-burst ages than we do; they also are biased against shorter duration starbursts that have specific star formation rates similar to our sample. Shocked POst-Starburst Galaxies (SPOGs; Alatalo et al., 2016c) have generally younger post-burst ages than ours, with 60% too young to have entered into our post-starburst selection. SPOGs with younger post-burst ages, but similar mass fractions and durations as our post-starbursts, may represent progenitors to our sample. However, an additional population (10%) of SPOGs exists at long duration (> 100 Myr) and small burst fraction ($< 10\%$), which will not evolve into our post-starburst population.

7. Combining these three samples of post-starburst galaxies, we observe a significant decline in their molecular gas to stellar mass fraction with increasing post-burst age, at 4σ significance. This trend persists when we control for the fraction of stellar mass produced in the recent burst(s). The best fit exponentially declining timescale is 90 ± 10 Myr, with the best fit initial molecular gas fractions $0.5 - 1$ at a post-burst age of zero. With the observed molecular gas depletion rate, the post-starburst galaxies should reach early-type levels of molecular gas in $600 - 800$ Myr. The rapid depletion rate implied by this trend of $5 - 200$ M$_\odot$yr^{-1} cannot be due to current star formation, given the upper limits on the current SFRs in these post-starbursts, suggesting that the molecular gas is expelled or destroyed in AGN-driven outflows.

8. We find significant ($> 3\sigma$) anti-correlations of the WISE [4.6]-[12] and [3.4]-[4.6] μm colors with the post-burst age of the galaxy. Given the anti-

correlations of bluer WISE colors with post-burst age, either the dust mass or sources of dust heating could be declining over time, as with the gas fraction. Various heating sources are possible during this phase: star-formation, young (A) stars, evolved stars (post-AGB or TP-AGB), or AGN.

Post-starburst galaxies are a critical laboratory for studying the evolution of starbursts, of galaxies onto the red sequence, and of galaxies onto the black hole - bulge relation (Ferrarese & Merritt, 2000). They are also the preferred hosts of tidal disruption events (Arcavi et al., 2014; French et al., 2016), and thus provide clues to what sets the rate of tidal disruption events (French et al., 2017). The UV-optical stellar population fitting method presented here will be a useful tool in timing the detailed evolution of individual galaxies from star-forming, through the post-starburst phase, and eventually to quiescence.

Table 3.1. Post-burst Ages

RA (J2000)[a]	Dec (J2000)	z	log M$_\star$/M$_\odot$	SFH[b]	Post-burst (16%)	Age (50%)	(Myr) (84%)	Age since (16%)	Burst Start (50%)	(Myr) (84%)	τ or (16%)	Δt^c (50%)	(Myr) (84%)
3.963556	-10.388311	0.1981	10.9	2	201	281	348	701	781	848	500	500	500
4.349453	-10.758440	0.1868	10.9	1	193	331	778	308	446	893	25	50	100
5.275367	-1.226071	0.1071	10.0	1	1490	1755	2083	1513	1778	2106	25	25	200
10.414436	1.068420	0.0430	10.5	2	574	668	761	1574	1668	1761	1000	1000	1000
11.246839	-8.889684	0.0196	10.2	2	723	841	959	1723	1841	1959	1000	1000	1000
13.103527	0.734070	0.0699	10.5	2	275	334	413	1275	1334	1413	1000	1000	1000
17.773197	14.266233	0.0994	10.4	2	179	211	287	1179	1211	1287	1000	1000	1000
19.925944	1.131008	0.0899	10.4	1	219	259	298	242	281	321	25	25	25
20.065347	-9.988923	0.1368	10.6	2	164	199	246	1164	1199	1246	1000	1000	1000
22.128778	0.965819	0.2541	11.4	1	375	443	512	433	501	570	25	50	50
26.017490	-9.032193	0.0180	8.5	1	206	243	290	228	266	313	25	25	25
26.196380	0.537470	0.1788	10.8	2	237	316	390	1237	1316	1390	1000	1000	1000
27.779240	-0.943535	0.1980	10.9	2	379	446	529	879	946	1029	500	500	500
31.007928	14.241354	0.0812	10.2	2	191	298	428	1191	1298	1428	1000	1000	1000
36.930046	-0.256401	0.2193	11.0	1	159	188	279	182	211	302	25	25	25
37.078604	-1.034778	0.0912	10.2	1	806	1239	1437	1152	1584	1782	200	200	200
37.972740	0.381079	0.1969	10.4	1	89	110	167	112	133	190	25	25	25
43.013658	-8.310950	0.1975	10.9	2	282	375	486	1282	1375	1486	1000	1000	1000
43.332198	-0.093190	0.1512	10.6	2	134	199	271	1134	1199	1271	1000	1000	1000
43.997130	-1.139745	0.1936	10.9	2	201	281	364	701	781	864	500	500	500
45.618457	-0.938369	0.1683	11.1	1	563	654	763	908	1000	1109	200	200	200
45.830014	-8.605536	0.0756	10.2	1	498	608	792	521	630	815	25	25	50
46.116831	-8.818506	0.1196	10.3	2	332	421	545	1332	1421	1545	1000	1000	1000
47.329110	-0.951473	0.2505	11.0	1	153	188	279	176	211	302	25	25	25

Table 3.1 (cont'd)

RA (J2000)[a]	Dec (J2000)	z	log M_*/M_⊙	SFH[b]	Post-burst (16%)	Age (50%)	(Myr) (84%)	Age since (16%)	Burst Start (50%)	(Myr) (84%)	τ or (16%)	Δt[c] (50%)	(Myr) (84%)
48.808796	-0.692948	0.1171	10.2	2	476	668	865	576	768	965	100	100	1000
49.688140	41.488764	0.0107	9.9	1	436	508	579	459	530	602	25	25	25
52.010897	0.750662	0.2019	11.0	2	302	473	545	802	973	1045	500	500	1000
59.218520	-6.175333	0.0370	9.6	2	512	595	679	1512	1595	1679	1000	1000	1000
113.059470	39.068281	0.1470	10.7	2	303	562	727	1303	1562	1727	1000	1000	1000
113.905520	39.562694	0.1083	10.5	1	303	353	402	326	375	425	25	25	25
114.350330	38.410780	0.1272	10.5	1	259	332	383	281	354	405	25	25	25
116.422740	22.139439	0.1229	10.7	1	136	224	260	193	281	317	25	25	50
117.737160	48.046090	0.0800	10.5	1	639	829	1041	754	944	1156	25	100	150
118.192530	38.491238	0.1267	10.7	2	242	281	321	342	381	421	100	100	100
118.346240	24.550155	0.0609	10.5	2	228	266	328	728	766	828	500	500	500
118.595940	37.875201	0.1652	10.8	1	201	259	323	224	281	346	25	25	25
118.667430	12.752982	0.2124	11.1	1	174	214	268	197	237	290	25	25	25
118.870700	21.510622	0.2731	11.2	1	351	770	893	581	1000	1123	100	150	150
119.245410	36.381982	0.1770	10.9	1	211	259	298	234	281	321	25	25	25
119.295590	14.460028	0.1915	10.9	1	189	243	320	211	266	342	25	25	25
120.067070	29.471422	0.0453	10.0	2	483	562	641	1483	1562	1641	1000	1000	1000
120.154410	26.232386	0.1764	10.7	1	125	155	179	148	177	201	25	25	25
120.265670	34.695715	0.1602	11.0	2	238	334	433	1238	1334	1433	500	1000	1000
120.366540	32.171468	0.1895	10.9	2	352	446	551	852	946	1051	500	500	500
120.576640	32.535504	0.0382	10.3	2	483	562	641	1483	1562	1641	1000	1000	1000
120.612090	20.086088	0.0911	10.5	2	358	530	762	858	1030	1262	500	500	1000
120.694210	8.853034	0.1129	10.9	2	323	375	445	823	875	945	500	500	500
121.768000	39.041129	0.2096	10.8	1	248	293	365	271	316	388	25	25	25

Table 3.1 (cont'd)

RA (J2000)[a]	Dec (J2000)	z	log $M_\star/M_\odot$	SFH[b]	Post-burst (16%)	Age (50%)	(Myr) (84%)	Age since (16%)	Burst Start (50%)	(Myr) (84%)	τ or (16%)	Δt[c] (50%)	(Myr) (84%)
123.564300	8.233306	0.2447	11.3	2	238	334	397	1238	1334	1397	1000	1000	1000
123.957070	18.827462	0.1758	10.8	1	824	958	1092	1054	1188	1322	150	150	150

[a]Notes: Table truncated after 50 rows, columns continue on next page. Columns 1-4 are from SDSS DR8 (Aihara et al., 2011) and MPA-JHU catalogs (Brinchmann et al., 2004; Tremonti et al., 2004).

[b]Number of recent bursts.

[c]If SFH = 1, burst duration (τ). If SFH = 2, separation between bursts (Δt).

Table 3.2.   Post-burst Ages (cont.)

Burst Light Fraction y_f [d]		Burst Mass Fraction m_{burst}			A_V (mag)
(burst 1)	(burst 2)[e]	(16%)	(50%)	(84%)	
0.24	0.58	0.09	0.16	1.00	0.6
0.41		0.04	0.05	0.06	0.5
1.00		0.75	1.00	1.00	0.3
0.27	0.66	0.25	0.52	0.88	0.2
0.31	0.63	0.42	0.66	1.00	0.6
0.25	0.72	0.08	0.58	1.00	1.1
0.20	0.80	0.28	1.00	1.00	0.7
0.46		0.05	0.06	0.07	0.3
0.18	0.77	0.11	0.32	1.00	0.5
0.51		0.06	0.09	0.11	0.4
1.00		0.77	1.00	1.00	0.9
0.19	0.59	0.07	0.12	0.17	0.3
0.28	0.56	0.16	0.26	0.55	0.5
0.18	0.55	0.05	0.10	0.16	0.7
0.60		0.06	0.08	0.10	0.7
1.00		0.66	1.00	1.00	0.5
1.00		0.66	1.00	1.00	1.1
0.25	0.72	0.08	0.66	1.00	0.8
0.16	0.67	0.04	0.10	0.26	0.8
0.21	0.51	0.07	0.10	1.00	0.7
1.00		0.73	1.00	1.00	1.3
0.36		0.06	0.07	0.10	0.3
0.29	0.71	0.11	1.00	1.00	0.5
0.62		0.07	0.09	0.11	1.0

Table 3.2 (cont'd)

Burst Light Fraction y_f [d]		Burst Mass Fraction m_{burst}			A_V
(burst 1)	(burst 2)[e]	(16%)	(50%)	(84%)	(mag)
0.23	0.28	0.07	0.12	0.30	0.3
0.36		0.05	0.07	0.09	0.7
0.25	0.50	0.11	0.16	1.00	0.7
0.32	0.68	0.67	1.00	1.00	0.5
0.20	0.51	0.05	0.14	0.76	0.4
0.46		0.06	0.07	0.09	0.4
0.39		0.04	0.05	0.07	0.4
0.62		0.06	0.09	0.11	1.0
0.69		0.16	0.23	0.30	0.5
0.22	0.27	0.05	0.06	0.07	0.4
0.18	0.42	0.05	0.06	0.07	0.8
0.52		0.05	0.07	0.09	0.7
0.51		0.05	0.06	0.08	0.6
0.94		0.45	0.67	1.00	0.9
0.48		0.05	0.06	0.08	0.6
0.36		0.03	0.04	0.05	0.4
0.24	0.52	0.17	0.22	0.28	0.4
0.50		0.04	0.05	0.06	0.5
0.15	0.46	0.04	0.06	0.16	0.8
0.29	0.58	0.14	0.30	1.00	0.6
0.27	0.65	0.22	0.46	0.65	0.5
0.20	0.39	0.05	0.10	0.28	0.2
0.20	0.41	0.06	0.08	0.10	0.3
0.50		0.05	0.07	0.09	0.7

Table 3.2 (cont'd)

Burst Light Fraction y_f [d]		Burst Mass Fraction m_{burst}			A_V
(burst 1)	(burst 2)[e]	(16%)	(50%)	(84%)	(mag)
0.25	0.75	0.05	1.00	1.00	0.7
0.93	0.49	0.49	0.67	1.00	0.5

[d] If SFH = 2 recent bursts, light fraction for each burst is shown (burst mass fractions are the same for each burst, so the light fractions will be different).

[e] If SFH = 2 recent bursts, burst mass fraction shown is combined from both recent bursts.

Table 3.3. Shocked Post-burst Ages

RA (J2000)[a]	Dec (J2000)	z	log M⋆/M⊙	SFH[b]	Post-burst (16%)	Age (50%)	(Myr) (84%)	Age since (16%)	Burst Start (50%)	(Myr) (84%)	τ or (16%)	Δt[c] (50%)	(Myr) (84%)
149.605340	-0.337055	0.0328	9.3	1	505	650	903	563	707	961	25	25	150
149.456450	-0.210932	0.0329	10.1	2	362	421	480	1362	1421	1480	1000	1000	1000
153.310060	-0.778171	0.0332	10.3	2	1641	1995	2274	2641	2995	3274	100	1000	1000
152.130420	0.356656	0.0330	9.2	2	66	89	101	166	189	201	100	100	100
161.738750	0.892871	0.1510	11.1	1	364	423	483	387	446	506	25	25	50
163.536210	-0.019730	0.1081	10.2	2	82	100	129	182	200	229	100	100	100
163.035860	-0.965405	0.1286	10.4	2	178	237	273	678	737	773	500	500	500
172.544810	0.542120	0.1277	10.6	2	158	211	287	1158	1211	1287	1000	1000	1000
179.087930	-0.705908	0.0691	10.0	1	98	145	424	121	167	447	25	25	100
179.087930	-0.705908	0.0691	10.0	1	125	155	194	148	177	217	25	25	50
182.904340	0.322504	0.0203	8.4	1	105	153	227	162	211	285	25	25	50
191.534130	-0.952258	0.0609	9.6	2	30	56	112	130	156	212	100	100	100
191.534130	-0.952258	0.0609	9.6	2	30	89	127	130	189	227	100	100	100
193.360370	0.377502	0.1813	11.0	2	42	89	159	1042	1089	1159	1000	1000	1000
193.251320	-0.128501	0.1989	11.0	2	48	79	188	548	579	688	500	500	500
198.946000	-0.060723	0.1971	11.1	2	85	149	253	385	449	553	200	300	300
205.550870	-0.293791	0.0861	10.5	2	406	473	539	906	973	1039	500	500	500
206.212440	1.216762	0.0771	9.8	1	136	176	234	159	199	256	25	25	50
212.559500	-0.578541	0.0258	9.3	2	113	167	199	1113	1167	1199	1000	1000	1000
214.000790	-1.104202	0.1397	10.8	1	233	275	318	256	298	341	25	25	50
214.198980	-1.070568	0.1250	11.2	1	233	271	481	463	501	711	150	150	150
213.299110	-0.399365	0.1261	10.7	1	-159	7	168	70	237	398	25	150	200
213.299110	-0.399365	0.1261	10.7	1	-95	217	262	249	562	607	150	200	200
224.329550	0.796431	0.0832	10.3	1	767	892	1033	997	1122	1263	25	25	150

Table 3.3 (cont'd)

RA (J2000)[a]	Dec (J2000)	z	log $M_\star/M_\odot$	SFH[b]	Post-burst (16%)	Age (50%)	(Myr) (84%)	Age since (16%)	Burst Start (50%)	(Myr) (84%)	τ or (16%)	Δt[c] (50%)	(Myr) (84%)
224.329550	0.796431	0.0831	10.3	2	526	668	825	1526	1668	1825	1000	1000	1000
230.675810	0.691707	0.0762	10.2	2	114	251	503	314	451	703	100	200	1000
233.260210	1.201785	0.0373	9.0	1	80	166	299	138	223	356	25	25	100
233.404200	1.144680	0.1231	10.9	2	68	125	213	568	625	713	500	500	1000
172.038980	-3.294851	0.1062	10.7	1	-196	-108	449	148	237	794	25	25	200
171.211040	-3.150728	0.0463	9.4	2	95	158	205	195	258	305	100	100	100
183.526050	-3.529469	0.0576	9.8	2	151	223	289	451	523	589	300	300	500
183.403730	-2.172503	0.0192	8.7	2	95	251	360	195	351	460	100	100	1000
188.998000	-2.693171	0.0917	10.1	1	40	92	416	98	149	473	25	25	100
196.464320	-1.317817	0.0960	10.6	1	40	83	297	98	141	355	25	25	100
263.012380	59.981915	0.0291	9.0	2	170	281	348	470	581	648	200	300	500
259.654380	61.154452	0.0534	10.0	2	389	473	644	1389	1473	1644	1000	1000	1000
233.404200	1.144680	0.1232	10.9	1	-110	285	325	235	630	670	25	200	200
233.260210	1.201785	0.0373	9.0	2	54	133	191	154	233	291	100	100	100
336.808380	-0.733339	0.0558	9.7	2	469	595	735	969	1095	1235	100	500	500
341.272340	0.754699	0.1950	11.0	2	59	79	102	159	179	202	100	100	100
345.121700	0.600378	0.0818	9.7	2	30	79	114	130	179	214	100	100	100
351.655090	-1.243082	0.1975	10.9	2	75	100	160	175	200	260	100	100	200
354.659150	-0.572634	0.0728	10.3	2	180	281	504	1180	1281	1504	1000	1000	1000
354.659150	-0.572634	0.0728	10.3	1	117	219	680	232	334	795	25	25	200
0.825899	0.812318	0.1390	10.8	2	96	199	286	296	399	486	100	200	300
2.938423	-0.908529	0.0476	10.2	1	664	783	976	721	841	1034	25	25	150
1.132990	-1.236591	0.0887	10.6	1	95	449	564	441	794	909	25	150	200
7.512109	-0.885154	0.0598	10.1	2	1051	1333	1815	1551	1833	2315	100	500	1000

Table 3.3 (cont'd)

RA (J2000)[a]	Dec (J2000)	z	$\log M_\star/M_\odot$	SFH[b]	Post-burst (16%)	Age (50%)	(Myr) (84%)	Age since (16%)	Burst Start (50%)	(Myr) (84%)	τ or (16%)	Δt[c] (50%)	(Myr) (84%)
8.541455	-0.288485	0.0580	9.2	1	-256	76	103	88	421	448	25	200	200
9.282580	0.410167	0.0806	10.2	2	301	354	404	1301	1354	1404	1000	1000	1000

[a]Notes: Table truncated after 50 rows, columns continue on next page. Columns 1-4 are from SDSS DR8 (Aihara et al., 2011) and MPA-JHU catalogs (Brinchmann et al., 2004; Tremonti et al., 2004).

[b]Number of recent bursts.

[c]If SFH = 1, burst duration (τ). If SFH = 2, separation between bursts (Δt).

Table 3.4. Shocked Post-burst Ages (cont.)

Burst Light Fraction y_f [d]		Burst Mass Fraction m_{burst}			A_V
(burst 1)	(burst 2)[e]	(16%)	(50%)	(84%)	(mag)
0.50		0.10	0.15	0.20	0.6
0.30	0.70	0.77	1.00	1.00	1.0
0.09	0.13	0.04	0.08	0.11	0.2
0.14	0.25	0.02	0.02	0.02	0.0
0.63		0.09	0.14	0.19	1.0
0.27	0.51	0.06	0.08	0.11	1.2
0.28	0.69	0.23	0.40	1.00	1.2
0.20	0.79	0.02	1.00	1.00	1.0
0.50		0.04	0.05	0.09	1.0
0.63		0.07	0.09	0.11	1.0
1.00		0.77	1.00	1.00	1.0
0.26	0.60	0.04	0.10	0.20	1.0
0.24	0.44	0.02	0.06	0.09	0.8
0.10	0.81	0.02	0.10	1.00	1.2
0.13	0.63	0.02	0.03	1.00	1.6
0.19	0.42	0.02	0.04	0.06	1.6
0.32	0.64	0.49	0.63	0.85	0.4
0.63		0.06	0.10	0.14	0.2
0.14	0.57	0.04	0.06	0.10	0.0
0.40		0.03	0.05	0.06	0.6
0.50		0.04	0.06	0.09	1.0
0.40		0.02	0.02	0.03	1.2
0.25		0.02	0.02	0.03	0.4
1.00		0.77	1.00	1.00	0.8

Table 3.4 (cont'd)

Burst Light Fraction y_f [d]			Burst Mass Fraction m_{burst}			A_V
(burst 1)	(burst 2)[e]	(16%)	(50%)	(84%)		(mag)
0.30	0.70	0.69	1.00	1.00	0.6
0.12	0.17	0.02	0.03	0.05	0.4
0.63		0.08	0.13	0.18	0.4
0.12	0.42	0.02	0.02	0.16	1.0
0.50		0.05	0.06	0.08	1.4
0.15	0.21	0.02	0.03	0.04	0.6
0.20	0.37	0.06	0.08	0.13	0.2
0.22	0.29	0.04	0.08	0.16	0.0
0.40		0.02	0.03	0.04	0.6
0.79		0.10	0.14	0.18	1.6
0.24	0.40	0.07	0.13	0.17	0.4
0.30	0.70	0.57	1.00	1.00	0.4
0.50		0.05	0.07	0.08	0.8
0.21	0.32	0.03	0.05	0.08	0.4
0.37	0.63	0.23	0.40	1.00	0.8
0.23	0.49	0.03	0.04	0.05	1.6
0.31	0.60	0.11	0.20	1.00	1.2
0.17	0.31	0.02	0.02	0.03	1.4
0.19	0.60	0.04	0.13	1.00	0.6
0.32		0.02	0.04	0.06	0.8
0.25	0.42	0.06	0.08	0.13	1.0
0.79		0.32	0.42	1.00	1.0
0.79		0.13	0.28	0.44	1.6
0.39	0.61	0.77	1.00	1.00	0.2

Table 3.4 (cont'd)

Burst Light Fraction y_f [d]		Burst Mass Fraction m_{burst}		A_V
(burst 1)	(burst 2)[e] (16%)	(50%)	(84%)	(mag)
0.50	0.04	0.07	0.15	0.0
0.27	0.72	0.45	0.80	1.00	0.8

[d]If SFH = 2 recent bursts, light fraction for each burst is shown (burst mass fractions are the same for each burst, so the light fractions will be different).

[e]If SFH = 2 recent bursts, burst mass fraction shown is combined from both recent bursts.

Table 3.5: Fit residuals

Data	Mean	rms
FUV	0.20	1.67
NUV	-1.58	2.21
u	-0.04	1.44
g	0.65	1.43
r	0.35	1.45
i	0.87	1.53
z	-1.62	1.98
D4000n	-2.76	2.91
CN2	-1.58	1.33
Ca4227	0.48	1.04
G4300	-0.58	1.09
Fe4383	1.22	1.43
Ca4455	-1.02	1.04
Fe4531	-0.62	1.21
Ca4668	0.29	1.67
Hb	-1.20	1.93
Fe5015	-0.90	1.92
Mg1	0.14	1.38
Mg2	0.54	1.48
Mgb	1.06	1.11
Fe5270	-0.12	1.22
Fe5335	-1.06	1.45
Fe5406	-0.44	1.16
Fe5709	-0.40	0.93
Fe5782	-0.25	0.93
TiO1	-0.25	1.01
TiO2	1.87	1.49
Hd A	-0.19	1.47
Hg A	-1.59	1.45

Table 3.6. Parameter residual covariance matrix

	FUV	NUV	u	g	r	i	z	D4000n	CN2	Ca4227	G4300	Fe4383	Ca4455	Fe4531	Ca4668	Hb	Fe5015	Mg1	Mg2
FUV	1.00	0.28	-0.02	-0.18	-0.23	-0.04	0.14	0.12	-0.08	-0.08	-0.17	-0.13	-0.08	-0.10	-0.05	0.15	-0.05	0.03	0.07
NUV	0.28	1.00	-0.45	-0.44	-0.37	-0.07	0.25	0.50	0.17	-0.18	-0.08	-0.31	-0.04	-0.12	-0.17	0.23	-0.01	-0.15	-0.24
u	-0.02	-0.45	1.00	0.37	0.09	-0.10	-0.18	-0.35	-0.07	0.00	-0.02	0.14	0.02	0.08	0.08	-0.13	0.04	0.12	0.10
g	-0.18	-0.44	0.37	1.00	0.49	0.07	-0.61	-0.25	-0.08	0.05	0.08	0.14	0.03	0.16	0.11	-0.24	0.03	0.11	0.10
r	-0.23	-0.37	0.09	0.49	1.00	0.63	-0.80	-0.10	0.02	0.20	0.22	0.26	0.09	0.15	0.14	-0.20	0.01	0.09	0.11
i	-0.04	-0.07	-0.10	0.07	0.63	1.00	-0.67	0.17	0.10	0.14	0.21	0.13	0.06	-0.00	0.03	-0.14	-0.02	0.08	0.07
z	0.14	0.25	-0.18	-0.61	-0.80	-0.67	1.00	-0.01	-0.06	-0.07	-0.20	-0.16	-0.01	-0.12	-0.08	0.26	-0.01	-0.11	-0.05
D4000n	0.12	0.50	-0.35	-0.25	-0.10	0.17	-0.01	1.00	0.13	-0.20	-0.05	-0.34	-0.05	-0.18	-0.15	0.05	-0.05	-0.23	-0.33
CN2	-0.08	0.17	-0.07	-0.08	0.02	0.10	-0.06	0.13	1.00	-0.11	0.18	-0.12	0.17	0.11	-0.12	0.20	0.14	-0.07	-0.22
Ca4227	-0.08	-0.18	0.00	0.05	0.20	0.14	-0.07	-0.20	-0.11	1.00	-0.02	0.23	0.07	0.03	0.16	0.04	0.02	0.06	0.21
G4300	-0.17	-0.08	-0.02	0.08	0.22	0.21	-0.20	-0.05	0.18	-0.02	1.00	-0.13	0.17	0.17	-0.08	-0.05	0.10	0.05	-0.04
Fe4383	-0.13	-0.31	0.14	0.14	0.26	0.13	-0.16	-0.34	-0.12	0.23	-0.13	1.00	0.20	0.13	0.17	0.07	0.03	-0.03	0.11
Ca4455	-0.08	-0.04	0.02	0.03	0.09	0.06	-0.01	-0.05	0.17	0.07	0.17	0.20	1.00	0.23	0.01	0.06	0.13	-0.04	-0.07
Fe4531	-0.10	-0.12	0.08	0.16	0.15	-0.00	-0.12	-0.18	0.11	0.03	0.17	0.13	0.23	1.00	0.07	0.11	0.16	0.02	-0.03
Ca4668	-0.05	-0.17	0.08	0.11	0.14	0.03	-0.08	-0.15	-0.12	0.16	-0.08	0.17	0.01	0.07	1.00	0.06	0.13	0.11	0.24
Hb	0.15	0.23	-0.13	-0.24	-0.20	-0.14	0.26	0.05	0.20	0.04	-0.05	0.07	0.06	0.11	0.06	1.00	0.31	-0.04	0.04
Fe5015	-0.05	-0.01	0.04	0.03	0.01	-0.02	-0.01	-0.05	0.14	0.02	0.10	0.03	0.13	0.16	0.13	0.31	1.00	0.05	0.04
Mg1	0.03	-0.15	0.12	0.11	0.09	0.08	-0.11	-0.23	-0.07	0.06	0.05	-0.03	-0.04	0.02	0.11	-0.04	0.05	1.00	0.51
Mg2	0.07	-0.24	0.10	0.10	0.11	0.07	-0.05	-0.33	-0.22	0.21	-0.04	0.11	-0.07	-0.03	0.24	0.04	0.04	0.51	1.00
Mgb	0.01	-0.23	0.03	0.07	0.09	0.07	-0.01	-0.25	-0.29	0.23	-0.11	0.17	-0.07	-0.03	0.17	-0.04	-0.01	0.12	0.53
Fe5270	-0.03	-0.15	-0.00	0.05	0.15	0.07	-0.03	-0.20	-0.01	0.26	0.02	0.15	0.22	0.21	0.12	0.04	0.10	0.09	0.16
Fe5335	-0.00	0.01	-0.07	-0.02	0.07	0.02	0.03	-0.04	0.05	0.12	0.07	0.08	0.29	0.28	0.04	0.09	0.11	-0.08	0.02
Fe5406	0.00	-0.02	-0.06	-0.01	0.03	0.05	0.03	-0.13	0.04	0.14	0.00	0.04	0.12	0.04	0.02	0.09	0.09	0.07	0.17
Fe5709	0.00	-0.01	0.01	-0.02	0.04	0.04	0.00	-0.02	0.07	0.10	0.11	-0.01	0.17	0.09	-0.04	-0.04	-0.06	-0.04	-0.07

Table 3.6 (cont'd)

Fe5782	0.02	-0.02	0.06	-0.02	0.05	0.06	-0.03	-0.04	-0.01	0.03	-0.06	0.04	0.06	0.06	0.01	0.01	0.04	0.04	0.08
TiO1	-0.01	-0.08	0.12	0.07	0.02	-0.01	0.01	-0.09	-0.05	0.07	-0.02	0.08	0.10	0.02	0.06	-0.07	-0.02	0.02	0.08
TiO2	-0.08	-0.27	0.22	0.07	0.10	0.03	-0.02	-0.35	-0.27	0.25	-0.11	0.23	-0.09	-0.01	0.12	-0.01	-0.09	0.07	0.32
Hd A	0.33	0.35	-0.12	-0.17	-0.30	-0.12	0.25	0.25	-0.31	-0.00	-0.20	-0.12	-0.06	-0.06	0.06	0.10	-0.11	0.07	0.20
Hg A	0.28	0.41	-0.15	-0.24	-0.41	-0.32	0.38	0.30	0.07	-0.06	-0.44	-0.24	-0.02	-0.04	-0.00	0.40	0.03	-0.04	-0.00

Table 3.7. Parameter residual covariance matrix (continued)

	Mgb	Fe5270	Fe5335	Fe5406	Fe5709	Fe5782	TiO1	TiO2	Hd A	Hg A
FUV	0.01	-0.03	-0.00	0.00	0.00	0.02	-0.01	-0.08	0.33	0.28
NUV	-0.23	-0.15	0.01	-0.02	-0.01	-0.02	-0.08	-0.27	0.35	0.41
u	0.03	-0.00	-0.07	-0.06	0.01	0.06	0.12	0.22	-0.12	-0.15
g	0.07	0.05	-0.02	-0.01	-0.02	-0.02	0.07	0.07	-0.17	-0.24
r	0.09	0.15	0.07	0.03	0.04	0.05	0.02	0.10	-0.30	-0.41
i	0.07	0.07	0.02	0.05	0.04	0.06	-0.01	0.03	-0.12	-0.32
z	-0.01	-0.03	0.03	0.03	0.00	-0.03	0.01	-0.02	0.25	0.38
D4000n	-0.25	-0.20	-0.04	-0.13	-0.02	-0.04	-0.09	-0.35	0.25	0.30
CN2	-0.29	-0.01	0.05	0.04	0.07	-0.01	-0.05	-0.27	-0.31	0.07
Ca4227	0.23	0.26	0.12	0.14	0.10	0.03	0.07	0.25	-0.00	-0.06
G4300	-0.11	0.02	0.07	0.00	0.11	-0.06	-0.02	-0.11	-0.20	-0.44
Fe4383	0.17	0.15	0.08	0.04	-0.01	0.04	0.08	0.23	-0.12	-0.24
Ca4455	-0.07	0.22	0.29	0.12	0.17	0.06	0.10	-0.09	-0.06	-0.02
Fe4531	-0.03	0.21	0.28	0.04	0.09	0.06	0.02	-0.01	-0.06	-0.04
Ca4668	0.17	0.12	0.04	0.02	-0.04	0.01	0.06	0.12	0.06	-0.00
Hb	-0.04	0.04	0.09	0.09	-0.04	0.01	-0.07	-0.01	0.10	0.40
Fe5015	-0.01	0.10	0.11	0.09	-0.06	0.04	-0.02	-0.09	-0.11	0.03
Mg1	0.12	0.09	-0.08	0.07	-0.04	0.04	0.02	0.07	0.07	-0.04
Mg2	0.53	0.16	0.02	0.17	-0.07	0.08	0.08	0.32	0.20	-0.00
Mgb	1.00	0.12	0.04	0.11	-0.04	0.01	0.06	0.29	0.13	-0.05
Fe5270	0.12	1.00	0.36	0.20	0.17	0.18	0.10	0.06	0.04	0.04
Fe5335	0.04	0.36	1.00	0.25	0.15	0.13	0.01	-0.03	0.07	0.12
Fe5406	0.11	0.20	0.25	1.00	0.03	0.11	-0.02	0.08	0.08	0.07
Fe5709	-0.04	0.17	0.15	0.03	1.00	0.06	0.08	0.05	0.00	-0.02

Table 3.7 (cont'd)

Fe5782	0.01	0.18	0.13	0.11	0.06	1.00	0.04	0.05	0.08	0.02
TiO1	0.06	0.10	0.01	-0.02	0.08	0.04	1.00	0.12	0.05	0.03
TiO2	0.29	0.06	-0.03	0.08	0.05	0.05	0.12	1.00	0.01	-0.10
Hd A	0.13	0.04	0.07	0.08	0.00	0.08	0.05	0.01	1.00	0.51
Hg A	-0.05	0.04	0.12	0.07	-0.02	0.02	0.03	-0.10	0.51	1.00

CHAPTER 4

Why Post-Starburst Galaxies Are Now Quiescent

Post-starburst or "E+A" galaxies are rapidly transitioning from star-forming to quiescence. While the meager star formation in post-starbursts is already at the level of early type galaxies, we recently discovered that many have large CO-traced molecular gas reservoirs, which are inconsistent with their star formation rates when compared to normal star-forming or early type galaxies. Here we present an ALMA search for the denser gas traced by HCN (1–0) and HCO$^+$ (1–0) in two CO-luminous, quiescent post-starburst galaxies. Intriguingly, we fail to detect either molecule. The upper limits are consistent with the low star formation rates and with early-type galaxies. The HCN/CO luminosity ratios are low compared to star-forming and many early type galaxies, implying a low dense gas mass fraction, leading to the low star formation efficiencies in the CO-traced molecular gas. We conclude that the post-starbursts are currently quiescent because no dense gas is available, in contrast to the significant CO-traced lower density gas reservoirs that still remain.

4.1   Introduction

The nature of how and when the molecular gas reservoirs are depleted in galaxies is essential to understanding the question of why galaxies become quiescent. To explore this question, we focus on a class of galaxies in the midst of rapid evolution in their star formation properties. The spectra of post-starburst, "E+A", or "k+a" galaxies show strong Balmer absorption, indicative of a recent starburst that ended in the last Gyr, yet little ongoing star formation, indicating a rapid change from star-forming to quiescent (Dressler & Gunn, 1983; Couch & Sharples, 1987). Despite their low

star formation rates (SFRs), many (over half of those studied) have large CO-traced molecular gas reservoirs (French et al., 2015; Rowlands et al., 2015; Alatalo et al., 2016b). These quiescent post-starburst galaxies have similar CO-traced molecular gas fractions as normal star-forming galaxies. This offset persists in the classical Kennicutt-Schmidt (Kennicutt, 1998) relation, suggesting a $\sim 4\times$ suppression of star formation efficiency in the CO-traced molecular gas.

Previous studies of the molecular gas content of post-starburst galaxies have used the CO (1–0) and CO (2–1) lines as tracers. The CO (1–0) line is sensitive to molecular gas at densities $\gtrsim 300$ cm^{-3}. Other molecules, like HCN (1–0), trace denser gas ($\gtrsim 10^4$ cm^{-3}). The HCN (1–0) luminosity correlates more linearly with SFR, and with less scatter, than does the CO (1–0) luminosity (Gao & Solomon, 2004), and extends down to the scales of star-forming clumps (Wu et al., 2005, 2010).

The dense gas luminosity ratio HCN/CO can be converted to a dense molecular gas to total molecular gas mass ratio, and is correlated with the star formation efficiency (SFE) in the CO-traced gas, SFR/L'(CO) (Gao & Solomon, 2004; Bigiel et al., 2015). If the high SFE in the CO-traced gas of starbursts arises from a high dense gas mass ratio, the low CO-traced SFE of their post-starburst descendants may be due to a low dense gas mass ratio.

While the tight linear relation between HCN luminosity and SFR has been interpreted as evidence of a threshold density for star formation (Wu et al., 2005; Heiderman et al., 2010; Lada et al., 2012), the difference in the L'(CO)–SFR vs. L'(HCN)–SFR relations can also be explained by whether the median gas density is above or below the critical density of each line (Krumholz & Thompson, 2007), and the subsequent relation between the gas density and line luminosity given the emission from sub-thermal gas (Narayanan et al., 2008). Furthermore, Stephens et al. (2016) find that the kpc-scale observations of integrated galaxy properties cannot be explained by a simple summation of clumps, and suggest the low scatter in the

L'(HCN)–SFR relation is due to a universal dense gas star formation efficiency, stellar IMF, and core/clump mass functions, with the kpc scale being sufficient to sample the full mass functions as well as various evolutionary states. Thus, we do not necessarily expect the HCN traced gas to trace gas where collapse to stars is inevitable, and such a threshold is likely much higher than 10^4 cm^{-3} (Krumholz & Tan, 2007).

We must measure the properties of this denser gas in post-starburst galaxies to understand why there is no significant star formation and why CO-traced molecular gas remains. Here, we present an ALMA survey of HCN (1–0) and HCO$^+$ (1–0) in two CO-luminous post-starburst galaxies.

4.2   Observations

The observations for this work were obtained during ALMA Cycle 4 (program 2016.1.00881.S; PI: French). We observe two post-starburst galaxies with CO (1–0) detections from French et al. (2015) with representative CO luminosities and SFRs and redshifts and declinations enabling observations with ALMA (labeled H02 and S05). We use the Band 3 receiver (84-116 GHz) with two spectral windows to observe HCN 1–0 (88.63 GHz rest frame), HCO$^+$ 1–0 (89.19 GHz rest frame), and HNC 1–0 (90.66 GHz rest frame). The redshift of H02 pushes HCN close to the edge of the Band 3 bandwidth, so we adopt narrow spectral windows, of 417, 831, 817 km/s for the lines, respectively. These spectral windows are still much larger than the 170 km/s linewidth of the CO (1–0) line for this galaxy. For S05, we adopt wider spectral windows of 1622-1660 km/s.

The observations of H02 were executed in one block on November 4, 2016. The observations of S05 were executed in three blocks on November 22 and 25, 2016. The 12m array was used for both datasets, using 43 antennas for H02 and 41-46 antennas for S05. We requested 1″ resolution for each galaxy to match the observed sizes of the resolved CO emission (ALMA program 2015.1.00665.S; PI: Smith), with

Table 4.1.   Post-Starburst ALMA Observations

Name	RA (deg)	Dec (deg)	z	$L'(\text{CO})^{\text{a}}$ (10^6 K km s^{-1} pc^2)	SFR$^{\text{a}}$ (M$_\odot$ yr^{-1})	$L'(\text{HCN})^{\text{b}}$ (10^6 K km s^{-1} pc^2)	$L'(\text{HCO}^+)^{\text{b}}$ (10^6 K km s^{-1} pc^2)
H02	141.580383	18.678055	0.0541	842.5 ± 174.2	0.09	< 16.8	< 17.4
S05	146.112335	4.499120	0.0467	304.6 ± 95.4	0.58	< 7.3	< 7.2

$^{\text{a}}$French et al. (2015)

$^{\text{b}}$$3\sigma$ upper limits

the aim of observing the dense gas on a comparable spatial scale without resolving out the dense gas tracer lines. The observations were carried out in configurations C40-5 and C40-4 for H02 and S05 respectively.

The data were pipeline-calibrated using CASA version 4.7.0-1. The H02 observations of HCN (1–0) have a final beamsize of 1.04 x 0.71″ and a sensitivity of 430 μJy/beam at a spectral resolution of 57 km/s. The H02 observations of HCO$^+$ (1–0) have a final beamsize of 1.011 x 0.71″ and a sensitivity of 450 μJy/beam at a spectral resolution of 57 km/s. Neither line is detected.

The S05 observations of HCN (1–0) and HCO$^+$ (1–0) are also nondetections, with a beamsize of $\sim$1.5″, and sensitivities of 368 μJy at 117 km/s spectral resolution.

4.3   Results

4.3.1   Upper Limits on Dense Gas Luminosities

We calculate the line luminosities using

$$L'_{line} = 3.25 \times 10^7 (1+z)^{-3} \, \nu_{\text{obs}}^{-2} \, S_{line}\Delta v \, D_L^2 \qquad (4.1)$$

where L' is the line luminosity in K km s^{-1} pc^2, z is the redshift, ν_{obs} is the observed line frequency in GHz, $S_{line}\Delta v$ is the integrated flux density in Jy km/s, and D_L

is the luminosity distance in Mpc. We integrate over the velocity width of the CO (1–0) lines as measured using the IRAM 30m (French et al., 2015). In Table 4.1, we present the 3σ upper limits on the HCN and HCO$^+$ line luminosities for the two post-starburst targets.

We compare the HCN upper limits to the SFRs and CO line luminosities in Figure 4.1. For comparison, we also show the rest of the French et al. (2015) post-starburst sample, as well as comparison samples of star-forming and early type galaxies with both HCN and CO measurements (Gao & Solomon, 2004; Crocker et al., 2012). For the early type galaxies, SFRs are from Davis et al. (2014), and we use the conversion factor from main beam temperature to flux density of 4.73 Jy/K from Young et al. (2011). While the post-starbursts have high CO luminosities for their SFRs, the observed offset does not persist for the denser HCN-traced gas; L'(HCN) upper limits are consistent with their low SFRs. The L'(HCN)/L'(CO) ratios for post-starbursts are low compared to the star-forming galaxies and most of the early types.

Similarly, we compare the HCO$^+$ upper limits to the SFRs for the post-starburst targets in Figure 4.2. The comparison samples of star-forming and starbursting galaxies are from Graciá-Carpio et al. (2008) and the early type galaxies from Crocker et al. (2012). Again, the upper limits from the post-starburst targets are consistent with their quiescent SFRs.

4.3.2   Dense Gas in Other Post-Starburst-Like Galaxies

There are two other post-starburst-like galaxies with dense gas observations in the literature. The first is NGC 5195 (M51b). While the nucleus of this galaxy shows a post-starburst signature (spectrum from Heckman et al., 1980), the integrated spectrum (Kennicutt, 1992) does not have the significant Balmer absorption required to be selected into our sample. This galaxy was observed in CO (1–0) and HCN (1–0) by Kohno et al. (2002) with the Nobeyama 45m. Subsequent observations
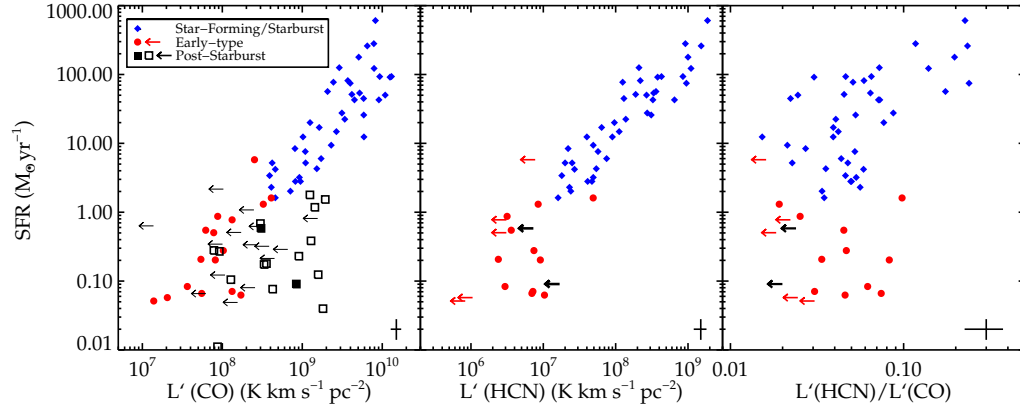
Figure 4.1: **Left:** SFR vs. $L'(\mathrm{CO})$ for star-forming and starbursting galaxies from Gao & Solomon (2004) (blue diamonds), early type galaxies from Crocker et al. (2012) (red circles), and post-starburst galaxies French et al. (2015) (black squares). Filled black squares represent the two galaxies targeted for dense gas observations. Characteristic error bars are shown in the bottom right of each panel. All upper limits are at the 3σ level. The post-starburst galaxies have systematically low SFRs for their CO luminosities. The post-starburst galaxies targeted for HCN observations span the post-starburst population. **Middle:** SFR vs. $L'(\mathrm{HCN})$ for the same samples. HCN is not detected for either post-starburst galaxy studied here, consistent with expectations from their low SFRs and with the early type galaxies. **Right:** SFR vs. dense gas luminosity ratio $L'(\mathrm{HCN})/L'(\mathrm{CO})$. The post-starburst galaxies targeted here have low HCN/CO luminosity ratios compared with the star-forming and many early type galaxies. The absence of denser gas traced by HCN reveals why the SFRs of post-starburst galaxies are so low. The low dense gas mass fractions implied by the low HCN/CO luminosity ratio leads to the low CO-traced SFEs.
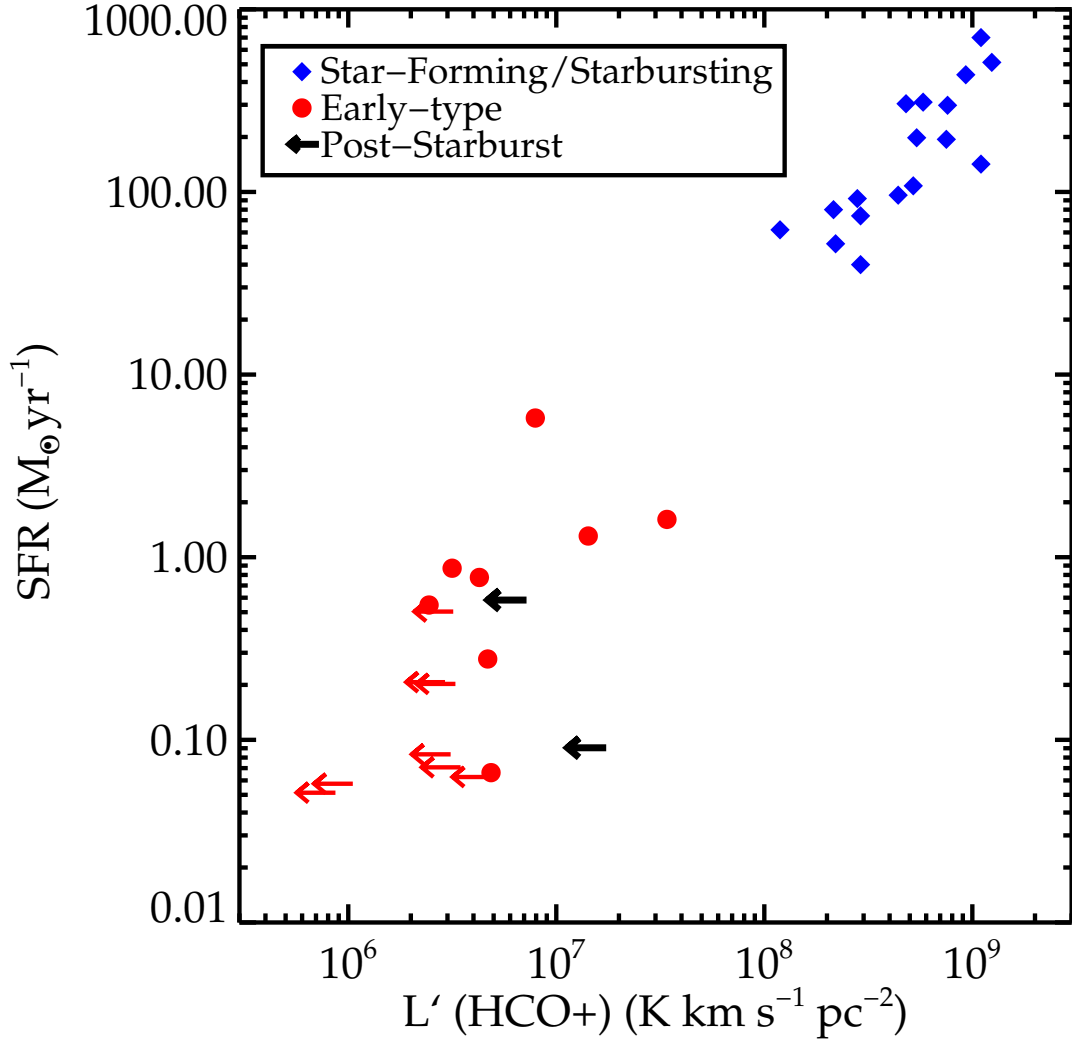
Figure 4.2: SFR vs. $L'(HCO^+)$ for star-forming and starbursting galaxies from Graciá-Carpio et al. (2008) (blue diamonds), early type galaxies from Crocker et al. (2012) (red circles), and post-starburst galaxies. All upper limits are at the 3σ level. In contrast to their large CO-traced gas reservoirs, HCO^+ is not detected for either gas-rich post-starburst studied here, consistent with expectations from their low SFRs.

by Matsushita et al. (2010) did not detect HCN. Observations of NGC 5195 are complicated by the nearby spiral arm of M51 in this interacting system. Resolved measurements by Kohno et al. (2002) using the Nobeyama Millimeter Array (NMA) are brighter than the 15″ beam unresolved observations. Alatalo et al. (2016a) reobserved this galaxy using the Combined Array for Research in Millimeter Astronomy (CARMA) and found a CO (1–0) line flux in between the two Kohno et al. (2002) measurements. NGC 5195 has both HCN *and* CO luminosities consistent with its SFR from Lanz et al. (2013), unlike our targets. Alatalo et al. (2016a) conclude this galaxy has a star formation efficiency consistent with normal early type galaxies.

Another galaxy with some post-starburst characteristics and dense gas measurements is NGC 1266 (Alatalo et al., 2014, 2015). HCN (1–0) and CO (1–0) measurements are part of the Atlas-3D survey of early type galaxies (Crocker et al., 2012). While this galaxy has nebular emission lines that would exclude it from our post-starburst sample, it is possible this "shocked" post-starburst galaxy is a precursor to our sample (Alatalo et al., 2016c). NGC 1266 has the highest HCN/CO line luminosity ratio of any of the galaxies in the Crocker et al. (2012) sample, in contrast to the low dense gas ratios seen here. This difference may be related to the molecular outflow in the nucleus of this galaxy (Alatalo et al., 2015), which could enhance the dense gas fraction in this region.

4.3.3 Matching HCN to CO observations

It is important to ensure that the HCN and CO emission is compared in matched apertures. The ALMA observations described here have a beam size of 1-1.5″ (or 1.0-1.4 kpc), with a maximum recoverable scale of 7.6″.

We compare the HCN luminosities from ALMA to the CO (1–0) luminosities from the IRAM 30m (French et al., 2015). While the IRAM 30m observations have a beam size of $\sim$22″, our companion ALMA program (2015.1.00665.S; PI: Smith; Smith et al. in prep) finds the CO (2–1) emission confined to the central 1-1.5″

of these galaxies. The resolved CO (2–1) fluxes are consistent with the unresolved IRAM 30m CO (2–1) observations (with $\sim$11$''$ beamsize), indicating a lack of significant CO emitting gas beyond the central 1-2 kpc of these galaxies. Additional HCN emission is therefore probably not resolved out by our ALMA observations, as HCN emission is expected to come from the central kpc of the galaxy (e.g., Aalto et al., 2012; Kepley et al., 2014; Scoville et al., 2015). Even when this dense gas is more extended or in outflows (e.g., Alatalo et al., 2014; Salas et al., 2014), the emission does not extend more than 500 pc from the main disk. Thus, the upper limits on HCN luminosity and the CO luminosities are comparable, and are not biased by a beam size mismatch.

4.4   Discussion

So far, we have learned that post-starburst galaxies have CO luminosities that are systematically high given their SFRs, when compared to the SFR-L'(CO) relation that is followed by star-forming and early type galaxies. However, the low HCN and HCO$^+$ luminosities implied by the ALMA non-detections *are* consistent with the low SFRs in the two post-starbursts targeted here. These dense gas luminosities are also consistent with those typical of early type galaxies, the likely end-points of post-starburst evolution.

To interpret our new results further, we need to convert L'(HCN) to a dense ($n \gtrsim 10^4$ cm^{-3}) molecular gas mass upper limit and L'(HCN)/L'(CO) into the dense molecular gas mass to total molecular gas mass ratio (i.e., the "dense gas mass fraction"). If the derived upper limit on the dense gas mass in our post-starburst sample is consistent with their low SFRs and with other quiescent galaxies, then we have discovered why there is no significant star formation. If the dense gas mass fraction is low compared to normal galaxies, then we know why the CO-traced gas has a low SFE.

4.4.1 Low Star Formation Rates Arise from Lack of Dense Gas

We assume the conversion factor from $L'(\mathrm{HCN})$ to dense molecular gas mass is the same for post-starbursts and other galaxies. Therefore, our non-detections of $L'(\mathrm{HCN})$ imply low dense gas masses. The lack of dense gas in these post-starburst galaxies explains their quiescence.

The lack of a discrepancy between the HCN luminosity and SFR excludes several of the scenarios proposed in French et al. (2015) for explaining the discrepancy between CO luminosity and SFR, including that the dust obscuration exceeds our estimate from the Balmer decrement or that significant low-mass star formation (a very bottom-heavy IMF) is hidden from our SFR tracers. It is also unlikely that significant star formation is missed in the aperture correction of the SFRs from the $3''$ SDSS fibers.

4.4.2 Why CO-traced Star Formation Efficiency is Abnormally Low

The two post-starburst galaxies targeted here have HCN/CO luminosity ratios which are low compared to star-forming galaxies and many early types. We perform a Monte-Carlo test, drawing pairs of galaxies at random from the comparison early type and star-forming samples, to test how unusual it is to find two galaxies with these HCN/CO luminosity ratios. Drawing from just the early type sample, we find that two galaxies have HCN/CO luminosity ratios this low 9% of the time. Drawing from both the early type and star-forming comparison samples, the probability is 1%.

What if $L'(\mathrm{HCN})/L'(\mathrm{CO})$ does not correlate with the dense gas mass fraction as it does for other galaxies? This scenario could occur if the CO luminosity to total molecular gas mass conversion factor α_{CO} and HCN luminosity to dense molecular gas mass conversion factor α_{HCN} vary differently with the state of the gas. A lower value of α_{CO} is usually invoked in ULIRGs and justified based on significant CO

emission from outside of GMCs, widening the linewidth. In French et al. (2015), we consider whether a ULIRG-like α_{CO} may be appropriate for post-starburst galaxies. While post-starbursts may be descendants of ULIRGs, we are observing them many dynamical times ($\sim 10^6 - 10^{7.5}$ yr, Genzel et al. 2010) after the starburst phase has ended ($\sim$0.3-1 Gyr ago). We estimate the influence of the stellar potential on increasing the linewidth and lowering α_{CO}, and find it is not sufficient to resolve the observed offset between $L'(\mathrm{CO})$ and the low SFRs. The dense gas conversion factor is similarly uncertain, but to resolve the discrepancies for the post-starburst galaxies in both SFR-$L'(\mathrm{CO})$ and SFR-$L'(\mathrm{HCN})$, α_{CO} would have to be lowered without a decrease in α_{HCN}.

We test this possibility using `DESPOTIC` (Krumholz, 2013) to model the change in α_{CO} and α_{HCN} for the typical Milky Way GMC and ULIRG conditions described by Krumholz (2013). ULIRG conditions result in α_{CO} values $\sim 5\times$ lower than in Milky Way GMC conditions, as expected. However, α_{HCN} is lowered by the same factor. Thus, even ULIRG-like conditions could not generate the low observed HCN/CO luminosity ratios of post-starburst galaxies. The low HCN/CO luminosity ratios in the post-starburst targets are thus likely due to low dense gas mass ratios.

A low dense gas mass ratio leads to the suppressed SFE in the CO-traced gas is suppressed just as the *high* dense gas mass ratios in starbursting galaxies leads to their *increased* CO-traced SFEs (Gao & Solomon, 2004; Bigiel et al., 2015). Whatever mechanisms are acting in these galaxies must disproportionately affect the denser gas, lowering both the dense gas mass fraction and the CO-traced SFE. For example, when turbulence is injected into the gas, the lower density gas traced by CO is more gravitationally stable, limiting its cooling into higher density gas like that traced by HCN and driving the dense gas mass fraction lower. This behavior is seen in "morphological quenching" (Martig et al., 2013). Lower hydrostatic pressure in the disk can also lower the dense gas mass ratio (Helfer & Blitz, 1997). Hopkins et al. (2013) predict that the dense gas mass ratio changes with the GMC

surface density when star formation is regulated by stellar feedback. This effect may increase the CO-traced SFE at high gas surface densities. Similarly, it may also decrease the CO-traced SFE in post-starburst galaxies.

4.4.3   Normal HCN-traced Star Formation Efficiency

The CO-traced gas undergoes a dramatic transition as the galaxy evolves from starbursting to the post-starburst phase over $\lesssim 1$ Gyr. Starburst galaxies have enhanced CO-traced SFEs compared to normal star-forming galaxies. After the starburst ends, we observe post-starburst galaxies to have suppressed CO-traced SFEs relative to normal star-forming galaxies. Over the $\sim$ Gyr of evolution between these two phases, the dense gas mass ratio also evolves from high to low. However, the HCN-traced SFE is consistent between starbursting, star-forming, and post-starburst galaxies. Thus, despite the fact that collapse to star formation is not guaranteed at the $n \gtrsim 10^4$ cm^{-3} densities traced by HCN, the processes which drive the starburst, the end of the starburst, and the dramatic change in CO-traced SFEs do not affect the HCN-traced SFE. This result is consistent with the idea proposed by Krumholz & Thompson (2007) and Stephens et al. (2016) that the dense gas SFE is universal on kpc scales. While these studies were based on star-forming and starbursting galaxies, our result suggests that this universality may extend to quiescent galaxies with low SFRs.

4.5   Conclusions

We survey the dense molecular gas content of two post-starburst galaxies possessing large reservoirs of CO-traced molecular gas, despite their lack of significant current star formation. ALMA does not detect either HCN (1–0) or HCO$^+$ (1–0) in these galaxies. This absence of dense gas is consistent with their low star formation rates. For the first time, we have direct evidence as to why post-starburst galaxies have

such low star formation rates, given their large reservoirs of CO-traced molecular gas: the denser gas required for star formation is absent.

The HCN/CO luminosity ratios are low compared to star-forming and many early type galaxies, and imply a low dense gas mass fraction, the fraction of dense molecular gas mass to total molecular gas mass. The low dense gas fraction leads to the low CO-traced star formation efficiency in these post-starburst galaxies (see French et al., 2015). The consistency of the dense gas star formation relation between post-starbursts and other galaxies implies the HCN-traced star formation efficiency is consistent among these types of galaxies and unaffected by the processes which drive the starburst and its end.

The low HCN luminosities of the post-starburst galaxies are already consistent with the early type galaxies into which they are expected to evolve. However, the presence of significant CO-traced gas necessitates a more detailed view of how these galaxies could evolve into gas-poor early types. The decline in the CO-traced molecular gas during the post-starburst phase (French et al. submitted) suggests that feedback processes from AGN activity may act at a later time, after the starburst has already ended. Thus, post-starbursts do not have significant star formation because of a lack of dense gas, and are unlikely to resume star formation after the rest of the molecular gas reservoirs are depleted, resulting in gas-poor galaxies passively evolving to early types. This picture of how star formation ends in galaxies undergoing rapid transition may be largely representative, as $\sim$40-100% of galaxies are expected to evolve through this phase (Snyder et al., 2011; Wild et al., 2016).

CHAPTER 5

Tidal Disruption Events Prefer Unusual Host Galaxies

Tidal Disruption Events (TDEs) are transient events observed when a star passes close enough to a supermassive black hole to be tidally destroyed. Many TDE candidates have been discovered in host galaxies whose spectra have weak or no line emission yet strong Balmer line absorption, indicating a period of intense star formation that has recently ended. As such, TDE host galaxies fall into the rare class of quiescent Balmer-strong galaxies. Here, we quantify the fraction of galaxies in the Sloan Digital Sky Survey (SDSS) with spectral properties like those of TDE hosts, determining the extent to which TDEs are over-represented in such galaxies. Galaxies whose spectra have Balmer absorption $H\delta_A - \sigma(H\delta_A) > 4\,\text{Å}$ (where $\sigma(H\delta_A)$ is the error in the Lick $H\delta_A$ index) and $H\alpha$ emission EW < 3 Å have had a strong starburst in the last $\sim$Gyr. They represent 0.2% of the local galaxy population, yet host 3 of 8 (37.5%) optical/UV-selected TDE candidates. A broader cut, $H\delta_A > 1.31\,\text{Å}$ and $H\alpha$ EW < 3 Å, nets only 2.3% of SDSS galaxies, but 6 of 8 (75%) optical/UV TDE hosts. Thus, quiescent Balmer-strong galaxies are over-represented among the TDE hosts by a factor of 33-190. The high-energy-selected TDE *Swift* J1644 also lies in a galaxy with strong Balmer lines and weak $H\alpha$ emission, implying a $> 80\times$ enhancement in such hosts and providing an observational link between the γ/X-ray-bright and optical/UV-bright TDE classes. [1]

---

[1] A version of this chapter originally appeared as a published paper in the Astrophysical Journal Letters (French et al., 2016). All of the work described below was carried out by me, with help from co-authors Iair Arcavi and Ann Zabludoff.

5.1   Introduction

If a star passes close enough to a supermassive black hole that the tidal forces overcome the self-gravity of the star, the star will be destroyed in a tidal disruption event (TDE; Hills, 1975). Such events are expected to generate an observable flare (Rees, 1988; Evans & Kochanek, 1989; Phinney, 1989) if the tidal radius is greater than the Schwarzschild radius.

Real-time discoveries of TDE candidates have enabled extensive followup observations and classification. The first was *Swift* J1644 (Bloom et al., 2011; Burrows et al., 2011; Levan et al., 2011; Zauderer et al., 2011), displaying non-thermal emission in γ-rays, X-rays, and the radio. Two additional events had similar properties: *Swift* J2058 (Cenko et al., 2012b) and *Swift* J1112 (Brown et al., 2015). Hereafter we refer to these events as "high energy TDEs".

In parallel, a different class of transients were also identified as likely TDEs. The first was PS1-10jh (Gezari et al., 2012), which had thermal optical and UV emission but no observed X-rays. Since the discovery of PS1-10jh, eight objects with similar TDE spectral features have been found. Arcavi et al. (2014, hereafter A14) discovered three in Palomar Transient Factory (PTF) data, PTF09axc, PTF09djl, and PTF09ge, grouping them together as a class with PS1-10jh, SDSS J0748 (identified in the Sloan Digital Sky Survey (SDSS); Wang et al., 2011), and ASASSN-14ae (Holoien et al., 2014). Recently, three additional members of this class have been discovered: ASASSN-14li (Holoien et al., 2016), ASASSN-15oi (Prentice et al., 2015), and PTF15af (in the galaxy SDSS J084828.13+220333.4; Blagorodnova et al., in prep). This optical/UV-selected class of transients all display hot blackbody ($\sim$ few $\cdot 10^4$K) emission and several-month-long smooth light curves peaking at an absolute optical magnitude of ~ -20. They are all located in the centers of their host galaxies. Their clear broad H and/or He emission lines (A14) cleanly distinguish them from other transient events. Hereafter we refer to these events as "optical/UV

TDEs".

Curiously, the host galaxy spectra of these eight[2] events show Balmer line absorption, and all but SDSS J0748 have weak or no emission lines. This combination of spectral features indicates low levels of current star formation, yet substantial star formation in the last $\sim$ Gyr, long enough ago for the ionizing O and B stars to have evolved away, but recently enough for A stars to dominate the stellar light. Galaxies with these spectral features are called Balmer-strong, Hδ-strong, E+A, k+a, or a+k galaxies, depending on the strength of the Balmer absorption and the authors' preference (Dressler & Gunn, 1983; Couch & Sharples, 1987; Dressler et al., 1999). Many are consistent with a post-starburst star formation history and galaxy-galaxy merger origin, and are likely in transition between star-forming spirals and passive early-type galaxies (Zabludoff et al., 1996; Y. Yang et al., 2004, 2008).

Similarly, the host galaxy of the high energy TDE candidate *Swift* J1644 was reported to have significant Balmer absorption with a low current star formation rate (SFR) predicted from its Hα flux (Levan et al., 2011). Yoon et al. (2015) find a young < 1 Gyr stellar population, suggesting a recent starburst. The two other known high energy TDE candidates do not yet have host galaxy spectra covering the full Balmer series.

The clear preference of optical/UV TDE candidates and at least one high energy TDE candidate for rare Balmer-strong galaxies has important implications for the mechanisms driving TDE rates. Here we examine the statistics of galaxies like the TDE candidate hosts to quantify the TDE-rate enhancement in such environments.

---

[2]As of submission, the TDE ASASSN-15oi was still ongoing, and no uncontaminated optical spectrum of the host galaxy was available.
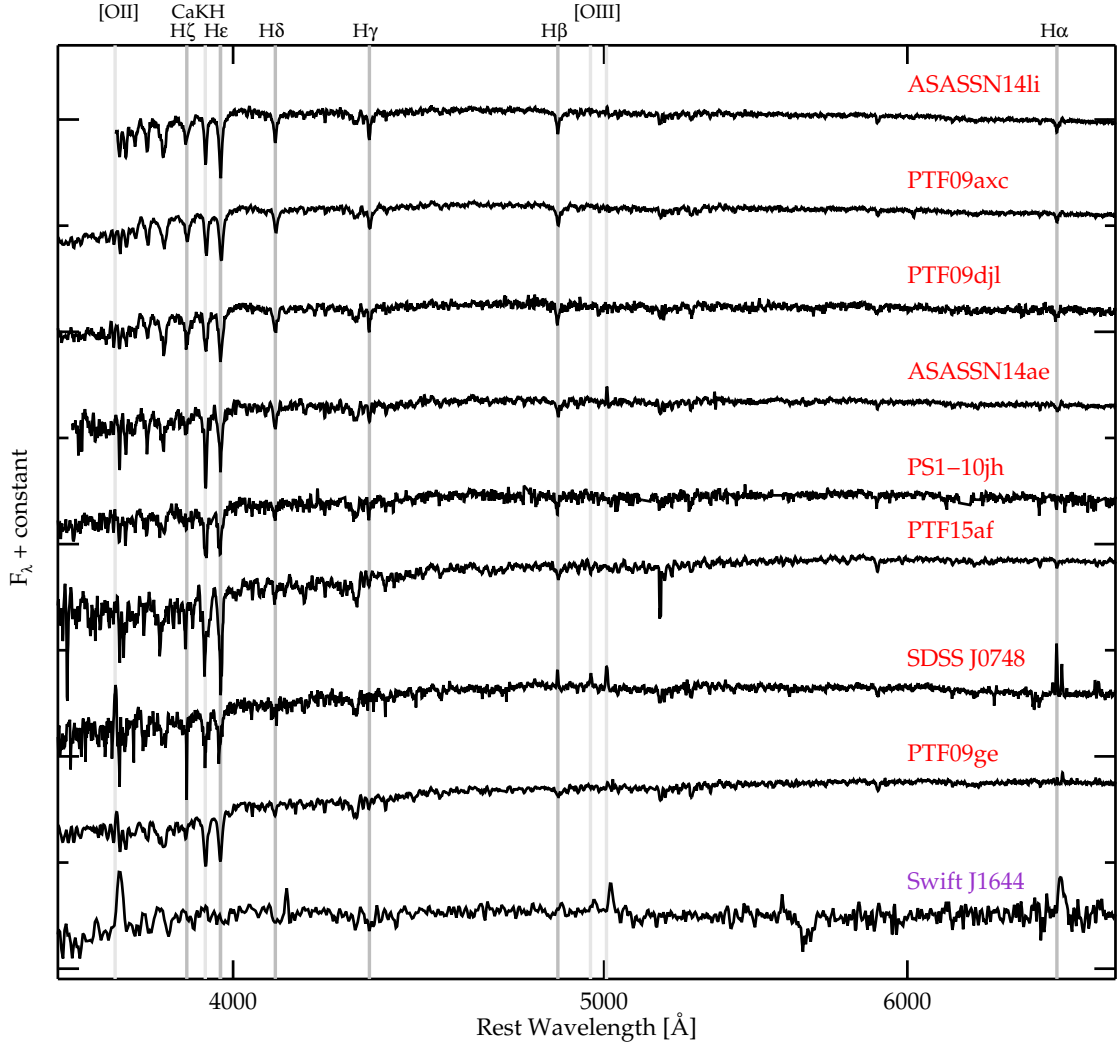
Figure 5.1: Spectra of the eight optical/UV TDE host galaxies, in order of decreasing strength of their Hδ_A index. Also shown is the lower-resolution host galaxy spectrum of the high energy TDE *Swift* J1644. Strong Balmer absorption, Ca II H+Hϵ absorption, and a lack of strong emission lines are characteristic of post-starburst galaxies. Both SDSS J0748 and *Swift* J1644 were selected differently from the rest of the sample, although the optical spectrum of the TDE itself in SDSS J0748 appears similar to the other optical/UV TDEs.
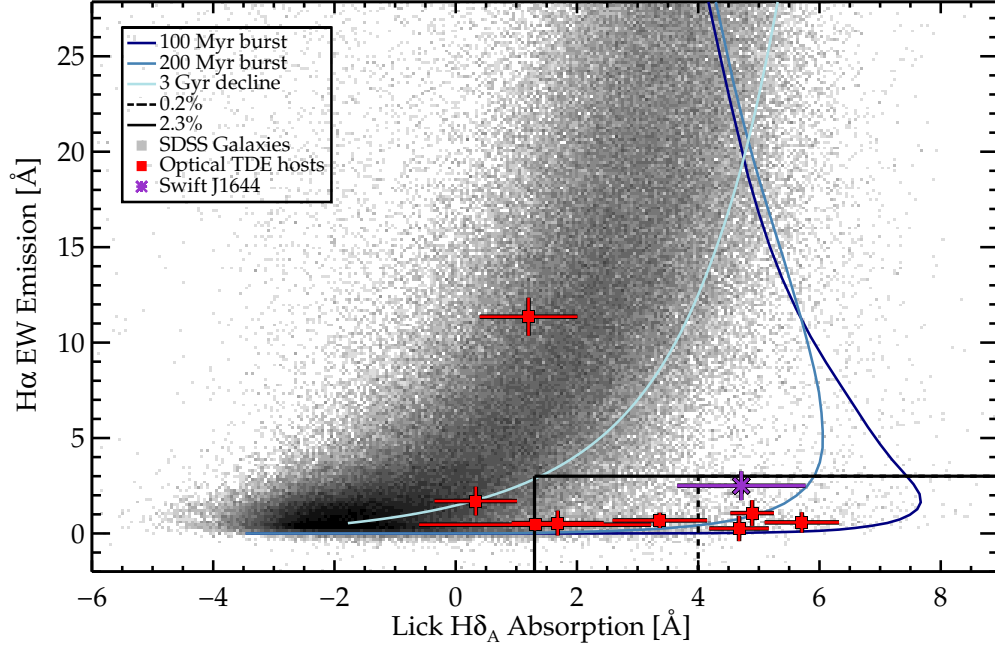
Figure 5.2: Spectral characteristics of SDSS galaxies (grey) and TDE candidate host galaxies (colored points): Hα EW emission (current star formation) versus Hδ_A absorption (from A stars, indicating star formation within the past $\sim$Gyr). The SDSS galaxies populate the "red sequence" (low Hα EW, low Hδ_A) and "blue cloud" (extending up to higher Hα EW at moderate Hδ_A). Many TDE hosts lie within the quiescent Balmer-strong galaxy "spur" extending to high Hδ_A at low Hα EW. Two cuts along the spur are shown: Hα EW <3 Å with H$\delta_A - \sigma($H$\delta_A) > 4$ Å (dashed boundary) and H$\delta_A > 1.31$ Å (solid boundary). These regions include only 0.2% and 2.3% of the SDSS galaxies, yet encompass 38% and 75% of the optical/UV TDE host galaxies, respectively. Three example star formation history tracks are shown. Short duration starbursts (dark and medium blue) on top of an existing old stellar population will pass through the strongest Hδ_A region once the starburst ends, evolving through the moderately strong Hδ_A region at later times. A gradually declining star formation history (light blue) cannot pass through the strictest Hδ_A cut. TDE host galaxies with the highest Hδ_A absorption thus have likely experienced a recent starburst. Galaxies with H$\delta_A = 1.3$ to 4Å have a range of possible star formation histories (see text), but have still experienced a recent decline in their star formation. The TDE hosts SDSS J0748 and PTF09ge do not lie in the spur, but among the star-forming and early-type populations, respectively. The high energy TDE candidate *Swift* J1644 (purple) has strong Hδ_A absorption (its errors place it just outside our strictest cut). Even if *Swift* J1644 turns out to be the only one of the three known high energy TDEs with a host that lies in this region, high energy TDE rates will be over-represented in quiescent Balmer-strong galaxies by $> 80\times$.

5.2 Spectral Properties of TDE Host Galaxies

5.2.1 Quiescent Balmer-Strong Classification

We wish to determine the Balmer stellar absorption line and nebular emission line properties of TDE hosts to quantify the incidence of galaxies like them. Balmer absorption is generally characterized using the Hδ line, due to its low emission filling and smooth nearby continuum regions. Dressler et al. (1999) identify quiescent galaxies with Hδ EW$>$ 3Å as "k+a" or "Balmer-strong" galaxies. Here, we parameterize Balmer absorption using the Lick Hδ_{A} index, which is optimized for the stellar absorption from A stars (Worthey & Ottaviani, 1997). The Hδ_{A} measure differs slightly from Hδ EW: a cut on H$\delta_{\mathrm{A}} > 4$Å is equivalent to Hδ EW > 3Å. For our strictest cut, we require H$\delta_{\mathrm{A}} - \sigma(\mathrm{H}\delta_{\mathrm{A}}) > 4\,$Å, where $\sigma(\mathrm{H}\delta_{\mathrm{A}})$ is the Hδ_{A} index measurement error included to eliminate spurious objects with large $\sigma(\mathrm{H}\delta_{\mathrm{A}})$. We do not correct H$\delta_{\mathrm{A}}$ for emission line filling, as the correction is smaller than the measurement error for galaxies with both strong Hδ and weak Hα emission.

We select for galaxies with little on-going star formation by requiring Hα EW $< 3\,$Å in emission in the rest frame, corresponding to a specific SFR $\lesssim 1 \times 10^{-11}$ yr^{-1}, well below the main sequence of star-forming galaxies (e.g., Elbaz et al., 2011). We correct Hα EW for stellar absorption, which is significant for quiescent Balmer-strong galaxies.

5.2.2 Data

Optical spectroscopy was obtained for the eight host galaxies of the optical/UV TDE candidates from A14, C. Yang et al. (2013), and the SDSS, and for the host of high energy TDE candidate *Swift* J1644 from Levan et al. (2011). We plot these host galaxy spectra in Figure 6.3, describing their features in Table 1.

For each TDE candidate host galaxy, we calculate Hδ_{A} as described above, and Hα EW using two pseudo-continuum bands (Blue: [6492.8-6532.8Å]; Red: [6592.8-

6632.8Å]). We use stellar population models from Conroy et al. (2009) and Conroy & Gunn (2010) to fit archival UV and optical photometry (from SDSS, *GALEX*, and *Swift* UVOT) together with the optical spectral features. We model the star formation history as an old population plus a recent, exponentially-declining burst of star formation. The age since the recent burst, mass produced and duration of the recent burst, and dust extinction are free parameters (French et al. in prep). From these models, we determine the stellar absorption correction to the Hα EW, which ranges from 1.5-2.5Å.

To quantify the rarity of these TDE hosts, we compare their spectral features to the SDSS main galaxy spectroscopic sample (Strauss et al., 2002), defining a parent sample from DR10 (Aihara et al., 2011). To prevent severe aperture bias, we exclude galaxies with $z < 0.01$ to eliminate those that are very large on the sky relative to the 3$''$ diameter of the SDSS fibers. We also exclude galaxies with unreliable [3] Hα equivalent widths (EW) or median signal-to-noise values of less than 10 per pixel over the whole spectrum. Our final parent sample is composed of 591,736 galaxies. We use the Hα EWs (corrected for stellar absorption) and Lick Hδ_{A} values from the MPA-JHU catalogs (Brinchmann et al., 2004). In the three cases where the TDE host galaxy spectrum is from the SDSS, our Hδ_{A} and corrected Hα EW measurements are consistent with the MPA-JHU catalog values.

---

[3]We require `h_alpha_eqw_err > -1`.

Table 5.1.　TDE Host Properties

TDE Host	Hα EW[a] [Å]	Hδ$_A$ [Å]	z	M_r[b] [mag]	Slit Width [arcsec (kpc)]	Data Source
SDSS J0748	-11.36±1.00	1.20±0.81	0.0615	-20.13±0.02	1.0 (1.2)	C. Yang et al. (2013)
ASASSN14ae	-0.68±0.40	3.37±0.79	0.0436	-19.75±0.02	3.0 (2.6)	SDSS
ASASSN14li	-0.59±0.53	5.71±0.61	0.02058	-19.20±0.02	3.0 (1.3)	SDSS
PTF09axc	-1.07±0.67	4.89±0.36	0.1146	-20.55±0.02	1.0 (2.1)	A14
PTF09djl	-0.26±0.66	4.67±0.49	0.184	-20.02±0.03	1.0 (3.1)	A14
PTF09ge	-1.70±0.75	0.33±0.68	0.064	-20.23±0.02	0.7 (0.9)	A14
PS1-10jh	-0.54±0.65	1.68±0.76	0.1696	-18.48±0.05	1.0 (2.9)	A14
PTF15af	-1.65±0.30	1.31±1.91	0.0790	-20.20±0.02	3.0 (4.5)	SDSS
Swift J1644	-2.50±0.76	4.71±1.06	0.3534	-18.44±0.1	1.0 (5.0)	Levan et al. (2011)

[a]Negative values indicate emission. Hα EW values are corrected for stellar absorption.

[b]Absolute magnitudes (*r* band, no extinction correction) from SDSS (model.mag) for optical/UV TDE hosts, and from Levan et al. (2011) for *Swift* J1644. We assume $H_0 = 70$ km s^{-1} Mpc^{-1}, $\Omega_\Lambda = 0.7$, and $\Omega_m = 0.3$.

5.3   Likelihood of Host Galaxy Properties

The scarcity of quiescent Balmer-strong galaxies makes it unlikely to see many TDE host galaxies in this class, were TDEs to occur in all types of galaxies. Our strictest selection cut, $H\delta_A - \sigma(H\delta_A) > 4\,\text{Å}$ and $H\alpha$ EW $< 3\,\text{Å}$ (emission), on the SDSS produces a sub-sample of 1207 galaxies (0.20%). Of the optical/UV TDE host galaxies studied here, three (ASASSN14li, PTF09axc, PTF09djl) of the eight satisfy these cuts. Quiescent Balmer-strong galaxies are thus over-represented in the TDE host galaxy sample by a factor of 190^{+115}_{-100} times.[4]

The significance of these cuts is illustrated in Figure 5.2. SDSS galaxies fall into the "blue cloud," with $H\alpha$ emission and moderate $H\delta_A$ absorption, and the "red sequence," with little-to-no $H\alpha$ emission and low $H\delta_A$. Quiescent Balmer-strong galaxies lie in the "spur" to the lower right, with weak $H\alpha$ emission and strong $H\delta_A$ absorption. Most of the TDE host galaxies lie along this spur.

The example model tracks in Figure 5.2 show how galaxies with different star formation histories evolve. Two tracks follow a recent burst of star formation (an exponentially-declining model of short duration; $\tau = 100$ or 200 Myr) on top of an existing old stellar population. We again use the stellar population models from Conroy et al. (2009, 2010), assuming that the recent burst created 10% of the stellar mass of the galaxy. A shorter burst with the same mass fraction produces higher $H\delta_A$ absorption. Star formation declining over $\tau > 200$ Myr does not generate high enough $H\delta_A$ to meet our strictest criterion. Thus, the three TDE host galaxies satisfying the strictest $H\delta_A$ cut have probably experienced a recent, strong, brief period of star formation, i.e., a true burst.

The $H\delta_A$ requirement can be relaxed to $> 1.31\,\text{Å}$ to encompass the three other optical/UV TDE host galaxies that also lie in the spur: ASASSN14ae, PTF15af, and PS1-10jh. This cut includes 13749 SDSS galaxies, or 2.3%, but six of the eight

---

[4]Errors represent 1σ binomial confidence intervals calculated using the small numbers tables from Gehrels (1986).

known TDE hosts. Thus, quiescent galaxies with at least moderately strong Balmer absorption are over-represented in the TDE host galaxy sample by a factor of 33^{+7}_{-11}. This lower $H\delta_A$ cut allows several possible star formation histories, including star formation that has declined over several Gyr, starbursts that have ended and evolved past the strong $H\delta_A$ region, and constant star formation with a sudden truncation (e.g., Shioya et al., 2004). Therefore, it is less straightforward to interpret the recent histories of the three lower $H\delta_A$ galaxies; all have recently-ended periods of star formation, but may not have experienced a strong starburst.

The two remaining TDE candidate host galaxies, SDSS J0748 and PTF09ge, do not lie in the spur of Figure 5.2. The TDE in SDSS J0748 was discovered in a search for high-ionization emission lines (Wang et al., 2011), not in a transient survey, a selection that might contribute to the distinct spectral properties of its host, which lies in the blue cloud of star-forming galaxies in Figure 5.2. In contrast, PTF09ge, found in the same manner as the other PTF A14 TDE candidates, has a host galaxy that lies closer to the red sequence of early-type galaxies.

Two of the optical/UV TDE host galaxies (PTF09djl and PS1-10jh) lie in the SDSS footprint, and have absolute magnitudes comparable to the other six host galaxies, but are too faint for the SDSS spectroscopic sample due to their slightly higher redshifts ($z = 0.1696, 0.184$). No significant galaxy evolution from $z \sim 0.2$ to 0.01 is expected (Snyder et al., 2011). Therefore, the quiescent Balmer-strong galaxy fraction should remain the same. To check this, we cut the parent sample to bound the redshifts of these two TDE hosts. The resulting TDE rate enhancements are within the 1σ errors of those quoted above.

The high energy TDE host galaxy *Swift* J1644 has some $H\alpha$ emission (Figure 6.3), but it is weak enough to meet our criteria for being quiescent. The host galaxy spectrum is noisy around $H\delta_A$, and thus does not meet our strictest Balmer-strong cut of $H\delta_A - \sigma(H\delta_A) > 4\,\text{Å}$. However, stronger $H\beta$ (EW $= 8.2 \pm 1.1\text{Å}$) and $H\gamma$ (EW $= 11.7 \pm 2.4\text{Å}$) absorption are reported by Levan et al. (2011). Because this galaxy

is at a higher redshift ($z = 0.3534$) than the optical/UV TDEs, we constrain the SDSS comparison sample to $z > 0.3$ in this case. A *Swift* J1644-consistent cut on $H\delta_A - \sigma(H\delta_A) > 3.65$ Å and $H\alpha$ EW < 3 Å yields 10 out of 2287 galaxies, or 0.4%. Although we do not have full optical spectra for the other two high energy TDEs, it is significant that at least 1/3 of that sample lies within only 0.4% of the parameter space.

5.4 Discussion

5.4.1 Preference of TDEs for Quiescent Balmer-Strong Galaxies

There are several unique characteristics of quiescent Balmer-strong galaxies that might act to boost the TDE rates. Many such galaxies have had a recent galaxy-galaxy merger, which might in turn lead to 1) a black hole binary, and/or 2) perturbed stellar orbits that pass closer to the black hole. A recent starburst associated with the merger could produce 3) a large A star population now evolving into more easily-disrupted giants, and/or 4) A stars concentrated in the galaxy's core. It is also not yet clear whether the high incidence of LINER-like emission in post-starburst galaxies (Yan et al., 2006; Y. Yang et al., 2006) is related to TDEs, perhaps via residual gas in the nucleus.

In post-merger systems, a subsequent merger of the central black holes is expected, with minor mergers producing unequal black hole binaries. Chen et al. (2009, 2011) suggest that the TDE rate will be higher for unequal mass black hole binaries, as stars around one black hole are scattered into the other. Li et al. (2017) predict an increased TDE rate for a few tens of Myr once two equal mass black holes form a bound binary. The range in $H\delta_A$ absorption in our sample suggests a range in merger ratios and/or a range of post-merger ages. In future work, it will be interesting to narrow down what TDE host physical properties correlate best with TDE rate enhancement.

A recent merger could also create an asymmetric central potential, which would alter stellar orbits near the nucleus, allowing for more centrophillic orbits than a spherically symmetric potential (Magorrian & Tremaine, 1999). Centrophillic orbits would bring more stars through the region where they could be tidally disrupted, increasing the TDE rate.

In galaxies that have experienced a starburst ending in the past $\sim$Gyr, the first A stars will be evolving off the main sequence. During their giant phase, these stars will be more easily disrupted due to their large envelopes (MacLeod et al., 2012). These evolving giants may also be susceptible to multiple epochs of mass loss to the black hole (and thus produce multiple TDEs), although such events might have different signatures than the TDEs here (MacLeod et al., 2013). It is not yet possible to tell if these TDEs are partial or full disruptions, and of which kinds of stars.

Post-starburst galaxies are known to have centrally concentrated distributions of A stars (Y. Yang et al., 2004, 2008) as a result of gas driven to the center during the merger. The increased stellar density in the core could serve to increase the TDE rate (Stone & Metzger, 2016), and could act in combination with the other effects discussed here.

Is there an observational bias favoring the detection of TDEs in quiescent Balmer-strong galaxies? We consider two possibilities—that somehow flares are more readily seen or broad H/He spectral features more easily distinguished in these hosts—and discount them. For example, while detecting a central transient would be easier in a dust-poor or bulgeless host, quiescent Balmer-strong galaxies have global extinctions between star-forming and early-type galaxies (e.g., Wild et al., 2009) and are bulge dominated with high Sérsic indices (Yang et al., 2008). Furthermore, their bright spectral continuum, arising from their recent star formation, makes broad emission line detection harder, not easier.

Several of the TDE rate enhancement mechanisms described above should also operate in *currently* starbursting galaxies. There, we might expect to see a bias

against the detection of TDEs, as starbursting/ULIRG galaxies will have significant dust attenuation (e.g., Casey et al., 2014). If TDEs occur mainly via black hole merger or starburst-related mechanisms, their lack of observability in starbursting galaxies must be considered in calculating the true rate of TDEs.

5.4.2 Implications for the TDE Rate

TDE rates derived from observations (e.g., van Velzen & Farrar, 2014; Holoien et al., 2016) are $\sim 10^{-5}$ yr^{-1} per galaxy, in tension with higher theoretical predictions of a few $\times 10^{-4}$ yr^{-1} per galaxy (Stone & Metzger, 2016).

Our results suggest that this rate is 33^{+7}_{-11} to 190^{+115}_{-100} times higher in quiescent galaxies with moderately strong and strong Hδ_{A} (Figure 5.2). Extrapolating the observed TDE rate, this implies a TDE rate of $2 - 4 \times 10^{-4}$ and $1 - 3 \times 10^{-3}$ yr^{-1} per galaxy, respectively. These TDE rate enhancements imply a lower TDE rate for normal star-forming and early-type galaxies, of $1 - 5 \times 10^{-6}$ yr^{-1} per galaxy.

These rate estimates do not include the high energy TDE *Swift* J1644. However, its host properties are so unusual that, even without knowledge of the two other TDE hosts, high energy TDE rates appear to be boosted by $> 80\times$ in quiescent Balmer-strong hosts.

We have focused on a homogeneous sample of TDEs whose broad H and/or He emission lines distingish them from other types of transients. In doing so, we have excluded three other optical/UV TDE candidates with spectral identifications, but without clearly broadened emission lines. The first, TDE2 (van Velzen et al., 2011), is the only borderline case, as its spectrum suggests a possible broad H feature, but with lower width and signal-to-noise. Its host's SDSS spectrum passes our H$\delta_{\mathrm{A}} > 1.3$Å cut, but including it in our analysis only changes the over-representation of TDEs in such hosts from 33 to 34$\times$. The last two, PTF10iya (Cenko et al., 2012a) and PS1-11af (Chornock et al., 2014), lie in a star-forming and quiescent galaxy, respectively, each with some evidence for Balmer absorption. Including these events

would not diminish the over-representation of Balmer-strong galaxies as TDE hosts.

5.5 Conclusions

We demonstrate the preference of tidal disruption events (TDEs) to occur in quiescent galaxies with strong Balmer line absorption. Quiescent galaxies with the strongest Balmer absorption, $H\delta_A - \sigma(H\delta_A) > 4\,\text{Å}$, make up only 0.2% of local galaxies, yet host 3 of 8 optical/UV TDE candidates. A softer cut, $H\delta_A > 1.31\text{Å}$, includes only 2.3% of local galaxies, but 6 of 8 optical/UV TDE host galaxies. The optical/UV TDE rates are thus enhanced by $190^{+115}_{-100}\times$ in the strongest $H\delta_A$ galaxies and by $33^{+7}_{-11}\times$ in galaxies with $H\delta_A > 1.31\text{Å}$. Because of this preference, the corresponding rates of optical/UV TDEs are $1-3\times10^{-3}$ yr^{-1} per galaxy, and $2-4\times10^{-4}$ yr^{-1} per galaxy, respectively. As a result, we predict a lower optical/UV rate in normal star-forming and early-type galaxies, of $1-5\times10^{-6}$ yr^{-1} per galaxy. Even the one high energy TDE with a full measured optical spectrum, *Swift* J1644, lies in a galaxy with strong Balmer absorption and weak nebular line emission, which implies a $> 80\times$ enhancement in such hosts, and a link between the optical/UV and high energy TDE classes.

Why do TDEs prefer quiescent, Balmer-strong hosts? This type of galaxy has several properties that make it special and may suggest an answer. Many have had a recent galaxy-galaxy merger (Zabludoff et al., 1996), increasing the possibility of a black hole binary, perturbed stellar orbits, a spatially-concentrated population of A stars, and/or an evolved population of easily-disrupted A giants. The high incidence of LINER-like emission (Yan et al., 2006; Y. Yang et al., 2006) may also play a role. In future work, we will explore these connections.

CHAPTER 6

The Post-Starburst Evolution of Tidal Disruption Event Host Galaxies

We constrain the recent star formation histories of the host galaxies of eight optical/UV-detected tidal disruption events (TDEs). Six hosts had quick starbursts of < 200 Myr duration that ended 10 to 1000 Myr ago, indicating that TDEs arise at different times in their hosts post-starburst evolution. If the disrupted star formed in the burst or before, the post-burst age constrains its mass, generally excluding O, most B, and highly massive A stars. If the starburst arose from a galaxy merger, the time since the starburst began limits the coalescence timescale and thus the merger mass ratio to more equal than 12:1 in most hosts. This uncommon ratio, if also that of the central supermassive black hole (SMBH) binary, disfavors the scenario in which the TDE rate is boosted by the binary but is insensitive to its mass ratio. The stellar mass fraction created in the burst is $0.5 - 10\%$ for most hosts, not enough to explain the observed $30 - 200\times$ boost in TDE rates, suggesting that the host's core stellar concentration is more important. TDE hosts have stellar masses $10^{9.4} - 10^{10.3}$ M$_\odot$, consistent with the SDSS volume-corrected, quiescent Balmer-strong comparison sample and implying SMBH masses of $10^{5.5} - 10^{7.5}$ M$_\odot$. Subtracting the host absorption line spectrum, we uncover emission lines; at least five hosts have ionization sources inconsistent with star formation that instead may be related to circumnuclear gas, merger shocks, or post-AGB stars. [1]

---

[1] A version of this chapter originally appeared as a published paper in the Astrophysical Journal (French et al., 2017). All of the work described below was carried out by me, with help from co-authors Iair Arcavi and Ann Zabludoff.

6.1 Introduction

Tidal Disruption Events (TDEs) are observed when a star passes close enough to a black hole that the tidal forces exceed the self-gravity of the star. Disruptions occurring outside the event horizon (typically for black hole masses $\lesssim 10^8 M_\odot$) are expected to be accompanied by an observable flare (Hills, 1975; Rees, 1988; Evans & Kochanek, 1989; Phinney, 1989). Rapid identification and followup enabled by transient surveys have produced a steadily increasing list of TDE candidate events, some detected primarily in X-ray/γ-ray emission (Bloom et al., 2011; Burrows et al., 2011; Levan et al., 2011; Zauderer et al., 2011; Cenko et al., 2012b; Brown et al., 2015) and others in the optical/UV (Gezari et al., 2012; Arcavi et al., 2014; Holoien et al., 2014, 2016; Prentice et al., 2015, Blagorodnova et al., in prep).

Curiously, the optical/UV class of TDEs preferentially occur in quiescent galaxies with strong Balmer absorption lines, indicating an intense period of star formation that has recently ended, which was likely a starburst (Arcavi et al., 2014; French et al., 2016). Several possibilities have been proposed to explain how the global star-formation history could be connected to the TDE rate. Many post-starburst galaxies show signs of a recent galaxy-galaxy mergers and have centrally concentrated young stellar populations (Zabludoff et al., 1996; Yang et al., 2004, 2008; Swinbank et al., 2012). If TDE host galaxies are post-starburst and post-merger, the TDE rate could be boosted by 1) 3-body interactions with the central supermassive black hole binary, 2) a high concentration of young stars in center-crossing orbits, or 3) residual circumnuclear gas.

In the sample of eight TDE hosts analyzed by French et al. (2016), we identified three that were quiescent and had Balmer absorption consistent with post-starburst galaxies ($H\delta_A - \sigma(H\delta_A) > 4\,\text{Å}$, where $\sigma(H\delta_A)$ is the error in the Lick $H\delta_A$ index, and Hα emission EW < 3 Å). Another three were identified as being just "quiescent Balmer-strong," with $H\delta_A > 1.31\,\text{Å}$ and Hα EW < 3 Å. While these features imply

an unusual recent star formation history, we could not differentiate between a recent short period of star formation (a true burst) and longer declines in the star formation rate, nor between older, stronger bursts and younger, weaker bursts.

In this paper, we use stellar population fitting to characterize the recent star-formation histories (SFHs) of TDE host galaxies. We consider the same sample of optical/UV - detected TDEs as in French et al. (2016). Using a new stellar population fitting method (French et al. 2016, submitted), we break the degeneracy between the duration of recent star formation, the time since its end, and the mass of stars it produced, to determine whether these galaxies have experienced a recent starburst and to use the burst characteristics to constrain possible mechanisms for enhancing the TDE rate. We also determine the galaxy's stellar mass. Our method is more accurate than those assuming a single stellar population, as a recent starburst will impact the mass-to-light ratio. These stellar masses are used to infer black hole masses, using measurements of the bulge mass and the black hole – bulge mass relation. In addition, we use the stellar population fitting results to uncover hidden emission lines, discriminating between ionization from star formation and from other sources. We compare these TDE host properties to the general quiescent Balmer-strong population (13749 galaxies) from the Sloan Digital Sky Survey (SDSS).

6.2   Data

We use optical photometry from the SDSS, UV photometry from *GALEX* and *Swift* UVOT, and optical spectroscopy to fit to stellar population models. For the SDSS photometry, we adopt the `modelmag` magnitudes, which provide stable colors while containing most of the galaxy light (Abazajian et al., 2004). We make small corrections to the u and z bands (-0.04 and 0.02 mag) to put them on the correct AB magnitude system. In addition to photometry errors given in the SDSS catalog, we add the magnitude zero-point errors (5%, 2%, 2%, 2%, and 3% in $ugriz$) in quadrature.

For each of the TDE host galaxies, we search for matching *GALEX NUV* and *FUV* detections using the *GALEX* GCAT catalog. We search for galaxies within $4''$ of the SDSS positions. This radius is similar to the FWHM of the *NUV* PSFs and much larger than the *GALEX* astrometric uncertainties ($0.59''$ in *FUV*). We have detections or upper limits in the *FUV* for the hosts of SDSS J0748, ASASSN-14li, and PTF09ge, and *NUV* detections or upper limits for all but the PTF09axc host. We obtain additional archival *Swift* UVOT data for the hosts of ASASSN-14ae, PTF09axc, PTF09djl, and PTF09ge.

We use optical spectra for the hosts of ASASSN-14ae, ASASSN-14li, and PTF15af from the SDSS (Aihara et al., 2011), for SDSS J0748 from Yang et al. (2013), and the rest from Arcavi et al. (2014).

In French et al. (2016), we also consider the high energy TDE Swift J1644. We do not present results for its host galaxy in this work, due to the absence of rest-frame *FUV* or *NUV* photometry, as well as the absence of a medium-resolution spectrum (R∼1000), required for our age-dating method.

We compare the TDE host galaxy properties with galaxies from the SDSS main galaxy spectroscopic sample (Strauss et al., 2002) DR10 (Aihara et al., 2011). As in French et al. (2016), we select quiescent, Balmer-strong galaxies to have $H\delta_A > 1.31$ Å and $H\alpha$ EW < 3 Å.

6.3 Methods: Age-Dating Host Galaxies

To constrain the detailed star formation histories of the TDE host galaxies, we fit the spectroscopic and photometric properties of these galaxies using stellar population models. The method is described and tested fully in (French et al. 2016, submitted), We describe it briefly here.

We use the flexible stellar population synthesis (FSPS) models of Conroy et al. (2009) and Conroy & Gunn (2010) to construct model template spectra. We assume a Chabrier IMF (Chabrier, 2003) and a Calzetti reddenning curve (Calzetti

et al., 2000). We model the spectra of quiescent Balmer-strong galaxies f_{model} as a combination of old and young stellar populations. The old stellar population's star formation history is modeled as a linear-exponential star formation rate over time t_{old}:

$$\Psi \propto t_{old} e^{-t_{old}/\tau_{old}} \qquad (6.1)$$

beginning 10 Gyr ago and characterized by the timescale $\tau_{old} = 1$ Gyr. The young stellar population's star formation history is modeled as an exponential decline in the star formation rate over time t_{young}:

$$\Psi \propto e^{-t_{young}/\tau}. \qquad (6.2)$$

We vary the time t_{SB} since this recent period of star formation began[2] as well as the characteristic timescale τ. The observed spectrum is modeled as a linear combination of the young and old stellar templates:

$$f_{model} = [y f_{young} + (1 - y) f_{old}] \times 10^{-0.4k(\lambda)A_V}, \qquad (6.3)$$

where $k(\lambda)$ is the reddening curve as a function of the wavelength λ, A_V is the amount of internal extinction expressed in magnitudes of V-band absorption, $f_{young}(\lambda; t_{SB}, \tau, Z)$ is the young stellar population spectrum (arising from Eq. 6.2), and $f_{old}(\lambda; Z)$ is the old stellar population spectrum (arising from Eq. 6.1). Z is the stellar metallicity assumed, using the priors described below. Each spectrum is normalized within the 5200–5800 Å wavelength window, and y represents the fraction of the total galaxy light in the young stellar template. The mass fraction of new stars m_f is derived from y and t_{SB} after the fitting is complete. Thus, we parameterize the spectrum using four free parameters, t_{SB}, A_V, y, and τ. The priors on these four parameters are: A_V, [0, 5] magnitudes, spaced linearly; t_{SB}, [30, 2000] Myr, spaced logarithmically; y, [0.01, 1], spaced logarithmically; τ, [25, 50, 100, 150, 200, 1000, 3000] Myr.

---

[2]Equations 1 and 2 are related by $t_{old} - t_{young} = 10$ Gyr $-t_{SB}$.

We compare the SDSS $ugriz$ and $GALEX\ FUV, NUV$ photometry, as well as 23 Lick indices (Worthey et al., 1994; Worthey & Ottaviani, 1997), to synthetic photometry and Lick indices calculated from the model spectra. The UV photometry is especially sensitive to the age and duration of the young stellar population, and with the Lick indices, which carry information about the young and old stellar populations, allows us to break the degeneracies between the age, duration, and mass fraction of the young stellar population. We determine the best fit model using χ^2 minimization, and marginalize over all other parameters to determine the 68% likelihoods for each parameter. Errors on the new stellar mass fraction are determined using a Monte Carlo method to propagate the errors on the age and new stellar light fraction.

We perform this fitting procedure twice. The first iteration, we assume solar metallicity. Using the stellar mass fit during the first iteration, we use the predicted metallicity from the mass-metallicity relation from Gallazzi et al. (2005) in the second iteration.

One consideration is the possibility of contamination from the current TDE or past TDEs. The $GALEX$ photometry for each galaxy used here was taken prior to the current TDE, while the $Swift$ photometry is post-TDE and thus may be contaminated. However, most of the $Swift$ data are upper-limits, and their removal does not change our derived parameters more than the quoted errors.

If there were a recent TDE prior to the current one, the $GALEX$ data could be contaminated. For the six quiescent Balmer-strong TDE host galaxies, the expected TDE rate is 2-4$\times10^{-4}$ year^{-1} per galaxy (French et al., 2016). The enhanced UV emission thus would need to persist for >400 years to affect our results: in that case, the calculated post-burst age of at least one of the hosts would be underestimated beyond the quoted errors. Even for the most TDE-active galaxies, with a TDE rate of 3×10^{-3} year^{-1} per galaxy, the enhanced UV emission must persist for >125 years to significantly alter at least one host galaxy's UV data.

However, the long-term UV-optical evolution of TDEs ASASSN-14ae and ASASSN-14li (Brown et al., 2016b,a) shows the emission declining rapidly over the first 100 *days* after the event, leveling off after 300 days. The optical emission, including the U-band flux, returns to that expected for the host. The UV light-curve declines over the same timescale, but levels off at brighter magnitudes than expected. We note that the UV spectra of post-starburst galaxies are not well-fit by single stellar populations, which may explain the discrepancies between the predicted final UV and optical fluxes for the host. Were the final host UV excess to be real, and to persist at 0.5-1 mag over the next 400 years, we would underestimate the post-burst age for at least one galaxy in our sample. That is unlikely; assuming a decline of $t^{-5/3}$ and the characteristic timescale of two months from Holoien et al. (2016), the TDE flux would drop by a factor of 60,000 in 125 years. Even for a shallower power law decline of $t^{-}5/12$ (as expected from disk emission at late times; Lodato & Rossi 2011), the TDE flux would drop by $> 15\times$ in 125 years, more than enough to be consistent with the host galaxy.

Table 6.1: TDE Host Galaxy Star Formation Histories

TDE	Starburst Age^a (Myr)	Post-Starburst Age^b (Myr)	Burst Mass Fraction m_f^c	Burst Duration τ^d (Myr)
SDSS J0748	354^{+177}_{-176}	-1150^{+177}_{-176}	$0.005^{+0.001}_{-0.001}$	1000 (50-1000)
ASASSN14ae†	501^{+37}_{-82}	155^{+37}_{-82}	$0.019^{+0.004}_{-0.004}$	150 (100-150)
ASASSN14li†	473^{+373}_{-67}	415^{+373}_{-67}	$0.055^{+0.016}_{-0.016}$	25 (25-200)
PTF09axc	1496^{+155}_{-155}	1036^{+155}_{-155}	$0.890^{+0.110}_{-0.211}$	200 (25-200)
PTF09djl	211^{+59}_{-23}	153^{+59}_{-23}	$0.023^{+0.005}_{-0.005}$	25 (25-200)
PTF09ge	530^{+730}_{-69}	415^{+730}_{-69}	$0.009^{+0.012}_{-0.012}$	25 (25-200)
PS1-10jh	118^{+722}_{-15}	61^{+722}_{-15}	$0.006^{+0.002}_{-0.002}$	1000 (25-1000)
PTF15af†	595^{+108}_{-191}	538^{+108}_{-191}	$0.005^{+0.002}_{-0.002}$	25 (25-100)

Notes: (a) Age since starburst began (t_{SB}), with 1σ errors. (b) Age since 90% of the young stars formed, or post-burst age, with 1σ errors. (c) Fraction of current stellar mass produced in the recent period of star formation, with 1σ errors. (d) Characteristic exponential timescale of the recent period of star formation, shown with 90% error bounds due to the coarseness of the fitting grid used and large uncertainties due to the small burst mass fractions. † TDE hosts for which the host spectra were obtained before the TDE.

Table 6.2: TDE Host Galaxy Properties

TDE	A_V	$M_\star^a$	M_{bulge}^b	M_{BH}^c	[NII]/Hα	[OIII]/Hβ	Hα EW^d
	(mag)	——	(log M$_\odot$)	——			(Å)
SDSS J0748	< 0.1	10.2	8.1	5.5	0.31±0.03	1.07±0.10	-11.36±1.00
ASASSN14ae†	< 0.1	9.9	9.6	6.9	0.55±0.17	6.28±2.16	-0.68±0.40
ASASSN14li†	0.3	9.7	9.6	6.9	0.89±0.14	< 12.5	-0.59±0.53
PTF09axc	< 0.1	9.7			0.90±0.14		-1.07±0.67
PTF09djl	0.4	10.2			< 3.96	< 3.4	-0.26±0.66
PTF09ge	< 0.1	10.2	10.0	7.5	0.80±0.04	3.41±0.93	-1.70±0.75
PS1-10jh	< 0.1	9.4			0.58±0.21		-0.54±0.65
PTF15af†	0.3	10.3			< 0.62		-1.65±0.30

Notes: (a) Log Stellar Mass, typical error 0.1 dex. (b) Log Bulge Mass, scaled from stellar mass, and bulge mass fraction from Mendel et al. (2013), typical error 0.25 dex. (c) Scaled from bulge mass and McConnell & Ma (2013) relation. The intrinsic scatter $(0.3 - 0.4$ dex) in this relation will dominate the errors. (d) Same as in French et al. (2016). † TDE hosts for which the host spectra were obtained before the TDE.

6.4   Results and Discussion

6.4.1   Star Formation Histories of TDE Host Galaxies

Evidence for Starbursts

With the fitted SFH information, we can distinguish whether the TDE hosts have experienced a true starburst ($\lesssim$200 Myr) or just a recent decline in a longer period of star formation. We allow for a range of possible durations for the recent star formation episode, from $\tau = 25$ Myr to 3 Gyr. Best-fit durations are shown for each galaxy in Table 6.1. Only two TDE hosts prefer a burst duration of 1 Gyr, longer than expected from a true starburst: SDSS J0748, which is still forming stars (so τ is less meaningful) and PS1-10jh. The other six TDE hosts are truly post-starburst, including PTF09ge, despite its weaker Balmer absorption (French et al., 2016). The fraction of TDE hosts at each burst duration is consistent with the number expected

from the comparison sample of quiescent Balmer-strong SDSS galaxies.

Post-Starburst Ages

We define two different ages for these galaxies: the age since the starburst began (t_{SB}) and the post-burst age (the age since the starburst "ended," when 90% of the stars in the recent burst had formed). Both sets of derived ages are shown in Table 6.1. These two age definitions differ depending on the burst duration τ. The youngest age is for the host of SDSS J0748, which is still star-forming and thus has a negative "post-burst age." The oldest is the host of PTF09axc, with a post-burst age of 1 Gyr. The range in ages is physical, and implies that TDEs are not limited to a specific point in their hosts post-starburst evolution.

We compare the derived properties of the TDE hosts with the SDSS quiescent Balmer-strong galaxies (Figure 6.1a). The shape of the SDSS sample contours is set by when Hδ absorption decreases (at later ages for stronger bursts) on the right hand side, and by a combination of effects on the left hand side. Because galaxies with SFR $\gtrsim$ 300 M$_\odot$ yr^{-1} rarely exist in the local universe, starbursts with high burst mass fractions must form stars over a longer duration, delaying their entry into our selection criteria. The TDE hosts, however, are not subject to these selection effects, so the absence of TDE hosts at long post-burst ages is physical.

When comparing the six quiescent Balmer-strong TDE hosts to the SDSS sample, there is a slight dearth of TDE hosts at post burst ages > 0.6 Gyr (five have post-burst ages < 0.6 Gyr and only one has a greater post-burst age). In contrast, 53% of the quiescent Balmer-strong SDSS galaxies have post-burst ages < 0.6 Gyr. Given the small numbers, the binomial confidence interval for the TDE host galaxies is 0.028 - 0.45, making the significance of this difference only 1.3σ. This difference persists if we compare the ages since the starburst began, instead of the ages since the starburst ended (which will differ depending on the burst duration). More TDEs are needed to establish whether they are preferentially found in younger post-burst

galaxies.

Starburst Mass Fractions

For 7/8 of the TDE hosts, the stellar mass of the young stellar population is $0.5-10\%$ of the total stellar mass. These burst mass fractions are consistent with those for the SDSS quiescent Balmer-strong galaxies; the distribution about 10% burst mass fraction is not significantly different between the two samples. These burst mass fractions are typically lower than those found in galaxies with stronger Balmer absorption ($H\delta_A - \sigma(H\delta_A) > 4\,\text{Å}$), which have burst mass fractions of $3-50\%$. Thus, the lower burst mass fractions (not longer duration periods of star formation nor more time elapsed since the starburst ended) are responsible for the weaker Balmer absorption seen in some of the TDE hosts.

As a comparison, normal star-forming galaxies with similar stellar masses as the TDE hosts have SFRs $\sim 1\ M_\odot \text{yr}^{-1}$ (Brinchmann et al., 2004), and so would form $0.25-2\%$ of their current stellar mass over the same 25-200 Myr period. While the TDE host burst fractions are typically higher, they do not produce enough new stars to account for the $30-200\times$ boost (French et al., 2016) in their TDE rates, relative to normal star-forming galaxies. If the number of newly formed stars is not the driver, the concentration of the stars in the core must be more important. More work is needed to determine if the stellar concentration near the nucleus is sufficient to explain the boosted TDE rates in these galaxies (e.g., Stone & van Velzen 2016).

Dust Extinction

In Table 6.2, we show the dust extinctions best fit to the spectra. The extinctions are low, $A_V < 0.4$ mag, consistent with those best fit in the SDSS quiescent Balmer-strong sample. In comparison, the extinctions fit by the MPA JHU group (Brinchmann et al., 2004) for early type galaxies (selected using a cut on $H\alpha$ EW < 3 Å) with similar stellar masses ($10^{9.5}-10^{10.5}$) are similar, with a median of $A_V = 0.28$

mag. Therefore, it is unlikely that the TDE preference for quiescent Balmer-strong hosts arises from easier detection, as the extinction tends to be comparable in early type galaxies where fewer TDEs are found.

Constraints on the TDE Progenitor Star

Using the post-burst ages, we can constrain the likely mass of the star that was tidally disrupted, assuming it formed in the recent burst or before. This constraint is independent of previous ones, which modeled the mass accreted during the TDE itself (e.g., Guillochon et al., 2014). We plot the post-burst ages vs. burst mass fractions in Figure 6.1a. On the top axis, we compare the post-burst ages to the stellar lifetimes of stars created near the end of the starburst. Stars more massive than these will have evolved off the main sequence by the time the TDE occurred. The range in post-burst ages is much larger than the expected post-main sequence evolution timescales, excluding a specific phase of post-main sequence evolution as the cause of the enhanced TDE rate after the starburst. Additionally, it is unlikely that the disrupted stars were giants evolving off the main sequence, because such stars are expected to be disrupted in multiple epochs, resulting in lower luminosity, longer duration TDEs than what was observed for these events (MacLeod et al., 2012, 2013). Therefore, we assume that the progenitor was a main sequence star and examine the implications.

We cannot place constraints on the star disrupted in SDSS J0748, as the host galaxy is still actively forming stars. For the seven quiescent hosts, the upper limits on the mass of the likely disrupted star range widely from $\sim$2.5, $\sim$4, $\sim$6, to $\sim$9 $M_\odot$. As a consequence, O stars, as well as most B and highly massive A stars, are excluded as TDE progenitors. Observations of TDEs in older post-starburst galaxies would place stronger constraints on the likely progenitor mass for the disrupted star in those hosts.

Constraints on the Black Hole Binary Mass Ratio

If the starburst was triggered by a galaxy-galaxy merger, one possible mechanism that could boost the TDE rate after the starburst is a supermassive black hole (SMBH) binary. The age since the starburst began constrains the galaxy merger mass ratio, assuming that the starburst coincided with the coalescence of the two galaxies. The SDSS images of the TDE host galaxies do not show a an obvious separation into two merging components (see Figure 6.2), so if the galaxies have recently interacted, they have already begun to coalesce. In an unequal mass merger, the dynamical friction timescale for the smaller galaxy to fall into the larger one depends on the mass ratio (Taffoni et al., 2003). In Figure 6.1b, we plot the age since the starburst began, with the top x-axis showing the corresponding merger mass ratio derived from the dynamical timescale (Taffoni et al., 2003). These merger ratios are the most unequal possible to have coalesced by the current starburst age. We assume the most conservative case considered by Taffoni et al. (2003), so many galaxy mergers with these mass ratios would have longer dynamical fraction timescales. All of the hosts but that of PTF09axc are consistent with a merger mass ratio more equal than 12 : 1.

The galaxy mass ratios should be comparable to the SMBH mass ratio formed in the merger, as SMBH mass correlates with galaxy bulge mass for a variety of galaxy types (e.g., McConnell & Ma, 2013). McConnell & Ma (2013) find the scatter in the SMBH mass - bulge mass relation to be 0.3-0.4 dex. We estimate the scatter in the bulge mass - stellar mass relation (0.56 dex) using the catalog by Mendel et al. (2013), and only considering galaxies with log stellar mass <10.5 to be consistent with the possible merger progenitors of the TDE host galaxies. Adding these uncertainties in quadrature produces an uncertainty in the total stellar mass to SMBH mass relation of 0.69 dex.

Chen et al. (2011) predict that the TDE rate scales with the SMBH mass ratio $q = M_{secondary}/M_{primary}$ as $N_* \propto q^\alpha$, where N_* is the number of TDEs during

the SMBH binary coalescence, $\alpha = (2 - \gamma)/(6 - 2\gamma)$, and γ is the slope of the inner stellar density profile $\rho_* \propto r^{-\gamma}$. If γ ranges from 1.5-2, as in Chen et al. (2011), the dependence of the number of TDEs on q is weak, with $\alpha = 0 - 0.16$. In this case, we would expect to see many more TDEs in minor mergers (lower q, or more unequal), because minor mergers are more common than major mergers. For example, simulations predict that the distribution of merger mass ratios is $\propto$ $q^{-0.3}(1-q)^{1.1}$ (Stewart et al., 2009). If the TDE rate were driven by SMBH binaries, TDEs would be primarily seen after minor mergers, unless the inner density profile is exceptionally flat ($\gamma < 0.5$). However, the inner density profile in post-starburst galaxies can be quite steep and may itself be driving the enhanced TDE rate (Stone & van Velzen, 2016). The preference of TDEs for post-merger galaxies with mass ratios more equal than 12 : 1 is thus inconsistent with arising from SMBH binary interactions, if the TDE rate does scale weakly with the SMBH mass ratio (Chen et al., 2011).

6.4.2   Stellar Masses of TDE Host Galaxies

We determine stellar masses of the TDE host galaxies as part of our stellar population fitting methodology. These stellar masses are more accurate than those derived assuming a single stellar population, as a recent starburst will impact the mass-to-light ratio. The derived stellar masses range from $10^{9.4} - 10^{10.3}$ M$_\odot$ (Table 6.2). The range in stellar masses is connected that of the supermassive black hole masses, through the black hole – bulge relation. To estimate bulge masses (also shown in Table 6.2), we use the bulge to total mass ratios from Mendel et al. (2013), for the four galaxies bright enough to have bulge:disk decompositions. We caution that bulge:disk decompositions can be unreliable for post-starburst galaxies, due to the bright, centrally concentrated A star population. We use the relation from McConnell & Ma (2013) to estimate black hole masses from the bulge masses. The black hole masses range from $10^{5.5} - 10^{7.5}$M$_\odot$. These are consistent with the black
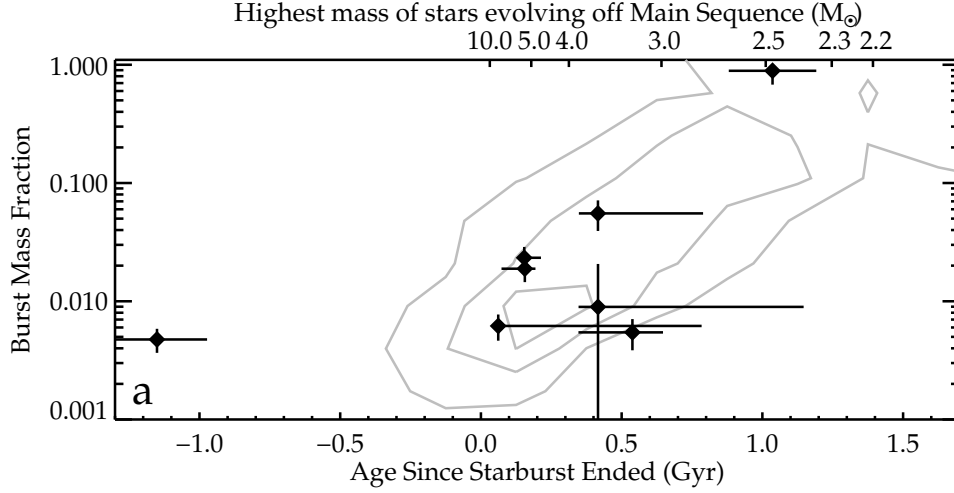
Figure 6.1: **a.** Post-burst age vs. burst mass fraction for TDE hosts and SDSS quiescent Balmer-strong comparison sample. There is a physical spread in the post-burst ages of the TDE hosts. The youngest galaxy (host of SDSS J0748) is still star-forming, and so has a "negative" post-burst age. The oldest is the host of PTF09axc, with a post-burst age of 1 Gyr. 25%, 68% and 95% contours are shown for the quiescent Balmer-strong ($H\delta_A > 1.31$ Å) sample. The TDE hosts have ages and burst mass fractions consistent with this sample. The shape of the SDSS sample contours is set by when $H\delta$ absorption decreases (at later ages for stronger bursts) on the right hand side, and by a combination of effects on the left hand side. Because galaxies with SFR $\gtrsim 300$ $M_\odot$ yr^{-1} rarely exist in the local universe, starbursts with high burst mass fractions must form stars over a longer duration, delaying their entry into our selection criteria. The TDE hosts, however, are not subject to these selection effects, and the absence of TDE hosts at long post-burst ages is physical. The top x-axis shows main sequence lifetimes corresponding to the highest mass stars that have not yet evolved off the main sequence for each post-burst age. The star disrupted in PTF09axc likely had a mass of M $\lesssim 2.5 M_\odot$. We cannot place constraints on the star disrupted in SDSS J0748, as the host galaxy is still actively forming stars. For the other host galaxies considered here, the constraints on the mass of the disrupted star range from M $\lesssim 3-10 M_\odot$, ruling out O, B, and the most massive A stars as likely disrupted stars.
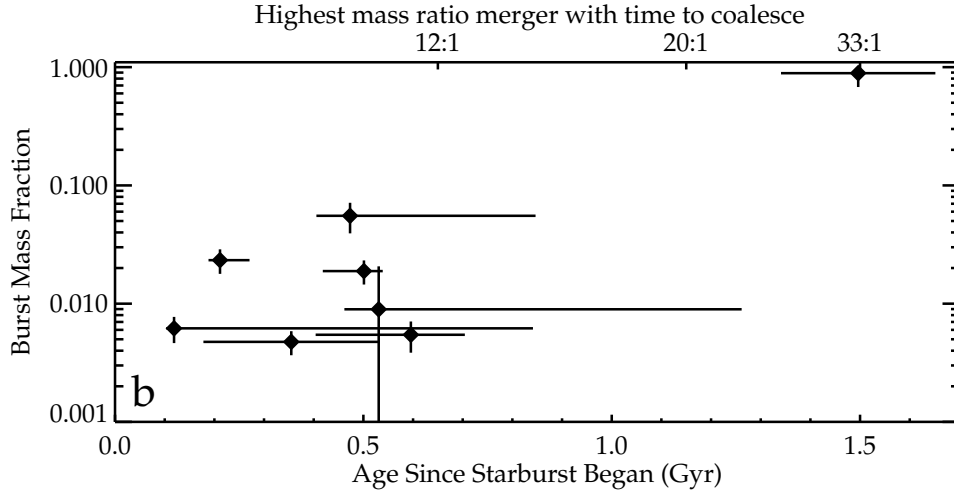
Figure 6.1: (continued) **b.** Age since the starburst began vs. burst mass fraction for TDE hosts, with the most unequal mass galaxy merger that could have coalesced via dynamical friction. All of the hosts but that of PTF09axc are consistent with a merger mass ratio more equal than 12 : 1. If supermassive black hole binaries were driving the TDE enhancement, and if the TDE rate enhancement were insensitive to the SMBH binary mass ratio (Chen et al., 2011), we would expect more unequal mass ratio mergers, since these are more common.
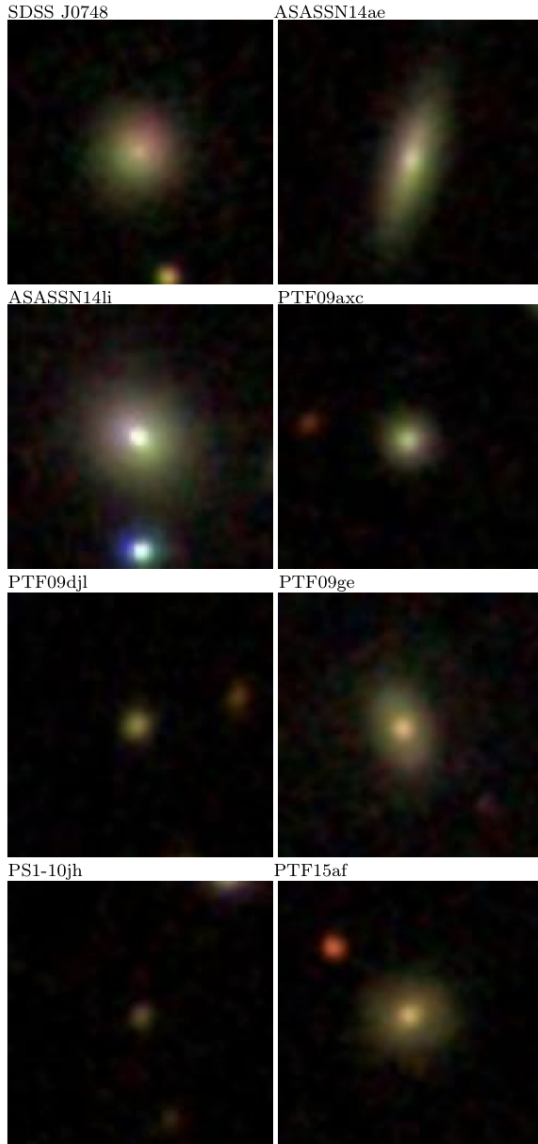
Figure 6.2: SDSS *gri* images of the TDE host galaxies. Images are $30'' \times 30''$. If these galaxies have experienced a recent merger, they are already in the coalescence phase.

hole masses expected of UV/optical TDEs (Stone & Metzger, 2016; Kochanek, 2016) and with an upper limit of $10^8 M_\odot$, above which the tidal radius is inside the event horizon and the TDE undetectable. Given these black hole masses, we also note the stellar progenitor masses predicted by Kochanek (2016) are consistent with our constraints in §6.4.1.

The stellar masses of the TDE hosts are low compared to the quiescent Balmer-strong galaxies from the SDSS, where 68% have stellar masses $10^{10.1} - 10^{11.2} M_\odot$. However, lower mass post-starbursts are too faint to be included in the SDSS spectroscopic survey at the redshifts of many of the TDE hosts. Therefore, we must compare the absolute r-band magnitudes of the TDE hosts to the volume corrected r-band galaxy luminosity function of the SDSS quiescent Balmer-strong galaxies. We calculate the volume corrections as in Simard et al. (2011). The volume corrections appropriate for the TDE host galaxies is unknown, so we crudely compare two bins in M_r: [-23, -21] mag and [-21, -18] mag. All eight TDE hosts are in the fainter bin. The ratio of the volume-corrected number of galaxies in the first bin to the second bin is 0.13, well within the binomial confidence error for the TDE host sample. Thus, if the TDE hosts have a luminosity function similar to the quiescent Balmer-strong sample, the lack of TDEs observed in intrinsically bright hosts is due to the low numbers of these bright galaxies.

With a theoretical upper limit of $10^8 M_\odot$ on the black hole mass of the TDE host galaxies, we expect to see host galaxy stellar masses of up to $\sim 10^{10.8} M_\odot$. With the current low number of TDEs, it is unclear whether the observed upper bound on TDE host stellar mass of $10^{10.3} M_\odot$ arises primarily from the falling galaxy stellar mass function, a preference of TDEs for lower stellar mass galaxies, or in fact from the limit on the black hole mass for which TDEs would be observable. With more events, a galaxy stellar mass function can be derived for the TDE hosts to search for any deviations from that expected for the quiescent Balmer-strong galaxies.

6.4.3   Hidden Emission Line Ratios

For TDE host galaxies, weak emission lines may be hidden in the strong absorption. Using the stellar population models, we can model the absorption masking the Balmer emission lines to disentangle the emission and absorption features. The emission line ratios [NII]λ6583/Hα and [OIII]λ5007/Hβ are shown in Table 6.2. To calculate the flux from each emission line, we subtract the stellar population best fit model from the data spectrum. The residual spectra are plotted in Figure 6.3. We additionally correct the zero point of the continuum by subtracting off the median level of the surrounding spectrum (λ 6400 - 6700 Å, λ 4800 - 5100 Å for each group of lines), excluding the line windows. For each line, we use the line windows defined by the MPA-JHU group (Brinchmann et al., 2004; Tremonti et al., 2004). The width of each line window is 20Å. For three of the galaxies (hosts of ASASSN-14ae, ASASSN-14li, and PTF15af), we also have the line fluxes fit by the MPA-JHU group. Our results and theirs are consistent within the measurement errors in these cases, and we choose the fit results with smaller errors (MPA-JHU line ratios for ASASSN-14ae and ASASSN-14li, our line ratios for PTF15af). For the host galaxy of PTF09ge, the [OIII]λ5007 line is contaminated, and we estimate its true flux by measuring the [OIII]λ4959 line and assuming a ratio of [OIII]λ4959/[OIII]λ5007= 1/3.

We plot the emission line ratios for the TDE host galaxies on a BPT (Baldwin et al., 1981) diagram in Figure 6.4. The host of SDSS J0748 is in the star-forming region, the hosts of ASASSN-14ae and PTF09ge are in the Seyfert region, the host of ASASSN-14li could be in the Seyfert or LINER regions, and the host of PTF09djl is largely unconstrained. We compare the BPT location of the TDE host galaxies to the quiescent Balmer-strong galaxies from SDSS with similar stellar masses, 9.5< log[M$_\star$/M$_\odot$] < 10.5, and find them consistent. Like the SDSS quiescent Balmer-strong galaxies, the TDE hosts often have emission line ratios inconsistent with ionization from star formation. We note that the high energy TDE Swift J1644 has a host galaxy with emission line ratios found to be consistent with star formation

(Levan et al., 2011).

There are several possible ionization sources in these galaxies, which might be related to the mechanism boosting the TDE rate. One possibility is a low luminosity AGN fueled by a circumnuclear gas reservoir. Interactions with the gas disk can increase the TDE rate by a factor of $10\times$ (Kennedy et al., 2016). However, in a recent merger or starburst, merger shocks (Rich et al., 2015; Alatalo et al., 2016c), which may persist through the post-starburst phase, and post-AGB stars (Yan & Blanton, 2012) also can produce emission line ratios in the LINER/Seyfert portions of the BPT diagram. Spatially resolved spectroscopy, such as that in Prieto et al. (2016), combined with stellar population modeling to account for the strong Balmer absorption, is needed to differentiate among these possibilities.

We plot the TDE host galaxies on a WHAN (Cid Fernandes et al., 2010) diagram in Figure 6.4. In comparison to the BPT diagram, the lack of a required $H\beta$ detection allows for more host galaxies to be considered. With the exception of the host of SDSS J0748, all galaxies lie in the LINER-like portion of this diagram. It is not surprising that some of the SDSS quiescent Balmer-strong and TDE host galaxies lie in the "Seyfert" portion of the BPT diagram, yet are in the "LINER-like" portion of the WHAN diagram, as this is common for galaxies with weak emission lines (Cid Fernandes et al., 2010). In the WHAN diagram, unlike in the BPT diagram, the TDE hosts lie offset from the centroid of the comparison sample of SDSS quiescent Balmer-strong galaxies. We note that the three TDE hosts with spectra from before the TDE, and thus not contaminated by the recent TDE, are more offset from the comparison galaxies. Their offset in $H\alpha$ EW is significant at 3σ, and that in [NII]/$H\alpha$ at 2σ, suggesting a lower electron density, a softer radiation field (Kewley et al., 2013), or a lower residual star formation rate. However, we caution that these conclusions rely on only three host galaxies.

The host galaxy of SDSS J0748 is an outlier in many of these comparisons. It is the only host galaxy with significant current star formation. This may not be

surprising, as its TDE was detected in a different manner than the rest, serendipitously from the SDSS (Wang et al., 2011) during a search for narrow high ionization coronal emission lines.

6.5 Conclusions

We fit stellar population models to UV and optical photometry and optical spectroscopy of eight host galaxies of optical/UV-detected tidal disruption events (TDEs). We determine the duration of the recent star formation episode, the time elapsed since it ended, and the fraction of stellar mass produced, breaking the degeneracy in these quantities. We also determine the stellar mass of the galaxies and measure residual emission line ratios in their model-subtracted spectra. We compare the TDE host galaxy properties to other quiescent galaxies with strong Balmer absorption and with the general galaxy population. We conclude the following:

1. Most (6/8) of the TDE hosts have short $(25-200$ Myr$)$ periods of star formation, consistent with a recent starburst rather than a long-term decline in star formation. The eight TDE host galaxies thus consist of six post-starburst galaxies, one star-forming galaxy, and one quiescent galaxy which experienced a long period of recent star formation.

2. Most (6/8) TDE host galaxies have post-burst ages of $60-600$ Myr. This range is physical, exceeding our measurement errors, and indicates that TDEs do not occur at a specific time after the starburst ends.

3. With the post-burst ages, we can constrain the mass of the disrupted star, assuming it formed in the burst or before. The range in post-burst ages is much larger than the expected post-main sequence evolution timescales, implying that a specific phase of post-main sequence evolution is unlikely to be the cause of the enhanced TDE rate after the starburst. If the disrupted star was
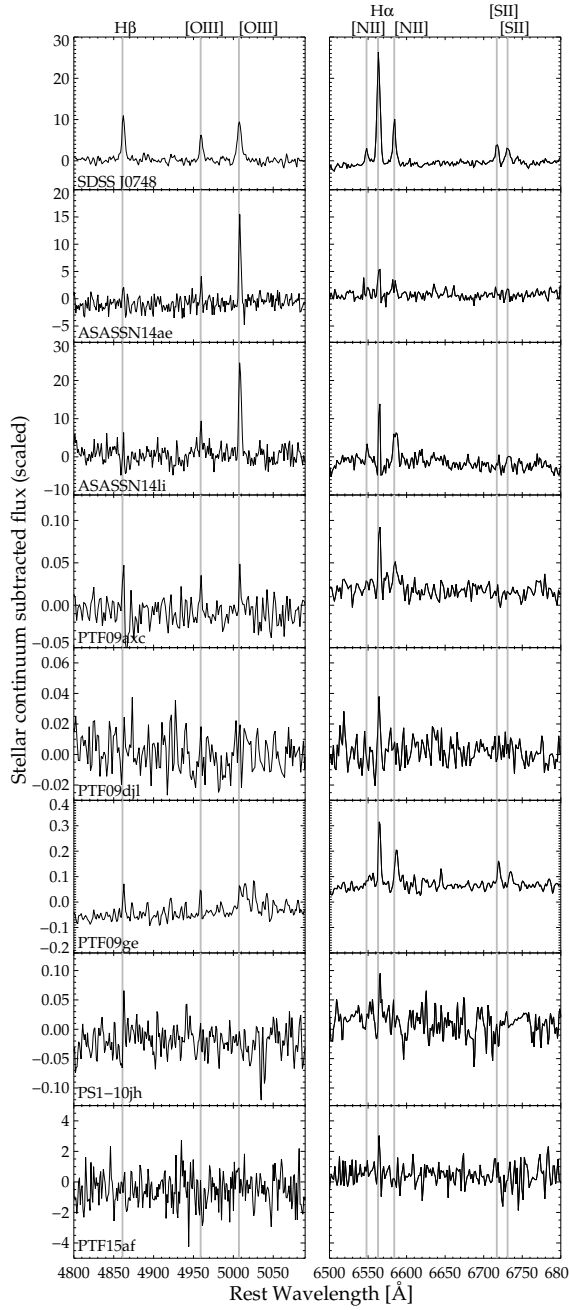
Figure 6.3: Residual TDE host galaxy spectra after subtraction of the best fit stellar population model. This corrects for the strong Balmer absorption, and uncovers hidden line emission (see Table 6.2).
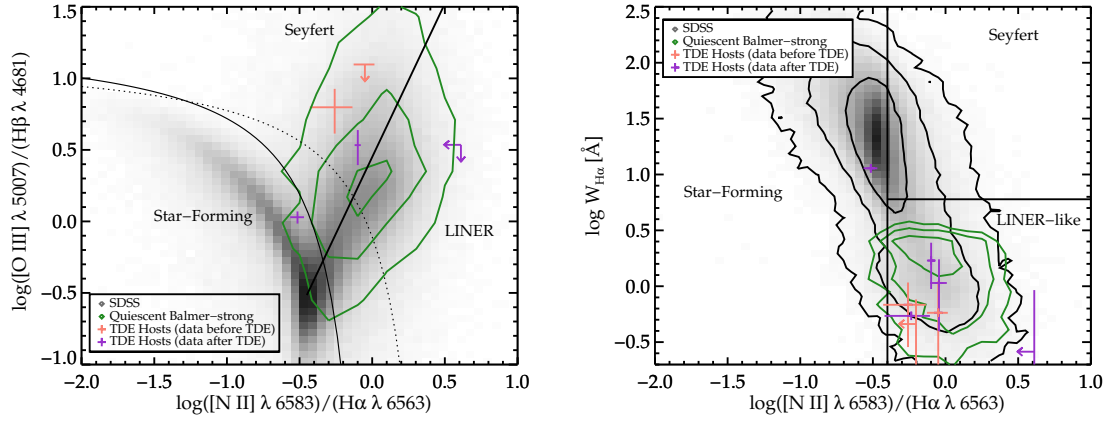
Figure 6.4: **Left:** BPT diagram for SDSS parent sample (shaded black), quiescent Balmer-strong galaxies with 9.5< $log[M_\star/M_\odot]$ < 10.5 (dark green contours: 20, 68, 95%), and TDE host galaxies (orange and purple crosses). The TDE host galaxies are consistent with the quiescent Balmer-strong comparison sample, with most having emission line ratios inconsistent with star formation. We overplot the Kewley et al. (2001) and Kauffmann et al. (2003b) separation lines as dotted and solid lines respectively. **Right:** WHAN diagram for SDSS parent sample, quiescent Balmer-strong galaxies with 9.5< $log[M_\star/M_\odot]$ < 10.5 (dark green contours: 30, 68, 85%), and TDE host galaxies. All but the SDSS J0748 host are in the LINER-like region of this diagram. The TDE hosts lie offset from the centroid of the quiescent Balmer-strong comparison sample, especially when considering only the three TDE hosts with spectra from before the TDE (shown in orange), which have no possible contamination from the TDE.

a main sequence star, the post-burst ages constrain the upper limits on its mass to be ~ 2.5, ~ 4, ~ 6, and ~ 9 M$_\odot$ for the seven non-starforming hosts. In other words, O stars, as well as most B and massive A stars, are excluded as TDE progenitors.

4. If the starburst arose from a galaxy-galaxy merger, the time elapsed since the starburst began constrains the coalescence timescale and thus limits the merger mass ratio to more equal than 12:1 in most (7/8) TDE hosts. This ratio is unusual, as more unequal galaxy mergers are more common. If this ratio also reflects that of the central supermassive black hole binary, it disfavors the scenario in which the TDE rate is boosted by the binary in a way that is insensitive to its mass ratio (e.g., Chen et al., 2011).

5. The fraction of stellar mass created in the burst is $0.5 - 10\%$ for most (7/8) of the TDE hosts. These burst mass fractions do not generate enough stars compared to those formed by a typical star-forming galaxy over the same time to account for the $30 - 200 \times$ boost in TDE ranges. If simply adding more stars does not explain the rate enhancement, their concentration in the core must be more important. Future work is needed to assess the spatial distribution of these newly formed stars in the core.

6. The TDE host galaxies have stellar masses $10^{9.4} - 10^{10.3}$, consistent with the SDSS volume-corrected distribution of post-starbursts. Using bulge:disk decompositions from Mendel et al. (2013) and the black hole – bulge relation from McConnell & Ma (2013), we infer black hole masses of $10^{5.5} - 10^{7.5}$M$_\odot$. These are consistent with the black hole masses expected for UV/optical TDEs (Stone & Metzger, 2016; Kochanek, 2016) and with an upper limit of 10^8M$_\odot$, above which the TDE would be hidden within the event horizon. With the current low number of observed TDEs, it is unclear whether the upper bound on TDE host stellar mass is primarily driven by the falloff in the galaxy stellar

mass function at high mass, by a preference of TDEs for lower stellar mass galaxies, or in fact by the upper limit on the black hole mass for which TDEs would be observable.

7. The TDE host galaxies that can be placed on a BPT (Baldwin et al., 1981) diagram have ionization sources inconsistent with star formation, except for the star-forming host of SDSS J0748. Their distribution is consistent with quiescent Balmer-strong galaxies from the SDSS at comparable stellar masses. The residual emission line ratios uncovered here point to shocks, post-AGB stars, or a low-luminosity AGN as possible ionization sources. In the case of an AGN, circumnuclear gas accreting onto the SMBH could boost the TDE rate (Kennedy et al., 2016).

8. On the WHAN (Cid Fernandes et al., 2010) diagram, at least 5/8 TDE host galaxies lie in the LINER-like region. The three TDE host galaxies with data from before the TDE (and thus uncontaminated by it) are offset to lower Hα EW and [NII]/Hα than the quiescent Balmer-strong galaxies from the SDSS at comparable stellar masses. This may indicate a lower electron density, a softer radiation field, or decreased levels of residual star formation in these TDE host galaxies.

CHAPTER 7

Conclusions

In this thesis, I have explored the evolution of the molecular gas properties and stellar populations in galaxies as they evolve through the post-starburst phase, as well as the preference of Tidal Disruption Events to occur in galaxies during this phase. In this Chapter, I summarize the main results of my work, and identify future directions.

7.1 The End of Star Formation in Galaxies

7.1.1 Conclusions from this Dissertation

In Chapter 2, we study molecular gas in a sample of 32 nearby $(0.01 < z < 0.12)$ post-starburst (aka "E+A") galaxies, whose optical spectra indicate a recent starburst that ended within the last $\sim$Gyr. We target the CO lines (1–0) and (2–1) with the IRAM 30m and SMT 10m telescopes, constraining the molecular gas mass remaining in these galaxies after the starburst. Molecular gas is detected in 17 (53%) galaxies with CO (1-0) observations from the IRAM 30m. Molecular gas masses are $M(H_2) = 10^{8.6}\text{-}10^{9.8} M_\odot$ $(\alpha_{\rm CO}/4M_\odot \,({\rm K\,km\,s^{-1}\,pc^2})^{-1})$, and molecular gas to stellar mass fractions of $f_{\rm gas} \sim 10^{-2}\text{-}10^{-0.5}$ $(\alpha_{\rm CO}/4M_\odot \,({\rm K\,km\,s^{-1}\,pc^2})^{-1})$, roughly comparable to those of star-forming galaxies and generally larger than for early types, for a range of likely CO-to-H_2 conversion factors $(\alpha_{\rm CO})$. The upper limits on $M(H_2)$ for the 15 non-detected galaxies range from $10^{7.7} M_\odot$ to $10^{9.7} M_\odot$, with the median more consistent with early-type galaxies than with star-forming galaxies.

We compare $M(H_2)$ to the star formation rate (SFR), using Hα and $D_n(4000)$ to calculate upper limits on the current SFR in this sample. When compared to

other star-forming, starbursting, and early type galaxies, the post-starbursts have $\sim 10 - 20\times$ lower SFRs for a given $M(\mathrm{H}_2)$. The post-starburst sample falls $\sim 4\times$ below other local galaxies on the Kennicutt-Schmidt relation (Kennicutt, 1998) of SFR surface density vs. $M(\mathrm{H}_2)$ surface density. The median locus of the post-starburst galaxies is offset from the relation defined by normal star-forming galaxies (K98) at 5σ significance. After considering sample selection effects, aperture bias, varying spatial extents of current star formation, optical light and H_2, CO not tracing H_2 (a different α_{CO}), and the effect of IMF assumptions, we conclude the observed offset is likely due to suppressed SFE, a low value of α_{CO} consistent with ULIRGs, and/or a bottom-heavy IMF.

Our results show that the end of the starburst in these galaxies cannot be attributed to the complete consumption, expulsion, or starvation of the molecular gas reservoirs. Understanding this possibly common phase in galaxy evolution will help reveal the physics of star formation in galaxies as well as their evolution through mergers.

This result raises two main questions: (1) How do these gas-rich post-starbursts lose their gas supplies, in order to evolve to early types? (2) Why don't post-starbursts have significant star formation, if the molecular gas remains? We address these questions in Chapters 3 and 4.

In Chapter 3, we fit stellar population models to 535 post-starburst galaxies, breaking the age - burst strength - burst duration degeneracy using a combination of UV photometry from *GALEX* (Martin et al., 2004) and optical photometry and spectroscopy from SDSS (Strauss et al., 2002; Ahn et al., 2014). We present a catalog of post burst ages, burst mass fractions, and burst durations. We derive post-burst ages and burst mass fractions, with median errors of 22% and 42%, respectively. 68% of the burst mass fractions are within 7.0%–69%, and 68% of the post-burst ages are within 240–680 Myr. We define the "post-burst" ages to be the time elapsed since 90% of the stars from the recent starburst(s) formed. The star

formation rates experienced during the starburst were ~10-100× above the stellar mass - specific star formation rate relation, consistent with those in starbursting galaxies (Schiminovich et al., 2007). Starbursts with specific star formation rates $> 10^{-8}$ yr^{-1} are rare ($< 1\%$ of the sample). As a consequence, those post-starburst galaxies with short duration (25 Myr) bursts generate 1-10% of their stellar mass in the burst, whereas galaxies with longer duration ($>$150 Myr) bursts produce 10-50% of their stellar mass in the burst. Many post-starbursts show signs of intermediate mass ($\sim$F) stellar populations; 50% of the post-starbursts are best fit by a single recent burst, 48% prefer a double recent burst, and 2% do not have a statistical preference. Lower stellar mass galaxies are more likely to experience two recent bursts, and the fraction of mass produced in their recent burst(s) is more strongly anti-correlated with their stellar mass.

We compare the SFHs selected via our selection criteria with those from other, differently-selected post-starburst samples. Rowlands et al. (2015) use the approach of Wild et al. (2007, 2009) to select longer duration ($>$150 Myr) starbursts, at a wider range of post-burst ages than we do; their sample is also biased against shorter duration starbursts that have specific star formation rates similar to our sample. Shocked POst-Starburst Galaxies (SPOGs; Alatalo et al., 2016c) have generally younger post-burst ages than ours, with 60% too young to have entered into our post-starburst selection. SPOGs with younger post-burst ages, but similar mass fractions and durations as our post-starbursts, may represent progenitors to our sample. However, an additional population (10%) of SPOGs exists at long duration ($>$ 100 Myr) and small burst fraction ($<$ 10%), which will not evolve into our post-starburst population.

Combining these three samples of post-starburst galaxies, we discover a significant decline in their molecular gas to stellar mass fraction with increasing post-burst age, at 4σ significance. This trend persists when we control for the fraction of stellar mass produced in the recent burst(s). The best fit exponentially declining timescale

is 90±10 Myr, with best fit initial molecular gas fractions of $0.5-1$ at a post-burst age of zero. With the observed molecular gas depletion rate, the post-starburst galaxies should reach early-type levels of molecular gas in $600-800$ Myr. The rapid depletion rate implied by this trend of $5-200$ $M_\odot \mathrm{yr}^{-1}$ cannot be due to current star formation, given the upper limits on the current SFRs in these post-starbursts, suggesting that the molecular gas is expelled or destroyed in AGN-driven outflows. We find significant ($> 3\sigma$) anti-correlations of the WISE [4.6]-[12] and [3.4]-[4.6] μm colors with the post-burst age of the galaxy. Given the anti-correlations of bluer WISE colors with post-burst age, either the dust mass or sources of dust heating could be declining over time, as with the gas fraction. Various heating sources are possible during this phase: star-formation, young (A) stars, evolved stars (post-AGB or TP-AGB), or AGN.

In Chapter 4, we survey the dense molecular gas content of two post-starburst galaxies possessing large reservoirs of CO-traced molecular gas, despite their lack of significant current star formation. ALMA does not detect either HCN (1–0) or HCO+ (1–0) in these galaxies. This absence of dense gas is consistent with their low star formation rates. For the first time, we have direct evidence as to why post-starburst galaxies have such low star formation rates, given their large reservoirs of CO-traced molecular gas: the denser gas required for star formation is absent.

The HCN/CO luminosity ratios are low compared to star-forming and many early type galaxies, and imply a low dense gas mass fraction, the fraction of dense molecular gas mass to total molecular gas mass. The low dense gas fraction leads to the low CO-traced star formation efficiency in these post-starburst galaxies (see French et al., 2015). The consistency of the dense gas star formation relation between post-starbursts and other galaxies implies the HCN-traced star formation efficiency is consistent among these types of galaxies and unaffected by the processes which drive the starburst and its end.

The low HCN luminosities of the post-starburst galaxies are already consistent

with the early type galaxies into which they are expected to evolve. However, the presence of significant CO-traced gas necessitates a more detailed view of how these galaxies could evolve into gas-poor early types. The decline in the CO-traced molecular gas during the post-starburst phase suggests that feedback processes from AGN activity may act at a later time, after the starburst has already ended. Thus, post-starbursts do not have significant star formation because of a lack of dense gas, and are unlikely to resume star formation after the rest of the molecular gas reservoirs are depleted, resulting in gas-poor galaxies passively evolving to "red and dead" early types. This picture of how star formation ends in galaxies undergoing rapid transition may be largely representative, as ~40-100% of galaxies are expected to evolve through this phase (Snyder et al., 2011; Wild et al., 2016).

7.1.2 Future Directions

While there is circumstantial evidence that AGN feedback is acting during the post-starburst phase, we lack direct evidence connecting the two. Our next step is to determine post-starburst galaxies' routes onto the black hole-bulge mass relation and how long they take to get there. Because the merger has coalesced, bulge growth has ended, and accurate bulge properties can be determined, avoiding the uncertainties associated with tying active mergers to the black hole-bulge mass relation, which has yielded conflicting results (Kormendy & Ho, 2013; Medling et al., 2015).

Given that we observe the molecular gas reservoirs declining during the post-starburst phase, after bulge growth has completed, if AGN feedback acts to preserve the black hole - bulge relation, we will observe a temporary offset until black hole growth ends. We expect to find young, gas-rich post-starbursts with undermassive black holes, and old, gas-poor post-starbursts to lie back on the black hole - bulge relation. With our molecular gas measurements and post-burst ages, we can identify an ensemble track of galaxies by measuring black hole masses and bulge masses of a sample of galaxies at various post-burst ages.

The stronger starbursts in our sample of post-starburst galaxies produced 30% of their current stellar mass. The new stellar mass is concentrated in the core, and grows the galactic bulges. Thus, the black hole mass should also grow by 30% during this process. For the molecular gas masses and estimated black hole masses of our sample, this represents accretion of $\sim$1% of the molecular gas by the black hole. With the typical physical scatter in the black hole - bulge relation ($\sim$ 0.3 dex; McConnell & Ma, 2013), the predicted effect will be observable.

7.2 Tidal Disruption Event Host Galaxies

7.2.1 Conclusions from this Dissertation

In Chapter 5, we demonstrate the preference of tidal disruption events (TDEs) to occur in quiescent galaxies with strong Balmer line absorption. Quiescent galaxies with the strongest Balmer absorption, $H\delta_A - \sigma(H\delta_A) > 4\text{Å}$, make up only 0.2% of local galaxies, yet host 3 of 8 optical/UV TDE candidates. A softer cut, $H\delta_A > 1.31\text{Å}$, includes only 2.3% of local galaxies, but 6 of 8 optical/UV TDE host galaxies. The optical/UV TDE rates are thus enhanced by $190^{+115}_{-100}\times$ in the strongest $H\delta_A$ galaxies and by $33^{+7}_{-11}\times$ in galaxies with $H\delta_A > 1.31\text{Å}$. Because of this preference, the corresponding rates of optical/UV TDEs are $1 - 3 \times 10^{-3}$ yr^{-1} per galaxy, and $2 - 4 \times 10^{-4}$ yr^{-1} per galaxy, respectively. As a result, we predict a lower optical/UV rate in normal star-forming and early-type galaxies, of $1 - 5 \times 10^{-6}$ yr^{-1} per galaxy. Even the one high energy TDE with a full measured optical spectrum, *Swift* J1644, lies in a galaxy with strong Balmer absorption and weak nebular line emission, which implies a $> 80\times$ enhancement in such hosts, and a link between the optical/UV and high energy TDE classes.

In Chapter 6, we fit stellar population models to UV and optical photometry and optical spectroscopy of eight host galaxies of optical/UV-detected tidal disruption events (TDEs). We constrain the duration of the recent star formation episode, the

time elapsed since it ended, and the fraction of stellar mass produced, breaking the degeneracy in these quantities. We also determine the stellar mass of the galaxies and measure residual emission line ratios in their model-subtracted spectra. We compare the TDE host galaxy properties to other quiescent galaxies with strong Balmer absorption and with the general galaxy population. Most (6/8) of the TDE hosts have short ($25-200$ Myr) periods of star formation, consistent with a recent starburst rather than a long-term decline in star formation. The eight TDE host galaxies thus consist of six post-starburst galaxies, one star-forming galaxy, and one quiescent galaxy which experienced a long period of recent star formation. Most (6/8) TDE host galaxies have post-burst ages of $60-600$ Myr. This range is physical, exceeding our measurement errors, and indicates that TDEs do not occur at a specific time after the starburst ends.

With the post-burst ages, we can constrain the mass of the disrupted star, assuming it formed in the burst or before. The range in post-burst ages is much larger than the expected post-main sequence evolution timescales, implying that a specific phase of post-main sequence evolution is unlikely to be the cause of the enhanced TDE rate after the starburst. If the disrupted star was a main sequence star, the post-burst ages constrain the upper limits on its mass to be ~2.5, ~4, ~6, and ~9 $M_\odot$ for the seven non-starforming hosts. In other words, O stars, as well as most B and massive A stars, are excluded as TDE progenitors. If the starburst arose from a galaxy-galaxy merger, the time elapsed since the starburst began constrains the coalescence timescale and thus limits the merger mass ratio to more equal than 12:1 in most (7/8) TDE hosts. This ratio is unusual, as more unequal galaxy mergers are more common. If this ratio also reflects that of the central supermassive black hole binary, it disfavors the scenario in which the TDE rate is boosted by the binary in a way that is insensitive to its mass ratio (e.g., Chen et al., 2011).

The fraction of stellar mass created in the burst is $0.5-10\%$ for most (7/8) of the TDE hosts. These burst mass fractions do not generate enough stars compared to

those formed by a typical star-forming galaxy over the same time to account for the $30 - 200\times$ boost in TDE ranges. If simply adding more stars does not explain the rate enhancement, their concentration in the core must be more important. Future work is needed to assess the spatial distribution of these newly formed stars in the core. The TDE host galaxies have stellar masses $10^{9.4} - 10^{10.3}$, consistent with the SDSS volume-corrected distribution of post-starbursts.

Using bulge:disk decompositions from Mendel et al. (2013) and the black hole – bulge relation from McConnell & Ma (2013), we infer black hole masses of $10^{5.5} - 10^{7.5} M_\odot$. These are consistent with the black hole masses expected for UV/optical TDEs (Stone & Metzger, 2016; Kochanek, 2016) and with an upper limit of $10^8 M_\odot$, above which the TDE would be hidden within the event horizon. With the current low number of observed TDEs, it is unclear whether the upper bound on TDE host stellar mass is primarily driven by the falloff in the galaxy stellar mass function at high mass, by a preference of TDEs for lower stellar mass galaxies, or in fact by the upper limit on the black hole mass for which TDEs would be observable.

The TDE host galaxies that can be placed on a BPT (Baldwin et al., 1981) diagram have ionization sources inconsistent with star formation, except for the star-forming host of SDSS J0748. Their distribution is consistent with quiescent Balmer-strong galaxies from the SDSS at comparable stellar masses. The residual emission line ratios uncovered here point to shocks, post-AGB stars, or a low-luminosity AGN as possible ionization sources. In the case of an AGN, circumnuclear gas accreting onto the SMBH could boost the TDE rate (Kennedy et al., 2016). On the WHAN (Cid Fernandes et al., 2010) diagram, at least 5/8 TDE host galaxies lie in the LINER-like region. The three TDE host galaxies with data from before the TDE (and thus uncontaminated by it) are offset to lower Hα EW and [NII]/Hα than the quiescent Balmer-strong galaxies from the SDSS at comparable stellar masses. This may indicate a lower electron density, a softer radiation field, or decreased levels of residual star formation in these TDE host galaxies.

7.2.2 Future Directions

The preference for TDEs to occur in post-starburst galaxies can be used as a tool to study TDEs in two different ways: to study what sets the TDE rate and to flag transient events as possible TDEs.

What drives the increased TDE rate in post-starburst galaxies? There are several reasons that the accretion rate of stars onto the central black hole could be connected to the recent star formation histories of their host galaxies: 1) if there was a recent galaxy-galaxy merger, the resulting supermassive black hole binary could have an increased rate of stellar accretion, 2) a high central concentration of newly formed stars would increase the number of stars available to the central black hole, or 3) a high central concentration of gas could funnel more stars to the central black hole. I am a co-I on on-going HST programs to address these questions. The first program will obtain multi-band WFC3 imaging and STIS spectroscopy for four known TDE host galaxies, and the second program will obtain multi-band WFC3 imaging of four nearby post-starburst galaxies at a spatial resolution high enough to resolve the black hole radius of influence.

To test the first possibility, we will quantify any signatures of recent galaxy-galaxy collisions from the high resolution images, and with the timing method described above, constrain the likely mass ratio of the two merged galaxies. Tidal features and disturbed morphologies are often seen in post-starburst galaxies (Zabludoff et al. 1996; Yang et al. 2004, 2008), but sufficient resolution images of the known TDE hosts have not yet been available. In the scheduled HST images, tidal tails and/or asymmetries arising from a recent major merger (with a mass ratio more equal than $\sim$4:1, depending on the post-burst age) should be visible. The time elapsed since the starburst provides a complementary constraint; given the ages we measure of the TDE host galaxies, merger ratios less equal than $\sim$12:1 will not have had time to coalesce via dynamical friction (French et al. 2016b).

To study the second reason, we will map the central concentrations of stars

in four nearby post-starburst galaxies. It is not possible to resolve the black hole radius of influence (typically 1-10 pc) of the known TDE hosts with any present-day instrument. Thus, we have identified a set of analog TDE host galaxies at closer distances, to study with our awarded *HST* program. A study of the central stellar density has been conducted for one nearby post-starburst galaxy (Stone & van Velzen 2016) with archival *HST* data, which shows a sufficiently high central stellar density to explain the observed TDE rate enhancement.

To study the third scenario, we will map the concentrations of gas and the spectral lines sensitive to the energetic gas immediately surrounding the black hole. I tested the source of the ionization sources in French et al. (2016b), using ground based spectra, sensitive to the inner 1-5 kpc of the galaxies. Most of the known TDE hosts have ionization sources inconsistent with star formation. This may indicate the presence of circumnuclear gas, also accreting onto the black hole, but other contaminating sources such as merger shocks or post-AGB stars could also explain our results. The awarded *HST* data will allow us to better localize the line emitting regions, and check for associations with the nucleus. The awarded ALMA observations of post-starburst galaxies discussed in the previous section will determine the typical distribution of the gas remaining in analog TDE host galaxies, to constrain the distribution likely for the TDE host galaxies.

The Large Synoptic Survey Telescope (LSST) will bring the opportunity to amass a sample of thousands of TDEs per year (van Velzen et al. 2011). TDEs must be identified early, so follow up observations can observe the lightcurve's rise and fall. While TDEs can in theory be identified from their optical time evolution and colors, flagging events in post-starburst hosts allows for TDEs to be followed-up *before* the time evolution is certain, and provides a way to identify TDEs that deviate from the expected template, as many already do (Holoien et al. 2016, Gezari et al. 2016) or are predicted to (MacLeod et al. 2013, Coughlin et al. 2016).

However, many of the events found by LSST will be in the southern hemisphere,

beyond the reach of galaxy spectroscopic surveys such as the SDSS, where post-starbursts can be reliably identified. In future work, I will use machine learning methods on post-starburst galaxies to develop an identification method, using only the data available for galaxies observed by LSST, to ensure that tidal disruption events can be selected for rapid follow-up observations.

REFERENCES

Aalto, S., Garcia-Burillo, S., Muller, S., et al. 2012, Astronomy and Astrophysics, 537, 44

Abazajian, K., Adelman-McCarthy, J. K., Agüeros, M. A., et al. 2004, The Astronomical Journal, 128, 502

Abazajian, K. N., Adelman-McCarthy, J. K., Agüeros, M. A., et al. 2009, The Astrophysical Journal Supplement Series, 182, 543

Ahn, C. P., Alexandroff, R., Prieto, C. A., et al. 2014, The Astrophysical Journal Supplement, 211, 17

Aihara, H., Allende Prieto, C., An, D., et al. 2011, The Astrophysical Journal Supplement Series, 193, 29

Alatalo, K., Aladro, R., Nyland, K., et al. 2016a, The Astrophysical Journal, 830, 137

Alatalo, K., Davis, T. A., Bureau, M., et al. 2013, Monthly Notices of the Royal Astronomical Society, 432, 1796

Alatalo, K., Nyland, K., Graves, G., et al. 2014, The Astrophysical Journal, 780, 11

Alatalo, K., Lacy, M., Lanz, L., et al. 2015, The Astrophysical Journal, 798, 31

Alatalo, K., Lisenfeld, U., Lanz, L., et al. 2016b, The Astrophysical Journal, 827, 106

Alatalo, K., Cales, S. L., Rich, J. A., et al. 2016c, The Astrophysical Journal Supplement Series, 224, 38

Alatalo, K., Lacy, M., Bitsakis, T., et al. 2016d, eprint arXiv:1608.00256

Arcavi, I., Gal-Yam, A., Sullivan, M., et al. 2014, The Astrophysical Journal, 793, 38

Baldwin, J. A., Phillips, M. M., & Terlevich, R. 1981, Publications of the Astronomical Society of the Pacific, 93, 5

Barger, A. J., Aragon-Salamanca, A., Ellis, R. S., et al. 1996, Monthly Notices of the Royal Astronomical Society, 279, 1

Becker, R. H., White, R. L., & Helfand, D. J. 1995, The Astrophysical Journal, 450, 559

Bergvall, N., Marquart, T., Way, M. J., et al. 2016, Astronomy & Astrophysics, 587, A72

Bigiel, F., Leroy, A. K., Blitz, L., et al. 2015, The Astrophysical Journal, 815, 103

Blanton, M. R., & Roweis, S. 2007, The Astronomical Journal, 133, 734

Bloom, J. S., Giannios, D., Metzger, B. D., et al. 2011, Science, 333, 203

Bolatto, A. D., Wolfire, M., & Leroy, A. K. 2013, Annual Review of Astronomy and Astrophysics, 51, 35

Boselli, A., & Gavazzi, G. 2006, Publications of the Astronomical Society of the Pacific, 118, 517

Bressan, A., Silva, L., & Granato, G. L. 2002, Astronomy and Astrophysics, 392, 377

Brinchmann, J., Charlot, S., White, S. D. M., et al. 2004, Monthly Notices of the Royal Astronomical Society, 351, 1151

Brown, G. C., Levan, A. J., Stanway, E. R., et al. 2015, Monthly Notices of the Royal Astronomical Society, 452, 4297

Brown, J. S., Holoien, T. W. S., Auchettl, K., et al. 2016a, Monthly Notices of the Royal Astronomical Society, 446, 4904

Brown, J. S., Shappee, B. J., Holoien, T. W. S., et al. 2016b, MNRAS, 462, 3993

Bruzual, G., & Charlot, S. 2003, Monthly Notices of the Royal Astronomical Society, 344, 1000

Burrows, D. N., Kennea, J. A., Ghisellini, G., et al. 2011, Nature, 476, 421

Buyle, P., Michielsen, D., De Rijcke, S., et al. 2006, The Astrophysical Journal, 649, 163

Cales, S. L., & Brotherton, M. S. 2015, Monthly Notices of the Royal Astronomical Society,, 449, 2374

Calzetti, D., Armus, L., Bohlin, R. C., et al. 2000, The Astrophysical Journal, 533, 682

Cappellari, M., Emsellem, E., Krajnović, D., et al. 2011, Monthly Notices of the Royal Astronomical Society, 413, 813

Cappellari, M., McDermid, R. M., Alatalo, K., et al. 2012, Nature, 484, 485

Carilli, C. C., & Walter, F. 2013, Annual Review of Astronomy and Astrophysics, 51, 105

Casey, C. M., Narayanan, D., & Cooray, A. 2014, Physics Reports, 541, 45

Cenko, S. B., Bloom, J. S., Kulkarni, S. R., et al. 2012a, Monthly Notices of the Royal Astronomical Society, 420, 2684

Cenko, S. B., Krimm, H. A., Horesh, A., et al. 2012b, The Astrophysical Journal, 753, 77

Chabrier, G. 2003, Publications of the Astronomical Society of the Pacific, 115, 763

Chang, T.-C., van Gorkom, J. H., Zabludoff, A. I., Zaritsky, D., & Mihos, J. C. 2001, The Astronomical Journal, 121, 1965

Charlot, S., & Fall, S. M. 2000, The Astrophysical Journal, 539, 718

Chen, X., Madau, P., Sesana, A., & Liu, F. K. 2009, The Astrophysical Journal Letters, 697, L149

Chen, X., Sesana, A., Madau, P., & Liu, F. K. 2011, The Astrophysical Journal, 729, 13

Chen, Y.-M., Kauffmann, G., Tremonti, C. A., et al. 2012, Monthly Notices of the Royal Astronomical Society, 421, 314

Choi, P. I., Yan, L., Im, M., et al. 2006, The Astrophysical Journal, 637, 227

Chornock, R., Berger, E., Gezari, S., et al. 2014, The Astrophysical Journal, 780, 44

Cicone, C., Maiolino, R., Sturm, E., et al. 2014, Astronomy & Astrophysics, 562, 21

Cid Fernandes, R., Stasińska, G., Schlickmann, M. S., et al. 2010, Monthly Notices of the Royal Astronomical Society, 403, 1036

Ciesla, L., Boselli, A., Elbaz, D., et al. 2016, Astronomy & Astrophysics, 585, 43

Condon, J. J. 1992, Annual Review of Astronomy and Astrophysics, 30, 575

Condon, J. J., Cotton, W. D., Greisen, E. W., et al. 1998, The Astronomical Journal, 115, 1693

Conroy, C., & Gunn, J. E. 2010, The Astrophysical Journal, 712, 833

Conroy, C., Gunn, J. E., & White, M. 2009, The Astrophysical Journal, 699, 486

Couch, W. J., & Sharples, R. M. 1987, Monthly Notices of the Royal Astronomical Society, 229, 423

Cox, T. J., Jonsson, P., Somerville, R. S., Primack, J. R., & Dekel, A. 2008, Monthly Notices of the Royal Astronomical Society, 384, 386

Crocker, A., Krips, M., Bureau, M., et al. 2012, Monthly Notices of the Royal Astronomical Society, 421, 1298

Crocker, A. F., Bureau, M., Young, L. M., & Combes, F. 2011, Monthly Notices of the Royal Astronomical Society, 410, 1197

Crockett, R. M., Kaviraj, S., Silk, J. I., et al. 2011, The Astrophysical Journal, 727, 115

Curtis, M., & Sijacki, D. 2016, Monthly Notices of the Royal Astronomical Society, 463, 63

Daddi, E., Dannerbauer, H., Krips, M., et al. 2009, The Astrophysical Journal Letters, 695, L176

Davies, R., Sanchez, F. M., Genzel, R., et al. 2007, The Astrophysical Journal, 671, 1388

Davis, T. A., Young, L. M., Crocker, A. F., et al. 2014, Monthly Notices of the Royal Astronomical Society, 444, 3427

de Vries, W. H., Hodge, J. A., Becker, R. H., White, R. L., & Helfand, D. J. 2007, The Astronomical Journal, 134, 457

Diamond-Stanic, A. M., Moustakas, J., Tremonti, C. A., et al. 2012, The Astrophysical Journal, 755, L26

Downes, D., & Solomon, P. M. 1998, The Astrophysical Journal, 507, 615

Dressler, A., & Gunn, J. E. 1983, The Astrophysical Journal, 270, 7

Dressler, A., Smail, I., Poggianti, B. M., et al. 1999, The Astrophysical Journal Supplement Series, 122, 51

Drory, N., MacDonald, N., Bershady, M. A., et al. 2015, The Astronomical Journal,, 149, 77

Du, W., Luo, A. L., Prugniel, P., Liang, Y. C., & Zhao, Y. H. 2010, Monthly Notices of the Royal Astronomical Society, 409, 567

Elbaz, D., Dickinson, M., Hwang, H. S., et al. 2011, Astronomy & Astrophysics, 533, A119

Evans, C. R., & Kochanek, C. S. 1989, The Astrophysical Journal, 346, L13

Falkenberg, M. A., Kotulla, R., & Fritze, U. 2009, Monthly Notices of the Royal Astronomical Society, 397, 1940

Ferrarese, L., & Merritt, D. 2000, The Astrophysical Journal, 539, L9

Feruglio, C., Maiolino, R., Piconcelli, E., et al. 2010, Astronomy and Astrophysics, 518, 4

French, K. D., Arcavi, I., & Zabludoff, A. 2016, ApJ, 818, L21

—. 2017, The Astrophysical Journal, 835, 176

French, K. D., Yang, Y., Zabludoff, A., et al. 2015, The Astrophysical Journal, 801, 1

Gallazzi, A., Charlot, S., Brinchmann, J., White, S. D. M., & Tremonti, C. A. 2005, Monthly Notices of the Royal Astronomical Society, 362, 41

Gao, Y., & Solomon, P. M. 2004, The Astrophysical Journal, 606, 271

Geha, M., Blanton, M. R., Yan, R., & Tinker, J. L. 2012, The Astrophysical Journal, 757, 85

Gehrels, N. 1986, The Astrophysical Journal, 303, 336

Genzel, R., Tacconi, L. J., Gracia-Carpio, J., et al. 2010, Monthly Notices of the Royal Astronomical Society, 407, 2091

Gezari, S., Chornock, R., Rest, A., et al. 2012, Nature, 485, 217

Goto, T. 2007, Monthly Notices of the Royal Astronomical Society, 377, 1222

Goto, T., Nichol, R. C., Okamura, S., et al. 2003, Publications of the Astronomical Society of Japan, 55, 771

Graciá-Carpio, J., García-Burillo, S., Planesas, P., Fuente, A., & Usero, A. 2008, Astronomy and Astrophysics, 479, 703

Guillochon, J., Manukian, H., & Ramirez-Ruiz, E. 2014, The Astrophysical Journal, 783, 23

Hayward, C. C., Lanz, L., Ashby, M. L. N., et al. 2014, Monthly Notices of the Royal Astronomical Society, 445, 1598

Heckman, T. M., Crane, P. C., & Balick, B. 1980, Astronomy and Astrophysics Supplement Series, 40, 295

Heiderman, A., Evans, N. J., Allen, L. E., Huard, T., & Heyer, M. 2010, The Astrophysical Journal, 723, 1019

Helfer, T., & Blitz, L. 1997, The Astrophysical Journal, 478, 233

Hemmati, S., Mobasher, B., Darvish, B., et al. 2015, The Astrophysical Journal, 814, 46

Hills, J. G. 1975, Nature, 254, 295

Hogg, D. W., Masjedi, M., Berlind, A. A., et al. 2006, The Astrophysical Journal, 650, 763

Holoien, T. W.-S., Prieto, J. L., Bersier, D., et al. 2014, Monthly Notices of the Royal Astronomical Society, 445, 3263

Holoien, T. W.-S., Kochanek, C. S., Prieto, J. L., et al. 2016, Monthly Notices of the Royal Astronomical Society, 455, 2918

Hopkins, P. F., Hernquist, L., Cox, T. J., et al. 2006, The Astrophysical Journal Supplement Series, 163, 1

Hopkins, P. F., Narayanan, D., Murray, N., & Quataert, E. 2013, Monthly Notices of the Royal Astronomical Society, 433, 69

Kauffmann, G. 2014, Monthly Notices of the Royal Astronomical Society, 441, 2717

Kauffmann, G., Heckman, T. M., Simon White, D. M., et al. 2003a, Monthly Notices of the Royal Astronomical Society, 341, 33

Kauffmann, G., Heckman, T. M., Tremonti, C., et al. 2003b, Monthly Notices of the Royal Astronomical Society, 346, 1055

Kauffmann, G., Heckman, T. M., Budavari, T., et al. 2007, The Astrophysical Journal Supplement Series, 173, 357

Kaviraj, S., Schawinski, K., Devriendt, J. E. G., et al. 2007, The Astrophysical Journal Supplement Series, 173, 619

Kennedy, G. F., Meiron, Y., Shukirgaliyev, B., et al. 2016, Monthly Notices of the Royal Astronomical Society, 460, 240

Kennicutt, J. 1998, The Astrophysical Journal, 498, 541

Kennicutt, R. 1992, The Astrophysical Journal Supplement Series, 79, 255

Kennicutt, R. C., Tamblyn, P., & Congdon, C. E. 1994, The Astrophysical Journal, 435, 22

Kennicutt, R. C., Hao, C.-N., Calzetti, D., et al. 2009, The Astrophysical Journal, 703, 1672

Kennicutt, Jr., R. C., Calzetti, D., Walter, F., et al. 2007, The Astrophysical Journal, 671, 333

Kepley, A. A., Leroy, A. K., Frayer, D., et al. 2014, The Astrophysical Journal Letters, 780, L13

Kewley, L., Jansen, R., & Geller, M. 2005, Publications of the Astronomical Society of the Pacific, 117, 227

Kewley, L. J., Dopita, M. A., Leitherer, C., et al. 2013, The Astrophysical Journal, 774, 100

Kewley, L. J., Dopita, M. A., Sutherland, R. S., Heisler, C. A., & Trevena, J. 2001, The Astrophysical Journal, 556, 121

Kochanek, C. S. 2016, Monthly Notices of the Royal Astronomical Society, 461, 371

Kohno, K., Tosaki, T., Matsushita, S., et al. 2002, Publications of the Astronomical Society of Japan, 54, 541

Kormendy, J., & Ho, L. C. 2013, Annual Review of Astronomy and Astrophysics, 51, 511

Kriek, M., Labbé, I., Conroy, C., et al. 2010, The Astrophysical Journal Letters, 722, L64

Krumholz, M. R. 2013, Monthly Notices of the Royal Astronomical Society, 437, 1662

Krumholz, M. R., & Tan, J. C. 2007, The Astrophysical Journal, 654, 304

Krumholz, M. R., & Thompson, T. A. 2007, The Astrophysical Journal, 669, 289

Lada, C. J., Forbrich, J., Lombardi, M., & Alves, J. F. 2012, The Astrophysical Journal, 745, 190

Lanz, L., Zezas, A., Brassington, N., et al. 2013, The Astrophysical Journal, 768, 90

Larson, R. B., Tinsley, B. M., & Caldwell, C. N. 1980, The Astrophysical Journal, 237, 692

Lavezzi, T. E., Dickey, J. M., Casoli, F., & Kazès, I. 1999, The Astronomical Journal, 117, 1995

Lee, J. C., Gil de Paz, A., Tremonti, C., et al. 2009, The Astrophysical Journal, 706, 599

Leitherer, C., Ekström, S., Meynet, G., et al. 2014, The Astrophysical Journal Supplement Series, 212, 14

Leonardi, A. J., & Rose, J. A. 1996, The Astronomical Journal, 111, 182

Leroy, A. K., Walter, F., Brinks, E., et al. 2008, The Astronomical Journal, 136, 2782

Levan, A. J., Tanvir, N. R., Cenko, S. B., et al. 2011, Science, 333, 199

Li, S., Liu, F. K., Berczik, P., & Spurzem, R. 2017, The Astrophysical Journal, 834, 195

Liszt, H. S., & Pety, J. 2012, Astronomy & Astrophysics, 541, A58

Liu, C. T., & Green, R. F. 1996, The Astrophysical Journal Letters, 458, L63

Lodato, G., & Rossi, E. 2011, MNRAS, 410, 359

MacLeod, M., Guillochon, J., & Ramirez-Ruiz, E. 2012, The Astrophysical Journal, 757, 134

MacLeod, M., Ramirez-Ruiz, E., Grady, S., & Guillochon, J. 2013, The Astrophysical Journal, 777, 133

Magorrian, J., & Tremaine, S. 1999, Monthly Notices of the Royal Astronomical Society, 309, 447

Maraston, C. 2005, Monthly Notices of the Royal Astronomical Society, 362, 799

Maraston, C., Daddi, E., Renzini, A., et al. 2006, The Astrophysical Journal, 652, 85

Maraston, C., & Strömbäck, G. 2011, Monthly Notices of the Royal Astronomical Society, 418, 2785

Marigo, P., Girardi, L., Bressan, A., et al. 2008, Astronomy and Astrophysics, 482, 883

Martig, M., Bournaud, F., Teyssier, R., & Dekel, A. 2009, The Astrophysical Journal, 707, 250

Martig, M., Crocker, A. F., Bournaud, F., et al. 2013, Monthly Notices of the Royal Astronomical Society, 432, 1914

Martin, D. C., Fanson, J., Schiminovich, D., et al. 2004, The Astrophysical Journal Letters, 619, L1

Martin, D. C., Wyder, T. K., Schiminovich, D., et al. 2007, The Astrophysical Journal Supplement Series, 173, 342

Matsushita, S., Kawabe, R., Kohno, K., Tosaki, T., & Vila-Vilaro, B. 2010, Publications of the Astronomical Society of Japan, 62, 409

McConnell, N. J., & Ma, C.-P. 2013, The Astrophysical Journal, 764, 184

McQuinn, K. B. W., Skillman, E. D., Cannon, J. M., et al. 2010, The Astrophysical Journal, 721, 297

Medling, A. M., U., V., Max, C. E., et al. 2015, The Astrophysical Journal, 803, 61

Melnick, J., & De Propris, R. 2013, Monthly Notices of the Royal Astronomical Society, 431, 2034

Mendel, J. T., Simard, L., Ellison, S. L., & Patton, D. R. 2013, Monthly Notices of the Royal Astronomical Society, 429, 2212

Mendel, J. T., Simard, L., Palmer, M., Ellison, S. L., & Patton, D. R. 2014, The Astrophysical Journal Supplement Series, 210, 3

Mihos, C., & Hernquist, L. 1994, Astrophysical Journal Letters, 431, L9

Morić, I., Smolčić, V., Kimball, A., et al. 2010, The Astrophysical Journal, 724, 779

Morrissey, P., Conrow, T., Barlow, T. A., et al. 2007, The Astrophysical Journal Supplement Series, 173, 682

Muratov, A. L., Keres, D., Faucher-Giguere, C.-A., et al. 2015, Monthly Notices of the Royal Astronomical Society, 454, 2691

Narayanan, D., Krumholz, M., Ostriker, E. C., & Hernquist, L. 2011, Monthly Notices of the Royal Astronomical Society, 418, 664

Narayanan, D., Krumholz, M. R., Ostriker, E. C., & Hernquist, L. 2012, Monthly Notices of the Royal Astronomical Society, 421, 3127

Narayanan, D., Cox, T. J., Kelly, B., et al. 2008, The Astrophysical Journal Supplement Series, 176, 331

Nesvadba, N. P. H., Boulanger, F., Salomé, P., et al. 2010, Astronomy and Astrophysics, 521, A65

Norton, S. A., Gebhardt, K., Zabludoff, A. I., & Zaritsky, D. 2001, The Astrophysical Journal, 557, 150

O'Donnell, J. E. 1994, The Astrophysical Journal, 422, 158

Osterbrock, D. E. 1974, Astrophysics of gaseous nebulae (San Francisco: Freeman)

Pawlik, M. M., Wild, V., Walcher, C. J., et al. 2015, Monthly Notices of the Royal Astronomical Society, 456, 3032

Petrosian, V. 1976, The Astrophysical Journal, 209, L1

Phinney, E. S. 1989, IAUSymp. 136, The Center of the Galaxy, ed. M.Morris (Dordrecht: Kluwer), 543

Pontzen, A., Tremmel, M., Roth, N., et al. 2016, Monthly Notices of the Royal Astronomical Society, 465, 547

Pracy, M. B., Kuntschner, H., Couch, W. J., et al. 2009, Monthly Notices of the Royal Astronomical Society, 396, 1349

Pracy, M. B., Owers, M. S., Zwaan, M., et al. 2014, Monthly Notices of the Royal Astronomical Society, 443, 388

Pracy, M. B., Croom, S., Sadler, E., et al. 2013, Monthly Notices of the Royal Astronomical Society, 432, 3131

Prentice, S., Ashall, C., Inserra, C., et al. 2015, The Astronomer's Telegram, No.7936

Prieto, J. L., Krühler, T., Anderson, J. P., et al. 2016, The Astrophysical Journal Letters, 830, L32

Quintero, A. D., Hogg, D. W., Blanton, M. R., et al. 2004, The Astrophysical Journal, 602, 190

Rees, M. J. 1988, Nature, 333, 523

Regan, M. W., Thornley, M. D., Helfer, T. T., et al. 2001, The Astrophysical Journal, 561, 218

Renaud, F., Bournaud, F., & Duc, P.-A. 2015, Monthly Notices of the Royal Astronomical Society, 446, 2038

Rich, J. A., Kewley, L. J., & Dopita, M. A. 2011, The Astrophysical Journal, 734, 87

—. 2015, The Astrophysical Journal Supplement Series, 221, 28

Rowlands, K., Wild, V., Nesvadba, N., et al. 2015, Monthly Notices of the Royal Astronomical Society, 448, 258

Rupke, D. S. N., & Veilleux, S. 2011, The Astrophysical Journal, 729, L27

Saintonge, A., Kauffmann, G., Kramer, C., et al. 2011, Monthly Notices of the Royal Astronomical Society, 415, 32

Saintonge, A., Tacconi, L. J., Fabello, S., et al. 2012, The Astrophysical Journal, 758, 73

Salas, P., Galaz, G., Salter, D., et al. 2014, The Astrophysical Journal, 797, 134

Salim, S., Rich, R. M., Charlot, S., et al. 2007, The Astrophysical Journal Supplement Series, 173, 267

Schawinski, K., Kaviraj, S., Khochfar, S., et al. 2007, The Astrophysical Journal Supplement Series, 173, 512

Schawinski, K., Lintott, C. J., Thomas, D., et al. 2009, The Astrophysical Journal, 690, 1672

Schawinski, K., Urry, C. M., Simmons, B. D., et al. 2014, Monthly Notices of the Royal Astronomical Society, 440, 889

Schiminovich, D., Wyder, T. K., Martin, D. C., et al. 2007, The Astrophysical Journal Supplement Series, 173, 315

Schruba, A., Leroy, A. K., Walter, F., et al. 2011, The Astronomical Journal, 142, 37

Scoville, N., Sheth, K., Walter, F., et al. 2015, The Astrophysical Journal, 800, 70

Sell, P. H., Tremonti, C. A., Hickox, R. C., et al. 2014, Monthly Notices of the Royal Astronomical Society, 441, 3417

Shioya, Y., Bekki, K., & Couch, W. J. 2004, The Astrophysical Journal, 601, 654

Shioya, Y., Bekki, K., Couch, W. J., & De Propris, R. 2002, The Astrophysical Journal, 565, 223

Simard, L., Trevor Mendel, J., Patton, D. R., Ellison, S. L., & McConnachie, A. W. 2011, The Astrophysical Journal Supplement Series, 196, 11

Simha, V., Weinberg, D. H., Conroy, C., et al. 2014, arXiv:1404.0402

Singh, R., van de Ven, G., Jahnke, K., et al. 2013, Astronomy & Astrophysics, 558, A43

Skrutskie, M. F., Cutri, R. M., Stiening, R., et al. 2006, The Astronomical Journal, 131, 1163

Smethurst, R. J., Lintott, C. J., Simmons, B. D., et al. 2015, Monthly Notices of the Royal Astronomical Society, 450, 435

Snyder, G. F., Cox, T. J., Hayward, C. C., Hernquist, L., & Jonsson, P. 2011, The Astrophysical Journal, 741, 77

Solomon, P. M., Downes, D., Radford, S. J. E., & Barrett, J. W. 1997, The Astrophysical Journal, 478, 144

Sparre, M., Hayward, C. C., Feldmann, R., et al. 2015, Monthly Notices of the Royal Astronomical Society, 446, 88

Sparre, M., & Springel, V. 2016, Monthly Notices of the Royal Astronomical Society, 462, 2418

Stephens, I. W., Jackson, J. M., Whitaker, J. S., et al. 2016, The Astrophysical Journal, 824, 29

Stewart, K. R., Bullock, J. S., Barton, E. J., & Wechsler, R. H. 2009, The Astrophysical Journal, 702, 1005

Stone, N. C., & Metzger, B. D. 2016, Monthly Notices of the Royal Astronomical Society, 455, 859

Stone, N. C., & van Velzen, S. 2016, The Astrophysical Journal Letters, 825, L14

Strauss, M. A., Weinberg, D. H., Lupton, R. H., et al. 2002, The Astronomical Journal, 124, 1810

Swinbank, A. M., Balogh, M. L., Bower, R. G., et al. 2012, Monthly Notices of the Royal Astronomical Society, 420, 672

Tacconi, L. J., Genzel, R., Smail, I., et al. 2008, The Astrophysical Journal, 680, 246

Taffoni, G., Mayer, L., Colpi, M., & Governato, F. 2003, Monthly Notices of the Royal Astronomical Society, 341, 434

Tremonti, C. A., Moustakas, J., & Diamond-Stanic, A. M. 2007, The Astrophysical Journal Letters, 663, L77

Tremonti, C. A., Heckman, T. M., Kauffmann, G., et al. 2004, The Astrophysical Journal, 613, 898

Utomo, D., Kriek, M., Labbé, I., Conroy, C., & Fumagalli, M. 2014, The Astrophysical Journal Letters, 783, L30

van Dokkum, P. G., & Conroy, C. 2010, Nature, 468, 940

—. 2012, The Astrophysical Journal, 760, 70

van Velzen, S., & Farrar, G. R. 2014, The Astrophysical Journal, 792, 53

van Velzen, S., Farrar, G. R., Gezari, S., et al. 2011, The Astrophysical Journal, 741, 73

Wang, T.-G., Zhou, H.-Y., Wang, L.-F., Lu, H.-L., & Xu, D. 2011, The Astrophysical Journal, 740, 85

Wild, V., Almaini, O., Dunlop, J., et al. 2016, Monthly Notices of the Royal Astronomical Society, 463, 832

Wild, V., Heckman, T., & Charlot, S. 2010, Monthly Notices of the Royal Astronomical Society, 405, 933

Wild, V., Kauffmann, G., Heckman, T., et al. 2007, Monthly Notices of the Royal Astronomical Society, 381, 543

Wild, V., Walcher, C. J., Johansson, P. H., et al. 2009, Monthly Notices of the Royal Astronomical Society, 395, 144

Wong, O. I., Schawinski, K., Kaviraj, S., et al. 2012, Monthly Notices of the Royal Astronomical Society, 420, 1684

Worthey, G., Faber, S. M., Gonzalez, J. J., & Burstein, D. 1994, The Astrophysical Journal Supplement Series, 94, 687

Worthey, G., & Ottaviani, D. L. 1997, The Astrophysical Journal Supplement Series, 111, 377

Wright, E. L., Eisenhardt, P. R. M., Mainzer, A., et al. 2010, The Astronomical Journal, 140, 1868

Wu, J., Evans, N. J., Shirley, Y. L., & Knez, C. 2010, The Astrophysical Journal Supplement Series, 188, 313

Wu, J., Evans II, N. J., Gao, Y., et al. 2005, The Astrophysical Journal Letters, 635, L173

Yagi, M., Goto, T., & Hattori, T. 2006, The Astrophysical Journal, 642, 152

Yamauchi, C., & Goto, T. 2005, Monthly Notices of the Royal Astronomical Society, 359, 1557

Yan, R., & Blanton, M. R. 2012, The Astrophysical Journal, 747, 61

Yan, R., Newman, J. A., Faber, S. M., et al. 2006, The Astrophysical Journal, 648, 281

Yang, C.-W., Wang, T.-G., Ferland, G., et al. 2013, The Astrophysical Journal, 774, 46

Yang, Y., Tremonti, C. A., Zabludoff, A. I., & Zaritsky, D. 2006, The Astrophysical Journal, 646, L33

Yang, Y., Zabludoff, A. I., Zaritsky, D., Lauer, T. R., & Mihos, J. C. 2004, The Astrophysical Journal, 607, 258

Yang, Y., Zabludoff, A. I., Zaritsky, D., & Mihos, J. C. 2008, The Astrophysical Journal, 688, 945

Yesuf, H. M., Faber, S. M., Trump, J. R., et al. 2014, The Astrophysical Journal, 792, 84

Yoon, Y., Im, M., Jeon, Y., et al. 2015, The Astrophysical Journal, 808, 96

York, D. G., Adelman, J., Anderson, Jr., J. E., et al. 2000, The Astronomical Journal, 120, 1579

Young, L. M., Bureau, M., Davis, T. A., et al. 2011, Monthly Notices of the Royal Astronomical Society, 414, 940

Zabludoff, A. I., Zaritsky, D., Lin, H., et al. 1996, The Astrophysical Journal, 466, 104

Zauderer, B. A., Berger, E., Soderberg, A. M., et al. 2011, Nature, 476, 425

Zibetti, S., Gallazzi, A., Charlot, S., Pierini, D., & Pasquali, A. 2012, Monthly Notices of the Royal Astronomical Society, 428, 1479

Zwaan, M. A., Kuntschner, H., Pracy, M. B., & Couch, W. J. 2013, Monthly Notices of the Royal Astronomical Society, 432, 8